PEARL
Web: https://www.pearl-hifi.com 1 - 94 Broadway St. West, Nakusp, BC V0G 1R0
E-mail: sales@pearl-hifi.com Land: + 403.244.4434 Mobile: + 587.578.4434
Perkins Electro-Acoustic Research Laboratory, Inc. Engineering and Intuition Serving the Soul of Music

Please note that the links in the PEARL logotype above are "live" and can be used to direct your web browser to our site or to open an e-mail message window addressed to ourselves.

To view our item listings on eBay, click here.

To see the feedback we have left for our customers, click here.

Vibration Patterns and Radiation Behavior of Loudspeaker Cones*

F. J. M. FRANKORT†

Hogere Technische School, Heerlen, The Netherlands

Many treatments of loudspeakers begin with the comment that the loudspeaker is the weakest link in the audio reproduction chain. The complex vibrational behavior of the conical loudspeaker diaphragm, which noticeably affects the frequency response of the loudspeaker, has been a frequent challenge to mathematical analysis. Only recently, however, with the availability of the computer to carry out extensive numerical computations, has it been possible to obtain any detailed picture of the behavior of the loudspeaker cone. The picture gives a satisfactory explanation of the irregularities in the behavior of the cone as a radiator, which had long been known from acoustic measurements. At the same time it has now become possible to indicate the dimensions and material properties that will produce the desired frequency response.

INTRODUCTION: The behavior of the conical diaphragm, a shape that was intuitively chosen for loudspeakers right from the beginning, is rather complex. The audible sound spectrum contains widely different frequencies (about 16 Hz to 20 000 Hz); when alternating currents of these frequencies are fed to a single loudspeaker, the diaphragm will be caused to vibrate in different modes of lower and higher order. It is only at low frequencies that the cone vibrates as a rigid body. It is not stiff enough to withstand the inertial forces that occur at higher frequencies; it starts to vibrate in parts and the cone is said to "break up." The higher order modes of vibration that now appear enable the loudspeaker to fulfill its function at higher frequencies and set the air in motion.

The amount of the air displacement depends to a great extent on whether the cone is caused to vibrate at its resonant frequencies; hence the marked variation of the sound radiation as a function of frequency. As can be seen in Fig. 1, measurement of the pressure response with a microphone at some distance from the loudspeaker produces a rather irregular curve.

In the ideal case the sound radiation would have the same amplitude at all frequencies, and the frequency response would be linear. Loudspeaker cones that approximate to this requirement have hitherto been designed mainly on empirical lines. An efficient design procedure requires detailed knowledge of the radiation behavior and its effect on the properties of the cone material. The necessary detailed information can be obtained by setting up the differential equations that describe the cone vibrations and then, in the absence of an analytical solution, solving them numerically for a large number of frequencies. This is now possible with the computer.

In this way frequency and directivity characteristics can be calculated. We have made such calculations and found that the general shape of the curves agrees well with the measured curves.[1] This agreement largely depends on the correct prediction of the various natural frequencies of the cone. Once these are known, together with various other characteristic frequencies, the shape of the frequency response can be broadly predicted. Conversely, in designing a loudspeaker cone, it is possible to derive the locations of the characteristic frequencies from the shape

* Reprinted with permission from the *Philips Technical Review*, vol. 36, no. 1, pp. 1–15 (1976).

†Formerly with Philips Research Laboratories, Eindhoven, The Netherlands.

[1] An extensive treatment is given in [1].

of the desired characteristic.

To obtain a good understanding of the numerical results it is necessary to take into account the behavior of the longitudinal and transverse waves on an elastic cone. Before presenting the results of the calculations, we shall therefore give a general picture of this behavior when certain simplifications are introduced. The complexities in the vibrational behavior of an elastic conical diaphragm are of course not encountered in the hypothetical case of a diaphragm in which every point describes the same movement, so that it moves to and fro like a rigid piston. This hypothetical case will serve to introduce some important concepts and define some characteristic frequencies.

1. RIGID CONE

Fig. 2 shows a cross section of a typical loudspeaker construction. The conical diaphragm D is flexibly mounted by means of an outer suspension or rim OS and an inner suspension IS. This method of suspension only allows an axial motion. The drive force is supplied by the voice coil VC, which moves in the air gap of a permanent magnet M. The mass of the cone and voice coil and the stiffness of the suspension form the elements of a spring-mass system whose resonant frequency is f_0.

Above this frequency the alternating drive force mainly serves to overcome the inertia of cone and voice coil. If the force is the same at all frequencies, the amplitude of the acceleration will also be the same at all frequencies; the velocity decreases with increasing frequency.

What consequences does this have for the sound radiation? To answer this question we calculate the sound pressure that the movements of the diaphragm produce at a point some distance away from the loudspeaker. We treat the vibrating diaphragm here as a collection of point sources uniformly distributed over the surface, and we add together the contributions from all these point sources. For simplicity we first consider the diaphragm as a flat piston and assume that it vibrates in an infinite baffle. Assuming that the amplitude of the piston velocity is fixed, we then find that the sound pressure at the point of observation increases linearly with the frequency. This increase exactly compensates for the velocity decrease due to inertia, and the result for a fixed drive force is thus a fixed frequency-independent sound pressure.

This is valid above f_0, but only for low frequencies. The pathlength to the point of observation is not the same for all the individual point sources on the piston, and therefore their contributions to the total sound pressure do not arrive exactly in phase. In the case of very long waves the difference in pathlength is not significant, but at shorter wavelengths, that is, higher frequencies, it leads to phase differences that cannot be neglected. These are greater for radiation to the sides, so that the piston does not radiate the same power in all directions; at higher frequencies the piston exhibits a directional effect. The forward radiation is the strongest, and therefore sound-pressure measurements are nearly always made with the microphone on the axis of symmetry of the loudspeaker.

When a frequency characteristic is recorded with a microphone on the axis of the piston, nothing is noticed of the directivity at higher frequencies (see the frequency characteristic in Fig. 3**a**, dashed curve). However, when the total sound power radiated in all directions is measured (for example, by using several microphones) a decrease is

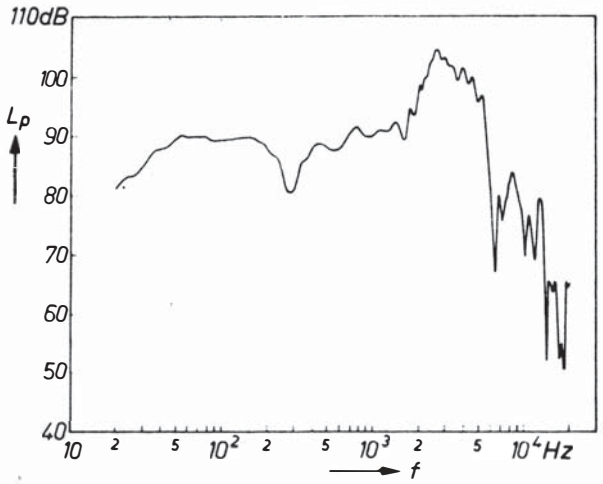

Fig. 1. Example of the frequency characteristic of a loudspeaker. The sound-pressure level L_p is measured as a function of the frequency f at a distance of 10 meters. The loudspeaker was mounted in a baffle.

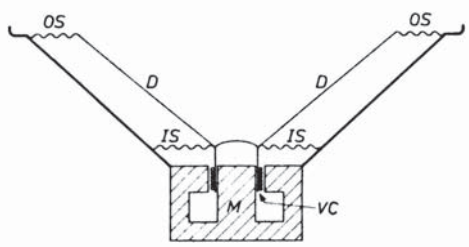

Fig. 2. Cross section of a loudspeaker. D—diaphragm; OS—outer suspension; IS—inner suspension; VC—voice coil; M—permanent magnet.

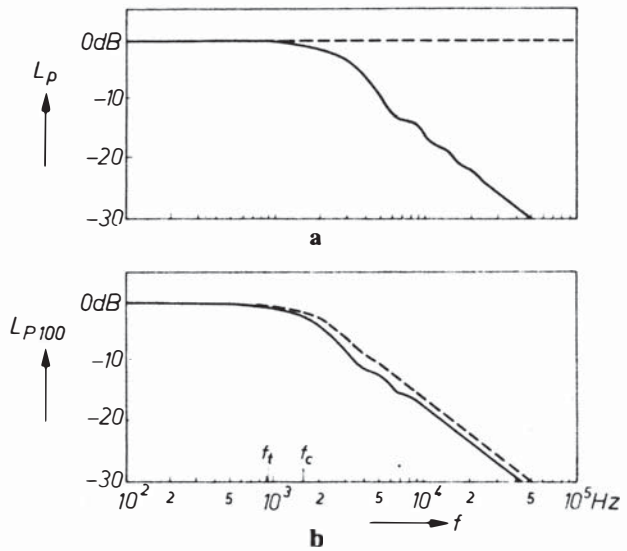

Fig. 3.**a**. Frequency characteristic of sound-pressure level L_p with a rigid piston (dashed curve) and with a rigid cone (solid curve). **b**. Frequency characteristic of the total sound power radiated inside a conical region of apex angle 100°. f_t — frequency above which a rigid piston gives a directional effect; f_c — frequency above which pathlength differences due to the depth of the cone reduce the sound radiation.

observed when the directivity starts to appear (Fig. 3**b**, dashed curve). The transition is gradual, but for practical reasons we define a transition frequency f_t. When the horizontal and sloping parts of the dashed curve in Fig. 3**b** are extended, they intersect at this frequency. The sound wavelength at this frequency is found to be approximately equal to the circumference of the piston.

We shall now go a step further and assume that the rigid piston has the shape of a loudspeaker cone. The calculation of the sound radiation now becomes more complicated. At higher frequencies, where the depth of the cone is no longer negligible compared with the wavelength, or may even be greater than the wavelength, the radiation deviates from that of the flat piston. The radiation from different parts of the cone then arrives at the point of observation with appreciably different phases, even when the point is on the axis of the loudspeaker. This results in a lower sound pressure at this point (see Fig. 3**a**, solid curve). For the beginning of this decrease a cut-off frequency f_c is defined, at which the sound wavelength is about three times the cone depth. Cones with a conventional apex angle have an f_c greater than f_t.

2. FLEXIBLE CONE

In reality a loudspeaker cone is by no means a rigid body. Above certain frequencies both transverse and longitudinal waves appear in the conical shell. These waves are coupled and together determine the vibration pattern, which considerably affects the air displacement. If we compare the measured frequency characteristic in Fig. 1 with the calculated solid curve in Fig. 3**a**, we see from the actual characteristic that the loudspeaker will function up to much higher frequencies.

In the discussion that now follows of the coupling between transverse and longitudinal waves we shall encounter a rather interesting resonant mode, which does not occur in a flat plate, and has an important bearing on the behavior of the cone as a radiator.

2.1 Two Types of Waves

In a flat plate the transverse and longitudinal waves do not affect one another. Both types of wave propagate faster the stiffer the medium. Since the plate is much stiffer for longitudinal compression and expansion than for bending, the longitudinal waves are much longer than the bending waves.

In a cone the situation is more complicated. In general the two wave motions cannot exist independently. A displacement normal to the cone surface leads to a displacement along the surface of the cone, and vice versa. This may be illustrated for a conical ring, on the inner edge of which a uniformly distributed longitudinal force F_l is exerted (Fig. 4**a**), giving a longitudinal displacement u. An increase in the diameter of the ring is therefore implied; as a result of the extension a tension appears in the ring, directed at all points along the tangent to the circumference. Considering a segment of the ring (Fig. 4**b**) we see that the tensile forces at the two ends of the segment result in a force F_c directed toward the center of the ring. This force lies in the plane of the ring (Fig. 4**c**) and can be resolved into a transverse component F_t and a longitudinal component F_l'. In the equilibrium position F_l' is equal and opposite to F_l. The applied longitudinal force F_l thus gives rise to a transverse force F_t, whose magnitude depends on the apex angle of the cone.

Both types of wave propagate from the apex of the cone to the edge and back as well as in circular paths parallel to the circumference of the cone. The outward-traveling waves are reflected at the edge and also at the point where the drive is applied. At certain frequencies standing waves occur (Fig. 5**a**), and the nodal lines then appear as concentric circles. These standing waves occur only at higher frequencies and greatly affect the sound radiation.

In the case of wave propagation in circular paths, standing waves occur at frequencies where a circular path is exactly two or more wavelengths long (Fig. 5**b**). Nodal lines then appear along generatrices of the cone. Since the bending stiffness of the cone is relatively small for circulating waves, the propagation velocity is low and these standing waves appear even at low frequencies, for example, at about 100 Hz for a typical 20-cm (8-inch) loudspeaker. They have very little effect on the sound radiation since the parts of the cone moving in antiphase are so close together that at these low frequencies their effects are practically canceled out, an effect known as "acoustical short-circuiting." This mode of vibration will therefore not be considered here.

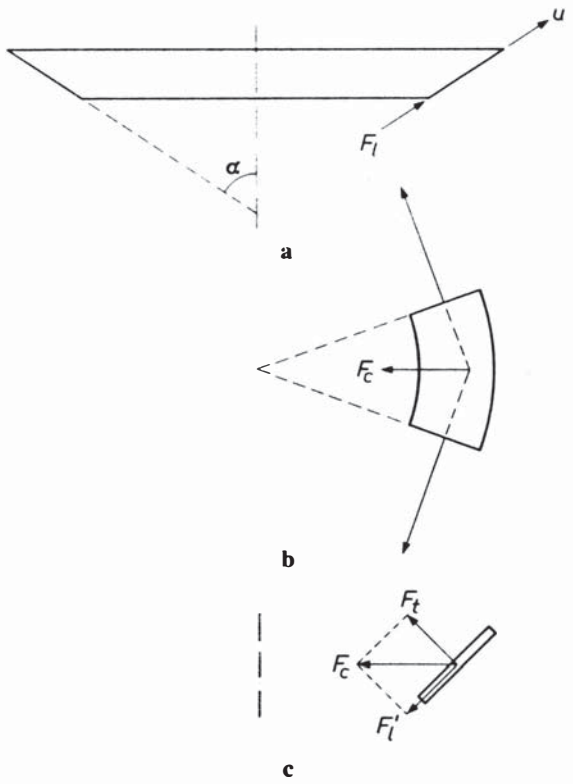

Fig. 4. Longitudinal diplacements in a cone set up transverse forces, and vice versa. **a**. Side view of a conical ring (semiapex angle x) on which a distributed force F_l acts in the longitudinal direction. u — Longitudinal displacement. **b**. Longitudinal displacement sets up a tension in the ring. The tensile forces at the ends of a part of the ring result in a force F_c directed toward the center. **c**. Cross section. F_c has a transverse component F_t and a longitudinal component F_l.

2.2 An Interesting Resonance Effect

If the loudspeaker diaphragm is a truncated cone, it has both an inner and an outer edge; the drive force is applied to the inner edge. When the waves propagated from the inner edge return to it in phase after reflection from the outer edge, they increase the amplitude of the displacement there; this is referred to as a resonance. There will also be frequencies, however, for which the waves return to the inner edge in antiphase and oppose the displacement; here we have an antiresonance. This holds both for longitudinal and for bending waves, and it applies not only for a cone but also for a flat ring.

In the case of a cone the coupling between longitudinal waves and bending waves gives rise to an antiresonance that is not encountered in a flat ring. The frequency at which this antiresonance occurs is a characteristic frequency of the cone: bending waves only occur above this frequency.

To explain this special mode of vibration we first consider a narrow conical ring to which, as in Fig. 4, a longitudinal force F_l is applied (see Fig. 6). We now assume, however, that F_l is a sinusoidally alternating force, which implies that inertia will come into the picture.

To begin with we can consider that the ring has a characteristic mode of vibration in which it alternately contracts and expands while retaining its shape; the ring vibrates in a plane perpendicular to the axis, and its center of gravity remains at rest (Fig. 6**a**). The elasticity of the ring provides the spring component of the spring-mass system. The mode occurs at the ring resonant frequency f_{rr}. If the drive force F_l alternates at this frequency, then the longitudinal displacements u and the transverse displacements w would both become infinitely large in the absence of damping, and so would the amplitude of the velocity in both directions. The mechanical impedance, defined as force divided by velocity, would then be zero at this frequency.

This mode of vibration is not specific to a conical ring; it also occurs in rings of other cross sections. However, in the case of the antiresonance mentioned above, which is confined to a conical ring and occurs only at a frequency $f_{ra} < f_{rr}$, a vibration is found at which, in spite of the longitudinal drive, the longitudinal amplitude is small (in the theoretical case with no damping it is in fact zero; Fig. 6**b**). We call frequency f_{ra} the ring antiresonant frequency. At this frequency the force F_l encounters a high mechanical impedance (*infinitely* high with no damping). Nevertheless, this antiresonance is essentially longitudinal, since the circumference of the ring becomes alternately larger and smaller. This longitudinal antiresonance can also be considered as a transverse resonance of the ring mass and the transverse component of the spring formed by the elasticity of the ring. In this form of motion, however, the center of gravity of the ring is *not* at rest. In other words, instead of a free vibrational mode of the ring we have a forced vibration, which can only occur when the drive is longitudinal as described above. The axial component of the drive produces the movement of the center of gravity, in accordance with Newton's laws of motion.

The resonance effects described related to a ring. We shall now, by way of approximation, consider the loudspeaker cone as a set of coupled conical rings. Each ring can be considered as a concentrated mass and a spring, so that the complete cone can be much more simply represented by a system of masses and springs (Fig. 7). Each ring can be excited at its antiresonant

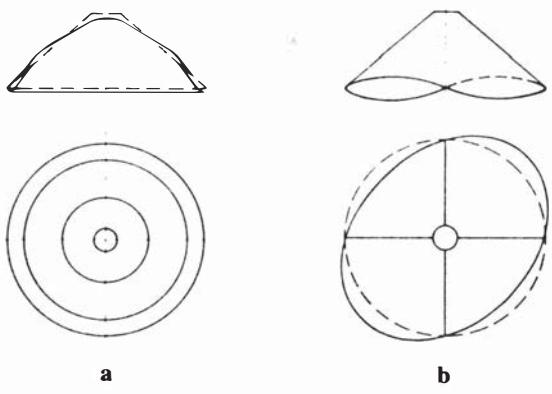

Fig. 5. Cone with standing-wave pattern. **a**. Outgoing and reflected waves. **b**. Circulating waves. The vibrational modes in **b** radiate little sound.

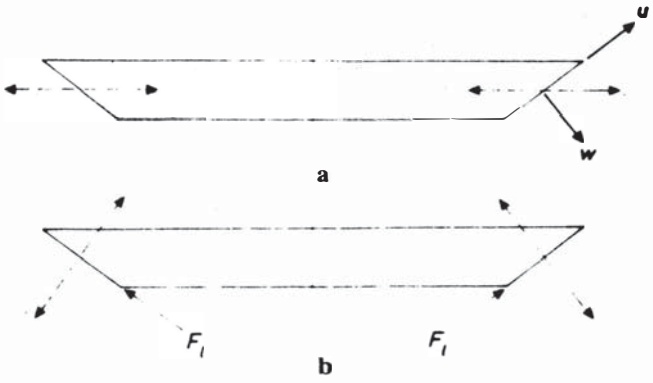

Fig. 6. Mode of vibration of a conical ring. **a**. Resonance. **b**. Antiresonance. u — longitudinal displacement; w — transverse displacement. At the antiresonance the longitudinal displacement is zero even though the drive is provided by a longitudinal force F_l.

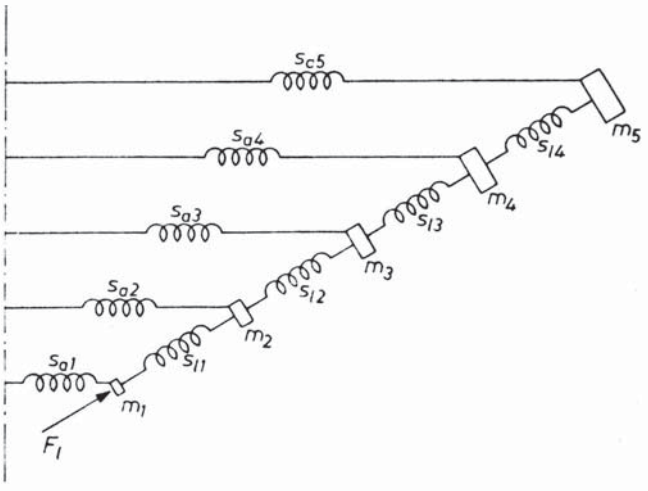

Fig. 7. Representation of a cone as a system of masses m and springs with stiffnesses s_l in the longitudinal direction and s_a in the azimuthal direction. The values of m increase the further they are from the center, and the values of s_a decrease.

frequency f_{ra}. The transverse amplitude then becomes large.

The frequency f_{ra} is lowest for the outer ring, since this is the largest mass and the weakest spring. As the frequency increases, the resonance effect gradually travels inwards, and eventually arrives at the inner edge. The ring in resonance marks a transition circle. On the stiffer part of the cone, inside this circle, the waves that occur are mainly longitudinal; on the part outside it, which is less rigid, they are mainly bending waves. On the transition circle itself there is an exchange of energy between longitudinal and bending waves.

The frequency at which the resonance at the outer edge begins is called f_{to}. The resonance reaches the inner edge at the frequency f_{ti}; the entire cone is then covered with bending waves.

In the vibrational behavior of a cone the longitudinal displacement u_i at the inner edge is of considerable importance. If the cone consisted of only one ring, this displacement would be zero at the ring antiresonant frequency f_{ra}. An actual cone can be approximated by a ring of radius equal to the outer radius R_0 of the cone, which is connected by a relatively stiff part to the inner edge of the cone. The stiff part transmits the force to the outer ring but adds mass to the system. For the cone as a whole, therefore, the frequency f_{ra} at which u_i is zero is lower than the antiresonant frequency f_{to} of the outer ring itself. The difference, however, is not very great, and instead of f_{ra} it may often be more convenient to use f_{to}, whose value is much easier to calculate. The value of f_{ra} can only be calculated numerically from the equations of motion of the complete cone.

3.CALCULATION OF THE CONE VIBRATIONS

The representation given in Fig. 7 is of course a considerable simplification. In reality, there are not only tensile stresses acting on an element of the conical shell, but bending moments as well. There is also damping, caused by the radiation of acoustical energy and also by internal losses in the material and suspension of the cone. If we wish to take all these factors into account, the simple models used so far are inadequate. We then have to resort to a complete mathematical treatment. A description that takes all the forces and moments into account, but not the damping, has eight simultaneous first-order differential equations with eight unknowns.

Disregarding the vibrational modes with diametric nodal lines (Fig. 5**b**) since they make no contribution to the sound radiation, we can reduce this set to six simultaneous differential equations. The six unknowns are all expressed as a function of the coordinate x along a generatrix of the cone (at the apex of the cone x is zero, at the inner edge a, at the outer edge b). For the solution of the six equations three boundary conditions are imposed at each edge of the cone. The equations are solved by direct numerical integration,[2] carried out for a large number of different frequencies. If the damping is included, all the fundamental variables become complex numbers, in which case we have twelve differential equations and twelve boundary conditions. In some of the results we shall later present the damping is taken into account.

The boundary conditions follow directly from the loudspeaker construction. The connection between the inner edge of the cone and the voice coil consists of a stiff rim strengthened by adhesive, and the inner suspension ensures that only axial motion is possible. We therefore assume in the calculations that the inner edge of the cone is clamped to an infinitely stiff ring of zero mass and that the movements of the ring are purely axial. The purely axial movement implies a fixed ratio between transverse and longitudinal amplitudes at the inner edge; this is one of the boundary conditions. Another boundary condition relates to the clamping of the inner edge ($\partial w/\partial x = 0$); the third boundary condition is that the forces at the inner edge are in equilibrium. The boundary conditions for the outer edge are that it has freedom of movement, implying that all forces and moments there are zero.

It can be shown that the mechanical impedance to the axial drive force is given by

$$Z_a = Z_t \sin^2\alpha + Z_l \cos^2\alpha.$$

In this expression Z_t is the transverse and Z_l the longitudinal impedance that would be present at the inner edge of the cone in the absence of the stiff ring. The transverse impedance, which is connected with the bending stiffness of the cone, is generally much smaller than the longitudinal impedance, which is determined by expansion and compression in the plane of the conical shell. It is primarily Z_l, therefore, that determines the amplitude of the displacements of the inner edge.

A diagram of the situation is shown in Fig. 8, where the impedances Z_t and Z_l are represented by springs with the stiffnesses s_t and s_l. It can be seen that if the stiffness s_t is much smaller than s_l, the axial motion depends mainly on s_l.

The outer suspension is not included in the calculations. The damping it normally introduces is accounted for by using a higher internal damping in the calculations than the actual value for the cone material.

3.1 Vibration Patterns in Different Frequency Regions

We have calculated the transverse and longitudinal displacements of a cone with characteristics like those encountered in practice. We shall refer to this as cone 50.1; the number 50 indicates the semiapex angle in degrees (the geometry and material parameters are given in Table 1). For simplicity the internal damping is assumed to be zero ($D = 0$).

From the transverse amplitude $w(x)$ and the longitudinal amplitude $u(x)$ we have plotted the magnitude and direction of the resultant motion for a number of points on the cone. The vibration patterns of a cone cross section obtained in this way are shown in Fig. 9**a-i**. Three frequency regions can be distinguished. The first (region I) contains the frequencies up to the appearance of the transition circle at the outer edge of the cone, that is, up to frequency f_{to}. In this region there are as yet no bending

[2] First applied to these problems by Goldberg *et al.* [2], and refined by Kalnins [3].

waves on the cone. These first appear in region II, in which the ring antiresonance gradually progresses from the outer to the inner edge. In the innermost part the cone motion is still almost uniform. At the frequency f_{ti} the ring antiresonance has reached the inner edge; this is the upper limit of region II. In region III the ring antiresonance has disappeared from the cone, and the entire surface of the cone is covered with bending waves.

Displacement patterns for frequency region I are given in Fig. 9**a, b,** and **c.** Fig. 9**a** shows the vibration behavior at 1000 Hz. At this relatively low frequency the cone may be considered as a first approximation to vibrate as a rigid body. When the frequency is raised, the amplitudes at the inner edge decrease whereas they increase at the outer edge. At the ring antiresonant frequency $f_{ra} = 1870$ Hz the longitudinal amplitude becomes zero at the inner edge; a node appears. Because of the assumed rigidity of the inner edge, this node also appears in the transverse amplitude (Fig. 9**b**). When the frequency is raised further, the node moves to the outer edge, as shown in Fig. 9**c** (2200 Hz). The upper limit of region I lies at $f_{to} = 2250$ Hz.

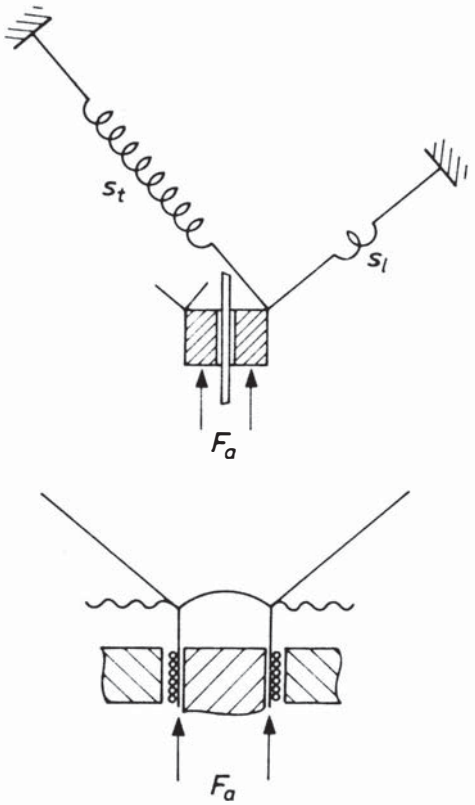

Fig. 8. Mechanical impedance to an axial force F_a on the inner edge of a cone. The impedance is represented by the simultaneous action of two springs. s_t—impedance to transverse displacements; s_l—impedance to longitudinal displacements. The inner edge is capable of axial motion only. In practice the longitudinal impedance predominates and mainly determines the displacements.

Above f_{to} standing bending waves appear on the cone at certain frequencies; these can be divided into bending resonant frequencies, for which $u(a)$ and $w(a)$ go to infinity, and bending antiresonant frequencies, at which $u(a)$ and $w(a)$ become zero.

At the first bending resonant frequency $f_{br1} = 2360$ Hz (Fig. 9**d**), w and u become very large. At the first bending antiresonant frequency $f_{ba1} = 2418$ Hz a new nodal circle appears in $w(x)$ at the inner edge (Fig. 9**e**); this moves relatively quickly to the outer edge when the frequency is further increased.

The vibration patterns at the second and third bending resonant and antiresonant frequencies are given in Fig. 9 **f–i**. The figures all show the same general picture: inside the transition circle the wavelength on the cone is long and the motion is approximately axial, because $u(x)$ and $w(x)$ have the same order of magnitude; outside it the vibration amplitude is mainly determined by the much shorter bending waves, which have a much greater amplitude than the longitudinal waves. In frequency region III the coupling between bending and longitudinal waves becomes weak. The wavelength of the bending waves, which now cover the entire cone, is approximately equal to the bending wavelength on an infinite plate. In Fig. 9**j** the transverse and longitudinal displacement patterns at $f = 13\,000$ Hz are of necessity shown separately, since in this case a combined picture would no longer give a clear picture of the vibration pattern.

4. HOLOGRAPHIC DISPLAY OF VIBRATION PATTERNS

Minute displacements or deformations of an object can be made visible by means of holography [4]. We have used the time-averaged holography technique to render visible the vibration patterns of a loudspeaker cone to

Table I. Dimensions and material constants of loudspeaker cones.

	Geometry				Material				
Cone Number	α (°)	R_i (mm)	R_o (mm)	h (mm)	E (10^9 N/m^2)	ρ (kg /m^3)	ν	D	
50.1	50	17	83	0.23	2	600	0.3	0.1	
50.2e	50	17	83	0.23	2.4	1200	0.35	0.014	PC
50.3	50	17	83	0.23	2.2	1160	0.3	0.1	
50.3e	50	17	83	0.27	2.2	1160	0.34	0.06	CAB
60.1	60	17	83	0.1	2	600	0.3	0.1	
60.2	60	17	83	0.26	2.2	1160	0.3	0.1	
60.2e	60	17	83	0.26	2.2	1160	0.34	0.06	CAB

The letter e after a number indicates an experimental cone; the others are calculated examples. α—semiapex angle; R_i—inner edge radius; R_o—outer edge radius; h—thickness of cone material; E—Young's modulus; ρ—density; ν—Poisson's ratio; D—internal loss factor; PC—polycarbonate; CAB—cellulose acetobutyrate.

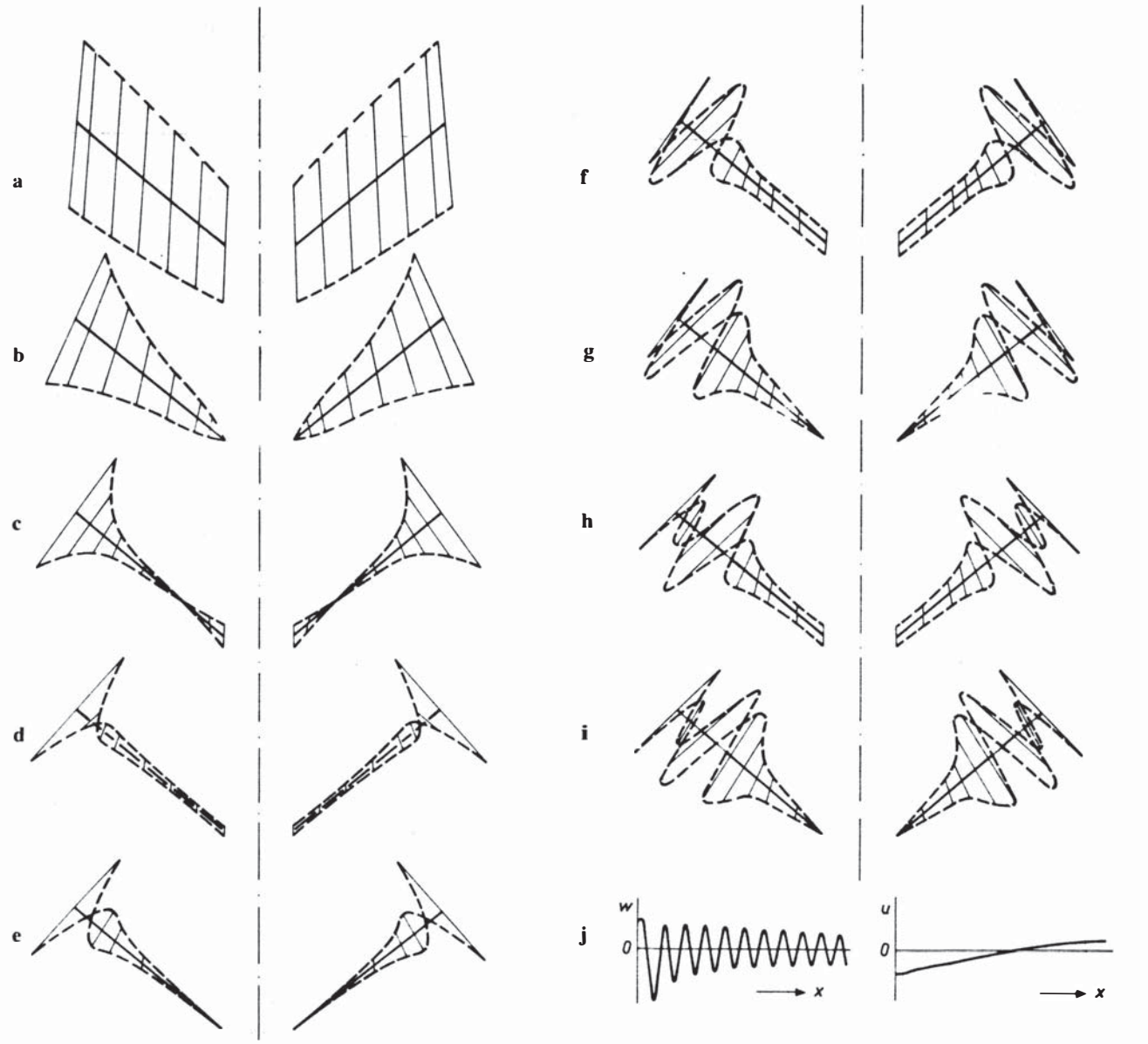

Fig. 9. Vibration patterns, composed of the calculated transverse and longitudinal displacements w and u on cone 50.1 (see Table I). The figures are not to the same scale.
a. 1000 Hz.
b. Ring antiresonance, f_{ra} = 1840 Hz.
c. 2200 Hz.
d. First bending resonance, f_{br1} = 2360 Hz.
e. First bending antiresonance, f_{ba1} = 2418 Hz.
f. Second bending resonance, f_{br2} = 2668 Hz.
g. Second bending antiresonance, f_{ba2} = 2750 Hz.
h. Third bending resonance, f_{br3} = 2993 Hz.
i. Third bending antiresonance, f_{ba3} = 3083 Hz.
j 13 000 Hz; the curves of w and u along the cone are plotted separately.

verify the results of the calculations qualitatively. We chose for the purpose a plastic cone (made of polycarbonate, cone 50.2e), since this material is more homogeneous than that of the more usual paper cone; the vibration patterns are consequently more regular and give a clearer picture. The geometry was the same as that of cone 50.1, but the constants of the material were of course different (see Table I). The recordings were made with the cone vibrating in air with a free outer edge.

The results are shown in Fig. 10. In the lighter parts the transverse amplitude is small (nodal lines), in the grey and black parts it is large. The calculated curve of the transverse amplitude $w(x)$ is shown beneath each photograph; damping was taken into account in the calculations.

Fig. 10**a** was recorded at the frequency f_{ra}. Besides the large amplitude at the outer edge, the picture shows a standing-wave pattern of circulating waves with ten nodal diameters. The grey ring near the edge is not anode but originates from the high local amplitudes. The patterns in Fig. 10**b, c,** and **d** were recorded at bending resonant and antiresonant frequencies; the transition circle is indicated in the graphs by a point. In Fig. 10**e** (6432 Hz) the transition circle has almost reached the inner edge; in Fig. 10**f** (8956 Hz, that is, just above f_{ti} = 8520 Hz) it has disappeared from the cone, which is now completely covered by bending waves. The holographic pictures provide a complete confirmation of the calculated transverse-amplitude patterns.

The inhomogeneities on a paper cone are usually greater and cause a more distorted pattern. Additional distortions

of the symmetry may be caused by the outer suspension. This is illustrated in Fig. 11, which shows a holographic presentation of the vibration pattern of a commercial loudspeaker with a paper rim. These irregularities do not adversely affect the sound reproduction from a paper cone, but make such a cone less suitable for demonstrating the vibration patterns.

5. SOUND RADIATION FROM A FLEXIBLE CONE

The sound radiation from a flexible cone may be calculated in essentially the same way as that from a rigid piston and rigid cone. Each element of the cone surface is regarded as a point source, and the contributions of all the point sources are added together. It is again assumed that the loudspeaker is enclosed in an infinite baffle. A compli-

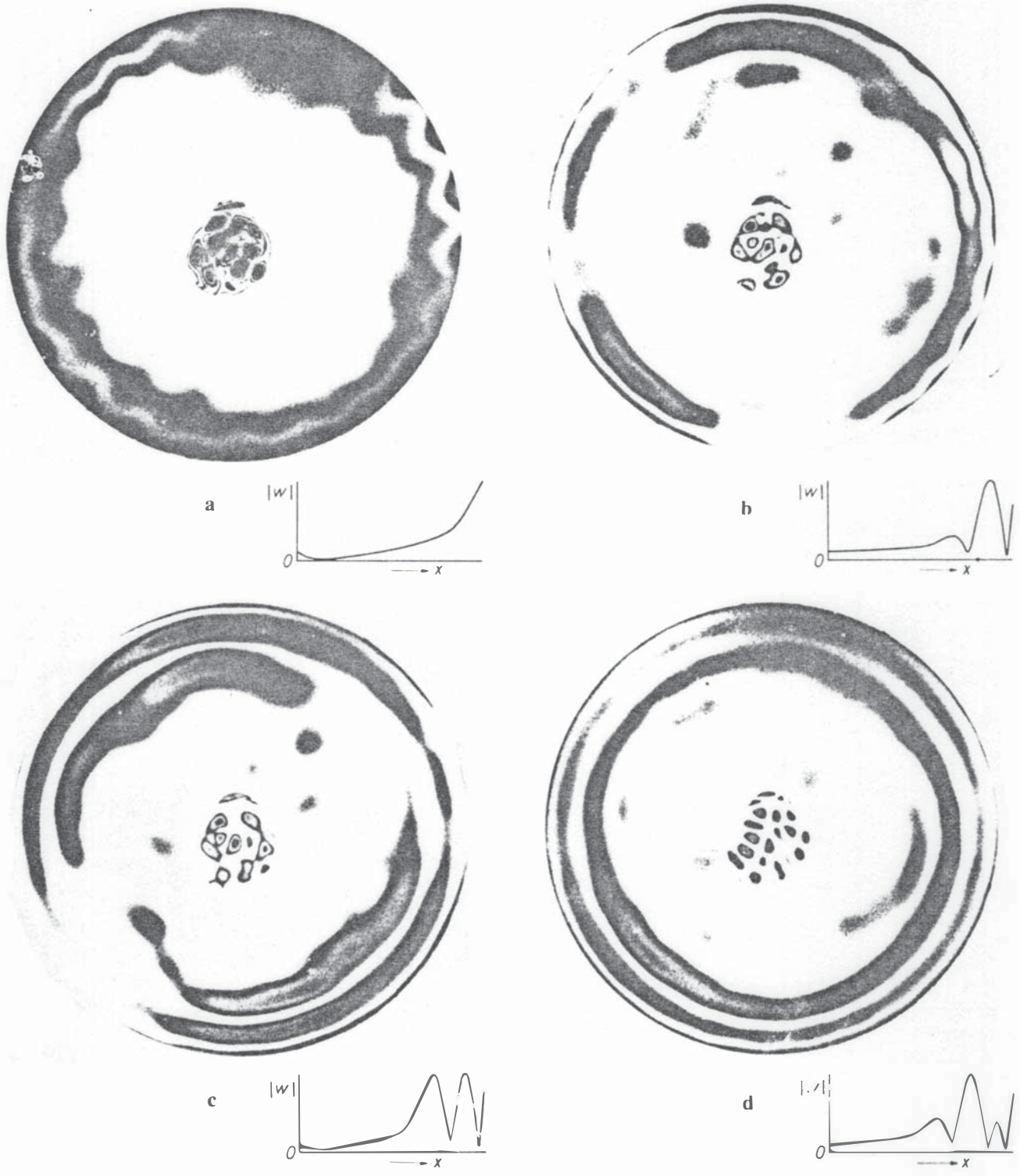

Fig. 10. Vibration patterns of a plastic cone (cone 50.2e), made visible by holography. White—low transverse amplitude (nodal lines); grey or black—high amplitude. The calculated amplitude curve is shown below each photograph ($x = 0$ at the inner edge of the cone). **a.** Ring antiresonance, $f_{ra} = 1646$ Hz. **b.** Second bending resonance, $f_{br2} = 2063$ Hz. **c.** Second bending antiresonance, $f_{ba2} = 2170$ Hz. **d.** Third bending resonance, $f_{br3} = 2337$ Hz.

cation here is that each surface element has its own transverse vibration amplitude, which must first be calculated and then included in the acoustic summation as a weighting factor.

Another complication is that, because of the succession of resonances and antiresonances in the flexible cone, the mechanical impedance to the motion of the voice coil varies considerably with frequency. With a constant drive force this means that there is great variation in velocity amplitudes at the inner edge of the cone. This variation is of course also reflected in the frequency response; for a given drive force the sound power radiated at a given frequency is inversely proportional to the mechanical impedance presented to the voice coil, or, in other words, directly proportional to the mechanical admittance. This quantity therefore deserves to be looked at more closely.

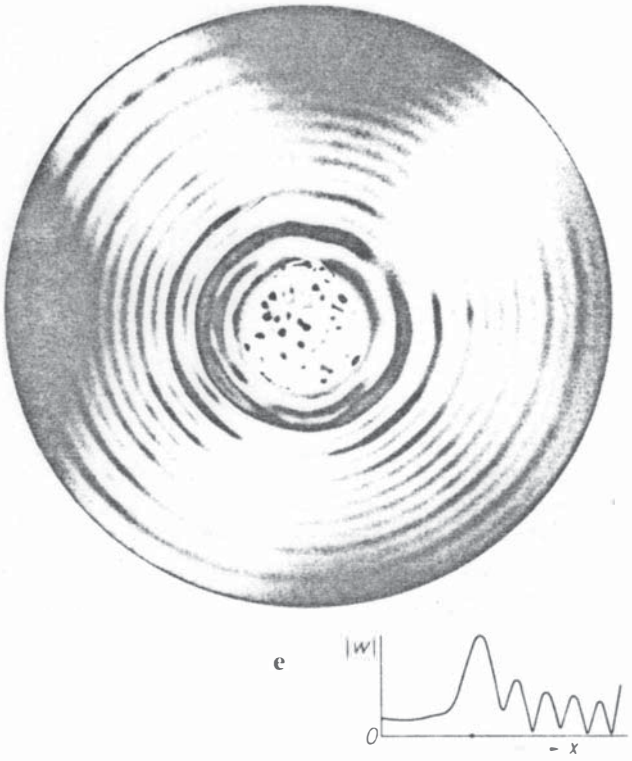

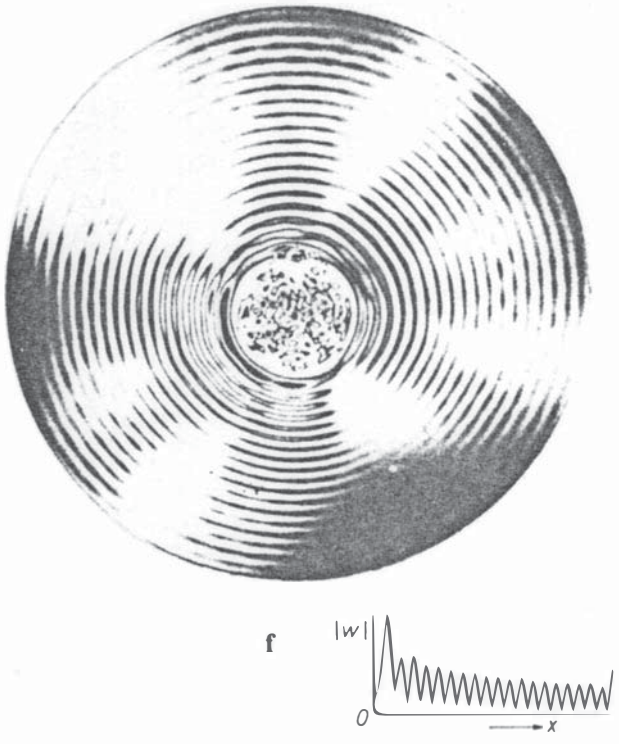

Fig. 10 continued. **e.** 6432 Hz. **f.** 8956 Hz (upper limit of region II f_{ti} = 8520 Hz.

5.1 Mechanical Admittance

Like the vibration pattern, the mechanical admittance at the inner edge can also be calculated for any frequency from the set of differential equations mentioned in the previous section. As an example Fig. 12 shows the calculated curve of the axial admittance Y_a as a function of frequency for cones 50.1 and 60.1 (see Table I). At low frequencies, where the cone vibrates as a single mass, inertia is the decisive factor and the admittance decreases with increasing frequency. A minimum is reached at f_{ra}; just above it is the frequency f_{to} (indicated by a point), where the bending resonances and antiresonances begin. In cone 50.1 these give a ripple in the admittance curve. Above f_{ti} (the second point) the bending resonances and antiresonances are no longer perceptible in the admittance curve. The marked oscillations of the curve are connected with the longitudinal resonances and antiresonances.

Cone 60.1 differs from cone 50.1 in its larger apex angle and thinner paper. Because of the larger apex angle the characteristic frequencies f_{ra}, f_{to}, and f_{ti} are lower. The thinner paper makes the cone lighter, so that the curve starts higher and the admittance variations associated with the bending waves are less pronounced; in Fig. 12 they can

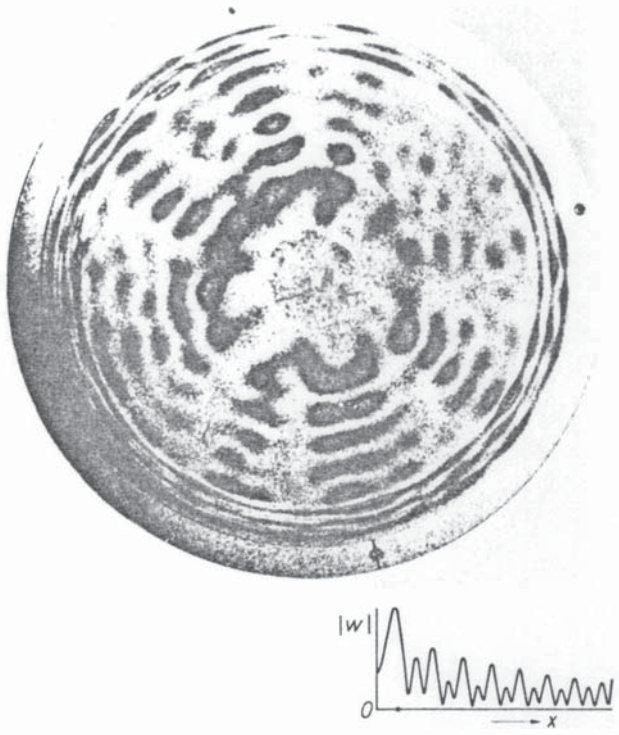

Fig. 11. Vibration pattern of a loudspeaker with paper cone (Philips 9710), made visible by holography. Frequency 5929 Hz. The pattern is less regular than that in Fig. 10 because a paper cone is less homogeneous than a plastic cone.

no longer be seen.

The mass of the voice coil is not taken into account in Fig 12. In practice its effect is considerable and can even be dominant at high frequencies; the admittance oscillations due to the longitudinal resonance effects cause no more than a ripple on the curve determined by the voice-coil mass (see Fig. 13).

5.2 Calculated Frequency Characteristics

To draw the frequency characteristic of a loudspeaker in sufficient detail it is necessary to perform calculations at some fifty well chosen frequencies. The calculation of localized vibration amplitudes takes a considerable amount of computer time (about 2 minutes for each frequency with an IBM 370/168; the acoustic variables take somewhat less). Our initial calculations were made with the mass of the voice coil taken as zero. This gives a basic curve, and very little extra computing time is required in correcting for the effect of the voice-coil mass, which is of a simple nature. This allows different values for this important parameter to be introduced at a later stage for a rapid determination of its effect on the curve.

Fig. 14 shows the result of calculations on cone 50.1. First of all we calculated the level L_p of the sound pressure at an axial distance of 10 meters from the loudspeaker (Fig. 14**a**). A drive force with an amplitude of 1 N is assumed. We also calculated the level L_{p100} of the acoustic power radiated in a conical region of apex angle 100° (Fig. 14**b**). Calculation of the sound pressure is unrealistic for field points lying outside this conical region, which is bounded by the loudspeaker cone itself with its apex angle of 100°.

The results may be compared with the solid curves in Fig. 3, relating to a rigid cone of the same dimensions. Below f_{ra} (1840 Hz) the sound radiation from both the flexible and the rigid cones is almost identical with that from a rigid piston. Since the mechanical admittance has a minimum at f_{ra}, we also expect a minimum there in the sound-pressure response; this is not found because of the compensation provided by the high transverse amplitude at the outer edge (see Fig. 10**a**). The decrease in the sound pressure expected for a cone above f_c (here 1580 Hz) cannot be seen because f_c and f_{ra} are relatively close together. The power response shows a slight decrease above f_t (920 Hz); see Fig. 14**b**.

In frequency region II ($f_{to} < f < f_{ti}$) the sound radiation is predominantly controlled by the relatively uniformly vibrating inner part of the cone; the short bending waves on the outer part of the cone are "acoustically short-circuited" and radiate little sound. The characteristics in this region have a broad maximum with a superimposed

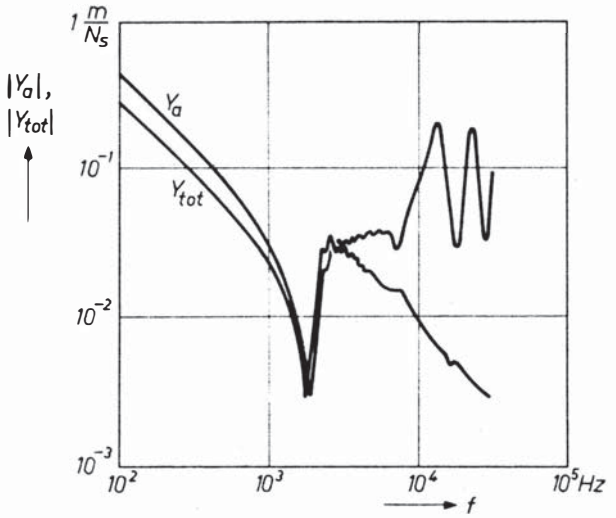

Fig. 13. Calculation of the total axial mechanical admittance Y_{tot} as a function of frequency after the addition of the voice-coil mass to cone 50.1. Curve Y_a from Fig. 12 has been added for comparison.

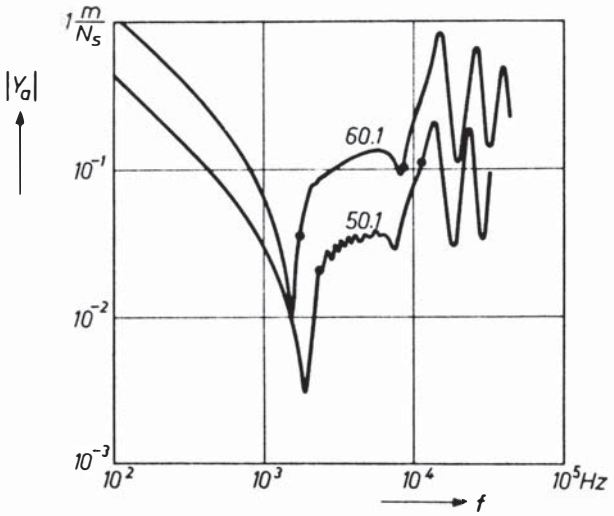

Fig. 12. Calculation of the axial mechanical admittance Y_a at the inner edge of cones 50.1 and 60.1 as a function of frequency. The "points" indicate the locations of frequencies f_{to} and f_{ti}. At low frequencies the cone mass predominates. At f_{ra} a minimum occurs; f_{to} lies just above it. Between f_{to} and f_{ti} the bending resonances and antiresonances in cone 50.1 give rise to a fine structure. Above f_{ti} the curve is determined by the longitudinal resonances and antiresonances.

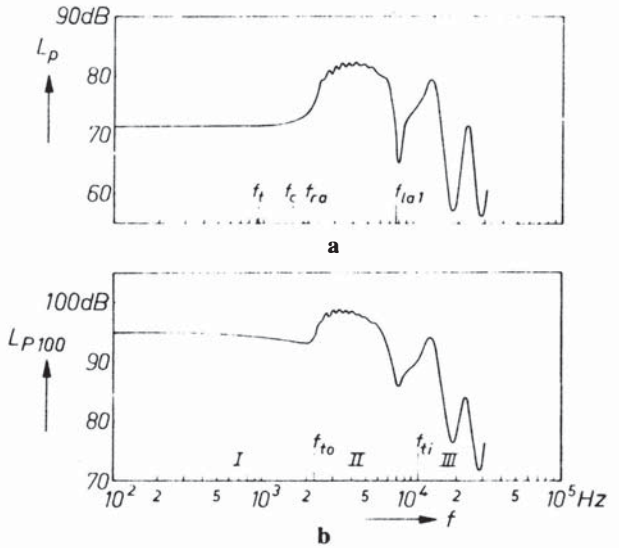

Fig. 14. **a**. Sound-pressure level L_p on the axis of cone 50.1 (calculated curve neglecting voice-coil mass; distance 10 m, drive force 1 N). The level is expressed in decibels relative to a reference level of 20 μPa. **b**. Acoustic power level L_{P100}, radiated within a conical region of apex angle 100°. The level L_{P100} is expressed in decibels relative to 10^{-12} W. Some characteristic frequencies and the frequency regions I, II, and III are given.

fine structure of bending resonances and antiresonances, followed by a deep minimum at the first longitudinal antiresonant frequency f_{la1} (7513 Hz), where there is a minimum in the mechanical admittance (Fig. 12, curve 50.1). In the high-frequency region (region III, $f > f_{ti}$) the pressure response shows the same oscillating character as the mechanical admittance; peaks and dips alternate at longitudinal resonant and antiresonant frequencies.

If we now take the voice-coil mass into account, the characteristics change shape at the high frequencies. We have already noted that the mechanical admittance at high frequencies is entirely determined by the voice-coil mass; in the acoustic response curves this appears in a steep drop in frequency region III (see Fig. 15). If this drop begins above the sharp minimum at the first longitudinal antiresonant frequency f_{la1}, this frequency will then in practice be the upper limit of the frequency range of the loudspeaker. The decrease due to the voice-coil mass, however, may begin in region II.

5.3 Comparison of Measured and Calculated Characteristics

To test the theory against practical experience, the sound radiation was both measured and calculated for cones of various apex angles. Here again, plastic cones were used, but this time of different compositon (cellulose acetobutyrate). The cones were provided with a rubber outer rim. The internal damping or loss factor of the material was 0.06, which is considerably more than that of the polycarbonate used for the holographic recordings. In those experiments it was important to make the bending waves visible, but in the acoustic measurements it was important to damp the bending resonances. A loss factor of 0.1 was assumed to allow for the damping at the rim and the radiation damping. The assumed infinite baffle was approximated by a closed acoustic box (volume 100 dm³) attached to the middle of a square baffle (1.5 × 1.5 m²).

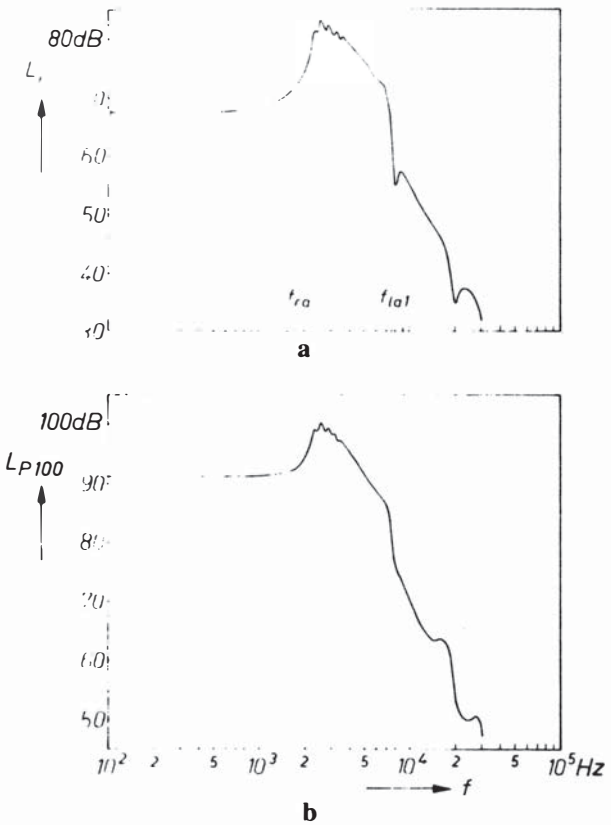

Fig. 15. **a**. Sound-pressure level L_p. **b**. Power level L_{P100}. Both calculated for cone 50.1, with the voice-coil mass assumed equal to half the cone mass.

In Fig. 16**a** the solid curve is the measured soundpressure response of a cone with a semiapex angle of 50° (cone 50.3e, Table I); the dashed curve is the calculated response for the same cone. The calculated values of the various characteristic frequencies are indicated. The main features of the measured curve can all be explained from these values. The maximum in frequency region II does indeed lie between f_{ra} and f_{ti}, and the characteristic does start to fall off at f_{la1}.

The dip in the measured curve at 300 Hz is related to the dimensions of the baffle. At low frequencies the rest of the measured curve lies above the calculated one, because of radiation from the outer suspension. Above f_{ra} this suspension contributes little to the sound radiation.

Measurements were also made of the total sound power radiated within a conical region of apex angle 100°, with ten microphones arranged in an arc around the loudspeaker. Because the ten signals had to be summed, measurements could only be made at a number of discrete frequencies, yielding the values indicated by the points in Fig. 16**b**. In Fig. 16**c** the measured and calculated directivity diagrams are compared.

The characteristics relating to a cone with a semiapex angle of 60° (cone 60.2e, Table I) are given in Fig. 17. They give a lower maximum in region II. Although they do not differ fundamentally from Fig. 16, most of the characteristic frequencies are lower.

It may be concluded from the good agreement between the calculated and measured characteristics that the calculation procedure gives a good approximation to the actual behavior of the cone.

6. DESIGN OF A LOUDSPEAKER CONE

The primary consideration in the design of a loudspeaker cone is to ensure that the characteristic frequencies are properly located.

All the requirements cannot be satisfied simultaneously. A flat pressure and power response, a large bandwidth, and a high efficiency cannot all be achieved at the same time. Every design must therefore be a compromise.

If the flattest possible characteristics are required, then to avoid the dip at f_{ra} in the power response, f_{ra} should not lie too far above f_t. This has consequences for the apex angle. If, for example, we take f_{ra} smaller than $2f_t$, the semiapex angle α of a paper cone, in which the propagation velocity c for longitudinal waves is 2700 m/s, must be greater than 70°. Such a large value of α implies a low maximum in region II, which will help to give a flat response. In this region, however, a distinct fine structure may easily arise, because with a large apex angle the frequencies of the bending resonances and antiresonances lie further apart; α should therefore not be made larger than is absolutely necessary.

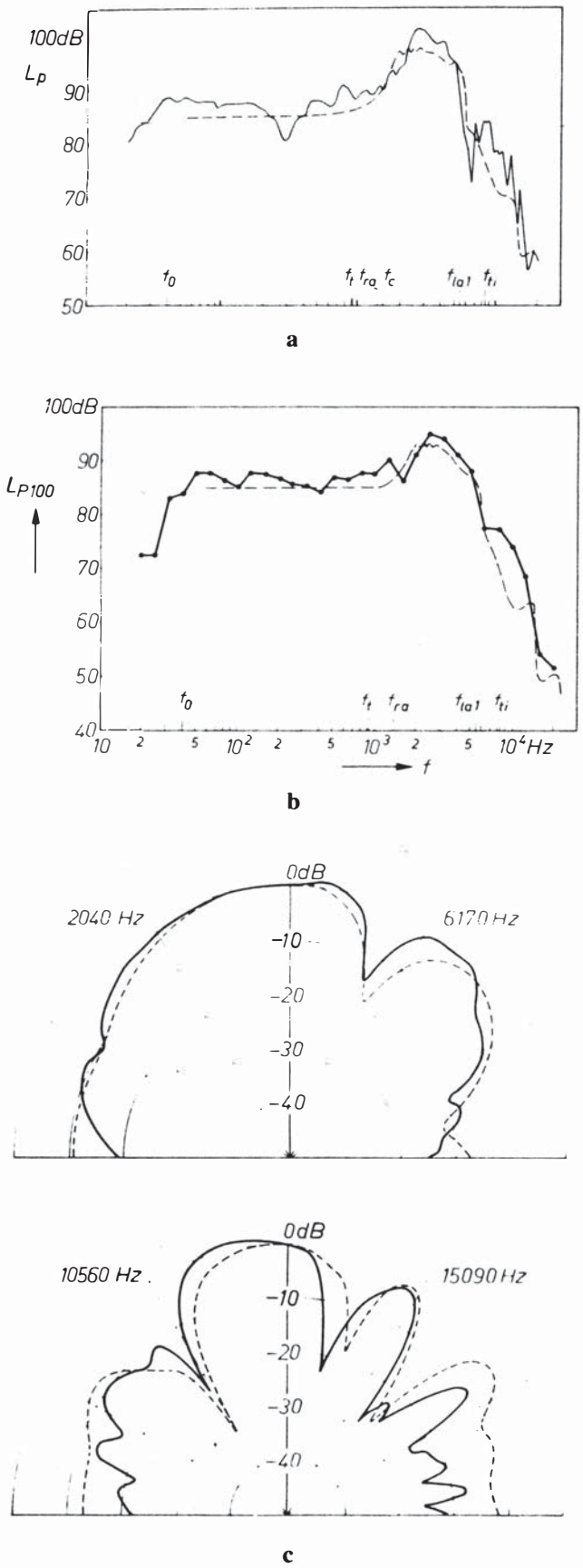

Fig. 16. Comparison of measured and calculated characteristics of cones 50.3e and 50.3; the dashed curve relates to cone 50.3. The calculated characteristic frequencies are given. **a**. Sound-pressure level. **b**. Level of total acoustic power radiated within a conical region of apex angle 100°. **c**. Directivity characteristics. The sound-pressure level is plotted as a function of the direction of radiation.

The steep decrease at high frequencies, caused by the voice-coil mass, generally determines the upper limit of the frequency range of the loudspeaker. To achieve a high cut-off frequency the ratio m_c/m_d between the masses of voice coil and diaphragm must be chosen as small as possible. This can never be higher, however, than f_{la1} or f_{ti}, whichever of the two is lower, since the cone behavior sets an upper limit here to the frequency response. The frequencies f_{la1} and f_{ti} depend on the radius of the inner edge; if the radius is smaller, f_{ti} is higher but f_{la1} lower.

The cone thickness h can be determined experimentally after the other geometrical parameters have been determined. A thin cone helps to suppress the fine structure of the bending waves but makes the ratio m_c/m_d worse. It also increases the danger of nonlinear distortion because the amplitudes of vibration become too large. One means of eliminating fine structure is to use a damping outer rim.

If the primary requirement is a large bandwidth, then as noted above, the ratio m_c/m_d must be given the smallest possible value. This implies a heavy cone and low efficiency. If dips in the response at f_{ra} and f_{la1} are acceptable, a small value of α should be taken and c made as high as possible; f_{ra}, f_{la1}, and f_{ti} then become higher. A semiapex angle of 50°, for example, can then be used, which makes the maximum in region II relatively high. The thickness is again chosen in such a way as to eliminate the fine structure.

If high efficiency is most important, the cone should be made as light as possible. The ratio m_c/m_d then becomes higher, however, and the bandwidth will consequently be small. A high maximum in region II can be obtained by

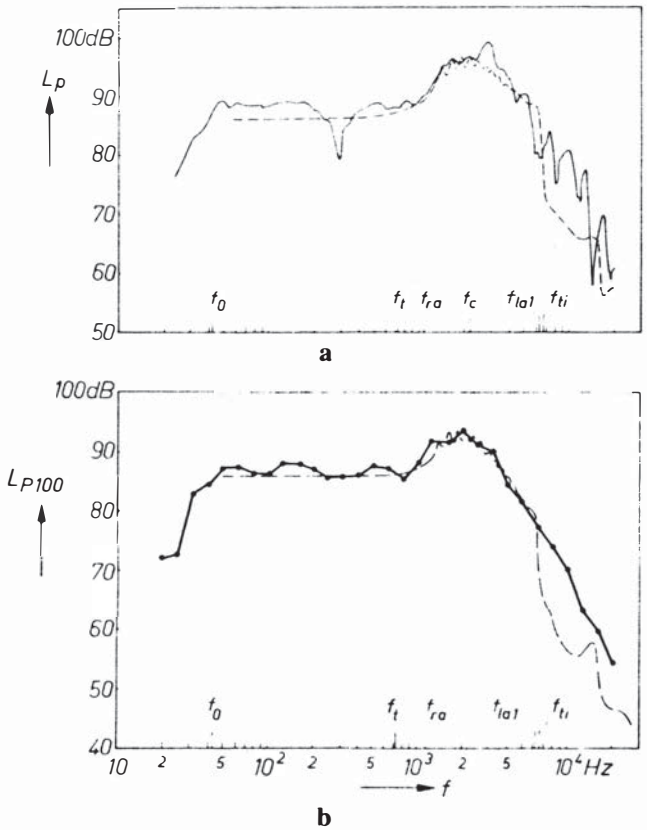

Fig. 17. Comparison of measured and calculated frequency characteristics of cones 60.2e and 60.2.

choosing a small apex angle. If a dip in the pressure response at f_{ra} is not allowed, Young's modulus of the cone material should be chosen such that f_{ra} is lower than $2f_c$.

6.1 Computer-Aided Design with Visual Display

It would be ideal if the designer could feed a sketch of the desired frequency characteristic into a computer and get back a little while later the corresponding dimensions and material constants for the cone. This is not feasible, however, since not all the curves can be realized in practice. Computer-aided design of a loudspeaker cone still has to be done the other way round: the designer types in some data and the computer calculates the resultant frequency characteristic. If it differs from the required curve, the designer then changes one or more parameters and the computer presents another result. An iterative procedure of this type is best carried out at a computer terminal with a visual display (Fig. 18).

Such a procedure requires a great deal of computer time: it can take an IBM 370/168 computer as long as an hour to calculate a single characteristic. If the procedure is to be used frequently, costs can be reduced by storing a number of standard characteristics in the computer memory and using these as the starting point for each new design. These characteristics can be adequately characterized by four parameters: the outer radius R_0, the inner radius R_i, the semiapex angle α, and the velocity c of longitudinal wave propagation in the cone material.

Poisson's ratio (of lateral to longitudinal strain) has little influence, and is set at ⅓ in all cases. The loss factor giving the internal damping of the cone material is taken at the relatively high value of 0.1, and the cone thickness is given the empirical value $R_0/800$; both values reflect the practical measures that need to be taken to avoid a fine structure.

Fig. 18. Computer-aided design of a loudspeaker cone using a visual display.

For R_0, for example, seven values can be taken [corresponding to the commercial diameters of 3, 4, 5, 6½, 8, 10, and 12 inches, (76.2, 101.6, 127, 153.7, 203.2, 254, and 304.8 mm)], for R_i three values (for example, 18, 35, and 50 mm), for α five values (50° to 70° in steps of 5°), and for c a single value (2500 m/s). The vibration patterns and frequency characteristics of 105 cones now have to be calculated and stored. From the stored vibration patterns the vibration patterns and frequency characteristics for other materials can be computed fairly quickly. If we take, for example, c = 1500 m/s and c = 3500 m/s, we can calculate the data for 315 cones and store them in the computer memory.

The designer can call up the characteristics of any one of these cones on his visual display. Having done this he types in a value for the ratio m_c/m_d of voice-coil mass to cone mass. The computer immediately calculates the effect of this ratio on the characteristics, which takes very little computer time.

If the desired characteristic is not sufficiently approximated, the designer can request calculations for intermediate values of the four basic variables; the programs for this are stored in the computer. The results are stored in the memory, so that the range of choices available is gradually widened.

After a trial model has been made in this way, it may be found that the characteristics have an undesired fine structure. The damping must then be increased or the cone thickness reduced; neither of these measures has much effect on the general shape of the frequency characteristics, provided the ratio m_c/m_d and the fundamental resonant frequency f_0 are kept constant.

The spring constant of the cone suspension and the characteristics of the electrodynamic drive can be included in the model with very little extra complication. Their influence can be immediately calculated by the computer from relatively simple formulas. In this way a very comprehensive loudspeaker design can be produced.

SUMMARY

A loudspeaker cone gives complex and highly frequency-dependent vibration patterns. With a computer numerical solutions can be found for the set of simultaneous differential equations that describe the vibration behavior of a flexible conical shell. Three frequency regions are distinquished: I—low frequencies, the cone vibrates as a rigid body; II—a ring on the cone gives a special resonance, bending waves occur outside this ring; III—high frequencies, the entire cone is covered with bending waves. For the frequency characteristics of the pressure response and total sound-power response of the cone to have the desired shape, it is necessary for the boundaries between the regions to be correctly located; this determines the choice of the radii of the outer edge and the voice coil, the apex angle, and the material constants of the cone. The bending resonances are less pronounced for a thinner cone or material with greater damping. For a high cut-off frequency the mass of the voice coil must be low compared with that of the cone. Computer-aided design is possible by calling up a visual display of

previously stored calculated characteristics and modifying the parameters.

REFERENCES

[1] F. J. Frankfort, "Vibration and Sound Radiation of Loudspeaker Cones," Thesis, Delft (1975); also *Philips Res. Rep. Suppl.*, no. 2 (1975).

[2] J. E. Goldberg, J. L. Bogdanoff, and L. Marcus, "On the Calculation of the Axisymmetric Modes and Frequencies of Conical Shells," *J. Acoust. Soc. Am.*, vol. 32, pp. 738-742 (1960).

[3] A. Kalnins, "Analysis of Shells of Revolution Subjected to Symmetrical and Nonsymmetrical Loads," *Trans. ASME E (J. Appl. Mech.)*, vol. 31, pp. 467-476 (1964); "Free Vibration of Rotationally Symmetric Shells," *J. Acoust. Soc. Am.*, vol. 36, pp. 1355-1365 (1964).

[4] C. H. F. Velzel, "Holographic Strain Analysis," *Philips Tech. Rev.*, vol. 35, no. 2/3, pp. 53-64 (1975).

PHILIPS RESEARCH REPORTS

SUPPLEMENTS

PHILIPS RESEARCH LABORATORIES

Philips Res. Repts Suppl. 1975 No. 2

Printed in the Netherlands

VIBRATION AND SOUND RADIATION OF LOUDSPEAKER CONES *)

*) Thesis, Delft University of Technology, April 1975.
Promotor: Ir. D. W. van Wulfften Palthe.

Philips Res. Repts Suppl. 1975, No. 2.

Abstract

This thesis is concerned with the vibration and the sound radiation of loudspeaker cones. The forced vibrational cone behaviour is studied theoretically with and without neglection of the cone bending stiffness for a great number of frequencies. The frequency characteristics of the radiated sound pressure and power as well as directivity diagrams are calculated. The influence of the geometrical and material parameters of the cone on the mechanical behaviour and the sound radiation is discussed. To verify the above calculations mechanical and acoustical measurements are carried out. Design rules are given.

CONTENTS

1. INTRODUCTION 1
   1.1. Plan of thesis 2

2. QUALITATIVE DESCRIPTION OF THE VIBRATION AND THE SOUND RADIATION OF LOUDSPEAKER CONES 3
   2.1. Introduction 3
   2.2. Basic assumptions 4
   2.3. The rigid-piston approximation 4
   2.4. The rigid-cone approximation 5
   2.5. The flexible cone 5
      2.5.1. Mechanical behaviour 6
         2.5.1.1. Wave types 6
         2.5.1.2. Resonant and antiresonant frequencies 8
         2.5.1.3. Mechanical impedance 10
         2.5.1.4. Displacement patterns 12
      2.5.2. Sound radiation 12
   2.6. Conclusion 15

3. THE ELECTRODYNAMIC LOUDSPEAKER 16
   3.1. Introduction 16
   3.2. Electromechanical equivalent circuit 16
   3.3. Measurement of the voice-coil velocity 19

4. MEMBRANE APPROXIMATION OF THE MECHANICAL CONE BEHAVIOUR 22
   4.1. Introduction 22
   4.2. Cone geometry 23
   4.3. Membrane differential equations 23
   4.4. A typical resonance 27
   4.5. Boundary conditions 31
   4.6. Approximate analytical solutions 32
      4.6.1. Low-frequency approximation 32
      4.6.2. High-frequency approximation 34
   4.7. Numerical solution of the membrane differential equations . . 38
      4.7.1. Introduction 38
      4.7.2. Frequency dependence of the vibration patterns and the longitudinal admittance of a typical cone 39
      4.7.3. Radially supported inner edge 46
      4.7.4. Longitudinal admittance in the presence of internal material damping 47

4.7.5. Influence of the apex angle on the longitudinal admittance 52
4.7.6. Longitudinal antiresonant frequencies versus cone geometry 53
4.8. Measurements 55
4.9. Conclusion 58

5. EXACT SOLUTION OF THE MECHANICAL CONE BEHAVIOUR 59
5.1. Introduction 59
5.2. Basic differential equations 60
5.3. Results of Ross's asymptotic approximation 62
5.4. Boundary conditions 64
5.5. Typical frequency dependence of the displacement patterns . . 69
5.6. Dependence of bending resonant and antiresonant frequencies and displacement patterns on the cone geometry and material . 74
5.6.1. Influence of the thickness 75
5.6.2. Influence of the apex angle 77
5.6.3. Influence of the ratio of outer- to inner-edge radius . . . 78
5.7. Frequency characteristic of the axial admittance 79
5.7.1. Influence of the thickness 83
5.7.2. Influence of the apex angle 83
5.7.3. Influence of the outer-edge radius 86
5.8. Membrane resonant frequencies 87
5.9. Comparison of the exact solutions and the solutions obtained with the membrane approximation 88
5.10. Influence of the voice-coil mass on the frequency characteristic of the axial admittance 92
5.11. Asymmetric vibrations 94
5.12. Measurements 96
5.12.1. Comparison of calculated and measured motional impedances 96
5.12.2. Comparison of calculated and measured vibration patterns 102
5.13. Conclusion 109

6. SOUND RADIATION 110
6.1. Introduction 110
6.2. Basic assumptions and definitions 110
6.3. Rigid-piston radiation 113
6.4. Rigid-cone radiation 115
6.5. Flexible-cone radiation 125

6.5.1. Introduction 125
6.5.2. Description of the problem 125
6.5.3. Radiation in the low-frequency region 128
6.5.4. Radiation in the high-frequency region 129
6.5.5. A typical example 134
6.5.6. Influence of the cone geometry 137
6.5.6.1. Influence of the cone thickness 137
6.5.6.2. Influence of the outer-edge radius 138
6.5.6.3. Influence of the apex angle 140
6.5.7. Influence of the cone material 142
6.5.8. Influence of a rigid cone top 146
6.5.9. Influence of the voice-coil mass 147
6.6. Measurements 150
6.6.1. Comparison of calculated and measured acoustical behaviour 151
6.6.2. Pressure responses of four commercial loudspeakers . . 161
6.7. Design rules 163
6.7.1. Realization of a flat pressure and power response . . . 164
6.7.2. Realization of a large bandwidth 164
6.7.3. Realization of a high efficiency 165
6.8. Conclusion 165

APPENDIX A. Differential equations for the mechanical cone behaviour 167
APPENDIX B. Description of a numerical method for the solution of a system of simultaneous differential equations 171
APPENDIX C. Strain-energy coefficient 179
APPENDIX D. Basic formulas for the rigid-piston radiation 180
APPENDIX E. Measuring circuit for the motional impedance 181
APPENDIX F. Time-average fringe holography 182
APPENDIX G. List of cones used in the calculations and measurements 185

List of symbols 186

REFERENCES 189

1. INTRODUCTION

The loudspeaker is generally known as the weakest link in the sound-reproduction chain. It should create a sound pressure proportional to the electric signal of the amplifier. In general, the common loudspeaker may be split into two parts: an electromechanical and a mechanical–acoustical part*). The latter mostly consists of a diaphragm, the vibration of which actually creates the sound pressure. This vibration is provided by the electromechanical driving system, the working principle of which classifies the loudspeaker as being of the electrodynamic (moving coil), electromagnetic (moving iron), electrostatic or piezoelectric type.

One of the greatest difficulties in the conversion of electrical into acoustical energy is the realisation of a prescribed (mostly flat) frequency response in a certain (mostly large) frequency range. The influence of the driving mechanism on the response being generally known, the basic theme of this paper is the vibration of the diaphragm and its influence on the sound radiation. The electromechanical driving system is of secondary importance here. We will fix our attention exclusively on the conical diaphragm which is commonly applied in to-day's mostly used loudspeaker: the electrodynamic type. This diaphragm shape is also very often used in the seldomly encountered electromagnetic and piezoelectric loudspeakers. The reason for the present study is the almost complete lack of any theoretical work on the sound-radiating properties of the conical diaphragm.

After the invention of the loudspeaker about a century ago it was undoubtedly McLachlan [11]) who (in the thirties) studied experimentally the electrodynamic loudspeaker most profoundly. There was however no thought of calculating the sound radiation; the radiative properties could only be approximated by assuming the cone to be a flat rigid piston, a model only valid for low frequencies where indeed the cone oscillates more or less rigidly. Later on, in 1951, Nimura et al. [2,3]) attacked the problem of theoretically describing the cone mechanical behaviour, but their attempts were little successful owing to the impossibility of solving analytically the differential equations for the cone vibration. It was not until the sixties that numerical methods were applied for the solution of these equations with high-speed computers [14]).

Ross [4,5]) in 1966 analytically studied the axisymmetric vibrational behaviour of a shell of revolution in an asymptotic approximation, but his work is of limited value here because the region of validity of his results falls mostly outside the bandwidth of the loudspeaker.

Even until now, the above-mentioned rigid-piston approximation forms the

*) This does not hold for the seldomly used ionophonic loudspeaker.

basis for all calculations of the radiated sound pressure and sound power. New loudspeakers are practically developed by trial and error and quasi-technical philosophies alternate with almost fashion-determined "improvements". Patents describing "the ideal loudspeaker" are numerous. All this has been the instigation for the underlying study which, we hope, will contribute to a better understanding and hence to better design of the electrodynamic loudspeaker.

1.1. Plan of thesis

It is characteristic of the calculation of the sound radiation by loudspeaker cones that, even to obtain numerical results for one typical loudspeaker cone, large computation times are required. It is therefore impractical, especially from the economic point of view, to make sound-radiation calculations for all types of loudspeaker cones. A feature of this study is that a great deal of the conclusions are based on the calculation of the sound radiation of a few typical cones, although some basic phenomena are studied more thoroughly. Therefore no extensive general characteristics must be expected with the aid of which the frequency response can be predicted exactly for any loudspeaker cone. Only typical phenomena such as characteristic peaks and dips, upper limit of the frequency response and the like can be calculated relatively easily for any cone geometry.

The plan of this thesis is the following. In chapter 2 the generation of sound by loudspeaker cones is qualitatively described without going into mathematical details or proofs; the accent is laid on making plausible all phenomena that influence the sound radiation. Mathematical details, numerical results and extensive discussions are given in the chapters 3 to 6, of which only the last chapter describes the sound radiation explicitly; in the others the mechanical cone behaviour is discussed. In these chapters one may find the basis of the explanations and conclusions stated in chapter 2. Further, typical properties concerning the cone mechanical behaviour and sound radiation, as well as their dependence on the cone geometrical and material parameters are discussed extensively on a theoretical basis and verified by measurements. Design rules are given.

The description of the sound radiation will be made in three steps. First, the well-known characteristics of the rigid piston will be summarized; the latter is a good approximation to the cone at low frequencies. Next, the radiation of a rigid cone will be discussed and compared with that of the rigid piston. Finally, the sound radiation of a flexible cone will be considered and compared with the other radiators. The discussion will be illustrated by typical examples of a rigid piston, a rigid cone and a flexible cone all having the same mass and outer radius; this allows easy comparison of the characteristics.

2. QUALITATIVE DESCRIPTION OF THE VIBRATION AND THE SOUND RADIATION OF LOUDSPEAKER CONES

2.1. Introduction

In this chapter the sound radiation of conical loudspeaker diaphragms will be briefly described. Details, especially mathematical ones, will be omitted; they can be found in subsequent chapters.

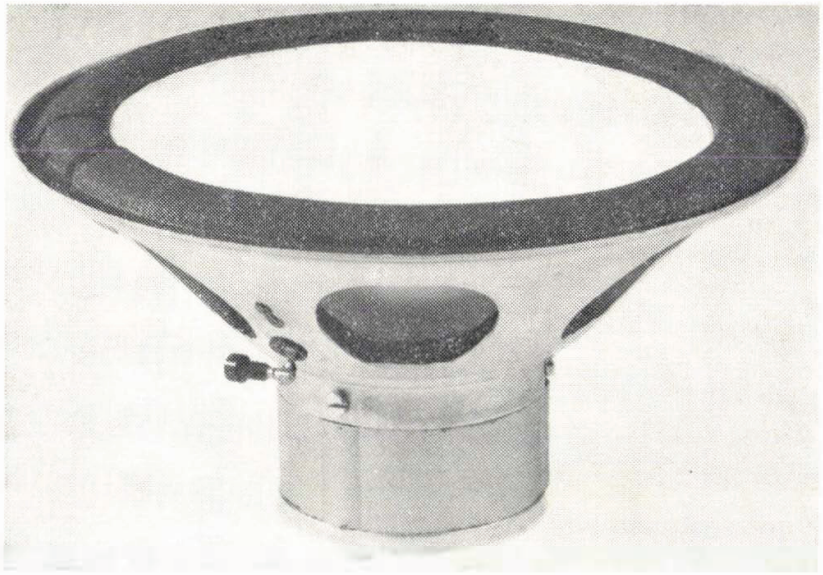

a)

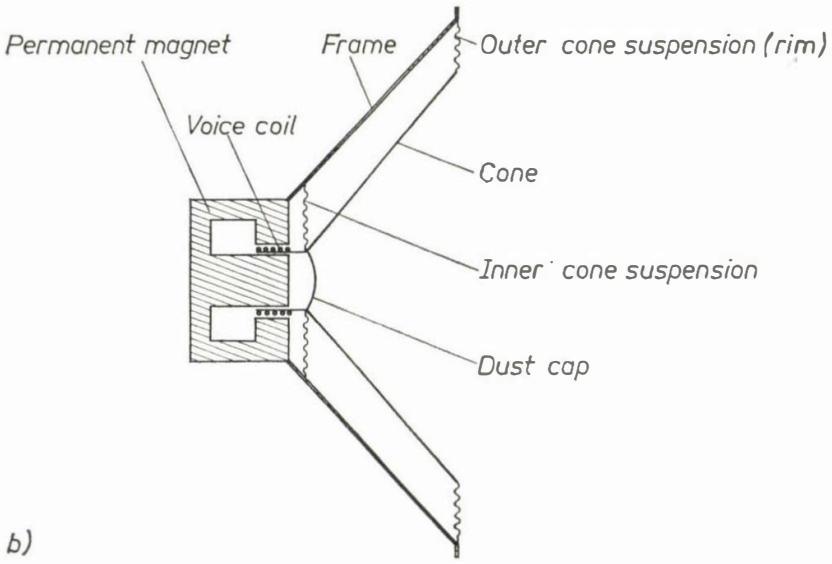

b)

Fig. 2.1. *a*) Photograph and *b*) cross-section of an electrodynamic loudspeaker. The photograph shows cone 50.2e used for the holographical visualization of vibration patterns (see sec. 5.12.2) and the driving mechanism used in all measurements.

A photograph and a cross-section of an electrodynamic loudspeaker is shown in figs 2.1*a* and *b*. The conical diaphragm, usually made of paper, is suspended by an outer suspension or rim and an inner suspension or spider. The latter limit the maximum excursion of the cone at low frequencies so that the voice coil remains inside the air gap of the permanent magnet. The voice coil is attached to the voice-coil cylinder, generally made of paper, which is glued to the inner edge of the cone. In most cases the spider is also attached to this edge. The voice coil is placed in the radial magnetic field of a permanent magnet and is fed with the signal current of the amplifier. In accordance with Lorentz's law this coil exerts an axial force on the cone; the latter is displaced and creates an air flux giving rise to a small disturbance of the atmospheric pressure. The amplitude of these pressure fluctuations is called the sound pressure.

2.2 Basic assumptions

In order to eliminate the (well-known) influence of the driving system it will be assumed that all radiators are driven by a sinusoidal axial force with a frequency-independent amplitude. For an electrodynamic driving system this means that the voice coil is supplied with an alternating current of constant amplitude, which can be assumed without loss of generality, since afterwards all characteristics may be easily multiplied by a possible frequency dependence of the current amplitude.

The influence of the fundamental resonance caused by the radiator mass and suspension is well known; below the fundamental resonant frequency f_0, the vibration is controlled by the stiffness of the suspensions, the inertia of the moving mass being relatively small (stiffness control). If the radiator vibrates in an infinite baffle, which in the following will always be assumed, the axial sound pressure and radiated sound power increase with 12 dB per octave [1]). Hence we only need to consider the frequency region above f_0 for which the inertia of the moving mass dominates over the stiffness of the suspension (mass control).

Further, the influence of the radiation impedance on the radiator vibration will be neglected. This neglection is based on Lax's proof [37]) that the influence of the radiation impedance on the lowest four vibration modes of a flat circular diaphragm can be neglected (cf. sec. 6.5.2). Finally, the sound pressure is only considered at a large distance from the radiator (far field or Fraunhofer region).

2.3. The rigid-piston approximation

The simplest model for the calculation of the sound radiation of a loudspeaker cone is the rigid piston. Then the driving force creates a uniform velocity of the radiating surface which is inversely proportional to the frequency, according to Newton's law. The axial sound pressure is frequency-independent (fig. 6.6*a*), its magnitude is proportional to the driving force and inversely pro-

portional to the piston mass and the distance.

The radiated sound power is frequency-independent up to the transition frequency f_t. The latter frequency, at which the sound wavelength λ_0 in air becomes about equal to the piston circumference, marks the transition from the more or less uniform radiation in all directions to a pronounced radiation in the axial direction, where the beam becomes narrower with increasing frequency. The latter is explained by a sound power decreasing inversely proportionally to the frequency (fig. 6.6*a*).

When we compare the results of the rigid-piston approximation with measurements on a real current-driven electrodynamic loudspeaker in a baffle (figs 6.19*a* and *b*), we can see that for low frequencies the agreement is quite satisfactory but in the high-frequency region the approximation deviates substantially: the measured sound pressure is all but constant and sound power is radiated over a wider frequency interval (about one decade wider). There are two obvious reasons for this deviation, directly inherent to the rigid-piston approximation. First the conical shape of the diaphragm and secondly the flexibility of the real loudspeaker cone considerably influence the sound radiation in the high-frequency region. They both cause their own typical deviation from the rigid-piston approximation; these deviations show up above certain typical (different) frequencies. In the following sections these influences will be discussed.

2.4. The rigid-cone approximation

Suppose a rigid loudspeaker cone, placed in an infinite baffle, to be driven by a force with a frequency-independent amplitude. At low frequencies, where the sound wavelength λ_0 is much greater than the cone dimensions, the radiation of cone and piston do not differ from each other. In that case the cone, like the piston, can be conceived as an acoustic point source.

However, above a certain frequency f_c, at which λ_0 becomes of the order of magnitude of the cone depth, concentric cone parts radiate waves that may arrive in antiphase at the field point. With increasing frequency the axial sound pressure then decreases (rigid-cone roll-off), since the distance between these concentric parts and hence their difference in area decreases, thus enhancing the mutual cancellation of the waves radiated by these parts (fig. 6.6*a*). The frequency f_c increases with decreasing cone depth and becomes infinite for a flat piston, in accordance with the rigid-piston approximation. The radiated sound power starts to decrease at the transition frequency f_t just as for the rigid piston (fig. 6.6*a*).

2.5. The flexible cone

In practice, the loudspeaker cone is far from rigid. Above a certain frequency f_{ra} (the subscripts will be explained later on) (axi-)symmetric bending and

longitudinal waves appear on the cone (the so-called cone break-up). The surface velocity is then far from uniform. Only symmetric wave motion is of interest here; asymmetric (i.e. not rotationally symmetric) waves already appear at a much lower frequency but they do not influence the sound radiation, as will be explained in sec. 2.5.1.1.

Below f_{ra} the measured sound radiation agrees very well with the calculated rigid-cone radiation. If f_c is greater than f_{ra}, even the rigid-piston approximation gives excellent results for $f < f_{ra}$. When we compare the calculated rigid-cone radiation with the measured non-rigid response it appears that the bandwidth of the loudspeaker is increased by cone break-up. Hence, to attain a large bandwidth, the cone should not be made as rigid as possible. In sec. 6.7 we will see that there are still other reasons for avoiding an extremely rigid cone.

In the following the mechanical behaviour and the sound radiation of the flexible cone will be discussed successively.

2.5.1. *Mechanical behaviour*

2.5.1.1. Wave types

We may distinguish between two wave types, which will be called bending and longitudinal (or extensional) waves. On a paper plate, the two wave types may exist independently; they do not influence each other. In that case the distinction is very clear. Bending waves have displacements normal to the plate surface, the wave velocity depends on the frequency and the bending stiffness. Longitudinal waves create displacements in the plane of the plate and the longitudinal wave velocity is much higher than the velocity of bending waves because of the relatively low bending stiffness of the plate. Therefore the longitudinal wavelength is much longer than the bending wavelength. Apart from that, it is independent of the thickness, at least for longitudinal wavelengths much greater than the thickness, which is always assumed.

For a cone, the situation is somewhat more complicated. In general the two wave motions cannot exist independently. A transverse displacement (normal to the cone surface) automatically leads to a longitudinal displacement (in the plane of the cone) and vice versa. This may be illustrated on the basis of fig. 2.2 which shows a conical ring, on the inner edge of which a longitudinal force F_l acts uniformly (upper figure). Statically we may explain the coupling mechanism by first allowing a longitudinal displacement u, which then instantaneously evokes an azimuthal stress because of the diameter increase. This azimuthal stress leads to a force F_c directed towards the ring centre (middle figure), which can be decomposed into a transverse force F_t giving a transverse displacement and a longitudinal force F_l' opposing F_l (lower figure). Equilibrium is reached when the azimuthal stress has become so high that F_l' equals F_l. In the dynamic case the situation is essentially the same, but then inertia forces must be taken

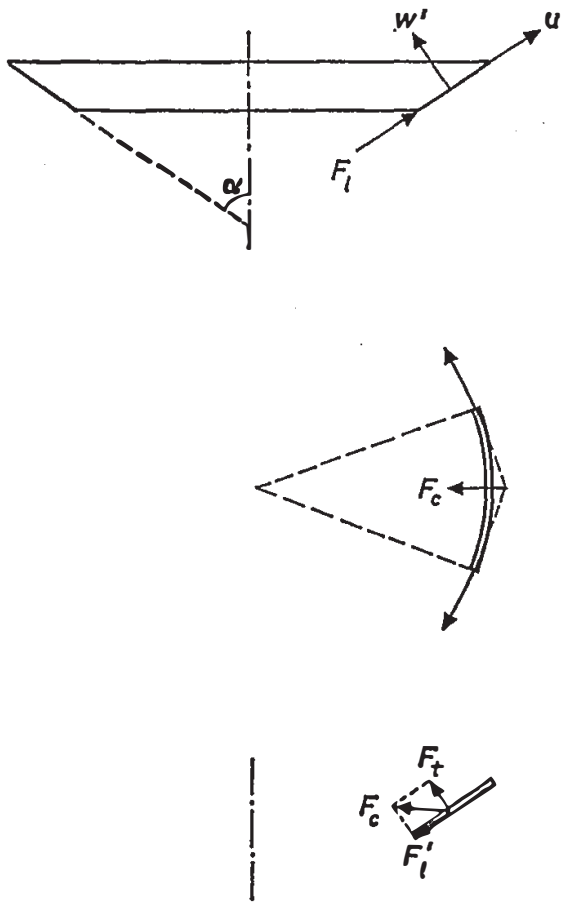

Fig. 2.2. Illustration of the coupling between a longitudinal and a transverse displacement.

into account. Hence, in general, longitudinal and transverse waves are coupled via the cone angle and we cannot speak of pure bending or pure extensional waves. We will make a distinction between the two wave types on the basis of the deformation energy of the cone surface. This energy is the sum of the deformation energy of bending and the deformation energy of stretching of the cone surface. If, for a certain wave, the former part is greater than the latter, we will call it a bending wave; otherwise the wave will be called longitudinal.

Both wave types may travel in azimuthal as well as in meridional direction. Let us first discuss the former. The travelling waves in both azimuthal directions may cause standing waves with nodal and antinodal lines in meridional direction (fig. 2.3). The standing-wave pattern is then called asymmetric (i.e. has no rotational symmetry). Since the bending stiffness of the cone in the azimuthal direction is relatively low, the wave velocity of these asymmetric waves will also be low. Therefore resonant frequencies, at which an integral number of half wavelengths fits on the cone circumference, are low (for a typical 8″ loudspeaker the standing-wave motion of fig. 2.3 already appears at about 100 Hz). Because of the small bending wavelength as compared to the sound wavelength these waves are in general acoustically short-circuited. This means that the air is merely pumped to and fro between neighbouring cone parts, which vibrate

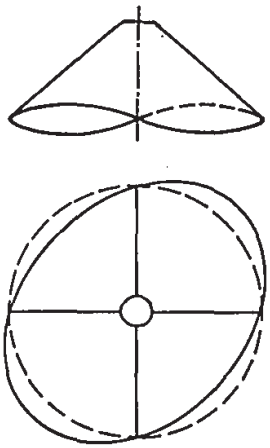

Fig. 2.3. Asymmetric vibration with two nodal diameters.

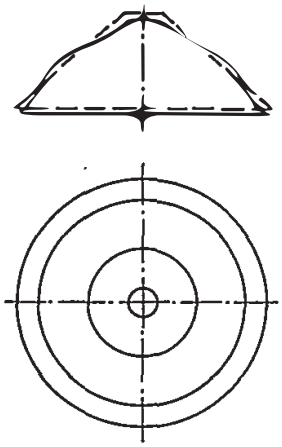

Fig. 2.4. Symmetric vibration with two nodal circles.

in antiphase; very little sound is radiated. Apart from that, these waves are exclusively excited by inhomogeneities: if the cone were perfectly homogeneous and driven purely axially and uniformly along the inner edge circumference, no asymmetric wave motion would appear at all. Of course the latter is not the case in practice, but the inhomogeneities will be small and consequently the same holds for the "driving force" of the asymmetric waves. Therefore the sound radiation of the asymmetric waves will be neglected.

In the following we will fix our attention exclusively on the symmetric waves, directly excited by the axial driving force and in fact providing the sound radiation. Here too, standing waves may occur, because the waves generated at the inner edge travel to the outer edge and are partly reflected there (part is absorbed by the outer suspension). The standing-wave pattern is symmetric with concentric nodal circles (fig. 2.4). In the presence of internal losses travelling waves appear on the cone as well, which blur the standing-wave pattern: at the nodal circles the amplitude becomes minimum but not quite zero.

In figs 5.30 and 5.32 holographic recordings of the standing-wave patterns of a polycarbonate and a paper cone are shown. Note that the paper cone is less homogeneous.

2.5.1.2. Resonant and antiresonant frequencies

At certain frequencies the displacements at the inner edge caused by the outgoing and the reflected waves are exactly 180 degrees out of phase. A node then appears at this place; the frequencies at which this occurs are called antiresonant frequencies. In general, at these frequencies an odd number of quarter wavelengths fits on the cone meridian (in the following for simplicity the outer edge is supposed to be free). At the so-called resonant frequencies the displacements caused by the outgoing and the reflected waves are in phase at the inner edge; an antinode then appears at this place. In general this occurs when an integral number of half wavelengths fits on the cone meridian.

The above holds for both bending as well as longitudinal waves. The spacing between the bending resonant and antiresonant frequencies is much smaller than that between the longitudinal ones because of the relatively low bending-wave velocity. All phenomena described until now are also encountered on a flat ring driven at the inner edge by an oblique force; the only difference lies in the coupling of longitudinal and transverse displacements in the case of a cone. This coupling leads to a typical phenomenon not encountered on a flat plate, viz. cone bending waves appear exclusively above a certain characteristic frequency f_{ra} which is practically independent of the cone thickness.

The typical vibration of the cone at f_{ra} can be explained with the aid of a conical ring in free vibration (fig. 2.5*a*): at the ring resonant frequency f_{rr}, it vibrates in a plane perpendicular to the axis (the centre of gravity remains at rest). If a longitudinal force F_l is applied at the inner edge (fig. 2.5*b*) an anti-resonance occurs at a frequency below f_{rr}. The ring circumference then also contracts and expands (hence the longitudinal nature of the resonance), the motion is however purely transverse. This frequency is called the ring anti-resonant frequency f_{ra}. The transverse amplitude w attains such a magnitude that the inertia force evoked by the displacement of the centre of gravity compensates the axial component of the applied force (sec. 4.4).

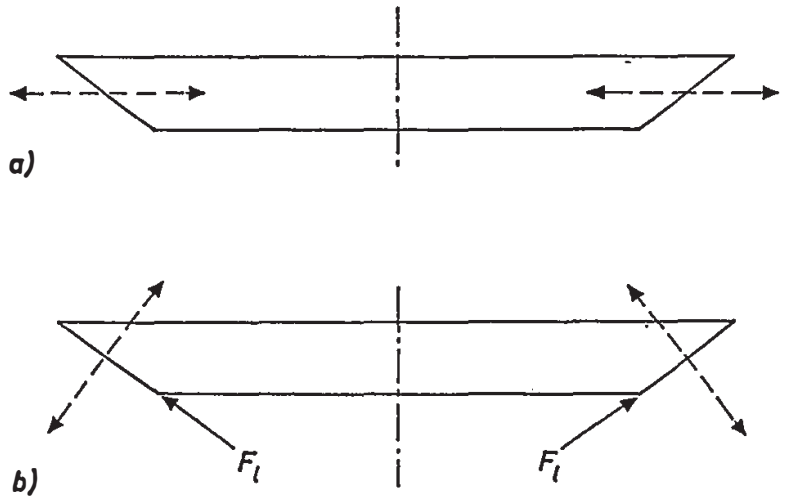

Fig. 2.5. Motion of a conical ring;
a) at the ring resonant frequency f_{rr},
b) at the ring antiresonant frequency f_{ra}.

A similar effect is observed if the conical ring has a greater meridional length. Then f_{ra} of the cone lies close to the ring antiresonant frequency of the outer edge. The typical motion of the cone at that frequency is illustrated in fig. 4.8.

The frequency f_{ra} marks the beginning of cone break-up. Below f_{ra} the cone motion is more or less uniform, whereas above f_{ra} bending and longitudinal waves appear on the cone, giving rise to bending and longitudinal resonant and antiresonant frequencies. It should be noted that the ring antiresonant frequency f_{ra} and the ring resonant frequency f_{rr} originate from extensional motion in the

azimuthal direction, i.e. to a first approximation they are independent of the meridional length of the cone. On the other hand, bending and longitudinal resonant and antiresonant frequencies originate from wave motion in the meridional direction and therefore depend strongly on the meridional length.

2.5.1.3. Mechanical impedance

Since we have a forced vibration, we will have to discuss the reaction of the cone to a driving force. An adequate quantity to express this reaction is the mechanical impedance, defined as the force per unit velocity at the inner edge. In the transverse direction, a much lower force is needed to attain a unit velocity than in the longitudinal direction, because of the small bending stiffness. Therefore the transverse impedance Z_t will be much lower than the longitudinal impedance Z_l. This has important consequences, as will be shown in the following.

The voice coil delivers an axial driving force at the inner cone edge. The inner suspension restrains the latter from moving in other directions than parallel to the cone axis; besides that, the attached inner suspension and voice coil make the inner edge relatively stiff. Now when an axial driving force F_a is exerted, the motion is opposed by the impedances in longitudinal and transverse directions, represented by the two springs in fig. 5.3*b* (it should be noted that in general the impedances Z_l and Z_t cannot be represented by springs). Because the inner edge has to move axially, the longitudinal impedance Z_l will determine the ultimate axial displacement ($Z_l \gg Z_t$). Hence, the axial impedance Z_a will mainly be determined by Z_l. Of course this also depends on the cone angle; if the cone were a flat ring, Z_l would not influence Z_a at all. Therefore, the typical frequency dependence of Z_l (peaks at the longitudinal antiresonant frequencies where a node appears at the inner edge and dips at the longitudinal resonant frequencies where an antinode appears at that place) will also be visible in the frequency characteristic of Z_a.

The foregoing is illustrated in fig. 5.23, which shows the modulus of the axial impedance Z_a at the inner edge of a typical cone *) with internal damping calculated as a function of frequency (drawn curve). This figure is obtained by solving numerically a system of simultaneous first-order differential equations describing the axisymmetric mechanical cone behaviour for a large number of frequencies. In the low-frequency region $|Z_a|$ increases proportionally to the frequency according to Newton's law; in that region the whole cone oscillates more or less uniformly in the axial direction. At the ring antiresonant frequency f_{ra} a relatively high peak occurs, because Z_l becomes maximum.

Above f_{ra}, small closely spaced peaks and dips are visible in $|Z_a|$ (fig. 5.23). These are caused by bending antiresonances, which is explained as follows. It

*) Material and geometrical parameters, see sec. 5.11.

has been remarked before that in general $Z_t \ll Z_l$; the mean value of $|Z_a|$ is determined by $|Z_l|$. However, at the bending resonant and antiresonant frequencies, Z_t becomes minimum and maximum respectively, which causes small dips and peaks (fine structure), which are superposed on a mean curve determined by Z_l. The spacing between the peaks (or dips) depends on the bending stiffness; their height depends on the damping of the bending waves on the cone, the bending wavelength and the meridional length of the cone. When the damping increases, the reflected wave becomes small and hardly interferes with the outgoing at the inner edge; this results in less-pronounced antiresonances and resonances. It may occur that the reflected wave has become negligibly small at the inner edge; in that case bending resonances or antiresonances do not show up at all and the axial velocity varies smoothly with frequency.

Bending resonances and antiresonances only appear above the cone break-up frequency f_{ra}; they gradually disappear with increasing frequency because the bending waves have to travel an increasing number of bending wavelengths before they arrive at the inner edge again. This means that in the high-frequency region only travelling bending waves show up.

For sufficiently high frequencies (above 10 kHz, fig. 5.23) the wavelength of the longitudinal waves becomes shorter than the cone meridional length and the waves "do not notice" the cone angle anymore: they behave as if they were travelling on a flat plate with the same meridional length as the cone. The axial impedance shows the typical behaviour of a longitudinally driven plate: $|Z_a|$ oscillates about a frequency-independent mean value (the characteristic longitudinal impedance of a plate is frequency-independent).

The frequency dependence of the axial impedance $|Z_a|$ shown in fig. 5.23 is characteristic of all loudspeaker cones. The longitudinal antiresonant frequencies, at which $|Z_a|$ becomes maximum are determined by longitudinal wave motion in the meridional direction. The heights and depths of the maxima and minima are determined by the internal loss factor; this holds for both longitudinal as well as bending resonances and antiresonances.

In the foregoing the mechanical behaviour of a cone has been considered without taking into account the voice-coil mass (and other additional masses at the inner edge, e.g. that of the dust cap). The reactance of this additional mass M_c must be added to Z_a, giving a total impedance Z_{tot}.

In the low-frequency region where the cone oscillates more or less rigidly, M_c only causes a upward shift of the Z_a curve (fig. 5.24). For high frequencies however, the reactance of M_c becomes higher than $|Z_a|$ (fig. 5.23) and Z_{tot} is practically entirely determined by M_c: it increases proportionally to the frequency. Then the maxima and minima at the longitudinal antiresonant and resonant frequencies appear only as small disturbances in the frequency characteristic of Z_{tot} (fig. 5.24).

2.5.1.4. Displacement patterns

The transverse-displacement pattern on the cone ultimately determines the sound radiation. We find characteristic displacement patterns in the various frequency regions.

For low frequencies ($f < f_{ra}$), the cone oscillates more or less rigidly in the axial direction. In the middle-frequency region (region II, fig. 5.23), two wave types appear simultaneously on the cone. Between the inner edge and a certain point x_t (transition point) on the cone the transverse displacement w is determined by a longitudinal wave with a relatively long wavelength. Between x_t and the outer edge, w is determined by a bending wave with a relatively short wavelength (see e.g. the transverse and longitudinal displacement patterns of fig. 5.4*h*, where x_t is indicated by a dot). This transition point shifts from the outer to the inner edge with increasing frequency in region II: at a frequency f_{tb} it lies at the outer edge, whereas it reaches the inner edge at a frequency f_{ta}.

In the high-frequency region (region III, fig. 5.23), bending waves cover the entire cone.

2.5.2. *Sound radiation*

Two important factors influencing the sound radiation are the conical shape of the radiating surface and the transverse velocity distribution on it. The transverse velocity distribution is determined by mechanical wave motion on the cone surface, created by the axial driving force. Because the latter is symmetric, we shall consider only the sound radiation by symmetric waves; the radiation of asymmetric waves is neglected as discussed above.

We may characterize the transverse velocity distribution by the wavelength and the wave amplitude, which both depend on the meridional coordinate. The sound radiation depends on the volume velocity *) created by the waves on the cone surface. The volume velocity is proportional to the wave amplitude and the latter depends on the amplitude of the inner edge where the driving force keeps everything in motion. The amplitude of the inner edge is determined by the axial impedance Z_a which is well approximated by the longitudinal impedance Z_l. Hence we may expect a high influence of Z_l on the sound-pressure response.

In this paper the sound radiation is calculated supposing the cone to be covered by simple point sources with strengths equal to the local volume velocity on the cone. The sound-pressure response is found by first calculating this volume velocity for a number of frequencies and then simply integrating these sources over the cone surface. This method is not realistic for directions outside the cone apex angle, because it does not allow for the screening-off effect. Therefore, we calculate the radiated sound-power level L_{W100} within a space

*) The volume velocity is the integral of the transverse velocity over the cone surface.

sector having an apex angle of 100 degrees (this is the smallest apex angle considered in this thesis).

For the same reason, the directivity index DI_{100} is defined as the difference in L_{W100} of a point source in an infinite baffle creating the same intensity on the cone axis as the cone itself and L_{W100} of that cone. The beam width β is defined as the angle at which the sound-pressure level has decreased by 3 dB as compared with the axial value.

The radiation of a flexible cone will be explained on the basis of a numerically calculated example. The radiation characteristics with voice-coil mass $M_c = 0$ are shown in fig. 6.7*a*. The cone dimensions are given in table 5-I, the frequency characteristic of $|Z_a|$ is shown by fig. 5.23. First, we will discuss the frequency characteristic of the axial sound-pressure level L_p (upper graph of fig. 6.7*a*). As before, we may divide the frequency spectrum into three regions.

In the low-frequency region ($f < f_{ra}$), the cone behaves as a rigid piston: L_p is frequency-independent. The peak in $|Z_a|$ at the ring antiresonant frequency f_{ra} does not show up as a dip in the sound pressure because, although the amplitude at the inner edge is relatively small, the rest of the cone vibrates vigorously in a mode which is not acoustically short-circuited (fig. 4.8). If the characteristic cone frequency f_c were sufficiently smaller than f_{ra}, L_p would decrease between f_c and f_{ra} (sec. 2.4). In the middle-frequency region ($f_{tb} < f < f_{ta}$) L_p shows a broad maximum on which small oscillations (fine structure caused by bending resonances and antiresonances) are superimposed. This maximum is found as a relative minimum in the frequency characteristic of Z_a (fig. 5.23). It shows up in the frequency response of L_p, because the wavelength on the inner part of the cone is longer than the sound wavelength in air. The acoustically short-circuited bending waves on the outer cone part are of minor importance (see e.g. fig. 5.4*h*). In this frequency region the cone effectively radiates as a rigid piston whose radius decreases with increasing frequency (sec. 2.5.1.4).

A minimum occurs at the first longitudinal antiresonant frequency f_{la1} (7500 Hz), where $|Z_a|$ becomes maximum. In most cases this frequency forms the upper limit of the frequency response *).

In the high-frequency region, the sound pressure oscillates about a mean value, showing peaks at the longitudinal resonant (14 and 23 kHz) and dips at the longitudinal antiresonant frequencies (18 and 28 kHz). This mean value decreases with increasing frequency, because acoustically short-circuited bending waves now cover the entire cone.

The frequency response of the radiated sound power L_{W100} has roughly the same shape as the axial sound-pressure response (fig. 6.7*a*, middle graph). A difference may appear in the low-frequency region; if the transition frequency

*) The upper frequency limit of a response is chosen more or less arbitrarily as the frequency at which the response has decreased by 8 dB relative to the low-frequency value.

for the rigid piston f_t were much smaller than f_{ra}, L_{W100} would show a roll-off at f_t with a minimum at f_{ra}.

The lowest graph of fig. 6.7*a* shows the frequency characteristic of the directivity index DI_{100} and the beam width β. On the average, DI_{100} of the flexible cone is higher than that of the rigid cone, because the latter radiates much energy normal to its surface, but lower than that of the rigid piston (cf. figs 6.6*b* and 6.7*a*).

In a discussion of the sound radiation, the directivity diagram of the radiator cannot be left out. The characteristics of this diagram are well known for the rigid piston: below f_t the radiation is practically uniform in all directions, above f_t the sound is mostly radiated in a central beam normal to the piston surface, which becomes narrower with increasing frequency. This is illustrated in figs 6.6*c*, *d* and *e*, in which the calculated directivity diagrams for the piston of fig. 6.6*a* are shown at 1, 5, 10 and 20 kHz (f_t = 900 Hz).

For the rigid cone the radiation below the characteristic cone frequency f_c (1600 Hz) is as uniform as that of the piston (fig. 6.6*c*). Above f_c the sound radiation in the direction normal to the cone surface increases at the expense of the radiation in axial direction (figs 6.6*d* and *e*). The cause of this sidelobe is clear: in the direction normal to the cone surface a relatively large part of the cone radiates waves which arrive in phase at the field point. In figs 6.6*c*, *d* and *e* the latter direction is indicated by an arrow.

The directivity diagrams of the flexible cone are in general smoother than that of the rigid cone or piston because of phase differences in the displacement patterns.

The voice-coil mass considerably influences the frequency characteristic of the axial impedance Z_a as discussed in sec. 2.5.1.3. In that section it was shown that above a certain frequency, $|Z_a|$ increases with frequency. The axial velocity and consequently the sound pressure and power will decrease with frequency. This is shown in fig. 6.17*a* for the present cone with a voice-coil mass equal to one fourth of the cone mass. The steep roll-off at the first longitudinal anti-resonant frequency f_{la1} is typical; for greater ratios of voice-coil mass to cone mass this roll-off starts at lower frequencies. In practice the upper limit of the pressure and power responses is determined by the voice-coil mass.

Finally we will compare calculated and measured curves of a (plastic) cone whose geometrical and material parameters are shown in tables 5-VI to 5-IX. The frequency characteristics are measured for the loudspeaker placed in an acoustic box of 0·1 m³; the front of the latter is formed by a 1·5 . 1·5 m² baffle. Figure 6.20*a* (lower graph) shows the calculated and measured sound-pressure responses of this cone. In the measured curve a baffle dip appears at about 300 Hz. Figure 6.20*b* shows the calculated and measured sound-power responses. Both characteristics show a general agreement between calculations and measurements. In the low-frequency region the measured curves run somewhat

higher due to the radiation by the outer suspension. In the high-frequency region the measured responses are higher than those calculated because the inner edge is not completely rigid, as assumed in the calculations.

The measured and calculated frequency characteristics of the directivity index DI_{100} and beam width β are shown in fig. 6.20*c*. On the average there is a satisfactory agreement. The same holds for calculated and measured directivity diagrams (fig. 6.20*d*).

2.6. Conclusion

In the preceding sections the mechanical behaviour and the sound radiation of a flexible loudspeaker cone were discussed and compared with that of the rigid piston and the rigid cone. We can summarize our conclusions as follows.

The mechanical cone behaviour is mainly determined by the longitudinal impedance Z_l at the inner edge. The frequency characteristic of the latter shows large peaks and dips at longitudinal resonant and antiresonant frequencies respectively. Bending waves appear on the cone above the ring antiresonant frequency f_{ra} (cone break-up); they cause bending resonances and antiresonances which show up as a fine structure in the frequency characteristic of the axial impedance Z_a. Above a certain frequency the voice-coil mass determines the vibration amplitude; this frequency increases with decreasing ratio M_c/M_d of the voice-coil mass to the cone mass.

As for the sound radiation, at low frequencies the cone behaves as a rigid piston; the response is frequency-independent. Above the break-up frequency f_{ra} a more or less broad maximum appears on which the above fine structure is superposed. Above a frequency determined by M_c/M_d the response decreases with increasing frequency. In practice this frequency usually lies below the first longitudinal antiresonant frequency f_{la1} where a deep minimum appears.

It has been shown that the pressure and power responses as well as the directivity diagrams of a loudspeaker cone can be calculated with acceptable accuracy. The upper frequency limit of the power response of an appropriately designed flexible cone is higher than that of a rigid cone or a rigid piston. From this point of view the cone should not be made as rigid as possible, as is sometimes proposed in literature. A high upper limit of the responses is obtained by a small ratio M_c/M_d of the voice-coil mass to the cone mass; however, this limit lies at most at the first longitudinal antiresonant frequency f_{la1}. Means to avoid the fine structure in the responses and the broad maximum above cone break-up will be discussed in sec. 6.7.

In the preceding sections the most important phenomena concerning the cone mechanical behaviour and sound radiation have been discussed briefly. These matters and other phenomena will be discussed extensively in the following chapters, where the dependence of the sound radiation on the geometrical and material properties of the cone will be treated as well.

3. THE ELECTRODYNAMIC LOUDSPEAKER

3.1. Introduction

In this chapter the working principle and characteristic properties of the electrodynamic loudspeaker will be discussed on the basis of an electromechanical equivalent circuit. Further, a measuring method for the voice-coil velocity is explained.

3.2. Electromechanical equivalent circuit

An electromechanical equivalent circuit for the electrodynamic loudspeaker is shown in the diagram of fig. 3.1*a*; the circuit is of the so-called mobility type [1]). It consists of a primary and a secondary circuit, coupled by a transformer. The primary circuit stands for the electrical side of the loudspeaker. It contains the voice-coil resistance R_c and inductance L_c. The electromechanical conversion is represented by the transformer, which delivers a current with amplitude F_a, standing for the force on the voice-coil cylinder. The transformation ratio $B\,l : 1$ follows from Lorentz's law

$$F_a = B\,l\,i,$$

where B is the magnetic induction in the air gap and l the total length of the voice-coil windings; i is the amplitude of the voice-coil current. The amplitude of the voice-coil velocity is v_a (represented by a voltage in fig. 3.1*a*). The mass of the voice coil and voice-coil cylinder (in the following abbreviated to voice-

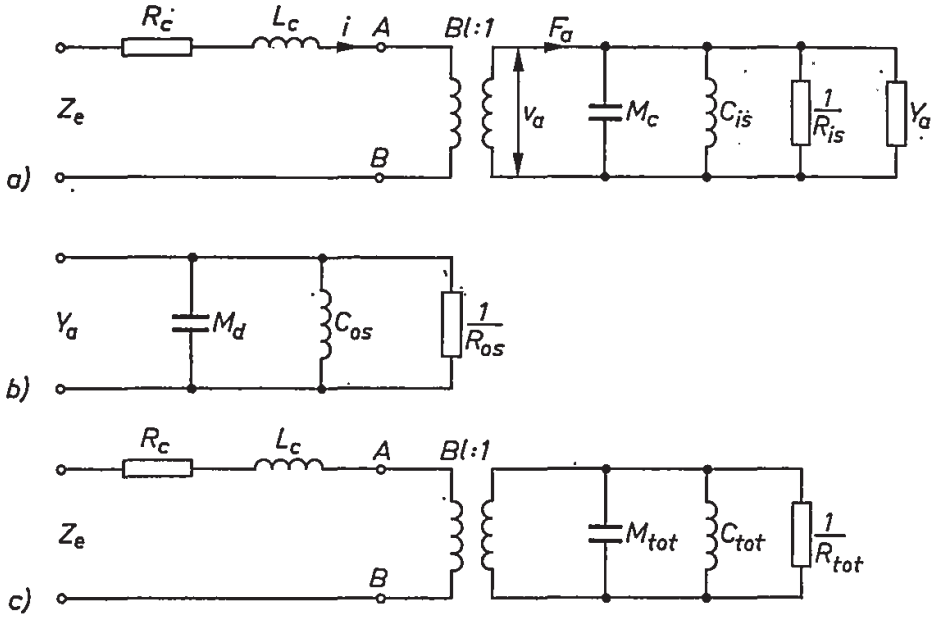

Fig. 3.1. (*a*) Equivalent circuit of the electrodynamic loudspeaker,
(*b*) equivalent circuit of the cone below cone break-up,
(*c*) equivalent circuit of the loudspeaker below cone break-up.

coil mass) is M_c, the total compliance of the inner suspension is C_{ts} and the mechanical resistance of the latter is R_{ts}. The total axial admittance (velocity per unit force) of the cone plus outer suspension is Y_a. In the latter the mechanical radiation impedance can be accounted for; this will however not be done for reasons discussed in sec. 2.2.

We find for the total electrical impedance Z_e of the electrodynamic loudspeaker (fig. 3.1*a*):

$$Z_e = R_c + j\omega L_c + Z_{\text{mot}}, \tag{3.1}$$

where the impedance between the points A and B is called the motional impedance Z_{mot}, because it originates from the electromotive force induced by the motion of the voice coil in a magnetic field. It will be further discussed in sec. 3.3.

We may write in general

$$Z_{\text{mot}} = (B\,l)^2\, v_a/F_a \tag{3.2a}$$

or

$$Z_{\text{mot}} = \frac{(B\,l)^2}{R_{ts} + j\omega M_c + 1/j\omega C_{ts} + Z_a}, \tag{3.2b}$$

where the axial impedance Z_a of the cone is the inverse of Y_a.

For frequencies below cone break-up the cone oscillates more or less rigidly in the axial direction and may be represented by the equivalent circuit of fig. 3.1*b*. In that case the axial admittance Y_a becomes

$$Y_a = \frac{1}{R_{os} + j\omega M_d + 1/j\omega C_{os}}, \tag{3.3}$$

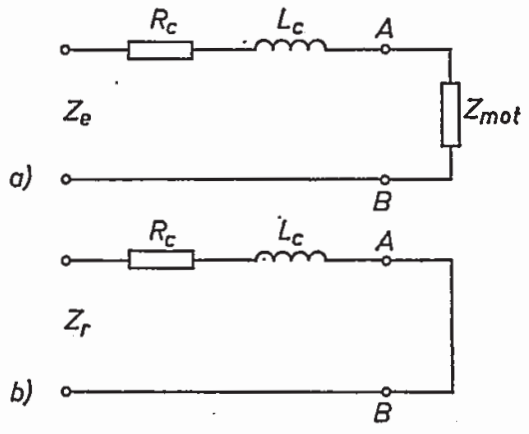

Fig. 3.2. Abridged equivalent circuit of
(*a*) the test loudspeaker,
(*b*) the reference loudspeaker with blocked voice coil.

where M_d is the cone mass, C_{os} the compliance of the outer suspension and R_{os} the mechanical resistance of the latter. In this frequency region the influence of the radiation impedance could easily be accounted for, as only the mass of the vibrating air on both sides of the cone must be added to M_d. This influence is discussed extensively in the textbooks [10,25]) and will further be left out of consideration.

Combination of figs 3.1*a* and *b* leads to the equivalent circuit of fig. 3.1*c*, valid for low frequencies. In the latter figure the total moving mass is

$$M_{\text{tot}} = M_c + M_d$$

and C_{tot} is the total compliance of the inner and outer suspension, determined by $1/C_{\text{tot}} = 1/C_{is} + 1/C_{os}$; $R_{\text{tot}} = R_{is} + R_{os}$ is the total mechanical resistance.

The total mass M_{tot} and compliance C_{tot} constitute a simple mass-spring system and create a resonance at the so-called fundamental resonant frequency f_0, determined by

$$f_0 = \frac{1}{2\pi\,(M_{\text{tot}}\,C_{\text{tot}})^{1/2}}\,. \tag{3.4}$$

This frequency is mostly chosen as low as possible since it determines the lower limit of the frequency response of the loudspeaker (in a sufficiently large baffle pressure and power responses decrease with 24 dB per octave with decreasing frequency below f_0).

For frequencies below cone break-up it follows that

$$Z_{\text{mot}} = \frac{(B\,l)^2}{R_{\text{tot}} + j\omega M_{\text{tot}} + 1/j\omega C_{\text{tot}}}\,. \tag{3.5}$$

This equation may be further simplified for frequencies well below the fundamental resonant frequency f_0, since then

$$\left|R_{\text{tot}} + j\omega M_{\text{tot}}\right| \ll \frac{1}{\omega C_{\text{tot}}}$$

and hence

$$\left|Z_{\text{mot}}\right| \approx (B\,l)^2\,\omega C_{\text{tot}} \tag{3.6a}$$

or

$$v_a \approx F_a\,\omega C_{\text{tot}}. \tag{3.6b}$$

Hence, for low frequencies the motion of the cone and voice coil is stiffness-controlled; if F_a is kept constant by driving the voice coil with a sinusoidal current with a frequency-independent amplitude i (which is always done to

eliminate the influence of R_c and L_c) the voice-coil velocity is proportional to the frequency.

Above f_0 (but still below cone break-up), where

$$\omega M_{tot} \gg |R_{tot} + 1/j\omega C_{tot}|,$$

the voice coil as well as the cone have a velocity determined by the total moving mass M_{tot} (mass control); we then can write

$$|Z_{mot}| \approx (B\,l)^2/\omega M_{tot} \tag{3.7a}$$

or

$$v_a \approx F_a/\omega M_{tot}. \tag{3.7b}$$

Hence v_a decreases inversely proportionally to the frequency. This has important consequences for the sound radiation, as will be shown in chapter 6.

Equation (3.3), giving the axial admittance Y_a of the cone itself, can be simplified for frequencies far above the resonance of the diaphragm mass M_d and the outer suspension C_{os}:

$$Y_a \approx \frac{1}{j\omega M_d}. \tag{3.8}$$

Equation (3.8) too is only valid below cone break-up.

For frequencies above cone break-up, eq. (3.2b) is very well approximated by

$$Z_{mot} \approx \frac{(B\,l)^2}{j\omega M_c + Z_a}, \tag{3.9}$$

where R_{is} and $1/j\omega C_{is}$ have been neglected, since then

$$\left|R_{is} + \frac{1}{j\omega C_{is}}\right| \ll |j\omega M_c + Z_a|.$$

3.3. Measurement of the voice-coil velocity

It has been stated in the foregoing section that the motional impedance given by eq. (3.2) originates from the electromotive force, generated in the voice coil moving with a velocity v_a in a magnetic field. Therefore v_a can be determined on the basis of the measurement of Z_{mot}. This will be described in the following.

The general equivalent circuit of fig. 3.1*a* is redrawn in fig. 3.2*a* where the impedance between the points A and B is represented by Z_{mot}. This leads to the total impedance Z_e as given by eq. (3.1). Now a second (reference) loudspeaker is used of exactly the same type as the test loudspeaker of which the motional impedance should be measured. The voice coil of this reference loudspeaker is

blocked by casting it into e.g. epoxy resin. Further the permanent-magnet part of the driving system is not magnetized. Although the latter introduces a difference in self-inductance L_c of test and reference loudspeakers, it appeared necessary to use a non-magnetized magnet, since even the very small vibrations of a blocked voice coil with a normal magnet excite resonances, which cause unwanted high peaks and dips in the motional-impedance curve. These measures completely prevent all voice-coil motion of the reference loudspeaker. Its motional impedance is therefore zero. The equivalent circuit of the reference loudspeaker is shown in fig. 3.2*b*. Its impedance is

$$Z_r = R_c + j\omega L_c. \tag{3.10}$$

With eq. (3.1) it follows that

$$Z_{\text{mot}} = Z_e - Z_r. \tag{3.11}$$

The motional impedance is measured as a function of frequency by supplying the test and reference loudspeakers with the same frequency-independent current and then subtracting the voltage drops across the terminals of both loudspeakers. In this way the absolute value of the motional impedance can be measured, which gives enough information to detect peaks and dips caused by resonances and antiresonances.

The measuring accuracy of this method is not very high, because Z_e and Z_r are almost equal. Small differences in the voice coils of the loudspeakers may thus cause considerable deviations, which may even become greater than Z_{mot}. This occurs especially in the high-frequency region where the difference in permeability of the two magnetic circuits (one magnetized, the other not) leads to great differences in L_c. This is however not important, since in general the method is not intended to assess the value of the motional impedance, but merely to detect peaks and dips in its frequency characteristic. These peaks and dips are caused by resonances and antiresonances of the cone (sec. 5.12). The frequencies at which they appear can be measured accurately by the above method.

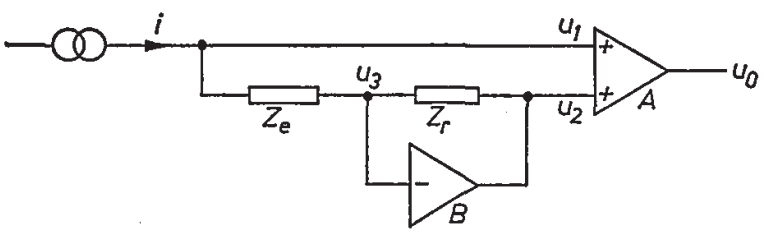

Fig. 3.3. Measuring circuit for the motional impedance.

A block diagram of the measuring circuit is shown in fig. 3.3. A current source drives a current with a frequency-independent amplitude i through the test and reference loudspeakers, represented by the impedances Z_e and Z_r

respectively. This current flows back to earth via the output terminal of the operational amplifier B, which has a very low output impedance (the input impedances of B and the summation network A are very high, so that the input currents of A and B can be neglected). Calling μ the gain of the operational amplifier B, the following equations hold:

$$i Z_e = u_1 - u_3, \tag{3.12}$$

$$i Z_r = u_3 - u_2, \tag{3.13}$$

$$u_2 = -\mu u_3. \tag{3.14}$$

The output voltage u_0 of the summation network A (of gain unity) is

$$u_0 = u_1 + u_2. \tag{3.15}$$

After elimination of u_1, u_2 and u_3 we find:

$$u_0 = i\left(Z_e - Z_r \frac{\mu - 1}{\mu + 1}\right), \tag{3.16}$$

which, owing to the high value of μ (10^5 or more), can be written as

$$u_0 \approx i\,(Z_e - Z_r),$$

or

$$Z_{mot} \approx u_0/i. \tag{3.17}$$

A detailed diagram of the measuring circuit is shown in appendix E.

4. MEMBRANE APPROXIMATION OF THE MECHANICAL CONE BEHAVIOUR

4.1. Introduction

An electrodynamic loudspeaker radiates sound because of mechanical displacements of the cone. The basis of a description of the sound radiation by a conical loudspeaker diaphragm must therefore inevitably be a description of its mechanical behaviour. The main difficulty is the solution of the system of differential equations which describes this mechanical behaviour. For normal loudspeaker cones this system can only be solved numerically (see chapter 5). It needs no further comment that it is difficult to understand the cone behaviour on the basis of numerical computations. For a better understanding it may therefore be advantageous to first explain the cone behaviour by means of an approximate theory of which the mathematical description is simpler.

The extensional or membrane theory is such a simplification. In this approximation the cone is supposed to have a negligible bending stiffness. This means that all bending moments are neglected and the cone motion is essentially controlled by in-plane stresses; the cone is then called a conical membrane. As a consequence the influence of the cone thickness is ruled out; the latter remains in the mechanical equations only as a proportionality factor in the mass per unit area. But even with this drastic simplification numerical calculations cannot be dispensed with, although analytical solutions can be given at very low and very high frequencies.

The usefulness of membrane theory will become clear in chapter 5 where its results are compared with those obtained with the exact theory including bending effects. There it will be shown, among other things, that the longitudinal resonant and antiresonant frequencies are very well predicted by membrane theory and that in the presence of internal material damping the frequency characteristic of the longitudinal admittance calculated with the membrane theory is a good approximation of the frequency characteristic of the axial admittance calculated with the exact equations.

In the past, the membrane theory has been used more than once to describe the vibrations of conical surfaces. In 1951, Nimura et al.[2]) gave approximate analytical expressions for the vibrational modes of the conical membrane with very small and very large apex angles, the cone being almost a cylinder and a flat membrane respectively. For common apex angles they resorted to a graphical determination of the lower eigenfrequencies in special frequency regions.

It was not until 1966 that Ross [4,5]) in an asymptotic approximation constructed analytical solutions for the membrane as well as for the bending behaviour of a shell of revolution. Although his work contributed much to the understanding of the general cone behaviour (see sec. 5.3), his results can-

not be applied in the essential part of the loudspeaker frequency range. Later on, in 1967 [6]), he also gave approximate analytical solutions for this part, but these are mainly intended to give insight into a special phenomenon (transition point) generally encountered in the vibration of conical shells (discussed in chapters 4 and 5). In order to obtain more-accurate results he suggests numerical solution of the differential equations.

In this chapter the forced vibration of the conical membrane will be described mainly on the basis of numerical computations. For very low and very high frequencies, relatively simple analytic expressions can be derived, which contribute considerably to the understanding of the cone behaviour. Only axisymmetric vibrations will be considered. Asymmetric vibrations, caused by inhomogeneities and the like, will be discussed briefly in the following chapter. Although neglecting the cone bending stiffness may seem at first sight a very crude approximation we shall see that very useful results can be obtained on the basis of membrane theory.

4.2. Cone geometry

We will simplify the configuration of the electrodynamic loudspeaker shown in fig. 2.1*b* by "stripping" inessential parts from the cone. It was shown in chapter 3 that the outer suspension does not fundamentally change the mechanical behaviour of the cone, though in the low-frequency region the outer suspension and the cone may vibrate in antiphase, which causes a dip in the frequency response (the so-called rim dip). This dip is usually easily recognized (see sec. 6.6.2) and will be left out of consideration.

In the following we will assume the outer edge to be free; the damping influence of the outer suspension will be accounted for by taking the internal loss factor of the cone material somewhat higher than the practical value. This procedure of distributing the edge damping over the vibrator surface is justified if the damping is not too high; it considerably simplifies the mathematical description.

Further, the influence of the driving mechanism (voice coil and inner suspension) will be left out of consideration. Later on its influence may be accounted for on the basis of the equivalent circuit of fig. 3.1*a*. These simplifications leave us with the configuration of the truncated conical shell, shown in fig. 4.1*a*, which will be the basic model for all computations. There are four geometrical parameters, viz. the inner and outer radii R_a and R_b respectively, the semi-apex angle α and the shell thickness h. The four material parameters are: Young's modulus E, the mass per unit volume ϱ, Poisson's ratio ν and the internal loss factor δ.

4.3. Membrane differential equations

The coordinates of a basic cone element are depicted in fig. 4.1*a*. The merid-

ional coordinate of this element is called x, the azimuthal coordinate θ. A quantity often encountered in the theory of the vibrations of shells is the principal radius of curvature r_2 in the θ-direction (also called second radius of curvature).

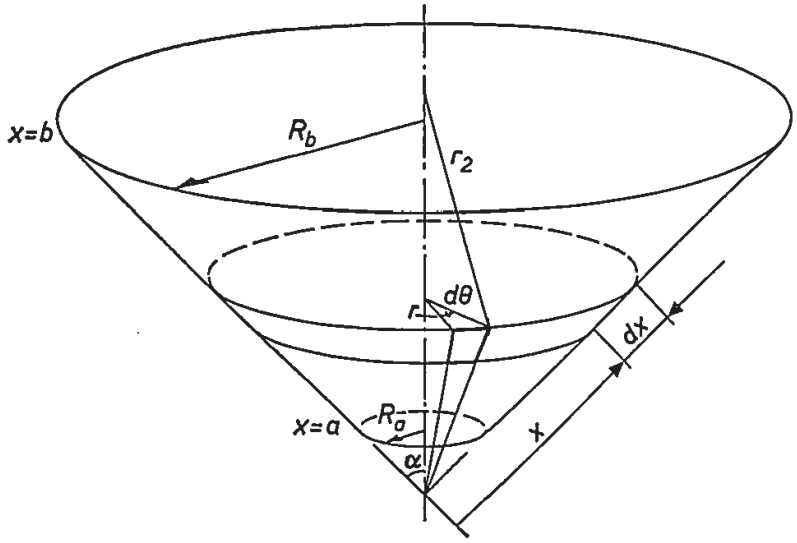

Fig. 4.1*a*. Cone geometry and coordinates of a cone element.

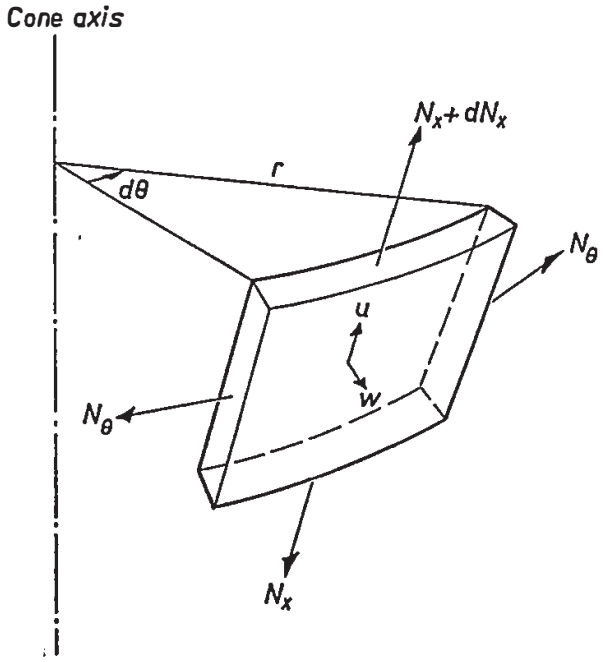

Fig. 4.1*b*. Cone element with the positive directions of the membrane stress resultants and displacements.

Figure 4.1*b* shows the positive directions of the membrane stress resultants *) and displacements. Since only axisymmetric vibration is considered, the displacement in the azimuthal direction is assumed to be zero. The displacements

*) A stress resultant is defined as the force acting on one side of a shell element per unit length of that side.

in transverse and meridional directions are w and u respectively. Further, the stress resultants N_x and N_θ in meridional and azimuthal direction are independent of θ. The internal loss factor is initially supposed to be zero; it will be introduced in sec. 4.7.4.

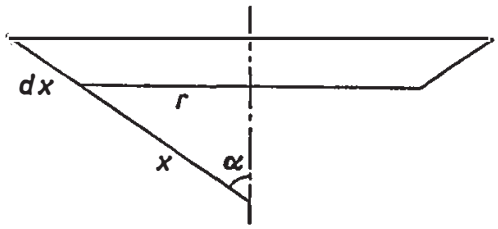

Fig. 4.2*a*. Elementary conical ring.

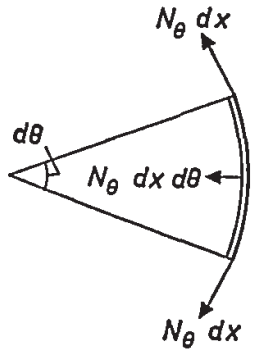

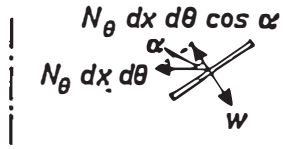

Fig. 4.2*b*. Illustration of the transverse force opposing a transverse displacement w.

Application of Newton's law to the cone element of fig. 4.2*b* in the meridional direction leads to

$$\frac{\partial}{\partial x}(N_x\, r\, \mathrm{d}\theta)\, \mathrm{d}x - N_\theta \sin\alpha\, \mathrm{d}x\, \mathrm{d}\theta = \varrho\, h\, r\, \mathrm{d}\theta\, \mathrm{d}x\, \frac{\partial^2 u}{\partial t^2}, \qquad (4.1a)$$

where the second term on the left-hand side is recognized as the meridional component of the azimuthal stress N_θ. Newton's law in the transverse direction reads

$$N_\theta \cos\alpha\, \mathrm{d}x\, \mathrm{d}\theta = -\varrho\, h\, r\, \mathrm{d}\theta\, \mathrm{d}x\, \frac{\partial^2 w}{\partial t^2}. \qquad (4.1b)$$

In these equations r is the distance of the cone element from the axis.

For sinusoidal vibration, eqs (4.1) may be written as

$$x\frac{dN_x}{dx} + N_x - N_\theta = -\omega^2 x \varrho h u, \tag{4.2a}$$

$$N_\theta = \omega^2 x \varrho h w \tan\alpha, \tag{4.2b}$$

where the symbols for the stress resultants and the displacements now represent the amplitudes of the sinusoidal variation in time; the time factor $\exp(j\omega t)$ has been left out. Further, we have the stress–strain relations (Hooke's law):

$$N_x = K(\varepsilon_x + \nu\,\varepsilon_\theta), \tag{4.3a}$$

$$N_\theta = K(\varepsilon_\theta + \nu\,\varepsilon_x), \tag{4.3b}$$

where K is the extensional stiffness, defined by

$$K = \frac{Eh}{1-\nu^2}.$$

Finally, the following strain-displacement relations hold:

$$\varepsilon_x = \frac{du}{dx}, \tag{4.4a}$$

$$\varepsilon_\theta = \frac{u\sin\alpha + w\cos\alpha}{r}, \tag{4.4b}$$

which can be easily derived by considering the elongation per unit length in the meridional and the azimuthal directions. All these equations can be found in any textbook on vibrations of shells [18]).

The above six equations form the basis of the membrane theory applied to a conical surface. Elimination of the strains ε_x and ε_θ leads to two simultaneous first-order differential equations:

$$\frac{dN_x}{dx} = \frac{\nu g - 1}{x} N_x + \frac{Eh}{x^2}(g - k^2 x^2)\,u, \tag{4.5a}$$

$$\frac{du}{dx} = -\frac{\nu^2 g - 1}{Eh} N_x - \frac{\nu g}{x} u. \tag{4.5b}$$

In eqs (4.5) the wavenumber k is defined as

$$k = \omega/c \tag{4.6}$$

where $c = (E/\varrho)^{1/2}$ is the longitudinal wave velocity in a bar; the factor g is given by

$$g = \frac{1}{1 - 1/(k\,x \tan\alpha)^2}\,; \tag{4.7}$$

$g = 1$ for a flat membrane.

The so-called membrane equations (4.5) express a relationship between the fundamental variables N_x and u. All other variables can be expressed in terms of these fundamental variables with the aid of eqs (4.2) to (4.4). Thus we find for instance for the transverse displacement

$$w = (g - 1)\left(u + \frac{\nu\,x}{E\,h} N_x\right) \tan\alpha \tag{4.8}$$

and for the meridional stress resultant

$$N_\theta = g\left(\frac{E\,h}{x} u + \nu\,N_x\right). \tag{4.9}$$

The membrane equations are singular at $x = 0$. In the solution this singularity is avoided by considering only truncated cones. A second singularity appears when $k\,x \tan\alpha = 1$; the factor g then becomes infinite. For a given frequency this singularity occurs at a specific point on the cone meridian. The meridional coordinate of this so-called transition point is

$$x_t = \frac{1}{k \tan\alpha}\,. \tag{4.10}$$

If $a \leqslant x_t \leqslant b$, where a and b are the meridional coordinates of the inner and outer edges respectively, this singularity corresponds to a circle on the cone surface. With increasing frequency this circle moves from the outer to the inner edge. It lies at the outer edge at a frequency f_{tb}, given by

$$f_{tb} = \frac{c \cos\alpha}{2\pi\,R_b} \tag{4.11}$$

and it reaches the inner edge at a frequency f_{ta}, where

$$f_{ta} = \frac{c \cos\alpha}{2\pi\,R_a}\,. \tag{4.12}$$

4.4. A typical resonance

The nature of the above singularity may be explained as follows. Let the cone be divided into rings of small meridional length (fig. 4.2*a*). A small part of such a conical ring is shown in fig. 4.2*c*.

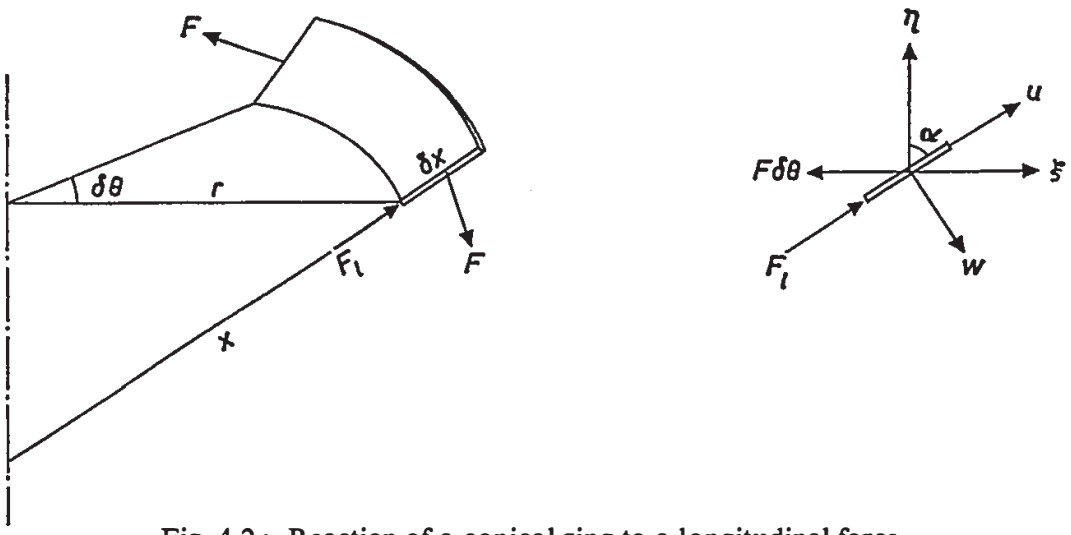

Fig. 4.2*c*. Reaction of a conical ring to a longitudinal force.

The element is driven by a longitudinal force F_l. The stress and the displacements are uniform throughout the element. Applying Newton's law in the ξ-direction we find:

$$F_l \sin \alpha - F\, \delta\theta = -\omega^2\, m\, \xi,$$

where F is the hoop force and $m = \varrho\, h\, r\, \delta x\, \delta\theta$ is the element mass. If the hoop stress is denoted by T, we have:

$$F = T\, h\, \delta x = \frac{\xi\, E}{r}\, h\, \delta x.$$

From these equations it follows for the radial displacement that

$$\xi = -\frac{r\, F_l \sin \alpha}{(k^2\, r^2 - 1)\, E\, h\, \delta x\, \delta\theta}.$$

The axial displacement follows directly from Newton's law:

$$\eta = -\frac{F_l \cos \alpha}{\omega^2\, \varrho\, h\, r\, \delta x\, \delta\theta}.$$

The displacements u and w in longitudinal and transverse directions are linear combinations of ξ and η (fig. 4.2*c*):

$$u = \xi \sin \alpha + \eta \cos \alpha,$$

$$w = \xi \cos \alpha - \eta \sin \alpha.$$

We find:

$$u = \frac{F_l}{E\,h\,r\,\delta x\,\delta\theta}\,\frac{k^2\,r^2 - \cos^2\alpha}{k^2\,(k^2\,r^2 - 1)},$$

$$w = -\frac{F_l \sin\alpha\cos\alpha}{E\,h\,r\,\delta x\,\delta\theta}\,\frac{1}{k^2\,(k^2\,r^2 - 1)}.$$

The displacements u and w become infinite at the frequency where $k\,r = 1$ *). At this so-called ring resonant frequency f_{rr}, given by

$$f_{rr} = \frac{c}{2\pi\,r}, \tag{4.13}$$

any ring, whether conical or not, will show a resonant motion. Further, at f_{rr}

$$\frac{u}{w} = \tan\alpha.$$

This means that the motion is purely in a plane perpendicular to the axis: the centre of gravity remains at rest. Hence, f_{rr} is a natural frequency.

It follows that the longitudinal displacement u becomes zero at a frequency where

$$k\,r = \cos\alpha$$

or

$$k\,x\tan\alpha = 1. \tag{4.14}$$

This frequency is called the ring antiresonant**) frequency f_{ra}; from the latter equation we find

$$f_{ra} = \frac{c}{2\pi\,x\tan\alpha}. \tag{4.15}$$

The transverse displacement at this frequency is

$$w = \frac{F_l\cot\alpha}{k^2\,E\,h\,r\,\delta x\,\delta\theta}. \tag{4.16}$$

The centre of gravity is displaced in accordance with Newton's law.

We may conceive the motion at f_{ra} as being caused by a simple mass-spring system formed by the element mass m and the stiffness s_t in the transverse direction. This can be shown as follows. The stiffness s_t is easily found from the transverse force F_t per unit transverse displacement for $u = 0$:

*) The same occurs for the static case ($k = 0$).

**) In membrane theory "antiresonant" refers to $u = 0$ at the driving point, in bending theory (chapter 5) to $u = w = 0$ at that point.

$$s_t = \frac{F_t}{w} = \frac{F \cos \alpha \, \delta\theta}{w} = \frac{\xi E h \cos \alpha \, \delta x \, \delta\theta}{w r} = \frac{E h \cos^2 \alpha}{r} \delta x \, \delta\theta.$$

The resonant frequency f_{res} of this mass-spring system is

$$f_{res} = \frac{1}{2\pi} \left(\frac{s_t}{m} \right)^{1/2} = \frac{c}{2\pi x \tan \alpha}.$$

Hence

$$k x \tan \alpha = 1$$

for this frequency, in accordance with eq. (4.14). Thus, at the ring antiresonant frequency f_{ra}, the ring in fact exhibits a transverse resonance.

The above may be summarized as follows. The ring resonant frequency f_{rr} is a natural frequency of the ring; for a forced vibration both the longitudinal displacement u and the transverse displacement w become infinite: the ring vibrates in a plane normal to the axis. At the ring antiresonant frequency f_{ra} the motion is purely transverse, the longitudinal displacement is zero. Because the centre of gravity is displaced, this motion can only be carried out in forced vibration. It should be noted that the motions at f_{rr} and f_{ra} are not a result of a wave equation and are therefore not a wave motion; they are developed from an equation of motion with a unique solution.

A complete cone may be considered to consist of interconnected conical rings. It may occur that $k x \tan \alpha = 1$ for one of these rings. At this place the membrane equations show a singularity (the transverse displacement w becomes infinite as $\delta x \to 0$ in eq. (4.16)); the meridional coordinate of this ring coincides with the transition point x_t (cf. eqs (4.10), (4.14)). Therefore, the nature of the singularity at x_t in the membrane equations is in fact a simple mass-spring resonance in the transverse direction; the transverse resonance lies at the inner and outer edges at the frequencies f_{ta} and f_{tb} respectively (eqs (4.11), (4.12)).

For the description of the forced vibration, the longitudinal displacement $u(a)$ at the inner edge is important. If the meridional cone length is infinitesimally small, $u(a)$ becomes zero at the ring antiresonant frequency f_{ra}. A finite cone may be conceived as a conical ring with radius R_b, which is extended into the direction of the apex by a relatively stiff inner part. This part passes on the applied force to the cone base but introduces additional inertia. Therefore, for a finite cone, $u(a)$ becomes zero at a frequency f_{ra} lying below the ring antiresonant frequency of the outer ring:

$$f_{ra} < f_{tb}.$$

In sec. 5.6.3 it is shown that in practice f_{ra} (which has to be calculated numer-

ically by solving the membrane equations) can be approximated by f_{tb} (which follows directly from eq. (4.11)).

A lumped-element representation of the conical membrane is given in fig. 4.3. The elementary masses m increase with increasing x; they are interconnected by longitudinal springs s_l. The hoop stresses are represented by the springs s_a, of which the stiffness decreases with increasing x. At the transition point the mass m_t and the transverse component of the spring s_{at} cause a resonance.

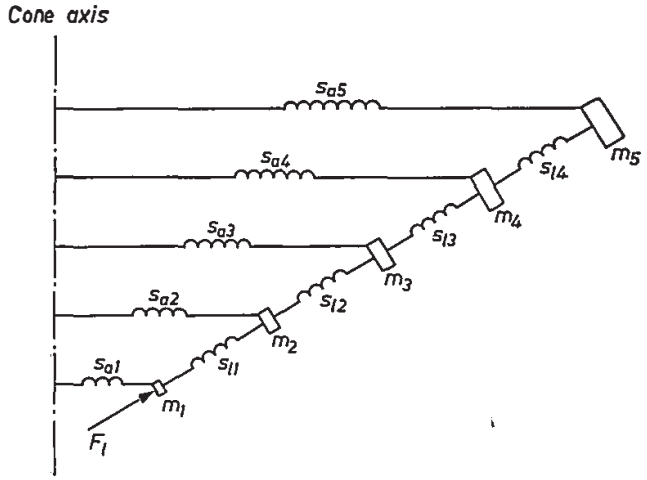

Fig. 4.3. Mechanical lumped-element representation of the conical membrane.

4.5. Boundary conditions

The conical membrane cannot be submitted to arbitrary boundary conditions, since it offers no resistance against transverse forces or moments. This means that the practical boundary condition of an axially driven inner edge cannot be applied to the membrane. The condition that the inner edge is free to move axially but restrained in other directions cannot be used either, as it inevitably leads to a transverse force. We can, however, study the forced vibration of a conical membrane by assuming a longitudinal driving force F_l at the inner edge. This leads to the following boundary condition:

$$N_x = -\frac{F_l}{2\pi R_a}, \qquad x = a. \tag{4.17}$$

This is the only condition imposed on the inner edge, we assume that it is free to move in the transverse and meridional directions. It has already been stated in sec. 4.2 that the outer edge is always assumed to be free. Hence,

$$N_x = 0, \qquad x = b. \tag{4.18}$$

With these two boundary conditions, illustrated in fig. 4.4, the system of dif-

ferential equations is solved analytically for low and high frequencies (sec. 4.6) and numerically for the entire audio region (sec. 4.7).

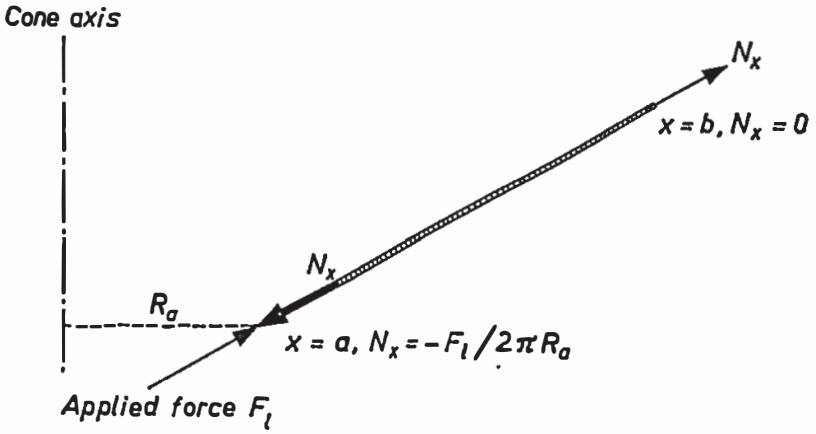

Fig. 4.4. Boundary conditions in membrane theory.

4.6. Approximate analytical solutions

It is found that approximate analytical solutions can be derived for certain frequency regions. These are in general the regions lying far from the frequency where a singularity appears on the cone. This means that we will consider frequency regions $f \ll f_{tb}$ (low-frequency approximation) and $f \gg f_{ta}$ (high-frequency approximation).

4.6.1. *Low-frequency approximation*

At low frequencies, where

$$(k\, b \tan \alpha)^2 \ll 1, \tag{4.19}$$

(i.e. $f \ll f_{tb}$), the factor g in eqs (4.5) approaches zero and the membrane equations simplify to

$$\frac{\mathrm{d}N_x}{\mathrm{d}x} = -\frac{N_x}{x} - \frac{E\, h\, k^2}{\cos^2 \alpha}\, u, \tag{4.20a}$$

$$\frac{\mathrm{d}u}{\mathrm{d}x} = \frac{N_x}{E\, h} + \nu\, k^2\, x\, u \tan^2 \alpha. \tag{4.20b}$$

By eliminating N_x, the Bessel differential equation results:

$$\frac{\mathrm{d}^2 u}{\mathrm{d}x^2} + \frac{1}{x}\frac{\mathrm{d}u}{\mathrm{d}x} + k_2^{\,2}\, u = 0, \tag{4.21}$$

where

$$k_2^{\,2} = k^2\, [1 + (1 - 2\nu) \tan^2 \alpha]. \tag{4.22}$$

The solutions are

$$u = A\,J_0(k_2\,x) + B\,N_0(k_2\,x), \tag{4.23}$$

$$N_x = -E\,h\,\{A\,[k_2\,J_1(k_2\,x) + \nu\,k^2\,x\,J_0(k_2\,x)\tan^2\alpha] + \\ + B\,[k_2\,N_1(k_2\,x) + \nu\,k^2\,x\,N_0(k_2\,x)\tan^2\alpha]\}, \tag{4.24}$$

where the latter equation is obtained with the aid of eq. (4.20b).

By applying the boundary conditions of fig. 4.4 to the solutions, the constants A and B are expressed in the applied force F_l, and the ratio u/N_x is determined. In this way the longitudinal admittance Y_l for sinusoidal motion, defined by

$$Y_l = \frac{j\omega\,u(a)}{F_l} \tag{4.25}$$

or

$$Y_l = -j\frac{\omega\,u(a)}{2\pi\,R_a\,N_x(a)}$$

is calculated.

If

$$k_2\,b \ll 1 \tag{4.26}$$

we may introduce the following approximations for Bessel functions with small argument [10]):

$$J_0(z) \approx 1, \qquad N_0(z) \approx -\frac{2}{\pi}\ln\left(\frac{2}{\gamma\,z}\right),$$

$$J_1(z) \approx \frac{z}{2}, \qquad N_1(z) \approx -\frac{2}{\pi\,z},$$

$$|z| \ll 1, \qquad \gamma = 1{\cdot}781072.$$

This leads to a simple expression for the longitudinal admittance at low frequencies:

$$Y_l = \frac{\cos^2\alpha}{j\omega M_d}, \tag{4.27}$$

where the cone mass M_d is

$$M_d = \varrho\,h\,\pi\,(b^2 - a^2)\sin\alpha. \tag{4.28}$$

Condition (4.26) follows automatically from (4.19) when

$$\alpha \geqslant \arctan\,(2\nu)^{-1/2}$$

or $\alpha \geqslant 52°$ for $\nu = 0{\cdot}3$, a condition fulfilled by many loudspeaker cones.

Equation (4.27) is simply interpreted as follows. The force F_l can be decomposed in an axial force F_a and a radial force F_r (fig. 4.5). At low frequencies, F_a has to work against the cone inertia, F_r against the elastic forces opposing a variation of the inner-edge radius. Because the cone inertia is low, the displacement caused by F_a will be much larger than that caused by F_r. The cone then oscillates freely with a displacement d practically in the axial direction (fig. 4.5). Neglecting the radial displacement and applying Newton's law

$$F_a = -\omega^2 \, d \, M_d \tag{4.29}$$

and the geometric relations

$$u = d \cos \alpha, \tag{4.30}$$

$$F_a = F_l \cos \alpha, \tag{4.31}$$

we find

$$Y_l = \frac{\cos^2 \alpha}{j\omega M_d},$$

in accordance with eq. (4.27).

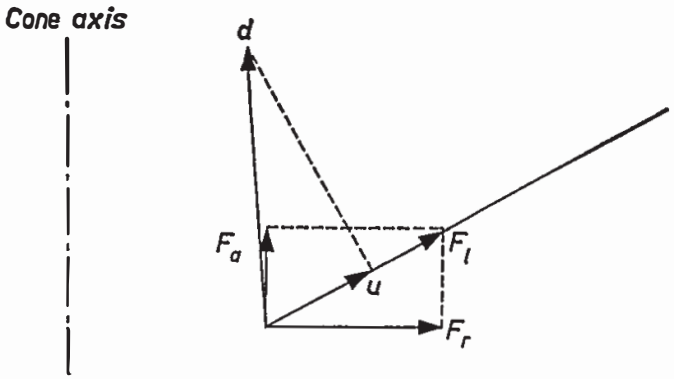

Fig. 4.5. Illustration of the displacement at the inner edge for low frequencies.

4.6.2. *High-frequency approximation*

At high frequencies, where

$$(k \, a \tan \alpha)^2 \gg 1, \tag{4.32}$$

(i.e. $f \gg f_{ta}$), the factor g approaches 1 and the membrane equations become

$$\frac{dN_x}{dx} = -\frac{1-\nu}{x} N_x - \frac{E\,h}{x^2}(k^2 x^2 - 1)\, u, \tag{4.33a}$$

$$\frac{du}{dx} = \frac{N_x}{K} - \frac{\nu}{x} u. \tag{4.33b}$$

Note that the cone angle α has disappeared from the equations. Elimination of N_x leads to the equation

$$\frac{d^2u}{dx^2} + \frac{1}{x}\frac{du}{dx} + \left(k_1^2 - \frac{1}{x^2}\right) u = 0, \tag{4.34}$$

where

$$k_1 = \omega/c_1 \tag{4.35}$$

and c_1 is the velocity of longitudinal waves in a plate:

$$c_1^2 = \frac{E}{\varrho\,(1-\nu^2)}. \tag{4.36}$$

Equation (4.34) is the common Bessel equation for longitudinal wave propagation in a plate. This result could be expected since the condition $k\,a\,\tan\alpha \gg 1$ means that either for a normal cone the wavenumber k is so high that the waves "do not notice" the cone angle or the angle α is so large (and $\tan\alpha$ as well) that the cone is nearly a flat plate. Of course in the latter case eq. (4.34) also holds for small wavenumbers.

The solution of eq. (4.34) is

$$u = A\,J_1(z) + B\,N_1(z), \tag{4.37}$$

where $z = k_1\,x$. The meridional stress resultant N_x is found with eq. (4.33b):

$$N_x = k_1\,K\left[A\left(J_0(z) - \frac{1-\nu}{z}J_1(z)\right) + B\left(N_0(z) - \frac{1-\nu}{z}N_1(z)\right)\right]. \tag{4.38}$$

The transverse amplitude w can be found by substituting the expressions for u and N_x in eq. (4.8).

The above equations describe longitudinal wave motion in the meridional direction. The motion is not purely longitudinal, as is the case for a plate; longitudinal and transverse displacements are coupled via the azimuthal stress N_θ which has a transverse component (fig. 4.2*b*). The wave, after being generated at the inner edge by the longitudinal force, travels in meridional direction and is reflected at the outer cone edge. The reflected wave interferes with the outgoing one in such a way that nodes and antinodes are created. Thus, at each frequency a standing-wave pattern is built up (zero losses are supposed).

Frequencies at which the longitudinal displacement pattern shows a node at the inner edge are called longitudinal antiresonant frequencies. At a longitudinal resonant frequency the longitudinal displacement pattern has an antinode at the

inner edge. According to eq. (4.25) the longitudinal admittance $|Y_l|$ becomes zero at a longitudinal antiresonant frequency and infinite at a longitudinal resonant frequency.

In view of the high-frequency condition eq. (4.32) we may use the following approximations for the Bessel functions:

$$J_n(z) \approx \left(\frac{2}{\pi z}\right)^{1/2} \cos\left(z - \frac{\pi}{4} - \frac{n\pi}{2}\right), \tag{4.39}$$

$$N_n(z) \approx \left(\frac{2}{\pi z}\right)^{1/2} \sin\left(z - \frac{\pi}{4} - \frac{n\pi}{2}\right), \tag{4.40}$$

which are valid for $|z| \gg 1$ with $n = 0$ or 1. This means that they may be used in the expressions for u and N_x if

$$k_1 a \gg 1. \tag{4.41}$$

In fact, the condition (4.41) automatically follows from eq. (4.32) if $\alpha > 44°$ which is nearly always the case in practice *).

On the basis of eq. (4.41) the expiessions for u and N_x may be simplified. After substitution of the approximations for the Bessel functions, we find

$$u = \frac{1}{(\pi z)^{1/2}} (C \sin z - D \cos z), \tag{4.42}$$

$$N_x = \frac{k_1 K}{(\pi z)^{1/2}} (C \cos z + D \sin z), \tag{4.43}$$

where C and D are constants. Applying the boundary conditions (4.17) and (4.18) (inner edge longitudinally driven, outer edge free), the following expressions result:

$$u = - F_l Y_{lc} \left(\frac{a}{x}\right)^{1/2} \frac{\cos [k_1 (b - x)]}{k_1 c_1 \sin (k_1 L)}, \tag{4.44}$$

$$N_x = - \frac{F_l}{2\pi R_a} \left(\frac{a}{x}\right)^{1/2} \frac{\sin [k_1 (b - x)]}{\sin (k_1 L)}, \tag{4.45}$$

where Y_{lc} is the characteristic admittance for longitudinal waves in a flat annular plate with inner radius R_a:

*) Poisson's ratio ν is taken 0·3.

$$Y_{lc} = \frac{1}{2\pi R_a \varrho h c_1} \tag{4.46}$$

and $L = b - a$ is the meridional cone length. With eq. (4.8) we find for the transverse displacement:

$$w = -F_l Y_{lc} \frac{\nu}{k_1 x \tan \alpha} \left(\frac{a}{x}\right)^{1/2} \frac{\sin [k_1 (b - x)]}{k_1 c_1 \sin (k_1 L)}, \tag{4.47}$$

provided

$$\frac{\nu}{1 - \nu^2} k_1 x \gg 1.$$

It follows from eq. (4.47) that w goes to zero when α approaches $\pi/2$, which confirms the well-known fact that in a plate longitudinal and transverse wave motions are uncoupled. The same occurs for increasing $k_1 x$.

The longitudinal admittance is found with eq. (4.25):

$$Y_l = -j Y_{lc} \cot (k_1 L). \tag{4.48}$$

The longitudinal resonant frequencies, at which $Y_l = \infty$, follow directly from this equation:

$$f_{lrn} = \frac{n c_1}{2L}, \tag{4.49}$$

where n is a positive integer which, in view of eq. (4.41), must satisfy the condition

$$n \gg \frac{L}{\pi a}. \tag{4.50}$$

For these resonant frequencies, n half wavelengths fit the cone, with antinodes at inner and outer edges. The transverse and longitudinal displacements at the first and the second longitudinal resonant frequencies of a typical cone (parameters in table 4-I) are shown in figs 4.12*a* and *b*.

The longitudinal antiresonant frequencies, at which $Y_l = 0$, are

$$f_{lan} = \frac{(2n - 1) c_1}{4L}, \tag{4.51}$$

where in view of eq. (4.41) n must satisfy the condition

$$n \gg \frac{L}{\pi a} + \tfrac{1}{2}. \tag{4.52}$$

An odd number $(2n-1)$ of quarter wavelengths now fits a cone meridian with a node at the inner and an antinode at the outer edge. Typical examples of the modes at the second and the third longitudinal antiresonant frequencies are shown in figs 4.11*a* and *b*.

At the antiresonant frequencies the longitudinal driving force F_l maintains a standing-wave pattern, although the driving point itself has a zero longitudinal displacement. This at first sight strange situation is explained by the fact that the vibration pattern is the stationary result of the driving force F_l, which began to work an infinite time ago. At that time there was no node, because there was no reflected wave. As a function of time the reflected wave gradually decreased the amplitude at the inner edge, thereby doubling the amplitude at the free outer edge. The result after an infinite time lapse is the typical standing-wave shape of which figs 4.11*a* and *b* are examples.

In sec. 4.7 the longitudinal resonant and antiresonant frequencies will be calculated numerically for various cones. It will be shown for a typical example that the numerically calculated resonant and antiresonant frequencies agree well with those calculated from the high-frequency approximations, even for $k_1 a$ of the order 1.

In fig. 4.6 the numerically calculated relative value of the longitudinal admittance defined by

$$y_l = Y_l / Y_{lc} \tag{4.53}$$

is shown for a certain cone *). In the low-frequency region, Y_l decreases inversely proportionally to the frequency, according to eq. (4.27); in the high-frequency region the typical plate behaviour is visible, y_l varying according to

$$y_l = -j \cot_a^2(k_1 L). \tag{4.54}$$

Figure 4.6 will be further discussed in the next section.

4.7. Numerical solution of the membrane differential equations

4.7.1. *Introduction*

The high-frequency approximation is mostly valid for frequencies lying above the frequency region for which the loudspeaker is designed and is therefore of limited value. In general it appears that for normal loudspeaker cones only the simple low-frequency approximation can be used successfully. For frequencies belonging neither to the low- nor to the high-frequency regions, the solution of the membrane differential equations must be obtained numerically. In the following these equations will be solved numerically for the whole frequency range of a specific loudspeaker. This allows the results of the low- and high-frequency approximations to be compared with the numerical solution.

*) Cone parameters in table 4-I.

The numerical-solution method of direct integration (appendix B) is chosen. This method yields the displacement patterns at a specified frequency for specified boundary conditions. This is in contrast with the eigenvalue approach, where first a great number of eigenfrequencies and modes must be calculated with a relatively high accuracy, before the solution at a specific frequency can be obtained by applying the boundary conditions to the combination of these modes. An additional advantage of the method of direct integration is that the number of simultaneous differential equations to be solved is unimportant; the same computer program can be used for any number of equations. This is very convenient, since the introduction of internal material damping will double the number of differential equations (sec. 4.7.4). Further, the same computer program can be used for the numerical solution of the general differential equations, in which bending is accounted for (chapter 5).

In the following section the frequency dependence of the numerically calculated vibration patterns and longitudinal admittance of a typical loudspeaker cone will be described. In sec. 4.7.3 the influence of a boundary condition at the inner edge, usually encountered in practice, viz. the radially supported inner edge, will be discussed. In sec. 4.7.4 the influence of internal material losses on the frequency characteristic of the longitudinal admittance is illustrated; the dependence of the latter on the apex angle will be discussed in sec. 4.7.5. Finally, in sec. 4.7.6, the longitudinal antiresonant frequencies, which strongly influence the sound radiation, will be shown as a function of the cone dimensions.

4.7.2. *Frequency dependence of the vibration patterns and the longitudinal admittance of a typical cone*

The membrane differential equations (4.5) are solved numerically for a typical loudspeaker cone with the geometry and material parameters as given in table 4-I *).

TABLE 4-I

Cone 50.1 **)

geometry		material	
semi-apex angle	$\alpha = 50°$	Young's modulus	$E = 2 \cdot 10^9$ N/m^2
inner-edge radius	$R_a = 17$ mm	mass density	$\varrho = 600$ kg/m^3
outer-edge radius	$R_b = 83$ mm	Poisson's ratio	$\nu = 0{\cdot}3$
thickness	$h = 0{\cdot}1$ mm	loss factor δ: specified locally (if unspecified: $\delta = 0{\cdot}1$)	

*) A list of cones used in this thesis can be found in appendix G.
**) The cones are numbered according to their value of α; the last digit is an ordinal number. The letter e is added for the experimental cones.

The cone thickness h is chosen more or less arbitrarily, since it is unimportant in membrane theory. It remains only as a proportionality factor in the mass per unit area of the conical membrane, hence all vibration amplitudes are inversely proportional to it. The discussion of the vibration patterns will be based on the frequency dependence of the reduced longitudinal admittance at the inner edge y_l, defined by eq. (4.53) and shown as a function of frequency in fig. 4.6. The frequency axis will be divided into three regions on the basis of the presence or absence of the singularity on the cone. As already indicated in sec. 4.4 this singularity or transition point appears on the cone within the frequency region $f_{tb} \leqslant f \leqslant f_{ta}$, where f_{tb} and f_{ta}, according to eqs (4.11) and (4.12), are the frequencies at which the transition point lies at the outer and inner edge respectively. This frequency region will be called region II. The frequency regions lying below and above region II are called regions I and III respectively. Since no energy is dissipated, all motion is of the standing-wave type and the longitudinal admittance is purely imaginary.

We will now start with the discussion of the membrane behaviour in the suc-

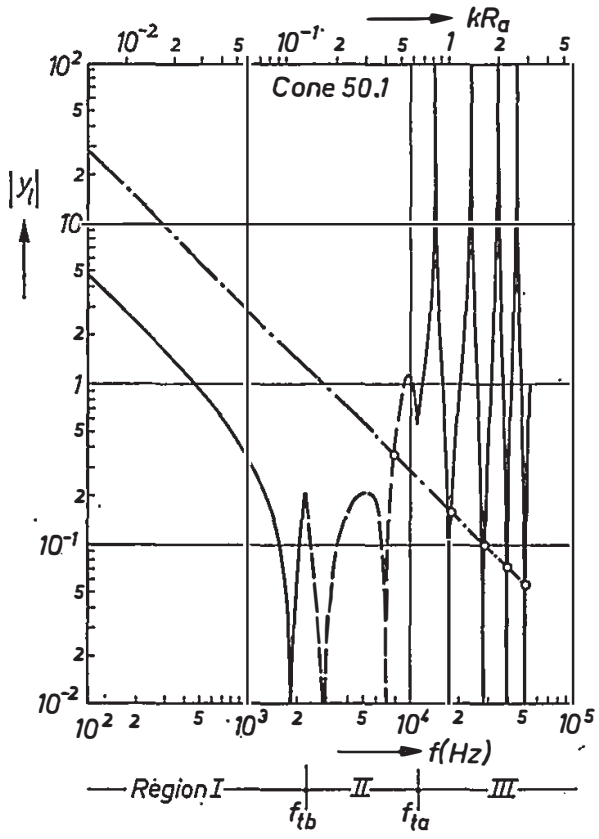

Fig. 4.6. Reduced longitudinal admittance $|y_l|$ versus frequency for cone 50.1 without damping (membrane solution); the natural frequencies when the inner edge is radially supported (membrane resonant frequencies) are indicated by ○.

cessive regions for cone 50.1, which may be considered as typical for the general cone.

Region I is defined by

$$f < f_{tb}, \tag{4.55}$$

where f_{tb} is the frequency at which the transition point lies at the outer edge. This is the region on the low-frequency side of the spectrum, where no singularity lies on the cone. For the cone with the parameters indicated above, region I extends up to 2250 Hz (fig. 4.6).

For very low frequencies ($f \ll f_{tb}$), $|y_l|$ decreases linearly with frequency in accordance with the result of the low-frequency approximation eq. (4.27). The cone then oscillates practically as a rigid body with an axial displacement d determined by

$$d = -\frac{F_l \cos \alpha}{\omega^2 M_d}. \tag{4.56}$$

The longitudinal and transverse displacements u and w are geometrically related to d:

$$\begin{aligned} u &= \quad d \cos \alpha, \\ w &= -d \sin \alpha. \end{aligned} \tag{4.57}$$

When the frequency is raised the longitudinal and transverse displacements at the inner edge decrease relative to those at the outer edge. This is shown in

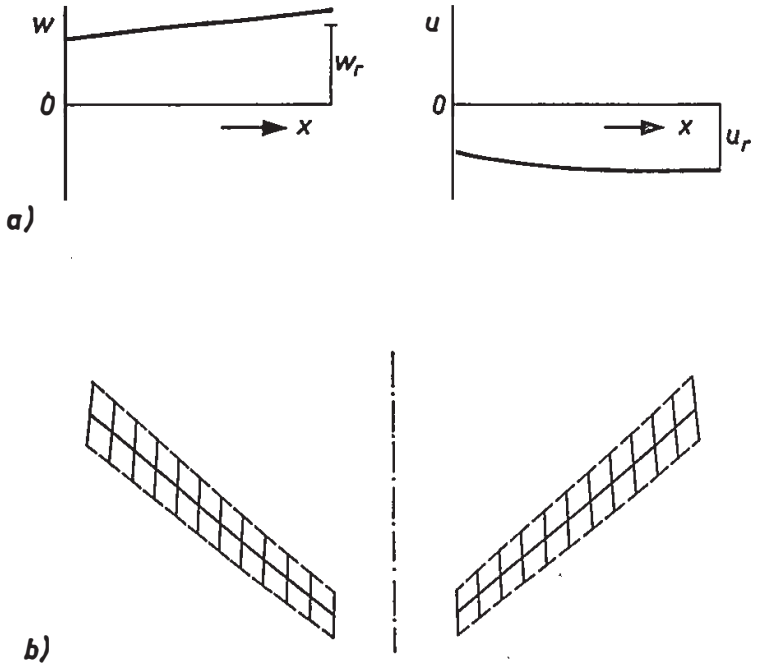

Fig. 4.7. Cone 50.1 at 1000 Hz (membrane solution);
(*a*) transverse and longitudinal displacement, (*b*) cone motion.
The displacements of a corresponding rigid cone are indicated by w_r and u_r.

fig. 4.7*a* for $f = 1000$ Hz. The origin of the decrease in u lies in the time that it takes a wave generated at the inner edge to travel to the outer edge and back again to the inner edge where it partly opposes the momentary motion.

The cone motion at 1000 Hz is drawn in fig. 4.7*b*. The dashed lines indicate the extreme vibrational positions of the cone surface. Points on the cone surface move between these extremes along straight lines, as indicated in fig. 4.7*b*. At 1000 Hz, the whole cone moves nearly uniformly in the axial direction (the displacements are greatly exaggerated). The cone surface shows very little extension or contraction.

When the frequency is raised the reflected longitudinal wave may arrive in antiphase with the outgoing one. A node in the u pattern arises at the inner edge at a frequency of about 1840 Hz (fig. 4.8*a*). The reduced longitudinal admittance y_l becomes zero there; there is only a small transverse motion at the inner edge. This is the ring antiresonant frequency f_{ra}. The cone motion is illustrated in fig. 4.8*b*. The vibration resembles a varying apex angle. This typical motion at f_{ra} was discussed in sec. 4.4. It was also shown there that for very short cones (i.e. with small meridional length L) f_{ra} is equal to the frequency where the cone mass and the transverse compliance come into resonance; the motion is purely transverse then. For longer cones f_{ra} lies just below the lowest frequency where a transition point appears on the cone.

The admittance y_l is a negative imaginary number up to f_{ra}: the cone reacts as a mass to the driving force. Above f_{ra} the admittance changes sign, the cone reacts as a spring. Inner and outer edges now vibrate in antiphase. When the frequency is raised further, the node in the longitudinal displacement shifts in

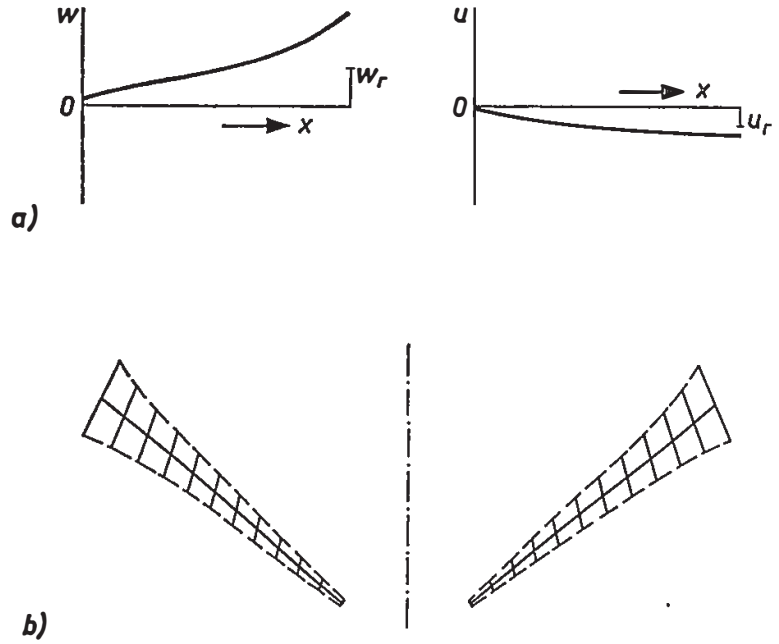

Fig. 4.8. Cone 50.1 at the ring antiresonant frequency $f_{ra} = 1840$ Hz (membrane solution); (*a*) mode shapes, (*b*) cone motion.
The displacements of a corresponding rigid cone are indicated by w_r and u_r.

the direction of the outer edge. The displacements u and w and the total cone motion at $f = 2200$ Hz are shown in fig. 4.9. This is just below the frequency at which the transition point appears at the outer edge: hence the relatively high value of w at that place. The upper limit or region I is 2250 Hz where $k\,b \tan \alpha$ becomes equal to 1.

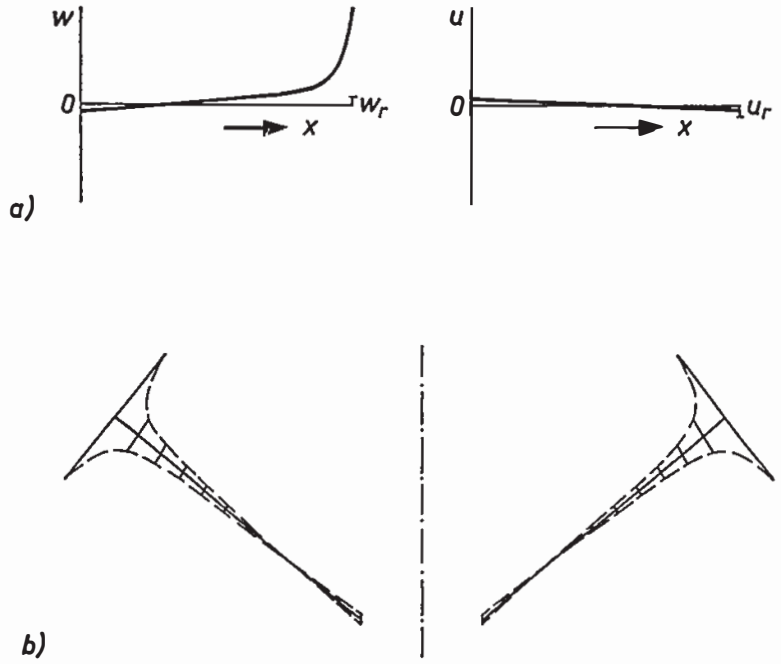

Fig. 4.9. Cone 50.1 at 2200 Hz (membrane solution);
(*a*) transverse and longitudinal displacement, (*b*) cone motion.
The displacements of a corresponding rigid cone are indicated by w_r and u_r.

Figures 4.7*a*, 4.8*a* and 4.9*a* are not drawn to the same scale; for comparison, the amplitudes of u_r and w_r of a rigid cone with the same total mass and driven by the same force F_l are indicated.

Region II is the frequency region where a transition point lies on the cone, the so-called transition region. It comprises the frequencies

$$f_{tb} \leqslant f \leqslant f_{ta}. \tag{4.58}$$

At 2250 Hz the transition point lies at the outer edge; it shifts to the inner edge with increasing frequency. At the transition point the transverse displacement changes from $+\infty$ to $-\infty$. This of course is physically impossible. In practice the bending stiffness will limit w. Neglect of the bending stiffness obviously is unjustifiable; the present solution for region II may thus be expected to be unrealistic (although the longitudinal antiresonant frequency is fairly well predicted, see below). For this reason $|y_l|$ is dashed in this region (fig. 4.6).

The maximum at about 5500 Hz is due to a perturbed ring resonance. It corresponds to the extensional resonance of a ring (conical or not) with small

meridional length L, vibrating in its own plane (fig. 2.5*a*); the resonant frequency is determined by (see sec. 4.4, eq. (4.13))

$$k\,r = 1, \tag{4.59}$$

where r is the ring radius. This frequency is called the ring resonant frequency f_{rr}. For a cone with finite length, $|y_l|$ shows a maximum which increases with increasing α; for a plate $|y_l|$ becomes infinite at f_{rr}. This frequency is well approximated by eq. (4.59) if instead of r the mean radius $(R_b + R_a)/2$ is substituted; for the present cone we then find $f_{rr} \approx 5800$ Hz. Remember that both the ring resonance at f_{rr} and the ring antiresonance at f_{ra} are simple mass-spring vibrations controlled by the azimuthal (hoop) stress, in contrast with the longitudinal resonances and antiresonances, which are caused by wave motion in the meridional direction.

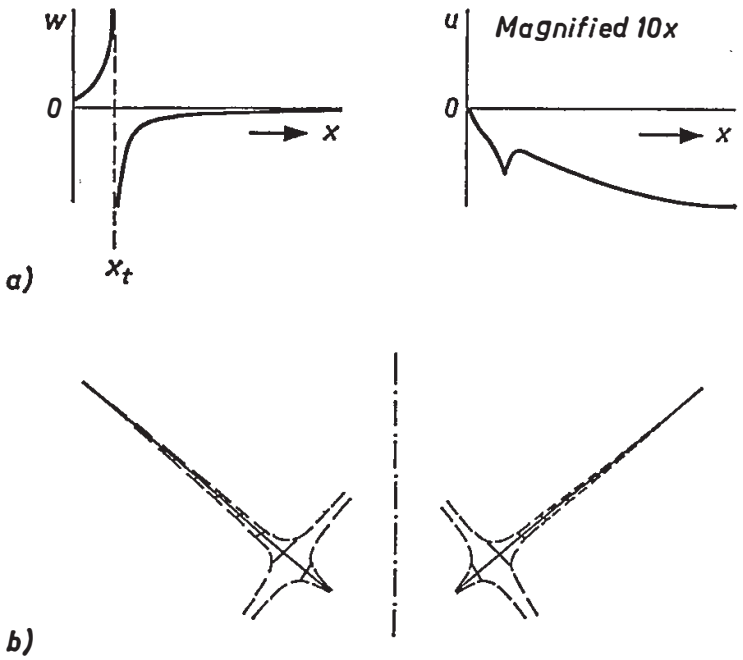

Fig. 4.10. Cone 50.1 at the first longitudinal antiresonant frequency $f_{la1} = 6963$ Hz (membrane solution);
(*a*) mode shapes, (*b*) cone motion.

At 6963 Hz a perturbed longitudinal antiresonance occurs; the transverse and longitudinal displacements at this first longitudinal antiresonant frequency f_{la1} are shown in fig. 4.10*a*. The quarter-wave shape of the longitudinal displacement pattern is clearly visible, although it is distorted by the singularity at the transition point x_t. The cone motion is illustrated in fig. 4.10*b*. The longitudinal resonances and antiresonances are also found on a longitudinally driven plate with the same meridional length L as the cone (see secs 4.7.5, 4.7.6).

The upper limit of region II lies at $f_{ta} = 10987$ Hz, where the transition point has reached the inner edge.

Region III is defined by

$$f > f_{ta}. \tag{4.60}$$

With increasing frequency longitudinal resonances ($|y_l| = \infty$) and antiresonances ($|y_l| = 0$) appear in successive order at frequencies which are increasingly well predicted by the high-frequency approximations (eqs (4.49) and (4.51)). For the present cone an illustration of this agreement can be found in table 4-II.

TABLE 4-II

Cone 50.1

resonant frequencies		antiresonant frequencies	
numerically computed	high-frequency approximation	numerically computed	high-frequency approximation
14210	11100	6963 *)	5550 *)
23439	22200	17480	16650
34074	33300	28261	27750
44976	44400	39228	38850

*) Belong to region II.

According to eq. (4.41) the high-frequency approximations are valid for $f \gg 14000$ Hz but the table shows that also for lower frequencies the agreement is rather good.

The wave propagation is determined by the wavenumber k_1 of longitudinal

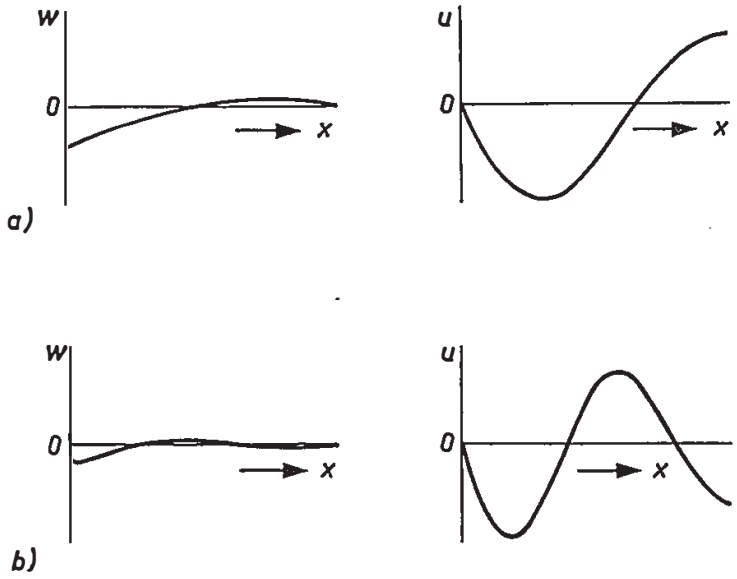

Fig. 4.11. Mode shapes of cone 50.1 at longitudinal antiresonant frequencies (membrane solution);
(*a*) $f_{la2} = 17480$ Hz, (*b*) $f_{la3} = 28261$ Hz.

waves in a plate. In this region transverse effects are almost completely ruled out. The transverse and longitudinal modes at two antiresonant frequencies (17480 and 28261 Hz) and two resonant frequencies (14210 and 23439 Hz) are shown in figs 4.11 and 4.12. These modes (and the higher ones) are well predicted by the high-frequency solutions eqs (4.49) and (4.51). Note the decreasing ratio w/u, which was already discussed in sec. 4.6.2 (see also sec. 5.3).

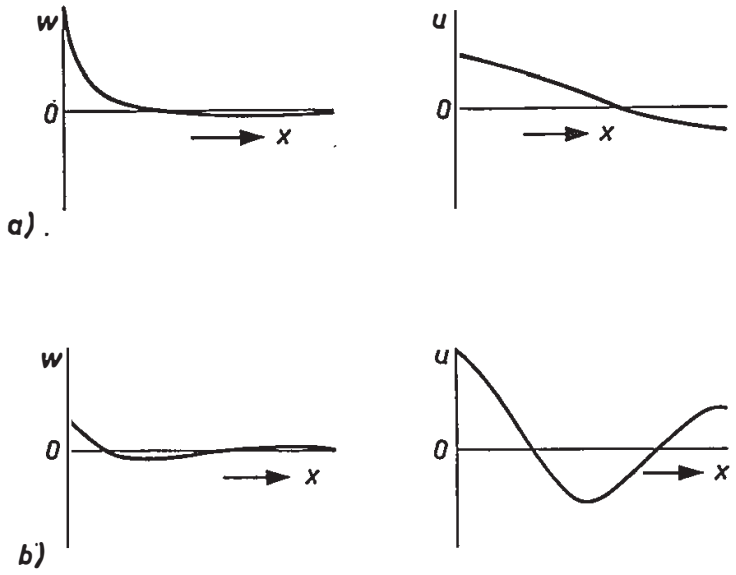

Fig. 4.12. Mode shapes of cone 50.1 at longitudinal resonant frequencies (membrane solution); (*a*) $f_{lr1} = 14210$ Hz, (*b*) $f_{lr2} = 23439$ Hz.

4.7.3. *Radially supported inner edge*

It has been remarked in sec. 3.1 that in practice the inner edge is stiff; this means that no motion is allowed in the radial direction *). Hence, at the inner edge

$$u \sin \alpha + w \cos \alpha = 0. \tag{4.61}$$

It was discussed in sec. 4.5 that this boundary condition cannot be applied to the conical membrane (it cannot withstand the transverse stresses accompanying such a support); the membrane was therefore driven longitudinally.

However, at certain frequencies eq. (4.61) is satisfied by the longitudinally driven conical membrane. Then, without disturbing the displacement pattern or introducing transverse forces, the inner edge may indeed be radially supported. These frequencies, which will be called natural frequencies of the conical membrane with a radially supported inner edge, or briefly membrane resonant frequencies f_{mrn}, can be obtained as follows.

*) This is of course only the case below the lowest symmetrical resonant frequency of the structure formed by the inner edge of the cone, the voice-coil cylinder and the inner suspension; in practice this frequency lies well above the frequency region for which the loudspeaker is designed.

Using eqs (4.8) and (4.25), the boundary condition (4.61) can be written as a condition on the reduced longitudinal admittance y_l:

$$y_l = j \frac{\nu}{k_1 a \tan^2 \alpha} . \tag{4.62}$$

In fig. 4.6 this condition is represented by the dash-dotted line. Obviously, it is in general not satisfied, except at the intersections of this line with the y_l-curve, which determine the membrane resonant fequencies. For the present cone, the lowest four lie at 7854, 17923, 28588 and 39475 Hz. Figure 4.6 also shows that the membrane resonant frequencies lie just above the longitudinal antiresonant frequencies; the spacing between the former and the latter decreases with increasing frequency. This can also be shown by substituting condition (4.62) into the high-frequency approximation eq. (4.54); we find that the following equation is satisfied at the membrane resonant frequencies:

$$\cot (k_1 L) = - \frac{\nu}{k_1 a \tan^2 \alpha} . \tag{4.63}$$

In the high-frequency region ($k a \tan \alpha \gg 1$) the right-hand side of eq. (4.63) approaches zero, which means that this equation is satisfied at frequencies just above the longitudinal antiresonant frequencies at which $\cot (k_1 L) = 0$. In this frequency region the mode shapes at the membrane resonant frequencies f_{mrn} may therefore be approximated by those at the longitudinal antiresonant frequencies f_{lan}. This is illustrated in fig. 4.13 which shows the mode shapes at f_{mr1}, f_{mr2} and f_{mr3} for the present cone (cf. figs 4.11*b*, 4.13*c*). Note that f_{mr1} lies in region II, which causes a singularity in the transverse pattern. It will be shown in chapter 6 that the membrane resonances may considerably influence the sound radiation.

4.7.4. *Longitudinal admittance in the presence of internal material damping*

Internal material damping considerably influences the cone mechanical behaviour. In practice, additional losses are introduced by the outer suspension. From the computational point of view it is expedient to distribute this rim damping over the whole cone and then further neglect the rim influence. This means introducing into the computations an internal damping higher than that encountered in practice *).

In this section we deal with the influence of internal material losses on the longitudinal admittance of a conical membrane with a free outer edge. The internal damping is introduced via a complex Young's modulus $\bar{E}$ [9])

*) At the same time the radiation damping is approximatively accounted for (see sec. 6.5.2).

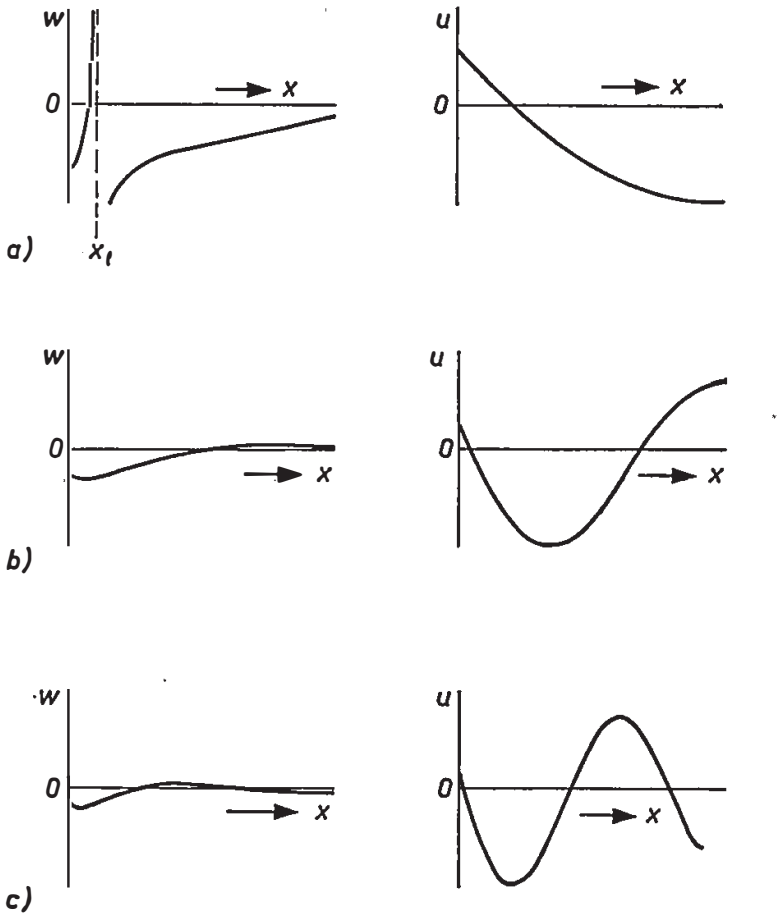

Fig. 4.13. Mode shapes of cone 50.1 at membrane resonant frequencies (natural frequencies for a radially supported inner edge, membrane solution);
(*a*) $f_{mr1} = 7844$ Hz, (*b*) $f_{mr2} = 17923$ Hz, (*c*) $f_{mr3} = 28588$ Hz.

$$\bar{E} = E(1 + j\delta) \tag{4.64}$$

where the loss factor δ is the ratio of the imaginary to the real part of $\bar{E}$. Poisson's ratio ν is taken real, which is a fair approximation for many materials [7]). The fundamental variables u and N_x now become complex:

$$u = u_1 + ju_2$$

and

$$N_x = N_{x1} + jN_{x2}.$$

The number of differential equations doubles; after some manipulation we find

$$\frac{dN_{x1}}{dx} = \frac{1}{x}[(\nu g_1 - 1) N_{x1} - \nu g_2 N_{x2}] + \\ + \frac{Eh}{x^2}[(g_1 - \delta g_2 - k^2 x^2) u_1 - (\delta g_1 + g_2) u_2], \tag{4.65a}$$

$$\frac{dN_{x2}}{dx} = \frac{1}{x}[\nu g_2 N_{x1} + (\nu g_1 - 1) N_{x2}] +$$

$$+ \frac{E h}{x^2}[(\delta g_1 + g_2) u_1 + (g_1 - \delta g_2 - k^2 x^2) u_2], \quad (4.65b)$$

$$\frac{du_1}{dx} = \frac{1}{E h (1 + \delta^2)}[(1 - \nu^2 g_1 - \nu^2 g_2 \delta) N_{x1} + (\delta - \nu^2 g_1 \delta + \nu^2 g_2) N_{x2}] +$$

$$- \frac{\nu}{x}(g_1 u_1 - g_2 u_2), \quad (4.65c)$$

$$\frac{du_2}{dx} = \frac{1}{E h (1 + \delta^2)}[-(\delta - \nu^2 g_1 \delta + \nu^2 g_2) N_{x1} + (1 - \nu^2 g_1 - \nu^2 g_2 \delta) N_{x2} +$$

$$- \frac{\nu}{x}(g_2 u_1 + g_1 u_2). \quad (4.65d)$$

The factors g_1 and g_2 are the real and imaginary parts of g:

$$g_1 = \frac{q^2 (q^2 - 1)}{(q^2 - 1)^2 + \delta^2}, \quad (4.66a)$$

$$g_2 = \frac{q^2 \delta}{(q^2 - 1)^2 + \delta^2}, \quad (4.66b)$$

where $q = k x \tan \alpha$. The above system of differential equations is solved numerically by the method of direct integration (appendix B) applying the boundary conditions (4.17) and (4.18).

The influence of the internal loss factor is illustrated by solving numerically the membrane equations for cone 50.1 with $\delta = 0{\cdot}01$ and $0{\cdot}1$ and then calculating the longitudinal admittance as a function of frequency. The complex longitudinal admittance Y_l is written as

$$Y_l = G_l + jB_l, \quad (4.67)$$

where G_l is the longitudinal conductance and B_l the longitudinal susceptance.

In fig. 4.14 the modulus of the reduced longitudinal admittance y_l is shown as a function of frequency for the same cone parameters as used in fig. 4.6 (cone 50.1), but now with an internal loss factor $\delta = 0{\cdot}01$. In general, dips become less deep and peaks are lowered to finite values. The internal damping is however more effective in region II than in the other regions. This is caused by the singularity at the transition point, where much energy is dissipated because of the high strains. Because of this relatively high damping in region II

the dip at 2800 Hz has completely disappeared, whereas the antiresonance at 6963 Hz is only visible as a small disturbance. In region III, $|y_l|$ oscillates about the value $|y_l| = 1$, the maximum deviations from this mean value being

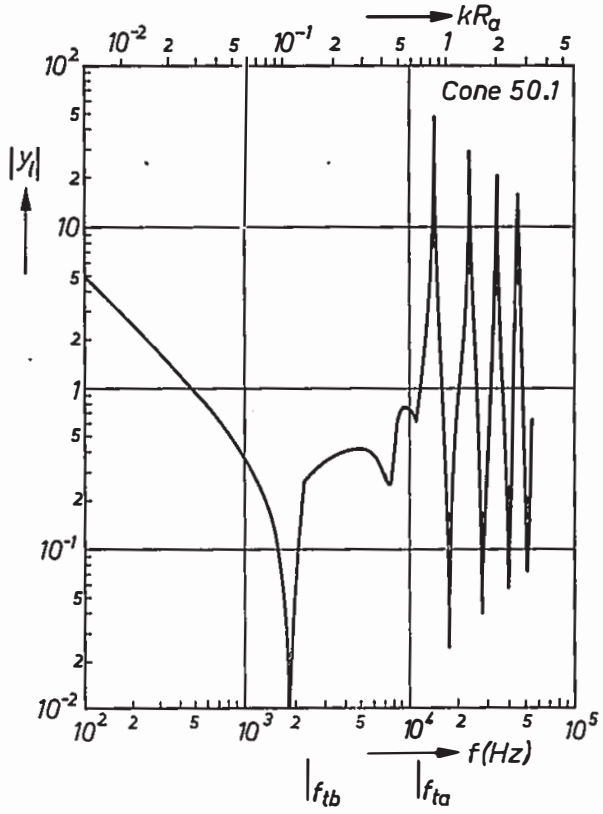

Fig. 4.14. Calculated reduced longitudinal admittance $|y_l|$ of cone 50.1 versus frequency with internal loss factor $\delta = 0{\cdot}01$ (membrane solution).

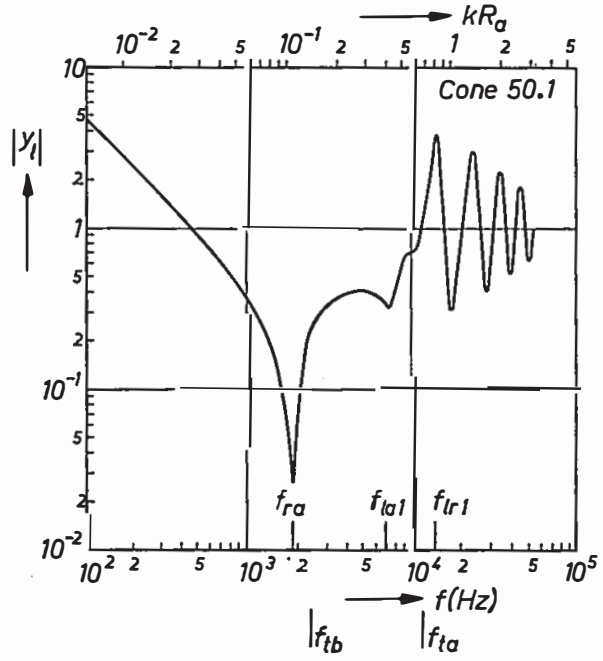

Fig. 4.15. Calculated reduced longitudinal admittance $|y_l|$ versus frequency of cone 50.1 with $\delta = 0{\cdot}1$ (membrane solution).

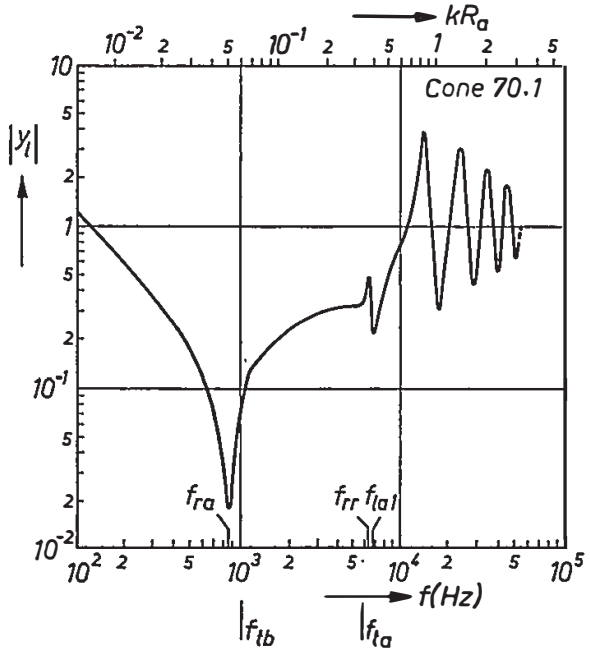

Fig. 4.16. Calculated reduced longitudinal admittance $|y_l|$ versus frequency of cone 70.1 (membrane solution).

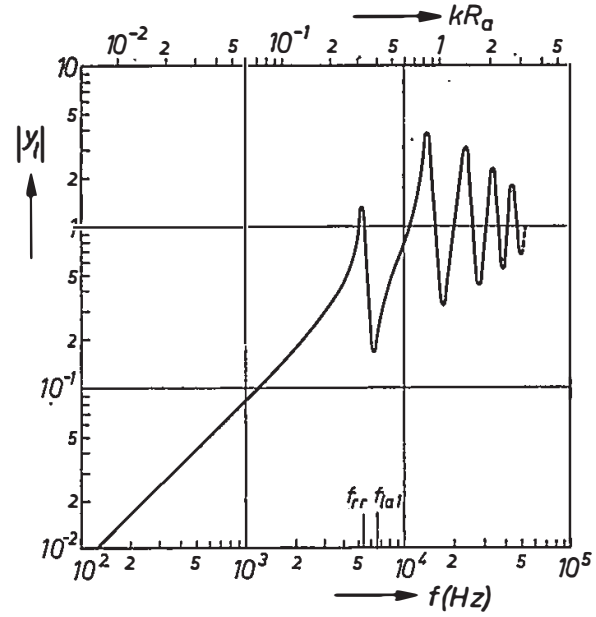

Fig. 4.17. Calculated reduced longitudinal admittance $|y_l|$ versus frequency of a flat ring with $\delta = 0{\cdot}1$ and the same R_a, L, h and material parameters as the cones 50.1 and 70.1 (membrane solution).

inversely proportional to the frequency. This result is well known from the plate theory [9]).

In fig. 4.15 $|y_l|$ is shown for $\delta = 0{\cdot}1$. This relatively high value of δ significantly smooths the curve of $|y_l|$. In the high-frequency region the peaks are reduced in height by a factor of 10, all dips are raised by the same factor as compared with fig. 4.14. At the top of figs 4.6, 4.14, 4.15 (and 4.16, 4.17) the

value of the dimensionless frequency parameter kR_a is indicated, which allows the characteristics to be used independently of the absolute cone dimensions and the cone material.

4.7.5. *Influence of the apex angle on the longitudinal admittance*

In order to demonstrate the influence of the apex angle on the frequency characteristic of the longitudinal admittance, the latter was calculated for a cone with $\alpha = 70°$ and for a flat ring. In all cases the meridional cone length $L = b - a$, the inner cone radius R_a and the cone material is the same as that of cone 50.1, which means that in the high-frequency region the characteristics of $|y_l|$ are exactly equal for all three cases.

Figure 4.16 shows $|y_l|$ as a function of frequency for cone 70.1, whose geometrical and material parameters are given in table 4-III.

TABLE 4-III

Cone 70.1

geometry		material	
semi-apex angle	$\alpha = 70°$	Young's modulus	$E = 2 . 10^9$ N/m²
inner-edge radius	$R_a = 17$ mm	mass density	$\varrho = 600$ kg/m³
outer-edge radius	$R_b = 98$ mm	Poisson's ratio	$\nu = 0{\cdot}3$
cone thickness	$h = 0{\cdot}1$ mm	loss factor	$\delta = 0{\cdot}1$

Comparing the frequency characteristic of $|y_l|$ of cone 70.1 with that of cone 50.1 (fig. 4.15), we notice the following differences. Firstly, the frequency f_{ta}, at which the transition point lies at the inner edge, has decreased (eq. (4.12)). The frequency f_{tb} has decreased as well; however, an additional decrease is caused by the fact that R_b of cone 70.1 is taken larger than that of cone 50.1 to obtain equal values of L for the two cones. The ring antiresonant frequency f_{ra} has decreased by about the same factor as f_{tb} and still lies just below this frequency, as discussed in sec. 4.4. Just above f_{ta} in fig. 4.16 the ring resonant frequency f_{rr}, now falling in region III, causes a distinct peak.

Finally, in fig. 4.17 the frequency characteristic of $|y_l|$ of a flat ring is shown, of which the inner radius R_a, the meridional length L and the material are equal to that for the cones 50.1 and 70.1 (this means that the outer radius R_b has increased to 103 mm). The stiffness against transverse displacements has become zero, which means that f_{ra} has also been shifted to zero. The same has happened to the frequencies f_{tb} and f_{ta}.

The disappearance of regions I and II for the flat membrane (plate) may also be explained on the basis of the well-known uncoupling of transverse and

longitudinal motions; because the plate is longitudinally driven, only pure longitudinal wave motion occurs. Therefore in the low-frequency region (now extending up to f_{rr}), $|y_t|$ is controlled by the stiffness of the plate against longitudinal displacements and consequently increases with frequency, in contrast with the cone admittance in region I, which is controlled by the total cone mass and therefore decreases with frequency. In the high-frequency region the longitudinal resonant and antiresonant frequencies, caused by wave motion in meridional direction, remain equal to those of cones 50.1 and 70.1.

4.7.6. *Longitudinal antiresonant frequencies versus cone geometry*

It will be shown in chapter 6 that the longitudinal antiresonant frequencies have considerable influence on the sound radiation of the cone. Therefore the lowest four antiresonant frequencies were calculated for various cone dimensions on the basis of the membrane equations for semi-apex angles α of 50, 60, 70 and 80 degrees. These values cover the range of cone angles used in practice.

Let us first consider the dependence of the regions I, II and III defined by eqs (4.55), (4.58) and (4.60) on the cone geometry. The boundaries of these regions are shown in fig. 4.18*a*, in which the dimensionless frequency parameter kR_2 is plotted as a function of the reduced meridional cone length L/R_2; R_2 represents the value of the second radius of curvature r_2 (see fig. 4.1*a*) at the inner edge:

$$R_2 \equiv r_2(a) = R_a/\cos\alpha. \tag{4.68}$$

If α and L/R_2 are kept constant and kR_2 is increased, we pass from region I (in which the transition point lies outside the outer edge on an imaginary extension of the cone surface) to region II (in which the transition point lies on the cone). The transition from region I to region II occurs at the frequency f_{tb} or at the value of kR_2 determined by the function

$$(kR_2)_{tb} = \frac{1}{1 + (L/R_2)\tan\alpha}, \tag{4.69}$$

which follows from eqs (4.11) and (4.68). Therefore, this lower boundary of region II is lower for larger apex angles.

When kR_2 is increased still further the transition point moves from the outer to the inner edge; it reaches the latter at $kR_2 = 1$ (eqs (4.12) and (4.68)). This value of kR_2 forms the upper boundary line of region II for all apex angles. If kR_2 is still further increased, the transition point moves from the cone to an imaginary extension of the cone surface inside the inner edge (region III).

Figure 4.18*a* illustrates that, with increasing α, region II increases at the cost of region I. It also follows from the function (4.69) that region II increases

for constant α and increasing cone length L, which is not difficult to explain as, with increasing L, part of the imaginary extension of the cone surface becomes real. When $L/R_2 \to 0$ (cone element with infinitesimal length Δx, see

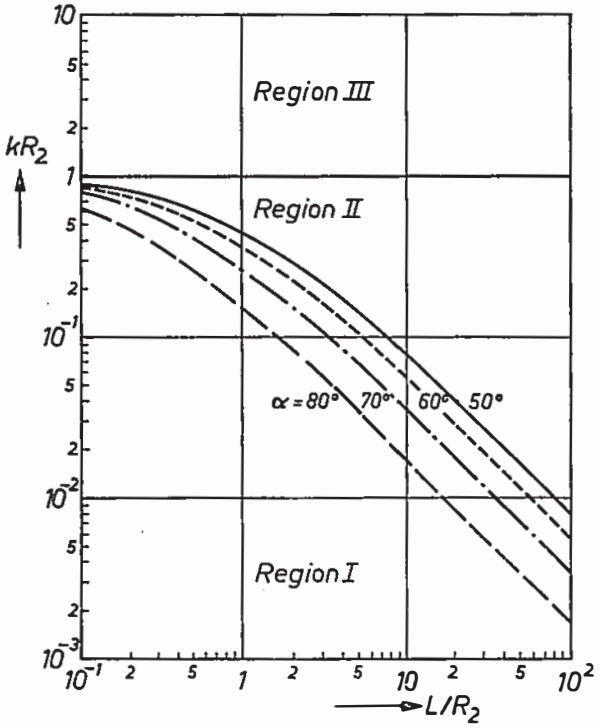

Fig. 4.18*a*. Regions in the kR_2 versus L/R_2 plane for four semi-apex angles α.

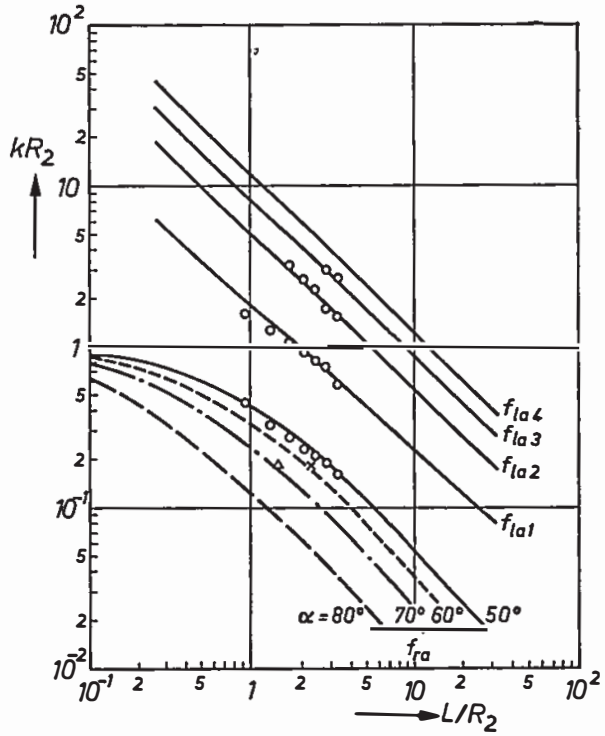

Fig. 4.18*b*. Ring antiresonant frequencies f_{ra} and lowest four longitudinal antiresonant frequencies f_{la} versus reduced meridional cone length L/R_2 for four values of the semi-apex angle α. Measured values are indicated by ○ for various cones with $\alpha = 50°$, × for a cone with $\alpha = 60°$, △ for a cone with $\alpha = 70°$.

fig. 4.2*a*), region II shrinks to a point at a frequency determined by $kR_2 = 1$.

In fig. 4.18*b* the value of kR_2 at the antiresonant frequencies is plotted as a function of L/R_2 for the above-mentioned cone angles. The lowest four curves represent the ring antiresonant frequency f_{ra} for $\alpha = 50$, 60, 70 and 80 degrees. These curves stay just below the lower boundary of region II (fig. 4.18*a*), as discussed in sec. 4.4. It was also shown in that section that the curves for f_{ra} approach asymptotically the horizontal line $kR_2 = 1$ (i.e. $k\,x \tan\alpha = 1$, cf. eq. (4.14)) as L/R_2 approaches zero.

As a consequence of the representation of kR_2 as a function of L/R_2, the longitudinal antiresonant frequencies of the same ordinal number coincide for all apex angles (fig. 4.18*b*). This follows directly from the high-frequency approximation eq. (4.51), which may be written as

$$(kR_2)_{lan} = (2n-1)\frac{\pi}{2(1-\nu^2)^{1/2}}\frac{R_2}{L}. \tag{4.70}$$

Though it was shown in sec. 4.6.2 that this approximation is only valid in region III well above the horizontal line $kR_2 = \tan\alpha/(1-\nu^2)^{1/2}$ (eq. (4.41)), it can be seen that the characteristic dependence on L/R_2 holds even in region II (we found that the longitudinal antiresonant frequencies could be calculated with sufficient accuracy in region II with the membrane equations up to a certain maximum value of L/R_2 which increased with α).

The high-frequency approximation eq. (4.70) shows that the longitudinal antiresonant frequencies depend slightly on Poisson's ratio ν; fig. 4.18*b* is calculated for $\nu = 0{\cdot}3$.

A representation which may be more useful in practice is illustrated in figs 4.19*a* and *b*. In these figures the dimensionless frequency parameter kR_a is shown as a function of the ratio of outer to inner radius R_b/R_a. Figure 4.19*a* shows the regions I, II and III (cf. fig. 4.18*a*) for four semi-apex angles.

In fig. 4.19*b* the value of kR_a for certain antiresonant frequencies is plotted versus R_b/R_a as follows. The lowest four lines represent the ring antiresonant frequency f_{ra} for $\alpha = 80$, 70, 60 and 50 degrees; these lines closely follow the boundary line of region I, running lower with increasing α (fig. 4.19*a*) and approaching the origin as α approaches 90°. The upper two drawn curves indicate the first and second longitudinal antiresonant frequencies for $\alpha = 50°$; when the apex angle is increased, these curves move upwards and approach asymptotically the dotted curves that represent the first and second longitudinal antiresonant frequencies for a flat ring.

4.8. Measurements

In order to verify the foregoing calculations of the ring and longitudinal antiresonant frequencies, measurements were carried out on a few polycarbonate

cones with different geometries, driven by the same electrodynamic driving system. The antiresonant frequencies were measured as follows.

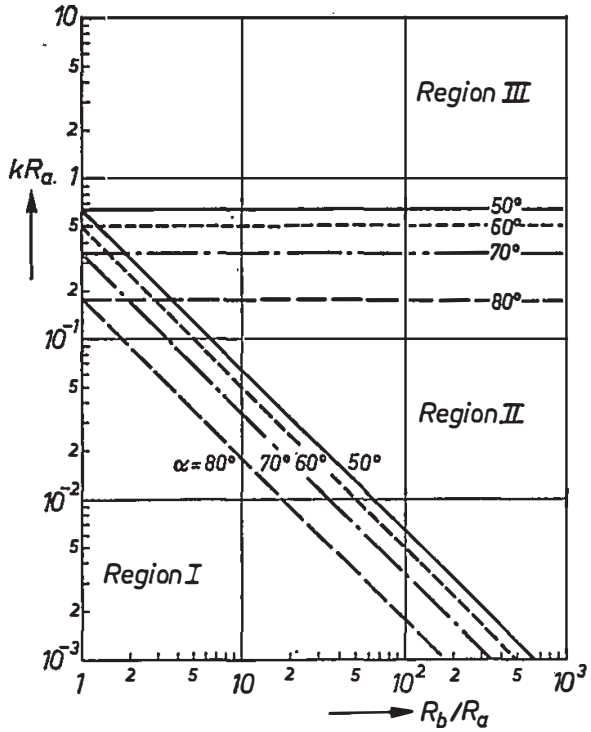

Fig. 4.19*a*. Regions in the kR_a versus R_b/R_a plane for four semi-apex angles α.

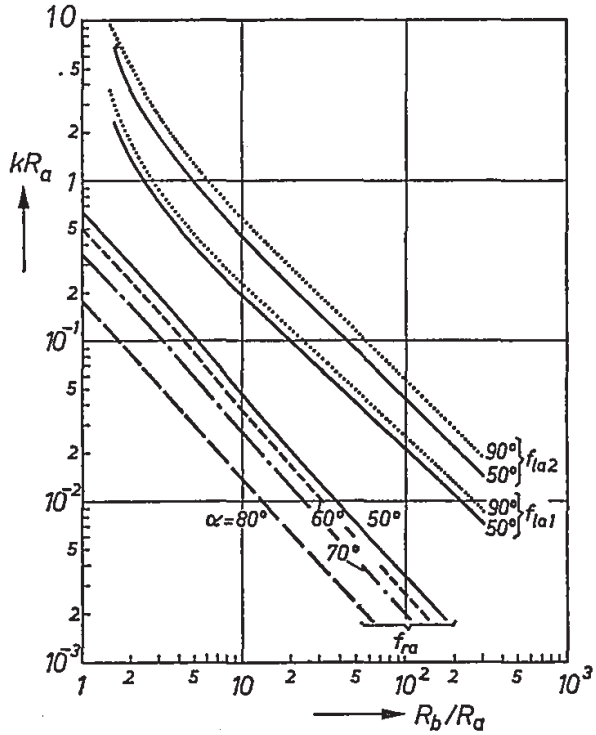

Fig. 4.19*b*. Ring antiresonant frequencies for four values of α (lowest four lines); lowest two longitudinal antiresonant frequencies for $\alpha = 50°$ (upper two drawn curves) and $\alpha = 90°$ (dotted curves).

At the antiresonant frequencies the inner-edge velocity in the meridional direction becomes minimum. Because in practice the inner edge is relatively stiff, its axial velocity becomes minimum as well. Hence the axial impedance Z_a becomes maximum and according to eq. (3.9) the motional impedance $|Z_{mot}|$ becomes minimum. The latter is recorded as a function of frequency by the method described in sec. 3.3.

A typical example of such a recording is shown in fig. 4.20 for a polycarbonate cone with geometrical and material parameters as given in table 4-IV. Apart

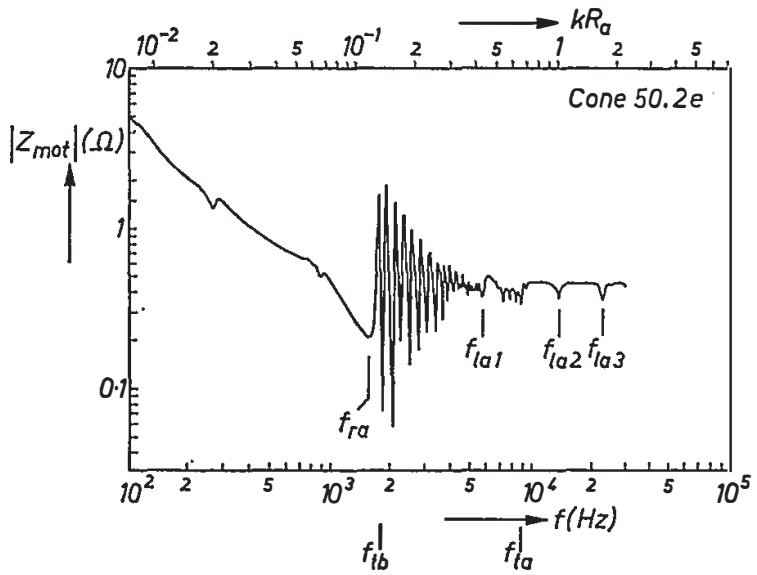

Fig. 4.20. Measured motional impedance of the polycarbonate cone 50.2e.

TABLE 4-IV

Cone 50.2e

geometry			material (polycarbonate)	
semi-apex angle	$\alpha = 50°$		Young's modulus	$E = 2{\cdot}4 \cdot 10^9$ N/m²
inner-edge radius	$R_a = 17$	mm	mass density	$\varrho = 1200$ kg/m³
outer-edge radius	$R_b = 83$	mm	Poisson's ratio	$\nu = 0{\cdot}35$
thickness	$h = 0{\cdot}23$	mm	loss factor	$\delta = 0{\cdot}014$

from the thickness (which practically has no influence on the antiresonant frequencies) this cone has the same geometry as cone 50.1; the material parameters of interest (E and ϱ) are different but this is of no importance as long as only the dimensionless frequency parameter kR_a is considered (see top of fig. 4.20). The electrodynamic driving system used to measure $|Z_{mot}|$ has an electromechanical conversion factor $(Bl)^2 = 20$ Wb²/m² and a voice-coil mass $M_c = 2$g.

The fundamental resonant frequency f_0 (sec. 3.2) of the total system lies at about 50 Hz. Below the ring antiresonant frequency f_{ra} (fig. 4.20), Z_{mot} is inversely proportional to the frequency, according to eq. (3.7a). At f_{ra} a dip occurs because Z_a attains a high value there. Just above f_{ra} a number of closely spaced peaks and dips appear, caused by bending resonances and antiresonances; these are obviously absent in the frequency characteristic of the longitudinal admittance $|y_l|$ calculated with the membrane equations. They will be discussed in the following chapter. The higher longitudinal antiresonant frequencies are indicated.

In fact the motional impedance should decrease with frequency in the high-frequency region $f > f_{ta}$, because there the term $j\omega M_c$ starts to dominate the value of Z_a in eq. (3.9). This is not the case in fig. 4.20, which may be imputed to the difference between the driving mechanisms of test and reference loudspeakers (sec. 3.3). Measured frequency characteristics of the motional impedance are further discussed in sec. 5.12.1. The antiresonant frequencies were measured for cone 50.2e of which the meridional cone length L was gradually decreased. The results are plotted in fig. 4.18*b*; in this figure the measured values of f_{ra} are also shown for polycarbonate cones with $\alpha = 60$ and 70 degrees. There is good agreement between the calculated and the measured values.

4.9. Conclusion

The conical membrane may be considered as the simplest model for the description of some basic phenomena, characteristic for the cone behaviour in general. The forced vibration of a typical conical membrane at characteristic frequencies has been discussed on the basis of displacement patterns and longitudinal admittance at the inner edge. It has been shown that an antiresonance occurs at a relatively low frequency. In a certain frequency region (region II), the membrane differential equations have an unrealistic solution. Below this region these equations have almost trivial solutions which show that the conical membrane oscillates as if it were completely rigid; above this region the solutions show that the cone maybe considered as a flat plate with the same meridional length as the cone.

The frequency dependence of the longitudinal admittance has been discussed for several apex angles. It has further been shown that a cone with a radially supported inner edge has natural frequencies lying close to the longitudinal antiresonant frequencies of a longitudinally driven cone. The dependence of these longitudinal antiresonant frequencies, which influence considerably the sound radiation (chapter 6), on the geometrical and material parameters of the cone has been illustrated.

5. EXACT SOLUTION OF THE MECHANICAL CONE BEHAVIOUR

5.1. Introduction

In the foregoing chapter the membrane behaviour of the cone was discussed. All bending moments and transverse forces were put equal to zero. This resulted in a longitudinal wave motion, coupled with transverse displacements. However, in practice bending moments and transverse forces do exist. They generate bending waves with transverse amplitudes in general much greater than those generated by longitudinal waves, because of the small bending stiffness of the cone. Further, this small bending stiffness results in a short bending wavelength; the bending waves are therefore acoustically short-circuited and radiate little sound (chapter 6). Nevertheless, the introduction of a bending stiffness is necessary to calculate the exact *) mechanical behaviour in region II (which is a crucial frequency interval for the loudspeaker); in this region the membrane equations yield an unrealistic solution.

The analytical description of the general *) behaviour of a shell of revolution is rather complicated. In literature, many approximations can be found which lead to a range of models for the description of the vibration of shells [17]). The simplest model for the axisymmetric vibration is obtained when the bending stiffness of the shell is neglected. A less approximative model is the shallow-shell theory in which the shell depth is assumed to be much smaller than its diameter; the effect of longitudinal inertia on the transverse modes can then be neglected (the shell is regarded as a slightly curved plate). For non-shallow shells, however, the neglect of the longitudinal inertia is unjustifiable [15]) and leads to considerable errors in the bending modes.

To describe the bending behaviour of loudspeaker cones we therefore resort to the classical bending theory of shells [17]). This theory accounts for longitudinal and rotatory inertia but neglects the effects of thickness shear. This leads to accurate results for frequencies well below the lowest natural antisymmetric thickness-shear frequency, which lies at about 1 MHz for an infinite paper plate with a thickness of 1 mm. Details of the assumptions on which this theory is based can be found in ref. 17.

The resulting differential equations are discussed in sec. 5.2. Ross [4,5,6]) gives an asymptotic approximation of these equations; his results, which may contribute to the general understanding of the cone behaviour, are reviewed in sec. 5.3. We introduce boundary conditions in sec. 5.4 and solve numerically the governing differential equations for a number of cone types; this forms the basis for a discussion of the dependence of the displacement patterns on frequency (sec. 5.5). Further, the dependence of bending resonant and antiresonant

*) In this context the adjectives "exact" and "general" refer to the accounting for bending effects.

frequencies and mode shapes on cone geometry and material are discussed in sec. 5.6. The frequency characteristic of the axial admittance is illustrated on the basis of numerically calculated examples in sec. 5.7. General and membrane solutions are compared with each other in secs 5.8 and 5.9, followed by a discussion of the very important influence of the voice-coil mass on the frequency characteristic of the axial admittance. Although sound radiation by asymmetric vibrations will be neglected these vibrations are briefly discussed in sec. 5.11. Finally in sec. 5.12 measurements on a few cones are reported, which are mainly intended to verify the calculations.

5.2. Basic differential equations

The cone geometry and coordinates are shown in fig. 4.1*a*. Figure 5.1 gives the positive directions of the stress resultants and displacements of a cone element.

The differential equations, which completely describe the stress and deformation conditions of a shell of revolution in asymmetric vibration, are based on

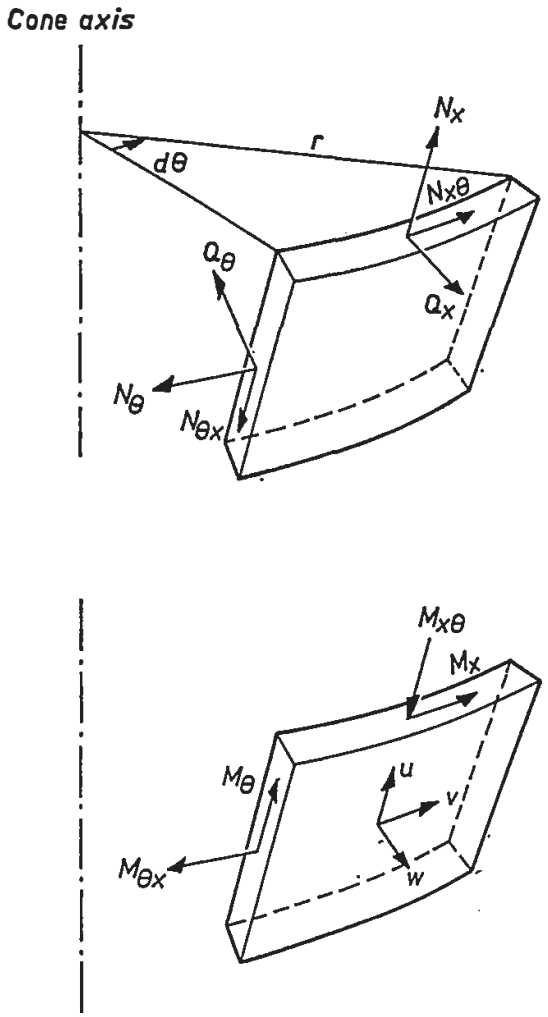

Fig. 5.1. Cone element showing positive directions of stress and moment resultants and displacements.

a derivation by Reissner [12]) and include the effects of translatory and rotatory inertia. They comprise 14 variables, which are assumed to be separable in the form (see List of symbols for the meaning of the variables):

$$\begin{bmatrix} w \\ u \\ \beta_x \\ Q \\ Q_x \\ N_x \\ N_\theta \\ M_x \\ M_\theta \end{bmatrix} = \begin{bmatrix} w_n \\ u_n \\ \beta_{xn} \\ Q_n \\ Q_{xn} \\ N_{xn} \\ N_{\theta n} \\ M_{xn} \\ M_{\theta n} \end{bmatrix} \cos(n\,\theta), \tag{5.1a}$$

$$\begin{bmatrix} v \\ N \\ N_{\theta x} \\ Q_\theta \\ M_{\theta x} \end{bmatrix} = \begin{bmatrix} v_n \\ N_n \\ N_{\theta xn} \\ Q_{\theta n} \\ M_{\theta xn} \end{bmatrix} \sin(n\,\theta), \tag{5.1b}$$

where the effective shear resultants Q and N are introduced because of their appearance in the boundary conditions of the cone in asymmetric vibration (see sec. 5.11, eq. (5.46)); they are defined by (see ref. 18, p. 58)

$$Q = Q_x + \frac{1}{x \sin\alpha}\frac{\partial M_{\theta x}}{\partial \theta},$$

$$N = N_{\theta x} + \frac{M_{\theta x}\cot\alpha}{x}.$$

The definition of the other stress and moment resultants can be found in ref. 12. The time factor $\exp(j\omega t)$ has been omitted.

The 14 first-order differential equations which describe the mechanical behaviour of the cone are not independent; after reduction a system of 8 independent differential equations with 8 independent variables remains. The fundamental variables taken are those quantities that appear in the boundary conditions at the cone edges. Following Kalnins [14,16]) we represent these fundamental variables as the elements of a vector $y(x)$:

$$y(x) = \begin{bmatrix} w_n(x) \\ u_n(x) \\ v_n(x) \\ \beta_{xn}(x) \\ Q_n(x) \\ N_{xn}(x) \\ N_n(x) \\ M_{xn}(x) \end{bmatrix} \tag{5.2}$$

where x is the independent variable, i.e. the distance along the cone meridian. The variables N_θ, $N_{\theta x}$, Q_θ, Q_x, M_θ and $M_{\theta x}$ may be expressed in the others.

The remaining 8 simultaneous differential equations can be written as

$$\frac{\mathrm{d}y(x)}{\mathrm{d}x} = A(x)\, y(x) \tag{5.3}$$

where $A(x)$ is an (8, 8) coefficient matrix, whose elements are given in appendix A. As sound radiation by asymmetric vibrations will prove to be unimportant (see sec. 6.2), special attention will be paid to the case of axisymmetric vibrations ($n = 0$). Then the number of fundamental variables reduces to the following six:

$$y(x) = \begin{bmatrix} w(x) \\ u(x) \\ \beta_x(x) \\ Q(x) \\ N_x(x) \\ M_x(x) \end{bmatrix}. \tag{5.4}$$

The number of differential equations likewise reduces to six. The (6, 6) matrix $A(x)$ is given in appendix A.

The solution $y(x)$ is obtained numerically by subjecting eq. (5.3) to three boundary conditions at each edge. The method of solution is that of direct integration, introduced by Goldberg et al.[13]) and refined by Kalnins [14,16]). With this method, which is briefly discussed in appendix B, the system (5.3) is solved for a number of frequencies. The same method was used for solving the membrane differential equations in the preceding chapter.

The introduction of an internal loss factor makes all fundamental variables complex and consequently doubles the number of differential equations and boundary conditions. The matrix $A(x)$ of eq. (5.3) for the complex axisymmetric case is given in appendix A.

Before illustrating the cone behaviour on the basis of typical examples, we will first review Ross's asymptotic solutions of the basic system of differential equations. These analytic approximations may contribute to the understanding of the vibrational behaviour of the cone.

5.3. Results of Ross's asymptotic approximation

The above system of six differential equations for six unknowns has six linearly independent solutions. In an asymptotic analysis of this system, Ross [4,5,6]) finds first approximations to these solutions which divide into two classes.

Four solutions show rapid spatial variation, and bending action is the pre-

dominant mechanism. The influence of stretching on these solutions is slight but not entirely negligible (otherwise we would be reduced to inextensional theory [8]), which has only rigid-body solutions for the axisymmetric case). The transverse displacements of these so-called bending solutions are much greater than the longitudinal displacements:

$$\frac{w}{u} = O(\varepsilon^{-1/2}) \gg 1 \tag{5.5}$$

where

$$\varepsilon = \frac{h}{a\,[12\,(1-\nu^2)]^{1/2}\tan\alpha} \ll 1. \tag{5.6}$$

Two of these bending solutions are non-propagating edge disturbances; they rapidly decrease with increasing distance from the inner or outer edge. The other two bending solutions are waves; for $k\,x\tan\alpha > 1$ (i.e. for meridional coordinates x greater than the coordinate x_t of the transition point) their wavenumber approaches the bending wavenumber k_B in an infinite plate:

$$k_B = \frac{\sqrt{\omega}}{\gamma} \tag{5.7}$$

where

$$\gamma^2 = c_1\,h/\sqrt{12}. \tag{5.8}$$

The plate bending-wave velocity is

$$c_B = \gamma\,\sqrt{\omega} \tag{5.9}$$

and the bending wavelength

$$\lambda_B = \frac{2\pi}{k_B} = \left(\frac{\pi}{\sqrt{3}}\frac{c_1\,h}{f}\right)^{1/2}. \tag{5.10}$$

The remaining two asymptotic solutions of the general system of differential equations are rather slowly varying functions of position: their wavelength is approximately equal to the longitudinal wavelength λ_1 in an infinite plate. The effect of bending in these solutions is negligible. Because the strain energy is almost entirely of the stretching type, these solutions are called membrane solutions. They are well approximated by the solutions of the membrane system of differential equations (chapter 4). The relation

$$\frac{u}{w} = O(k\,a\tan\alpha) \tag{5.11}$$

shows that transverse and longitudinal displacements have equal order of magnitude for $k\,a \tan\alpha = O(1)$ (i.e. for frequencies in the vicinity of f_{ta}). Membrane and bending solutions are nearly independent except at the transition point. At this point both the membrane theory and the asymptotic bending theory fail. This indicates that the classification of solutions into membrane and bending types is impossible near such points. Therefore, transition points can be interpreted as the sites of localized interaction between bending and stretching effects.

Applying boundary conditions to the asymptotic solutions leads to two sets of natural frequencies, called membrane and bending frequencies. Ross shows that the membrane frequencies can be obtained by applying a membrane edge condition to the solution of the membrane system of differential equations. He also shows that for a free outer edge the modes associated with the membrane frequencies are of the membrane type and the modes associated with the bending frequencies are wholly of the bending type (within a first approximation). Further he proves that in region I ($f < f_{tb}$) natural frequencies associated with modes of the bending type cannot occur; however this need not be true for $f \approx f_{tb}$, where transitional effects may play a part.

We may summarize Ross's results as follows. Bending resonances and anti-resonances only appear for $f > f_{tb}$. For $f \gg f_{ta}$ bending and longitudinal waves exist almost independently. First approximations show that the waves behave as if they were propagating on an infinite plate. For loudspeaker cones, however, this frequency region lies too high to be of practical value; this will be discussed in chapter 6. At the transition point considerable interaction occurs between bending and stretching effects.

Although Ross's analytic expressions will not be used in this thesis, his results and conclusions may contribute to the understanding of the numerically obtained solutions of the general differential equations, discussed in the following sections.

5.4. Boundary conditions

The boundary conditions applied for numerically solving the general system of differential equations (eq. (5.3)) are directly derived from the situation in practice. As discussed in chapter 3, the inner edge, to which the voice coil and inner suspension are attached, is relatively stiff so that it can move in an axial direction only. Further, the cone is usually rather stiffly glued to the voice coil and inner suspension. We therefore assume in the calculations that the cone is clamped to an infinitely stiff massless ring at the inner edge, which can only vibrate axially. This means that the displacement normal to the cone axis must be zero at $x = a$ (fig. 5.2):

$$u(a) \sin\alpha + w(a) \cos\alpha = 0. \tag{5.12a}$$

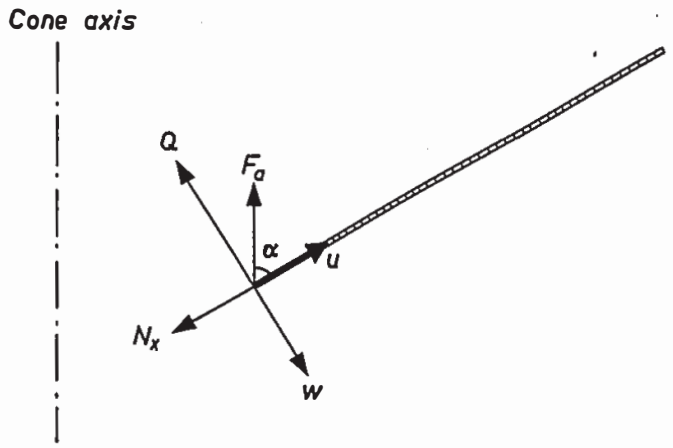

Fig. 5.2. Illustration of the boundary conditions at the inner cone edge.

From the clamping condition it follows that the transverse displacement must have a zero derivative at $x = a$:

$$\left.\frac{\mathrm{d}w(x)}{\mathrm{d}x}\right|_{x=a} = \beta_x(a) = 0. \tag{5.12b}$$

Finally, the axial components of the transverse and longitudinal stress resultants Q and N_x must be balanced by the applied axial force F_a (fig. 5.2):

$$Q(a)\sin\alpha - N_x(a)\cos\alpha = \frac{F_a}{2\pi R_a}. \tag{5.12c}$$

The outer edge is again assumed to be free (the damping influence of the outer suspension is accounted for by taking a higher internal loss factor in the calculations than the real value, as discussed in chapter 4). This means that at $x = b$ all stress and moment resultants must be zero:

$$Q(b) = N_x(b) = M_x(b) = 0. \tag{5.13}$$

The above boundary conditions will be used in all following computations.

In the following an important approximate relation will be derived between the axial impedance Z_a and the longitudinal impedance Z_l at the inner edge. The former is defined by

$$Z_a = \frac{F_a}{v_a(a)}, \tag{5.14}$$

where $v_a(a)$ *) is the axial velocity at the inner edge (fig. 5.3*a*); Z_l shows up in the four-pole equations for the unconstrained inner edge:

*) Note that in the context of asymmetric vibrations the letter v is used for the azimuthal displacement. However, confusion is hardly possible since v stands for velocity only in symmetric vibrations and is then always provided by one of the subscripts *a* (axial), *l* (longitudinal) or *t* (transverse).

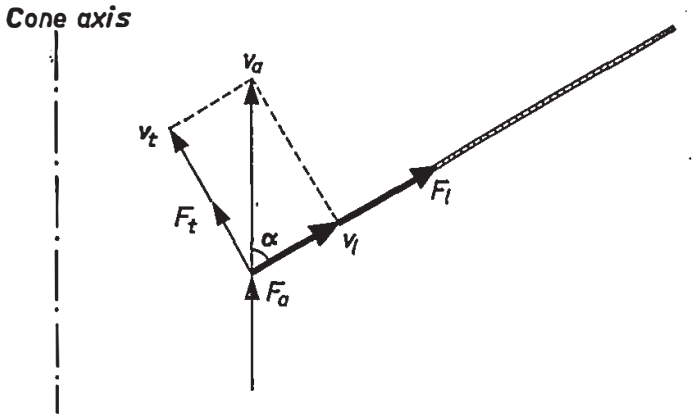

Fig. 5.3*a*. Definition of forces and velocities at the inner edge.

$$F_l = Z_l\ v_l(a) + Z_{lt}\, v_t(a),$$
$$F_t = Z_{tl}\, v_l(a) + Z_t\ v_t(a), \tag{5.15}$$

where $F_{l,t}$ and $v_{l,t}(a)$ are the forces and velocities at the inner edge in the longitudinal and transverse directions. To simplify the present discussion the positive directions of the forces and velocities are defined as shown in fig. 5.3*a* *). The latter equations account for the coupling between the longitudinal and the transverse forces and velocities. For $f > f_{ta}$, however, the longitudinal and transverse (i.e. bending) waves gradually uncouple with increasing frequency (see sec. 5.3). Then, the cross-terms may be neglected; hence

$$F_l \approx Z_l\, v_l(a),$$
$$F_t \approx Z_t\, v_t(a). \tag{5.16}$$

The boundary conditions at the inner edge are rewritten in terms of forces and velocities. The condition that the inner edge can only move in axial direction (eq. (5.12a)) is expressed by

$$v_t(a) = v_a(a) \sin \alpha,$$
$$v_l(a) = v_a(a) \cos \alpha. \tag{5.17}$$

The axial components of the transverse and longitudinal forces F_t and F_l must be equal to the axial force F_a, exerted by the voice coil:

$$F_t \sin \alpha + F_l \cos \alpha = F_a. \tag{5.18}$$

The components of F_t and F_l in a direction normal to the cone axis are neutral-

*) Note that the longitudinal force F_l and the transverse velocity v_t are defined oppositely to the longitudinal stress resultant N_x and the transverse displacement w respectively. If follows that $F_l = -2\pi\, R_a\, N_x$ and $v_t = -j\omega\, w$ (cf. figs 5.2, 5.3*a*).

ized by the infinitely stiff ring. On the basis of the latter three equations, we now easily arrive at the following expression:

$$Z_a = Z_t \sin^2 \alpha + Z_l \cos^2 \alpha. \tag{5.19}$$

Of course, eq. (5.19) only holds for the present boundary conditions at the inner edge. For a cylinder Z_a is equal to Z_l; for a flat plate $Z_a = Z_t$. The transverse impedance Z_t is mainly controlled by the cone bending stiffness, which is relatively small in practice. The longitudinal impedance Z_l is mainly determined by the extensional stiffness of the cone surface and is usually much higher than Z_t. We write eq. (5.19) as

$$Z_a = Z_l \left(1 + \frac{Z_t}{Z_l} \tan^2 \alpha\right) \cos^2 \alpha \tag{5.20}$$

and estimate the frequency average of $\left|Z_t/Z_l\right| \tan^2 \alpha$ as follows.

At high frequencies ($f > f_{ta}$), the frequency characteristic of the longitudinal impedance Z_l oscillates about the characteristic longitudinal impedance Z_{lc} of a semi-infinite plate (see eq. (4.46)), given by

$$Z_{lc} = 2\pi R_a h \varrho c_1. \tag{5.21}$$

The transverse impedance Z_t oscillates about the characteristic bending impedance Z_{tc} of a semi-infinite plate [40]), where

$$Z_{tc} = 2\pi R_a h \varrho c_B. \tag{5.22}$$

The amplitude of the oscillations of Z_l and Z_t about their characteristic values in the frequency domain are proportional to $1/\delta\, k_1 L$ and $1/\delta\, k_B L$ respectively. Since in practice in the audio region

$$\frac{k_1}{k_B} = \left(\frac{\omega h}{c_1 \sqrt{12}}\right)^{1/2} \ll 1 \tag{5.23}$$

we may neglect the amplitude of the oscillations of Z_t as compared with those of Z_l. Therefore, the frequency average of $\left|Z_t/Z_l\right| \tan^2 \alpha$ may be written as

$$\left\langle \left|\frac{Z_t}{Z_l}\right| \tan^2 \alpha \right\rangle \approx \frac{Z_{tc}}{Z_{lc}} \tan^2 \alpha = \frac{k_1}{k_B} \tan^2 \alpha, \tag{5.24}$$

which in practice is much smaller than 1. For instance, if we substitute the following practical values in the latter equation: $\alpha = 60°$, $h = 0{\cdot}3$ mm and $c = 2700$ m/s we find at $f = 10$ kHz:

$$\left\langle \left|\frac{Z_t}{Z_l}\right| \tan^2 \alpha \right\rangle \approx 0{\cdot}1.$$

Hence, it follows from eq. (5.20) that

$$Z_a \approx Z_l \cos^2 \alpha. \tag{5.25}$$

Equation (5.25) means that in the high-frequency region (region III) the axial impedance Z_a is determined by the longitudinal impedance Z_l. In the transition region (region II) Z_l is higher than Z_{lc} (see fig. 4.15) at all frequencies. Then the frequency average of $|Z_t/Z_l| \tan^2 \alpha$ will certainly be negligible with respect to unity and eq. (5.25) also holds in region II. This approximation for Z_a will not be used in the numerical computations, it only serves to illustrate the high influence of Z_l on Z_a and the relationship between the frequency characteristics of the axial impedance calculated with the exact equations and the longitudinal impedance calculated with the membrane equations.

Equation (5.25) may be illustrated on the basis of fig. 5.3*b*, which is a simplified representation of the situation at the inner edge. The latter can only move along the vertical axis; the transverse and longitudinal impedances are represented by two springs with stiffnesses s_t and s_l respectively *). It is clear that, if $s_t \ll s_l$, then s_l will determine the ultimate axial displacement.

Equation (5.25) also holds at low frequencies (region I), which can be shown as follows. Then the cone oscillates practically as a rigid body with a mass M_d. The motion is determined by Newton's law:

$$F_a \approx j\omega M_d v_a(a) \tag{5.26}$$

and F_t and F_l cannot be described by (independent) four-pole equations. On the contrary, they can be considered as components of F_a (fig. 5.3*c*):

$$\begin{aligned} F_t &= F_a \sin \alpha, \\ F_l &= F_a \cos \alpha, \end{aligned} \tag{5.27}$$

and are consequently directly proportional to F_a. The inner-edge constraint which only allows motion in the axial direction is completely superfluous, because the axially driven rigid cone will move axially; eq. (5.18) turns into an identity. With eqs (5.17), (5.26) and (5.27) we arrive at

$$Z_a \approx j\omega M_d, \tag{5.28}$$

$$Z_l \approx Z_a/\cos^2 \alpha, \tag{5.29a}$$

$$Z_t \approx Z_a/\sin^2 \alpha. \tag{5.29b}$$

Equation (5.29a) agrees with eq. (4.27) which was found from the low-frequency solutions of the membrane equations for a longitudinally driven unconstrained edge. This shows indeed that the inner-edge constraint does not affect the motion in the low-frequency region.

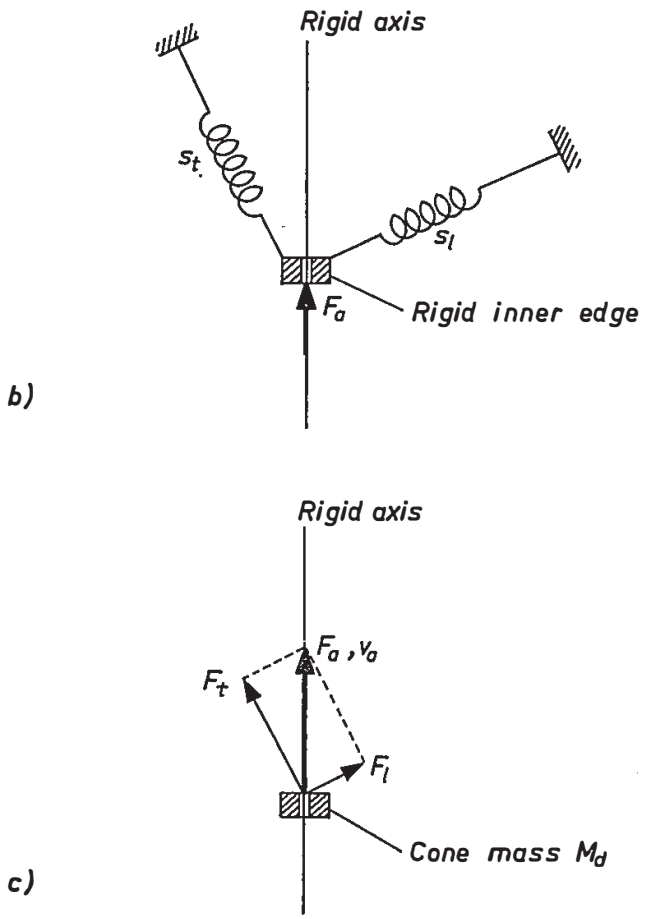

Fig. 5.3. (*b*) Simplified illustration of the infiuence of the transverse impedance Z_t (represented by the spring s_t) and the longitudinal impedance Z_l (represented by the spring s_l). The inner edge is forced to move along the rigid vertical axis.
(*c*) Simplified illustration of the forces and cone velocity at a very low frequency.

We conclude that the mean frequency characteristic of Z_a is determined by Z_l; the latter can be calculated with the membrane equations. Oscillations about the mean value are caused by bending resonances and antiresonances at which Z_t becomes minimum and maximum; their amplitude decreases with increasing frequency and increasing loss factor. This will be explicitly illustrated in the next sections.

5.5. Typical frequency dependence of the displacement patterns

In this section the axisymmetric transverse and longitudinal displacement patterns $w(x)$ and $u(x)$ are calculated for cone 50.3 (see table 5-I) by solving numerically the general system of differential equations at a number of fre-

*) Of course this representation of the cone reaction by stiffnesses serves an illustrative purpose; at certain frequency intervals the cone reacts as a mass.

TABLE 5-I

Cone 50.3

geometry		material	
semi-apex angle	$\alpha = 50°$	Young's modulus	$E = 2 \cdot 10^9$ N/m^2
inner-edge radius	$R_a = 17$ mm	mass density	$\varrho = 600$ kg/m^3
outer-edge radius	$R_b = 83$ mm	Poisson's ratio	$\nu = 0{\cdot}3$
thickness	$h = 0{\cdot}23$ mm	loss factor: specified locally (if unspecified: $\delta = 0{\cdot}1$)	

quencies. Except for the greater thickness this cone has the same geometry and material parameters as cone 50.1 whose longitudinal behaviour was discussed in chapter 4. Therefore, the frequency regions are equal and the longitudinal resonant and antiresonant frequencies are practically equal to those of cone 50.1. The greater thickness of cone 50.3 serves to illustrate more clearly the effects of bending on the frequency characteristic of the axial admittance (see sec. 5.7.1). For simplicity the internal loss factor is assumed to be zero. This means that the displacement patterns are of the standing-wave type.

Transverse and longitudinal displacement patterns calculated with the general equations at typical frequencies in the three frequency regions are shown in figs 5.4*a* through 5.4*h* which are not drawn to the same scale.

Region I ($f < f_{tb}$)

Figure 5.4*a* shows $w(x)$ and $u(x)$ at $f = 1000$ Hz. At this relatively low frequency the cone motion is almost uniform; in a first approximation the cone may be considered to be rigid. When the frequency is raised the amplitudes at the inner edge decrease whereas they increase at the outer edge, as discussed in chapter 4. At the ring antiresonant frequency $f_{ra} = 1840$ Hz the longitudinal displacement $u(x)$ becomes zero at the inner edge: a node appears. Because of the assumed rigidness of the inner edge, this node also appears in w (fig. 5.4*b*). When the frequency is raised further, the node shifts to the outer edge, as shown by fig. 5.4*c* (2200 Hz). The upper limit of region I lies at $f_{tb} = 2250$ Hz.

Region II ($f_{tb} \leqslant f \leqslant f_{ta}$)

Above f_{tb} the cone shows natural frequencies associated with bending modes. Because a forced vibration is considered here, it is expedient to divide these natural frequencies into so-called bending resonant frequencies at which $u(a)$

and $w(a)$ become infinite, and bending antiresonant frequencies at which $u(a)$ and $w(a)$ become zero.

These bending resonant and antiresonant frequencies are easily distinguished from longitudinal resonant and antiresonant frequencies, since the spacings between the latter are relatively large for normal loudspeaker cones. Moreover, each time a bending antiresonant frequency is passed, the number of nodes in $w(x)$ increases by 1, whereas that in $u(x)$ remains unaltered. While passing a longitudinal antiresonant frequency, both $w(x)$ and $u(x)$ show another node. For instance, at the first bending resonance $f_{br1} = 2360$ Hz (fig. 5.4*d*), u and w become very large and a phase change of 180 degrees occurs. At the first bending antiresonant frequency $f_{ba1} = 2418$ Hz another node arises in $w(x)$ at the inner edge (fig. 5.4*e*), which shifts relatively quickly to the outer edge when the frequency is further increased.

The mode shapes at the second and third bending resonant and antiresonant frequencies are shown in figs 5.4*f* through 5.4*i*. The above figures show the typical amplitude distribution encountered in region II. In this region, a transition point lies on the cone at $x = x_t$, which is indicated by a dot in figs 5.4*d* through 5.4*i*. On the inner cone part $a < x < x_t$, the vibration is predominantly of the membrane type. The wavelength is rather long. The motion on this part is practically axial, because u and w have the same order of magnitude (eq. (5.11)). At the transition point considerable interaction occurs between membrane and bending waves (sec. 5.3). On the outer cone part $x_t < x < b$, the vibration amplitude is predominantly determined by bending waves with a wavenumber approximately equal to the bending wavenumber k_B in an infinite plate and with transverse amplitudes much higher than the longitudinal ones (figs 5.4*g* through 5.4*i*). These figures illustrate that in region II the general vibration patterns completely deviate from the membrane patterns; the latter show a singularity at x_t and no bending waves.

The different nature of the motion on the two sides of the transition point can be further demonstrated on the basis of the strain-energy coefficient η. This coefficient indicates the fraction of the total strain energy that is due to bending:

$$\eta = \frac{V_B}{V_S + V_B}, \tag{5.30}$$

where V_B is the strain energy due to bending and V_S the strain energy due to stretching of the middle surface of the cone. This coefficient was originally introduced by Kalnins [15]) for the classification of modes. Expressions for V_S and V_B are given in appendix C. The value of η, calculated numerically at regular intervals along a cone meridian is plotted as a function of x in fig. 5.5. This figure shows that η becomes small for $x < x_t$, which indicates the mem-

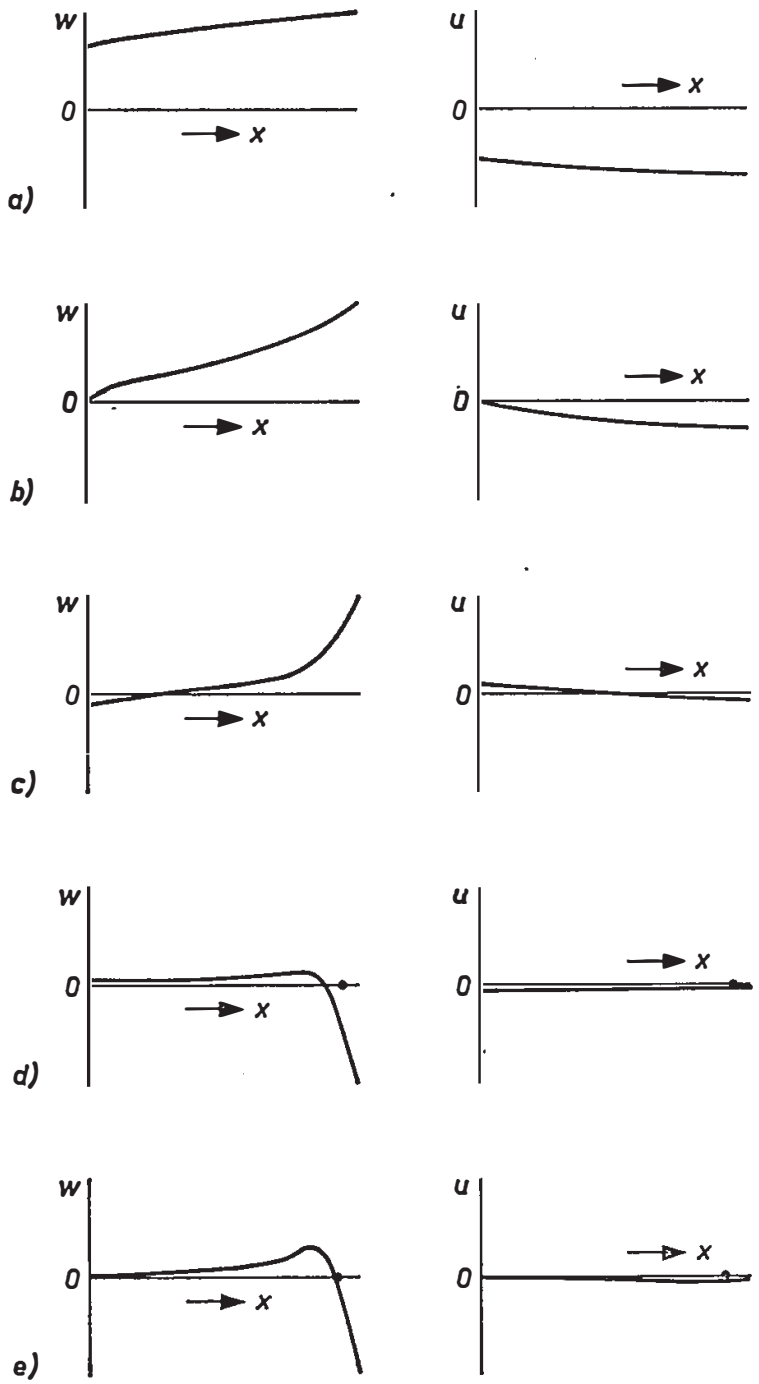

Fig. 5.4. Calculated transverse and longitudinal displacement patterns of cone 50.3 (exact solution) at
(*a*) 1000 Hz,
(*b*) the ring antiresonant frequency $f_{ra} = 1840$ Hz,
(*c*) 2200 Hz,
(*d*) the first bending resonant frequency $f_{br1} = 2360$ Hz,
(*e*) the first bending antiresonant frequency $f_{ba1} = 2418$ Hz.

brane character of the motion, whereas for $x > x_t$, η approaches 1, indicating that the wave motion is of the bending type.

The relatively long wavelength for $x < x_t$ and short wavelength for $x > x_t$ is characteristic of all cones vibrating with frequencies in region II. This has

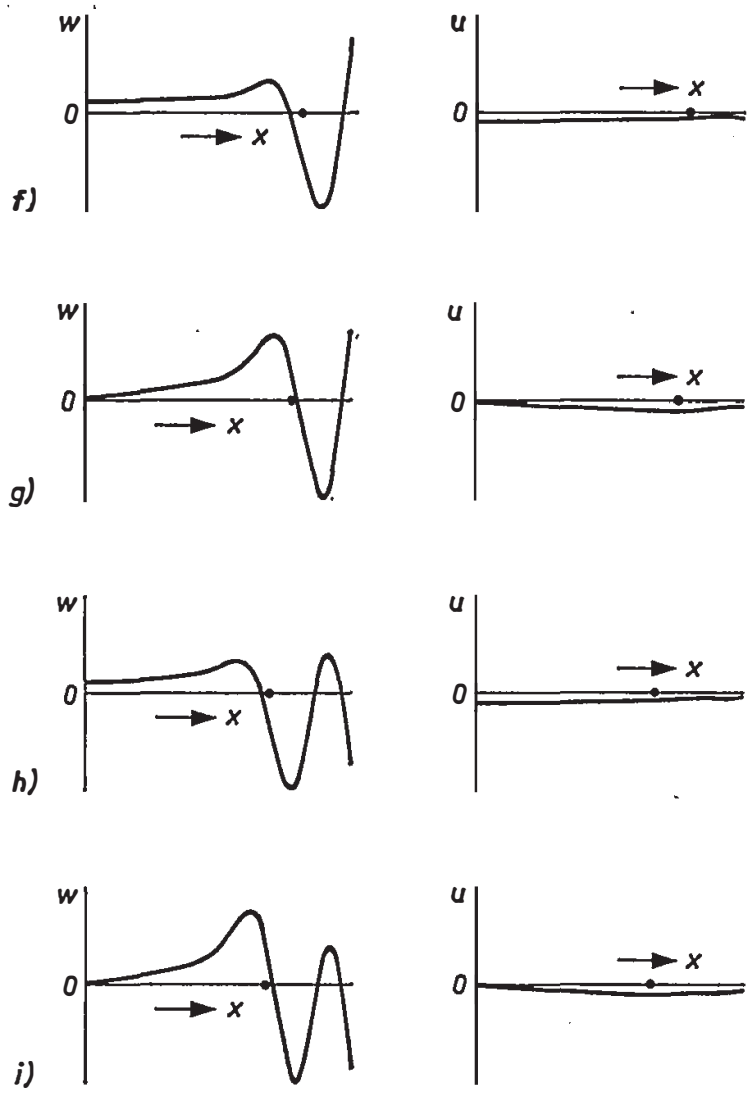

Fig. 5.4 (continued):
(*f*) the second bending resonant frequency $f_{br2} = 2668$ Hz,
(*g*) the second bending antiresonant frequency $f_{ba2} = 2750$ Hz,
(*h*) the third bending resonant frequency $f_{br3} = 2993$ Hz,
(*i*) the third bending antiresonant frequency $f_{ba3} = 3083$ Hz.
The dot indicates the position of the transition point.

considerable influence on the sound radiation, as will be shown in chapter 6. A comparison of the displacement patterns obtained with the membrane and the general equations at the first longitudinal antiresonant frequency f_{la1} and the first membrane resonant frequency f_{mr1}, both lying in region II, will be made in sec. 5.9.

Region III ($f > f_{ta} = 11000$ Hz)

In region III the coupling between bending and membrane waves becomes weak. The transition point has disappeared from the cone. The transverse displacement pattern is well approximated by that on a transversely driven semi-infinite plate, except at certain discrete frequencies, viz. at the natural frequencies for a radially supported inner edge (membrane resonant frequencies); these

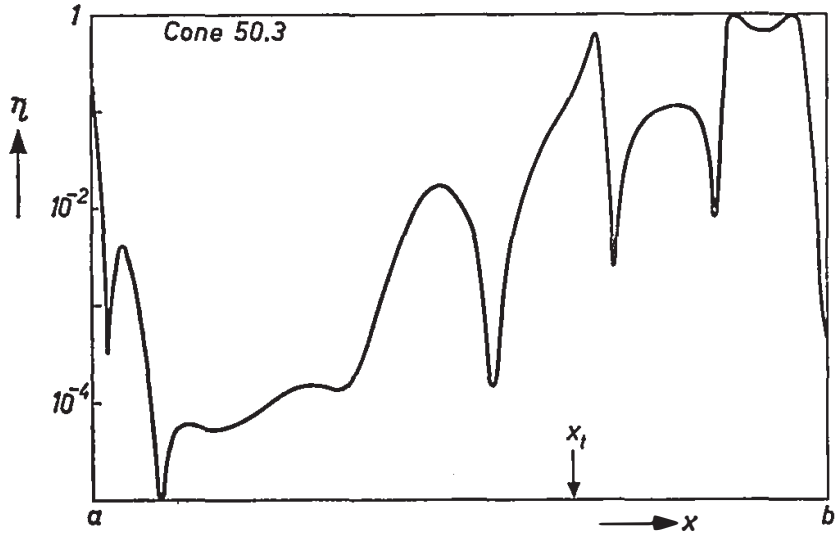

Fig. 5.5. Strain-energy coefficient η versus meridional coordinate x for cone 50.3 at the third bending antiresonant frequency $f_{ba3} = 3083$ Hz.

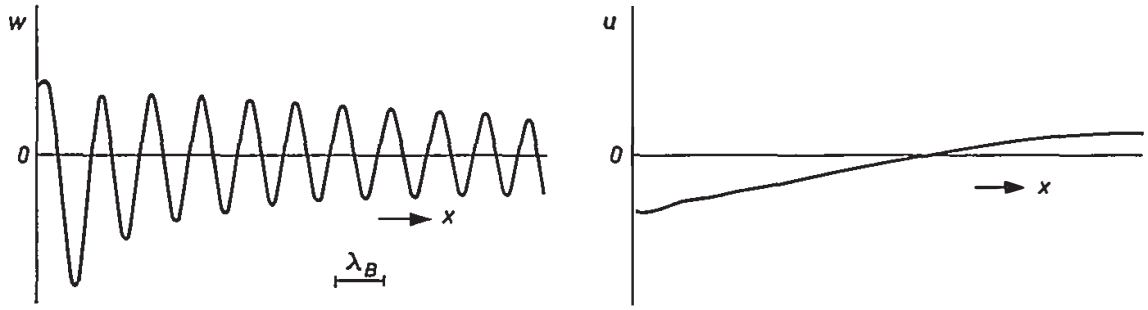

Fig. 5.6. Calculated transverse and longitudinal displacement patterns of cone 50.3 at $f = 13000$ Hz (exact solution).

will be discussed in sec. 5.8. In the present frequency region the cone is entirely covered by bending waves; the wavelength is approximately equal to the bending wavelength λ_B in an infinite plate. This is illustrated in fig. 5.6, which shows the transverse and longitudinal displacement patterns at $f = 13000$ Hz; the value of λ_B calculated with eq. (5.10) is indicated.

5.6. Dependence of bending resonant and antiresonant frequencies and displacement patterns on the cone geometry and material

In region III the bending resonant and antiresonant frequencies can easily be approximated since the cone is entirely covered by bending waves with a wavelength about equal to λ_B. As the outer edge is free, an antinode will appear there. At bending resonant frequencies f_{brn} an antinode also appears at the inner edge. At these frequencies an integral number of half wavelengths fits on the meridional length L of the cone; hence we find with eq. (5.10):

$$f_{brn} \approx \frac{\pi}{4\sqrt{3}} \frac{n^2 h c_1}{L^2}. \tag{5.31}$$

Since at bending antiresonant frequencies f_{ban} a node appears at the inner edge, an odd number of quarter wavelengths must fit on L, so that

$$f_{abn} \approx \frac{\pi}{16\sqrt{3}} \frac{(2n+1)^2\, h\, c_1}{L^2}. \tag{5.32}$$

These equations can be written as functions of the reduced geometry variables h/R_b and R_b/R_a as follows:

$$kR_a\big|_{brn} \approx \frac{\pi^2\, n^2}{2\,[3\,(1-\nu^2)]^{1/2}} \frac{h}{R_b} \frac{R_b/R_a}{(R_b/R_a-1)^2} \sin^2\alpha, \tag{5.33}$$

$$kR_a\big|_{ban} \approx \frac{\pi^2\,(2n+1)^2}{8\,[3\,(1-\nu^2)]^{1/2}} \frac{h}{R_b} \frac{R_b/R_a}{(R_b/R_a-1)^2} \sin^2\alpha, \tag{5.34}$$

where $kR_a\big|_{brn}$ and $kR_a\big|_{ban}$ are the values of the dimensionless frequency parameter kR_a at the nth bending resonant and antiresonant frequencies respectively.

In region II bending waves only appear on the outer cone part and the above frequencies must be numerically calculated with the general differential equations. This is carried out as follows. At the resonant frequencies the axial admittance $|Y_a|$ becomes infinite if $\delta = 0$; at the antiresonant frequencies $|Y_a| = 0$. This admittance is numerically calculated for a sufficient number of frequencies (usually about 5 points between adjacent resonant frequencies). Inverse Newton interpolation of $|Y_a|$ and $1/|Y_a|$ then yields the resonant and antiresonant frequencies. In this way the dependence of the lowest five bending antiresonant frequencies on the cone geometrical parameters is determined. The bending resonant frequencies lie between the bending antiresonant frequencies (though in general not halfway between them); they will not be shown.

The above-mentioned dependence will be discussed in the next subsections on the basis of figs 5.7 through 5.9 in which the longitudinal and bending antiresonant frequencies are represented by drawn and dashed curves respectively. The longitudinal antiresonant frequencies are calculated with the membrane equations. The points labelled alphabetically on the curve f_{ba3} in these figures correspond to the modes labelled similarly in fig. 5.10. In these modes the transition point is again indicated by a dot. The dependence on the material parameters E and ϱ follows implicitly from the dimensionless variable kR_a.

5.6.1. *Influence of the thickness*

Figure 5.7 shows the dimensionless frequency kR_a at the lowest five bending antiresonant frequencies as a function of the reduced cone thickness h/R_b for $\alpha = 60°$ and $R_b/R_a = 5$. The spacing between the bending antiresonant

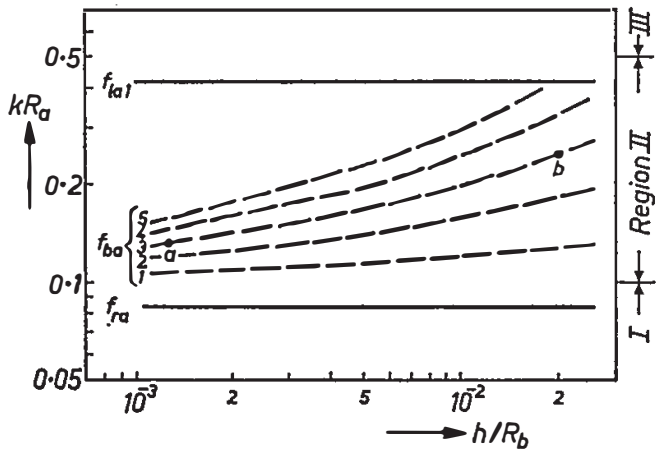

Fig. 5.7. Calculated dependence of the ring antiresonant frequency f_{ra}, the first longitudinal antiresonant frequency f_{1a1} (drawn lines) and the lowest five bending antiresonant frequencies (dashed) on the reduced cone thickness h/R_b for $\alpha = 60°$ and $R_b/R_a = 5$.

frequencies decreases with decreasing h/R_b. In the limit, as $h/R_b \to 0$, all bending resonant and antiresonant frequencies coincide at $kR_a = \cos\alpha$ or $kR_2 = 1$, where R_2 is the second radius of curvature at the inner edge (eq. (4.68)). In region III the bending resonant and antiresonant frequencies are proportional to h/R_b (eqs (5.33), (5.34)).

Figures 5.10*a* and *b* show the displacement patterns at the third bending antiresonant frequency for $h/R_b = 1{\cdot}25 \cdot 10^{-3}$ and $h/R_b = 2 \cdot 10^{-2}$ respectively (points a and b in fig. 5.7).

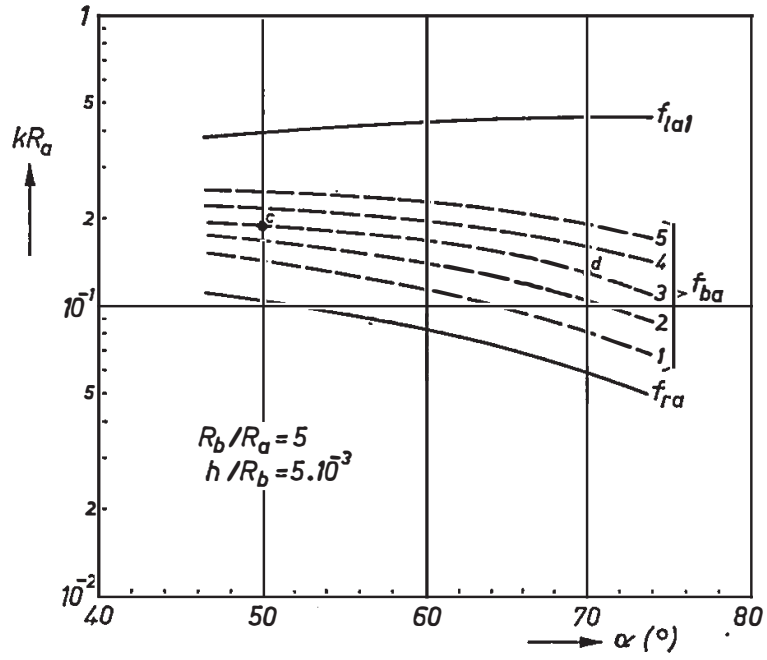

Fig. 5.8. Calculated dependence of the ring antiresonant frequency f_{ra}, the first longitudinal antiresonant frequency f_{1a1} (drawn curves) and the lowest five bending antiresonant frequencies (dashed) on the semi-apex angle α for $R_b/R_a = 5$ and $h/R_b = 5 \cdot 10^{-3}$.

5.6.2. *Influence of the apex angle*

The influence of the apex angle on the lowest five bending antiresonant frequencies is shown in fig. 5.8 for $R_b/R_a = 5$ and $h/R_b = 5 \cdot 10^{-3}$. The ring antiresonant frequency decreases with increasing α (see sec. 4.4). It becomes zero at $\alpha = 90°$. The lower bending antiresonant frequencies show the same tendency. However, as α approaches 90° the latter become equal to the lower bending antiresonant frequencies of a flat annular ring. The spacing between the antiresonant frequencies increases with increasing α, because the meridional cone length L decreases (R_b/R_a is kept constant). At higher bending antiresonant frequencies the slope of the curves therefore becomes positive, as predicted by eq. (4.35) for $f > f_{ta}$ (not shown in fig. 5.8).

The displacement patterns at f_{ba3} for $\alpha = 50$ and 70 degrees (points c and d in fig. 5.8) are shown in figs 5.10*c* and *d*. Although the value f_{ba3} for $\alpha = 50°$ is higher than that for $\alpha = 70°$ the transition point of the latter lies closer to the inner edge. This is caused by the fact that f_{tb} and f_{ta} decrease faster with increasing α than the bending antiresonant frequencies.

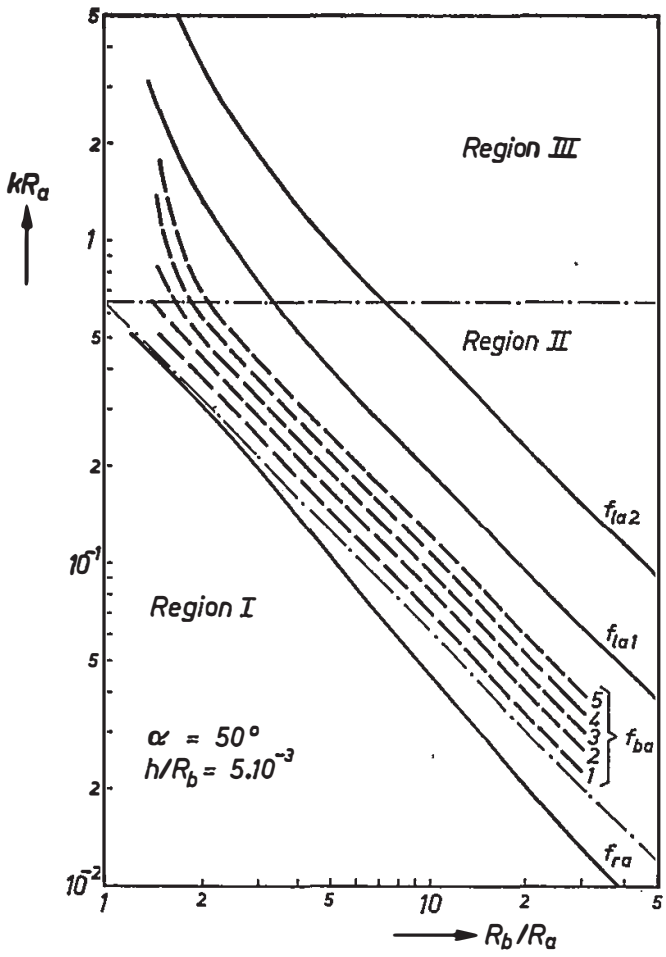

Fig. 5.9*a*. Calculated dependence of the ring antiresonant frequency f_{ra}, the lowest two longitudinal antiresonant frequencies (drawn curves) and the lowest five bending antiresonant frequencies (dashed) on R_b/R_a for $h/R_b = 5 \cdot 10^{-3}$ and $\alpha = 50°$.

5.6.3. *Influence of the ratio of outer- to inner-edge radius*

The dependence of five lowest bending antiresonant frequencies on R_b/R_a is shown in figs 5.9*a*, *b* and *c* for $\alpha = 50$, 60 and 70 degrees respectively and $h/R_b = 5 \cdot 10^{-3}$ (this value holds approximately for many practical loudspeaker cones). These figures show that for $R_b/R_a > 3$, the bending antiresonant frequencies are inversely proportional to R_b/R_a, which is predicted by eq. (5.34) for $f > f_{ta}$. The same holds for the longitudinal antiresonant frequencies (cf. fig. 4.19*b*). For $R_b/R_a < 3$ the higher bending antiresonant frequencies increase faster with decreasing R_b/R_a than the higher longitudinal antiresonant frequencies. The figures also show that in practice the ring antiresonant frequency f_{ra} can be approximated by the upper-boundary frequency f_{tb} of region I (lower dash-dotted lines in figs 5.9*a*, *b* and *c*). The displacement patterns at f_{ba3} for $\alpha = 50°$ and for $R_b/R_a = 2{\cdot}5$ and $R_b/R_a = 10$ are shown by figs 5.10*e* and *f* respectively (points e and f in fig. 5.9*b*). In general fig. 5.10 shows that the influence of the cone geometry on the longitudinal displacement patterns at f_{ba3} is rather small.

In the preceding sections the dependence of the lower bending antiresonant frequencies and the modes on the cone geometry was discussed. Calculations

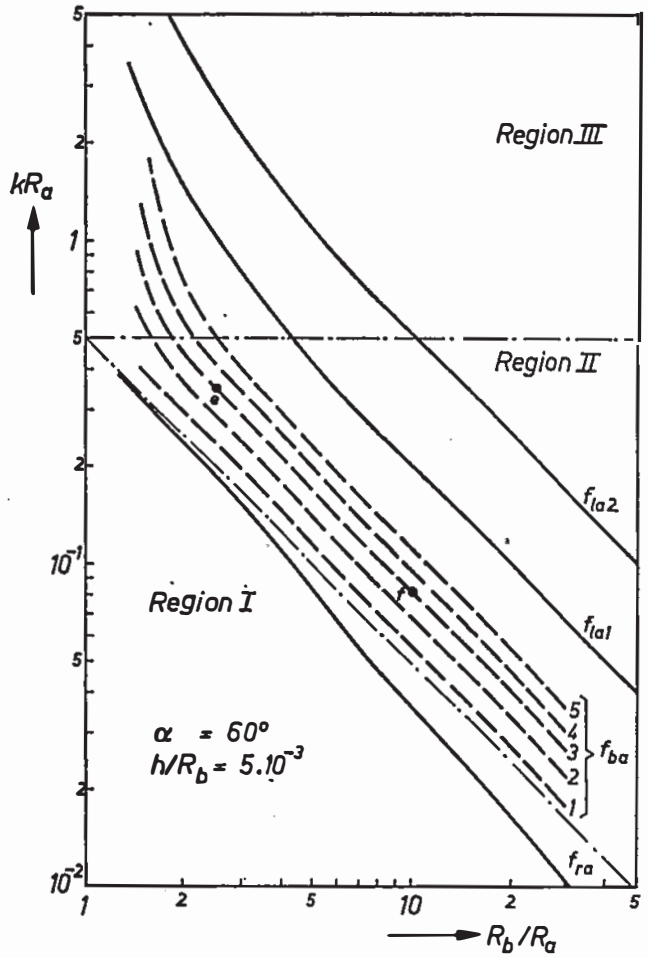

Fig. 5.9*b*. See legend to fig. 5.9*a*; $\alpha = 60°$.

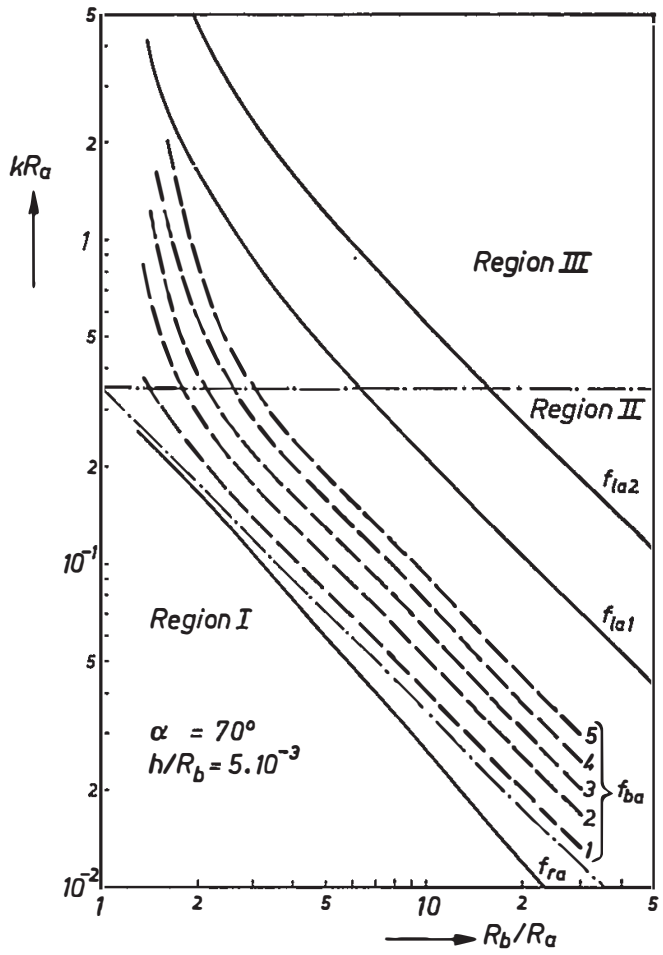

Fig. 5.9c. See legend to fig. 5.9a; $\alpha = 70°$.

on cones with other boundary conditions [19]) show that the boundary conditions have little influence on the bending antiresonant frequencies. In region II, a change of boundary conditions at the outer edge has much more influence on frequencies and modes than at the inner edge.

5.7. Frequency characteristic of the axial admittance

In this section the typical course of the frequency characteristic of the axial admittance Y_a at the inner edge, calculated with the general equations, will be discussed. On the basis of eq. (5.25) we introduce the reduced axial admittance y_a, defined by

$$y_a = \frac{Y_a}{Y_{lc}} \cos^2 \alpha. \tag{5.35}$$

Figure 5.11 shows the frequency characteristic of y_a of cone 50.3 for $\delta = 0$ in region I and the lower part of region II. At very low frequencies ($f \ll f_{tb}$), $|y_a|$ is inversely proportional to the frequency, according to the low-frequency approximation (eq. (5.28)):

$$Y_a \approx 1/j\omega M_d. \tag{5.36}$$

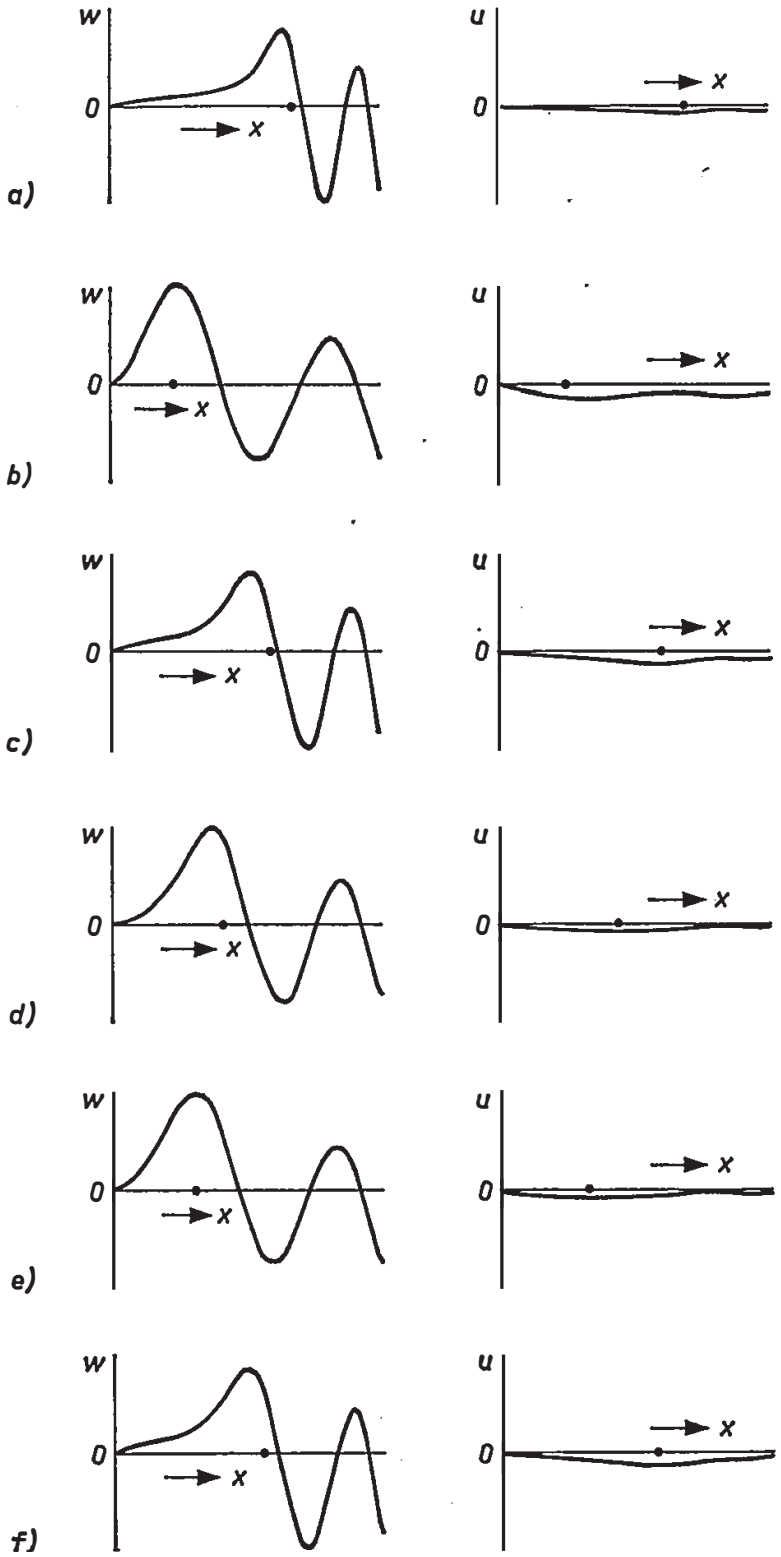

Fig. 5.10. Calculated transverse and longitudinal displacement patterns at the third bending antiresonant frequency f_{ba3} for various cone geometries; the characters in each figure correspond to those indicated in figs 5.7 to 5.9 (exact solution).

(*a*) $\alpha = 60°$, $R_b/R_a = 5$, $h/R_b = 1{\cdot}25 \cdot 10^{-3}$, (*d*) $\alpha = 70°$, $R_b/R_a = 5$, $h/R_b = 5 \cdot 10^{-3}$,
(*b*) $\alpha = 60°$, $R_b/R_a = 5$, $h/R_b = 2 \cdot 10^{-2}$, (*e*) $\alpha = 60°$, $R_b/R_a = 2{\cdot}5$, $h/R_b = 5 \cdot 10^{-3}$,
(*c*) $\alpha = 50°$, $R_b/R_a = 5$, $h/R_b = 5 \cdot 10^{-3}$, (*f*) $\alpha = 60°$, $R_b/R_a = 10$, $h/R_b = 5 \cdot 10^{-3}$.

Above the ring antiresonant frequency f_{ra} (1840 Hz), at which y_a becomes zero for the first time, bending resonances (at which $|y_a| = \infty$) and antiresonances (at which $y_a = 0$) appear. At each antiresonant frequency, another node appears at the inner edge which shifts to the outer edge when the frequency is further increased (cf. figs 5.4*d* through 5.4*i*).

As for the numerical calculations, the introduction of internal losses doubles the number of differential equations, bringing it to 12 for axisymmetric vibrations; the method of solution remains the same (see appendices A and B). Figure 5.12 shows $|y_a|$ as a function of frequency for cone 50.3 with $\delta = 0{\cdot}01$

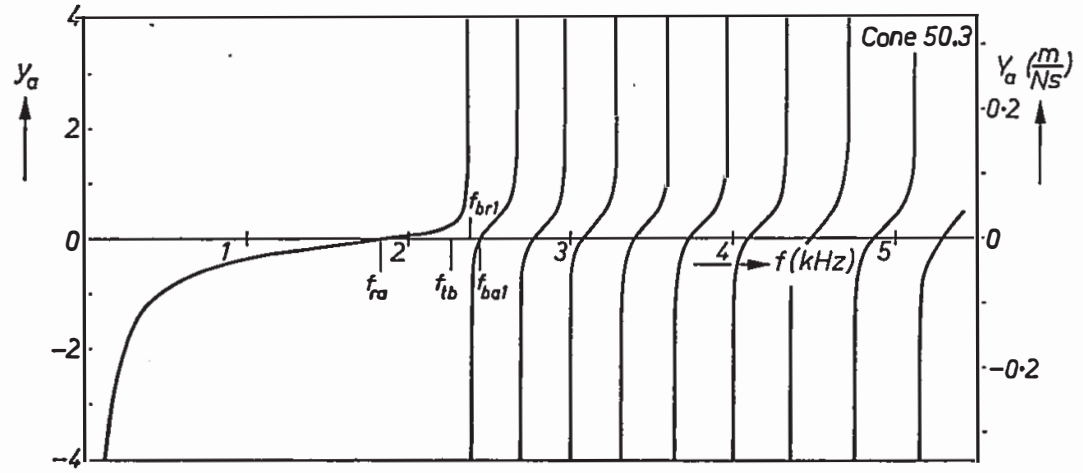

Fig. 5.11. Calculated frequency characteristic of the reduced axial admittance y_a of cone 50.3 for $\delta = 0$.

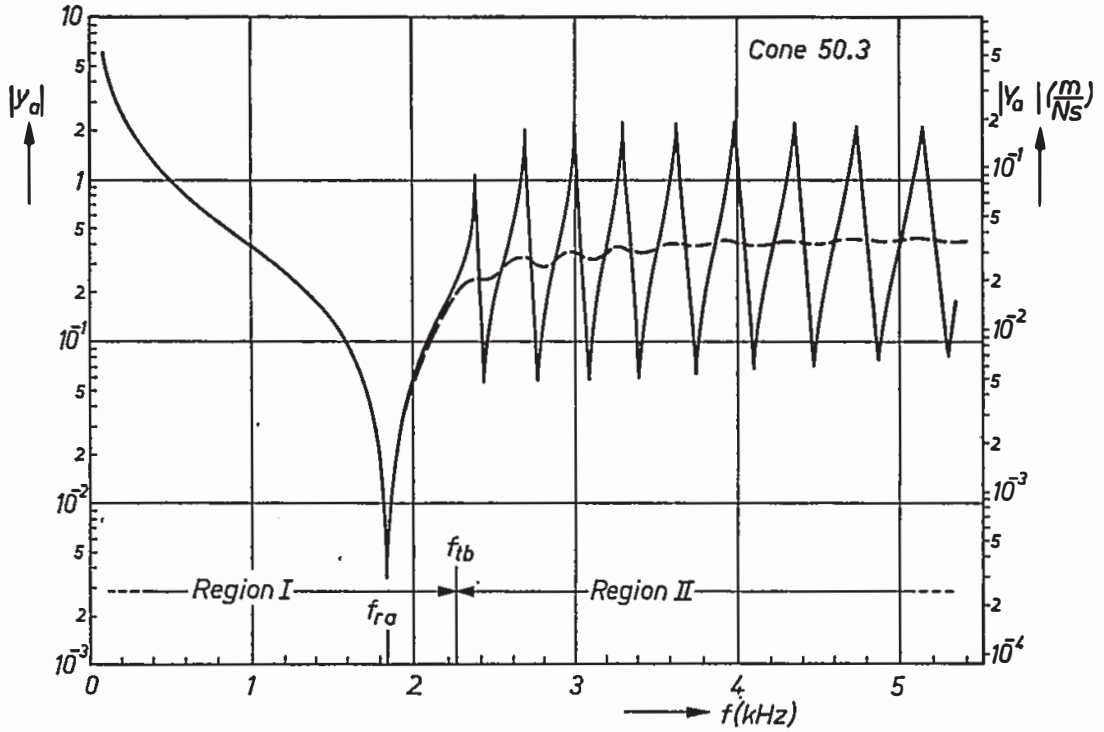

Fig. 5.12. Calculated frequency characteristics of the reduced axial admittance $|y_a|$ of cone 50.3 for $\delta = 0{\cdot}01$ (drawn curve) and $\delta = 0{\cdot}1$ (dashed curve).

(drawn curve) and $\delta = 0{\cdot}1$ (dashed curve). Figure 5.12 is more realistic than fig. 5.11: internal losses limit $|y_a|$ to finite values at resonant frequencies, whereas at antiresonant frequencies $|y_a|$ no longer becomes zero. In region II bending resonances and antiresonances cause $|y_a|$ to oscillate about a mean value, determined by Y_l (eq. (5.25)). The magnitude of these oscillations is proportional to $1/\delta k_B L$. This is well known from plate bending theory [9]) and can be easily explained by considering the ratio of the amplitude of the wave received back at the inner edge after reflection to that of the outgoing wave; this ratio decreases when either δ, k_B or L is increased, because the wave has to cover more wavelengths before arriving at the inner edge again. Consequently resonances and antiresonances cannot fully build up. It may also be explained by comparing the bandwidth of each bending resonance with the spacing between the bending resonant frequencies; if the former becomes greater than the latter, the oscillations practically disappear.

Figure 5.13 shows the frequency characteristic of $|y_a|$ of cone 50.3 for $\delta = 0{\cdot}1$ in a greater frequency interval. On the average, this characteristic follows the same course as that of fig. 4.15, which was calculated with the membrane equations. The only difference is the appearance of small oscillations (fine structure) in $|y_a|$ just above f_{tb}, which are caused by bending resonances and antiresonances. In region III, $|y_a|$ oscillates about the value 1, which is easily explained as follows. It was shown in sec. 5.4 that Y_a is determined by the longitudinal admittance Y_l; with eq. (5.25) we find

$$Y_a \approx Y_l/\cos^2 \alpha. \tag{5.37}$$

For high frequencies, $|Y_l|$ oscillates around a frequency-independent charac-

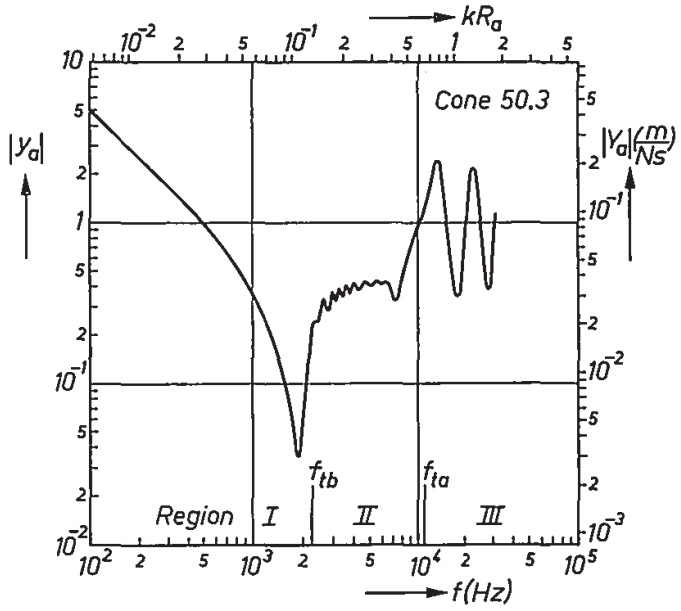

Fig. 5.13. Calculated frequency characteristic of the reduced axial admittance $|y_a|$ of cone 50.3 for $\delta = 0{\cdot}1$.

teristic value Y_{lc} (eq. (4.48)); these oscillations are caused by longitudinal resonances and antiresonances. The frequency average of $|Y_a|$ in region III is therefore

$$\langle |Y_a| \rangle = Y_{lc}/\cos^2 \alpha. \tag{5.38}$$

Hence

$$\langle |y_a| \rangle = 1 \tag{5.39}$$

in this region.

Figure 5.14 shows the frequency characteristic of $|y_a|$ of cone 50.1, which has a smaller thickness than cone 50.3. For this cone 50.1 the fine structure has fully disappeared, the characteristics of figs 4.15 and 5.14 are almost equal. In the latter figure the real part of y_a is shown dashed. This part is very small in region I, where bending is negligible; in region III, y_a becomes virtually real (the characteristic longitudinal impedance Z_{lc} is real and bending has a negligible influence since $Z_{tc} \ll Z_{lc}$, see sec. 5.4).

The influence of the cone geometrical and material parameters (except the thickness h) on y_a can therefore be examined by calculating y_l with the membrane equations. Of course, this may only be done as long as eq. (5.25) is satisfied. This is nearly always the case in practice. However, to compute the sound radiation in the next chapter we need in any case to calculate the exact transverse velocity distribution with the twelve general differential equations for a great number of frequencies. Further, to illustrate the influence of the cone geometry and material on the sound radiation these calculations must be carried out for various cones of different geometry. Therefore we may as well show the frequency characteristics of $|y_a|$ of these cones. In the following this is done for cone 50.1 of which one parameter is varied at a time.

5.7.1. *Influence of the thickness*

The influence of the cone thickness h on the axial admittance $|y_a|$ was discussed in the preceding sections: it has no influence on the frequency average of $|y_a|$ but merely influences the amplitude of the fine structure: this amplitude is proportional to $1/k_B$ or $h^{1/2}$ (eq. (5.10)). When h is sufficiently small, this fine structure completely disappears (cf. figs 5.13 and 5.14). The relatively small value of $h = 0{\cdot}1$ mm has therefore been chosen for the following cones to reduce the number of frequencies at which y_a has to be calculated. Further, to approximatively account for the rim damping and the radiation damping we take $\delta = 0{\cdot}1$, as discussed in sec. 4.7.4.

5.7.2. *Influence of the apex angle*

In sec. 4.7.5 the influence of an increasing semi-apex angle α on the frequency characteristic of $|y_l|$ was discussed; the meridional cone length L was kept constant. This resulted in a slight decrease of the ring antiresonant frequency f_{ra};

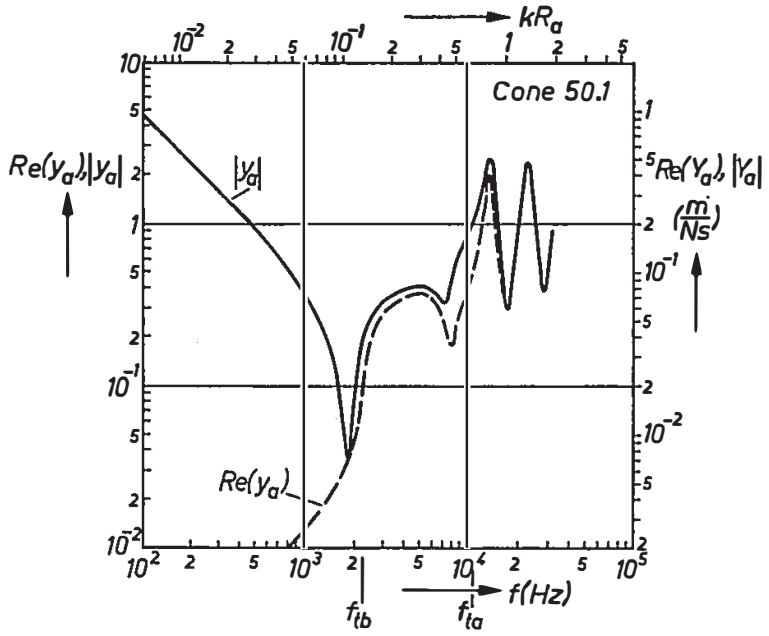

Fig. 5.14. Calculated frequency characteristic of the real part and the modulus of the reduced axial admittance y_a of cone 50.1.

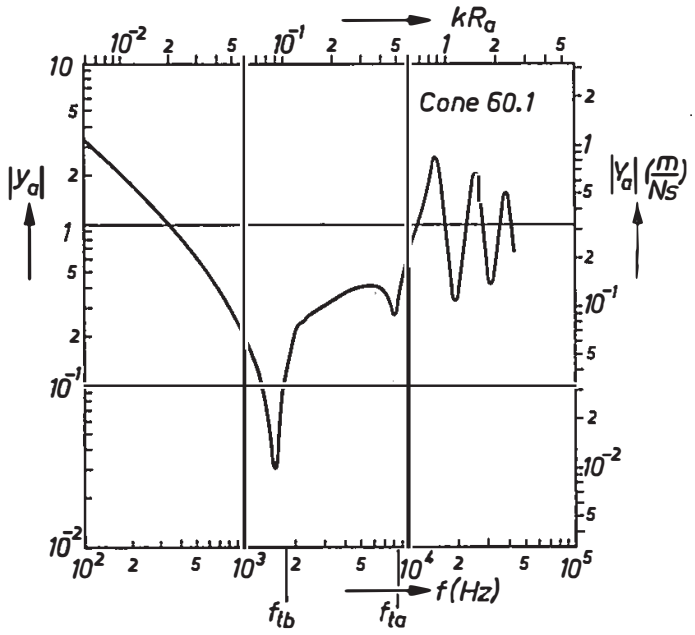

Fig. 5.15. Calculated frequency characteristic of the reduced axial admittance $|y_a|$ of cone 60.1.

the longitudinal resonant and antiresonant frequencies remained practically unaltered. To show the influence of α on the sound radiation it is more expedient, however, to keep the inner- and outer-edge radii R_a and R_b constant. A variation of α then implies a variation of L and a shift of all longitudinal resonant and antiresonant frequencies. The following examples will illustrate this.

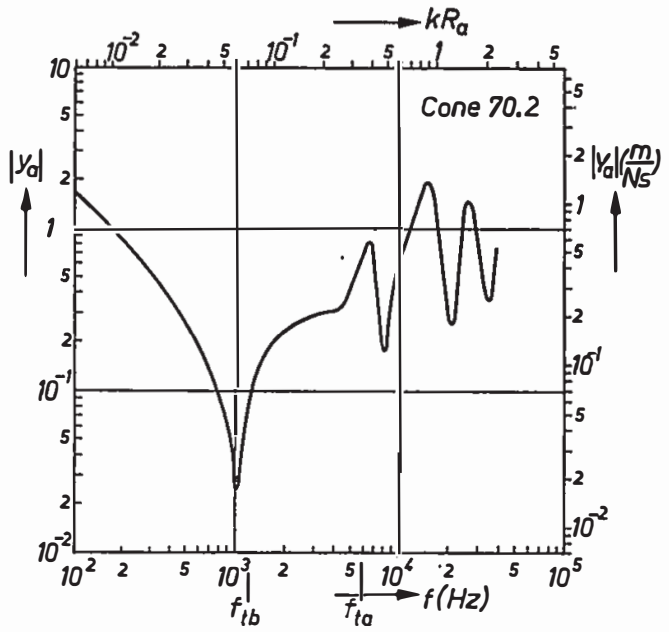

Fig. 5.16. Calculated frequency characteristic of the reduced axial admittance $|y_a|$ of cone 70.2.

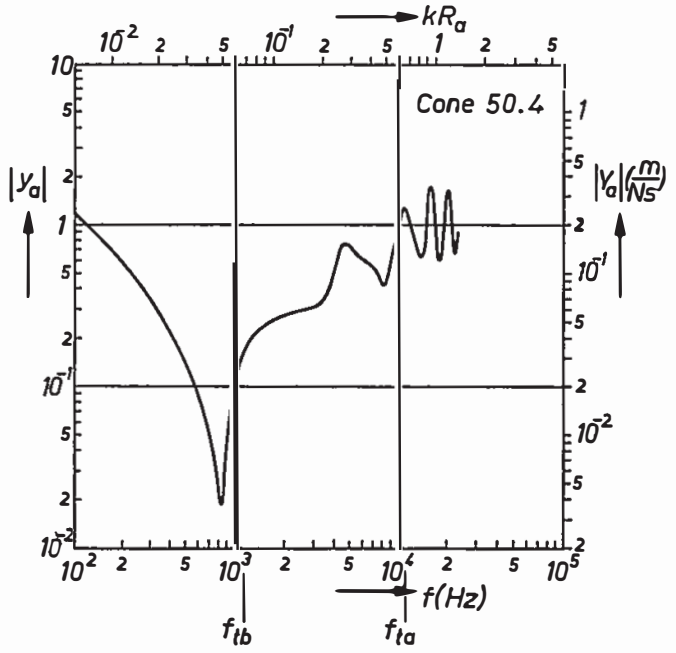

Fig. 5.17. Calculated frequency characteristic of the reduced axial admittance $|y_a|$ of cone 50.4.

The frequency characteristic of the reduced axial admittance $|y_a|$ of cone 60.1 is shown in fig. 5.15. Except for α, this cone has the same geometry and material parameters as cone 50.1 (see table 5-II). According to eqs (4.11) and (4.12) the values of f_{tb} and f_{ta} are lowered relative to those of cone 50.1 (cf. figs 5.14, 5.15). The same holds for f_{ra} lying just below f_{tb}. The longitudinal resonant and anti-resonant frequencies have increased due to the decrease of the meridional cone length L.

TABLE 5-II

Cone 60.1

geometry		material	
semi-apex angle	$\alpha = 60°$	Young's modulus	$E = 2 \cdot 10^9$ N/m^2
inner-edge radius	$R_a = 17$ mm	mass density	$\varrho = 600$ kg/m^3
outer-edge radius	$R_b = 83$ mm	Poisson's ratio	$\nu = 0{\cdot}3$
thickness	$h = 0{\cdot}1$ mm	loss factor	$\delta = 0{\cdot}1$

TABLE 5-III

Cone 70.2

geometry		material	
semi-apex angle	$\alpha = 70°$	Young's modulus	$E = 2 \cdot 10^9$ N/m^2
inner-edge radius	$R_a = 17$ mm	mass density	$\varrho = 600$ kg/m^3
outer-edge radius	$R_b = 83$ mm	Poisson's ratio	$\nu = 0{\cdot}3$
thickness	$h = 0{\cdot}1$ mm	loss factor	$\delta = 0{\cdot}1$

Because the cone mass M_d is decreased as well, the $|Y_a|$-curve is shifted upwards in region I. In regions II and III, $|Y_a|$ has increased by a factor $\cos^2 50°/\cos^2 60°$ (eq. (5.38)). Relative to the low-frequency curve the average high-frequency value of $|Y_a|$ of cone 60.1 is therefore higher than that of cone 50.1.

The above is further illustrated by fig. 5.16, which shows the frequency characteristic of $|y_a|$ for cone 70.2 (parameters in table 5-III). The frequencies f_{ra}, f_{tb} and f_{ta} of cone 70.2 are lower than those of the foregoing cones, whereas the longitudinal resonant and antiresonant frequencies are shifted upwards. The ring resonant frequency f_{rr} (6500 Hz) now falls above region II, which causes a distinct peak.

5.7.3. *Influence of the outer-edge radius*

To illustrate the influence of a variation of the ratio of the outer- to inner-edge radius R_b/R_a, the axial admittance $|y_a|$ is calculated for a cone with R_b twice that of cone 50.1. This cone, numbered 50.4, otherwise has the same parameters as cone 50.1, see table 5-IV. The doubling of R_b causes a halving of f_{ra} and f_{tb} (cf. figs 5.14, 5.17). Because the cone length L is approximately doubled relative to cone 50.1, the longitudinal resonant and antiresonant frequencies are also approximately halved (eqs (4.49) and (4.51)). The frequency f_{ta} remains

TABLE 5-IV

Cone 50.4

geometry		material	
semi-apex angle	$\alpha = 50°$	Young's modulus	$E = 2 \cdot 10^9$ N/m²
inner-edge radius	$R_a = 17$ mm	mass density	$\varrho = 600$ kg/m³
outer-edge radius	$R_b = 166$ mm	Poisson's ratio	$\nu = 0{\cdot}3$
thickness	$h = 0{\cdot}1$ mm	loss factor	$\delta = 0{\cdot}1$

unchanged. This results in an increase of region II, which now covers two longitudinal antiresonant frequencies, viz. $f_{la1} = 3500$ Hz and $f_{la2} = 8500$ Hz. The former is not clearly visible in fig. 5.17, because of the relatively high damping in region II; the ring resonance at about 3200 Hz is not visible either. For the same reason the height of the peak at the first longitudinal resonance (4500 Hz) is considerably reduced as compared with that of cone 50.1.

In the low-frequency region the value of $|Y_a|$ has decreased by a factor of 4 (influence of M_a). In region III, $|Y_a|$ oscillates around the same mean value as cone 50.1 (fig. 5.14), because Y_{lc} and α are not changed (eq. (5.38)). The amplitude of the oscillations around $|y_a| = 1$ is approximately halved since they are proportional to $1/\delta k_1 L$.

5.8. Membrane resonant frequencies

It was seen in sec. 4.7.3 that at certain frequencies the inner-edge displacement of the conical membrane is purely axial. At these so-called membrane resonant frequencies the inner edge can be radially supported without violating the membrane requirement (no resultant force in transverse direction). Since it is assumed in this chapter that the inner edge is radially supported, the cone exhibits a purely longitudinal resonance at these frequencies, which overshadows all bending effects.

This may be illustrated on the basis of the frequency characteristic of the strain-energy coefficient η (eq. (5.30)) of cone 50.3 for $\delta = 0$, shown in fig. 5.18. Below f_{ra} the cone is hardly bent at all and η is very low. After a sharp rise above f_{ra}, where bending waves appear, η asymptotically approaches 1. At the membrane resonant frequencies f_{mr} (7968, 17960, 28610 Hz), however, the characteristic shows a pronounced dip indicating that the strain energy caused by bending becomes very small. The displacement patterns at these frequencies are very well approximated by those calculated with the membrane equations; this will be illustrated in the next section.

The above frequencies f_{mr}, obtained with the exact equations by minimizing η, are slightly different from those calculated with the membrane equations. The

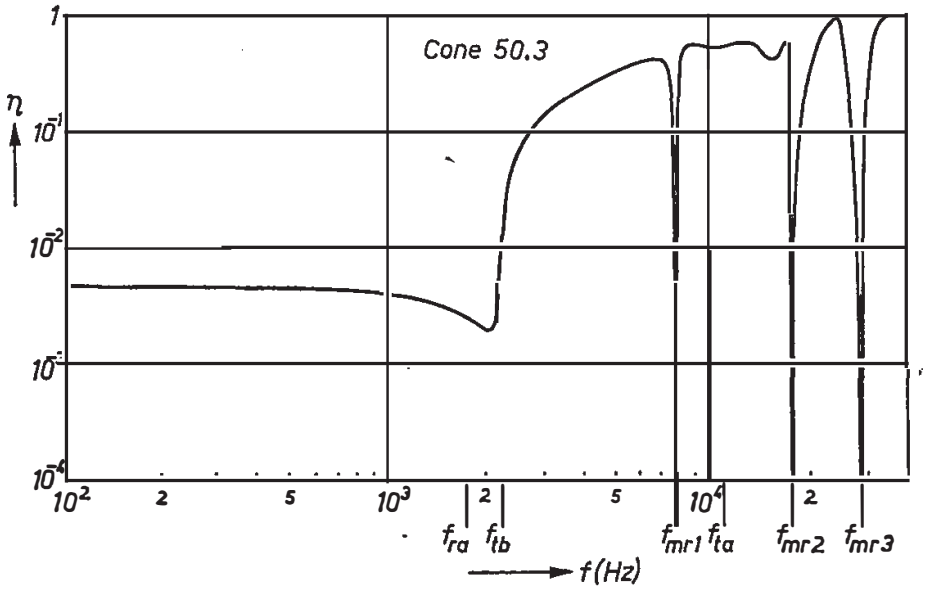

Fig. 5.18. Calculated frequency characteristic of the strain-energy coefficient η of cone 50.3 for $\delta = 0$.

difference is greater for f_{mr1} than for the higher frequencies because of the singularity on the cone. This difference decreases with increasing frequency. As shown in sec. 4.7.3 the higher membrane frequencies are practically equal to the longitudinal antiresonant frequencies.

5.9. Comparison of the exact solutions and the solutions obtained with the membrane approximation

It was shown in sec. 5.7 that the frequency characteristic of the reduced longitudinal admittance $|y_l|$ calculated with the membrane equations is a very good approximation of the frequency characteristic of the reduced axial admittance $|y_a|$ calculated with the exact equations (the moduli of Y_l and Y_a differ approximately by a factor $\cos^2 \alpha$). In this section, the transverse and longitudinal displacement patterns $w(x)$ and $u(x)$ of cone 50.1 calculated with the membrane equations (membrane patterns) are compared with those of cone 50.3 calculated with the exact equations (exact patterns), both for $\delta = 0$. Cone 50.3 is used here because its exact behaviour was already calculated in sec. 5.5. The fact that cone 50.1 is thinner than cone 50.3 has no influence on the shape of the membrane patterns. It should further be noted that, if the same driving force is used, the amplitudes of the exact patterns are a factor $1/\cos \alpha$ larger than the amplitudes of the membrane patterns owing to the different direction of the driving force.

To facilitate discussion, the characters u and w will be provided with the subscript m (for membrane) or e (for exact). Since only the shape of the patterns is important, the displacements are normalized by the maximum value of $w(x)$. At each frequency, $u_e(x)$ and $w_e(x)$ are drawn to the same scale, although these

scales are different for different frequencies (this was also done for the membrane patterns in chapter 4).

In region I the membrane patterns are a very good approximation of the exact patterns because bending effects are very small. The exact patterns $w_e(x)$ and $u_e(x)$ at $f = 1000$ Hz are shown in fig. 5.4*a*, which should be compared with the membrane patterns of fig. 4.7*a*. At the ring antiresonant frequency f_{ra} (1840 Hz) a small difference appears between membrane and exact patterns (cf. figs 4.8*a*, 5.4*b*): the rigid inner edge forces $w_e(a)$ to zero at all frequencies where $u_e(a)$ becomes zero (eq.(5.12a)). At the membrane approximation the inner edge is free in the transverse direction (see sec. 4.5); therefore $w_m(a)$ attains a small but nonzero value. The difference between the membrane and the exact patterns increases when the lower boundary of region II is approached. However, even at 2200 Hz the agreement is still good (cf. figs 4.9*a*, 5.4*c*).

In regions II and III the displacement patterns in general differ considerably. In region II the membrane patterns show a singularity at the transition point x_t, whereas the exact patterns show bending waves for $x > x_t$. This is illustrated in fig. 5.19, which shows $w_m(x)$ and $u_m(x)$ for cone 50.3 at 3083 Hz. These patterns should be compared with the exact patterns of fig. 5.4*i*; both figures are drawn to the same scale. The longitudinal displacement patterns closely resemble each other; there is some resemblance in the transverse displacement patterns for $x < x_t$, where longitudinal stresses predominate.

At the longitudinal antiresonant frequencies, $u_e(x)$ is equal to $u_m(x)$ (besides a sharp singularity of $u_m(x)$ at x_t in region II). This is illustrated by fig. 5.20, which

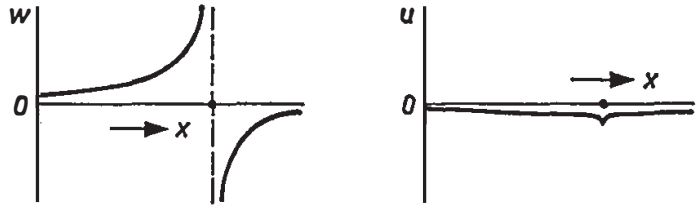

Fig. 5.19. Calculated transverse and longitudinal displacement patterns of cone 50.3 with $\delta = 0$ at 3083 Hz (membrane solution, cf. the exact solution of fig. 5.4*i*).

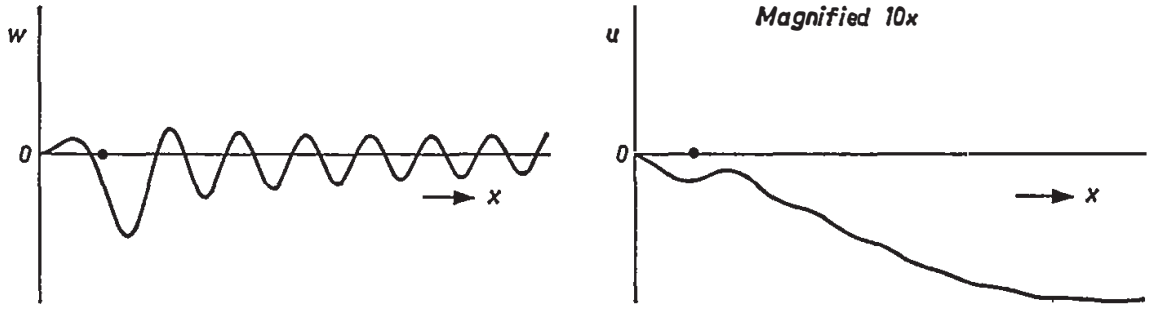

Fig. 5.20. Calculated transverse and longitudinal displacement patterns of cone 50.3 with $\delta = 0$ at the first longitudinal antiresonant frequency $f_{la1} = 7513$ Hz (exact solution, cf. the membrane solution of fig. 4.10*a*).

shows $w_e(x)$ and $u_e(x)$ at the first longitudinal antiresonant frequency f_{la1}; these patterns should be compared with the membrane solutions of fig. 4.10. The transverse displacement patterns $w_e(x)$ and $w_m(x)$ differ considerably.

At the membrane resonant frequencies f_{mr} the cone exhibits a pure longitudinal resonance with negligible bending; both $w_m(x)$ and $u_m(x)$ are then excellent approximations of $w_e(x)$ and $u_e(x)$ (except $w_m(x)$ for $x \approx x_t$ in region II). This is illustrated by fig. 5.21, which shows the exact patterns at f_{mr1}. These mode shapes should be compared with the membrane patterns of fig. 4.13*a*. The exact patterns at the higher membrane resonances are equal to the membrane patterns (figs 4.13*b* and *c*).

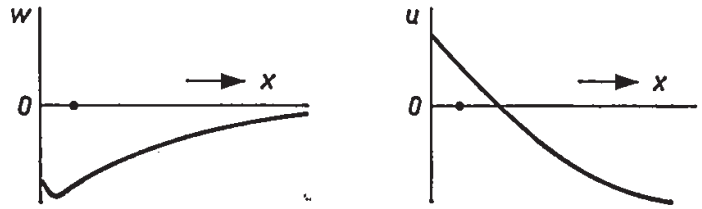

Fig. 5.21. Calculated transverse and longitudinal displacement patterns of cone 50.3 with $\delta = 0$ at the first membrane resonant frequency $f_{mr1} = 7968$ Hz (exact solution, cf. the membrane solution of fig. 4.13*a*).

For small values of n the transverse displacement patterns $w_e(x)$ at f_{mrn} and f_{lan} differ considerably owing to the appearance of bending waves at f_{lan}. As n increases and f_{mrn} approaches f_{lan} the amplitude of the bending wave decreases and the patterns $w_e(x)$ show an increasing resemblance at these frequencies. The longitudinal displacement patterns $u_e(x)$ at f_{mrn} and f_{lan} always resemble one another closely owing to the small influence of the bending waves at f_{lan} on $u_e(x)$.

If there are internal losses, the cone cannot build up a pure longitudinal resonance at the membrane resonant frequencies: the displacements caused by longitudinal wave motion become lower. In that case bending waves become visible as a superposition on the longitudinal wave (figs 5.22*a* and *b*). Nevertheless, the amplitude of the transverse displacement caused by the longitudinal wave remains relatively high compared to the amplitude of the bending wave. Because the former displacement has a relatively long wavelength, it considerably influences the sound radiation, as will be shown in the next chapter.

We may summarize the foregoing as follows. The frequency characteristic of the mechanical admittance of the cone, calculated with the membrane equations is a good approximation of the exact characteristic apart from some small deviations in region II, which disappear for a sufficiently high loss factor. As the vibration patterns are concerned, the membrane approximation is rather good in region I. In general, however, it leads to wrong results in regions II and III.

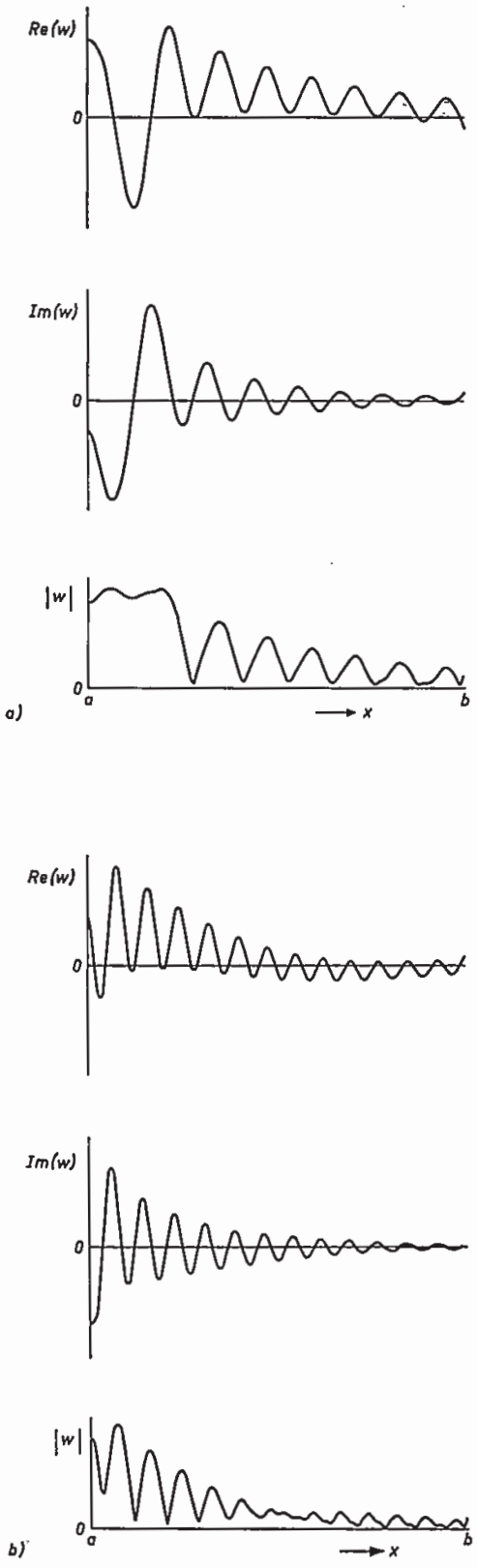

Fig. 5.22. Calculated transverse displacement patterns (exact solution) of cone 50.3 with $\delta = 0{\cdot}1$ at the membrane resonant frequencies
(*a*) $f_{mr1} = 7968$ Hz, (*b*) $f_{mr2} = 17960$ Hz.

5.10. Influence of the voice-coil mass on the frequency characteristic of the axial admittance

In all preceding calculations the mass of the voice coil and of other parts attached to the inner edge has been omitted. The influence of this additional mass is relatively easy to describe on the basis of the equivalent circuit of the electrodynamic loudspeaker, shown in fig. 3.1*a*. The compliances of the inner and outer suspensions C_{is} and C_{os} as well as the mechanical resistance R_s have a negligible influence since we assume the driving frequency to lie far above the fundamental resonant frequency f_0 of the loudspeaker mass-spring system. The total mechanical impedance Z_{tot} is

$$Z_{tot} = Z_a + j\omega M_c \tag{5.40}$$

where M_c is the voice-coil mass with inclusion of all other additional masses at the inner edge (inner suspension, dust cap). Figure 5.23 shows the absolute value of the axial impedance Z_a of cone 50.3 with mass M_d and the mechanical reactance ωM_c of the voice coil for $M_c = M_d/2$ and $M_c = M_d/4$ as a function of frequency.

The frequency characteristic of $|Z_{tot}|$ of cone 50.3 with $M_c = M_d/4$ is shown in fig. 5.24. Below the frequency at which $|Z_a|$ and ωM_c intersect in fig. 5.23, $|Z_{tot}|$ has the same shape as $|Z_a|$ and is only shifted upwards. At very low frequencies ($f \ll f_{ra}$), Z_{tot} remains proportional to the frequency; then

$$Z_{tot} = j\omega\,(M_c + M_d).$$

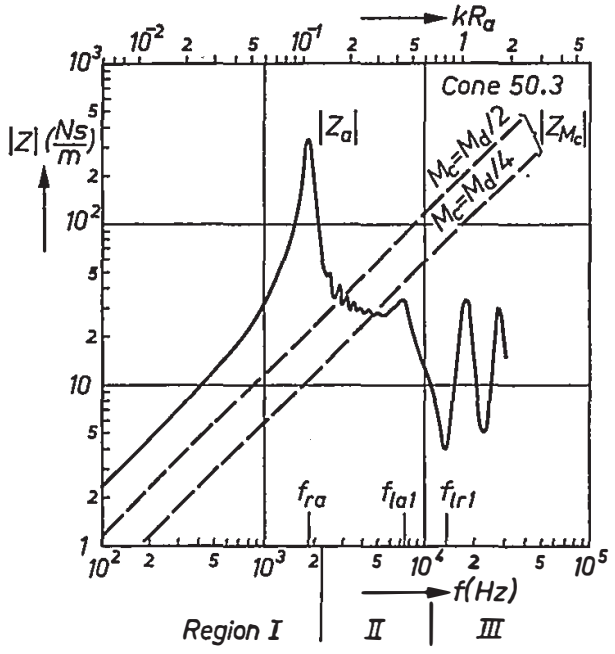

Fig. 5.23. Comparison of the calculated mechanical impedances of cone 50.3 with mass M_d and a voice coil with mass $M_c = M_d/2$ and $M_c = M_d/4$.

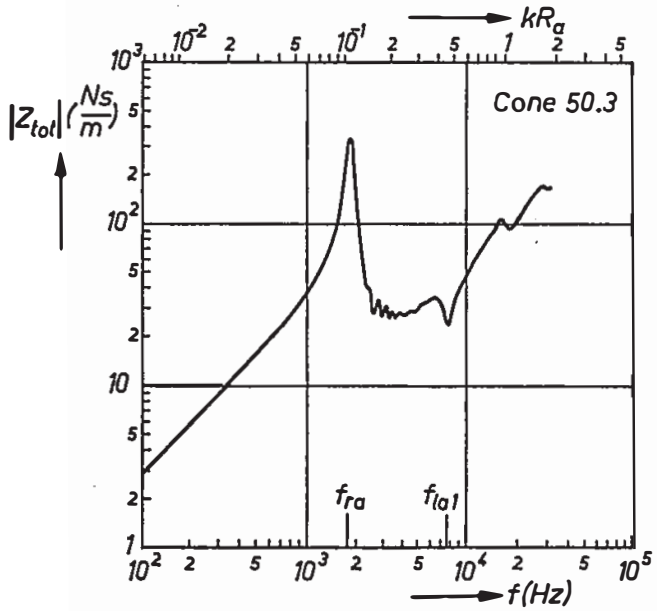

Fig. 5.24. Calculated frequency characteristic of the total mechanical impedance $|Z_{tot}|$ of cone 50.3 with $M_c = M_d/4$.

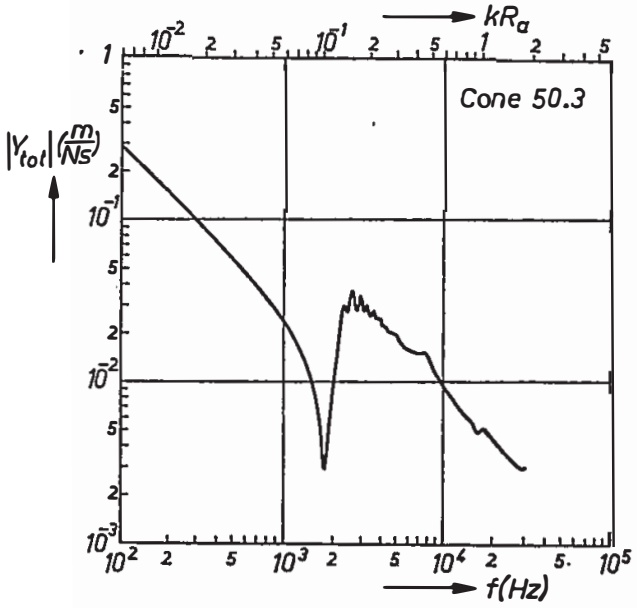

Fig. 5.25. Calculated frequency characteristic of the total mechanical admittance $|Y_{tot}|$ of cone 50.3 with $M_c = M_d/2$.

Above the frequency at which $|Z_a|$ and ωM_c are equal, $|Z_{tot}|$ is determined by ωM_c and the mean value therefore increases in proportion to the frequency; peaks and dips in $|Z_a|$ only appear as small disturbances in $|Z_{tot}|$. The maxima in $|Z_a|$ at f_{la1}, f_{la2}, etc., fall at somewhat lower frequencies in the frequency characteristic of $|Z_{tot}|$. A further influence of M_c is that the minima in $|Z_{tot}|$ do not at all coincide with the minima in $|Z_a|$ at the longitudinal resonant frequencies.

Figure 5.25 shows the total mechanical admittance $|Y_{tot}|$ of cone 50.3 with

$M_c = M_d/2$ as a function of frequency. On the average, $|Y_{tot}|$ decreases by 6 dB per octave over the whole frequency range, except at f_{ra} where a sharp rise occurs. These figures illustrate the dominant influence of an additional mass in the middle- and high-frequency region: the shape of the $|Y_a|$ characteristic is completely changed (cf. figs 5.13, 5.25).

5.11. Asymmetric vibrations

In the foregoing only axisymmetric vibrations have been discussed. If the loudspeaker cone were perfectly homogeneous and rotationally symmetric and if the driving force were uniformly applied at the inner edge and perfectly parallel to the cone axis, then indeed no asymmetric vibrations would occur. However, in practice, misalignment of the cone and the voice-coil axis as well as inhomogeneities excite waves travelling in both azimuthal directions, which at certain frequencies cause asymmetric standing waves with radial nodal lines. The latter are superposed on the symmetric standing waves with circular nodal lines.

By analogy with the wave types on a cylinder [20]) we may distinguish between asymmetric bending, extensional and torsional waves. Only the first-mentioned type is important here because of its significant transverse amplitude. The other wave types have predominant amplitudes in the meridional and azimuthal directions respectively. Asymmetric standing waves of the bending type occur at natural frequencies which are much lower than the symmetric ones because of (1) the low bending stiffness and (2) the absence of a transition frequency, as encountered with the symmetric waves, above which the bending resonances can only occur.

This is illustrated by our calculations on cone 52.1 (parameters in table 5-V).

TABLE 5-V

Cone 52.1

geometry	material
semi-apex angle $\alpha = 52°$	Young's modulus $E = 2 \cdot 10^9$ N/m²
inner-edge radius $R_a = 17$ mm	mass density $\varrho = 600$ kg/m³
outer-edge radius $R_b = 83$ mm	Poisson's ratio $\nu = 0{\cdot}3$
thickness $h = 0{\cdot}3$ mm	loss factor $\delta = 0$

The natural frequencies for asymmetric bending vibrations are calculated on the basis of the eight general differential equations for forced asymmetric vibration (appendix A). In principle, the same boundary conditions as in the symmet-

ric case are applied, viz. an inner edge which can only move axially *) and to which the cone is clamped, and a free outer edge.

In order to calculate the eigenfrequencies we assume the driving force to vary sinusoidally over the circumference of the inner edge:

$$F_a = F_{an} \cos(n\theta). \tag{5.41}$$

The boundary conditions read:

$$u_n(a) \sin\alpha + w_n(a) \cos\alpha = 0, \tag{5.42}$$

$$v_n(a) = 0, \tag{5.43}$$

$$\beta_{xn}(a) = 0, \tag{5.44}$$

$$Q_{xn}(a) \sin\alpha - N_{xn}(a) \cos\alpha = \frac{F_{an}}{2\pi R_a}, \tag{5.45}$$

$$Q_n(b) = N_{xn}(b) = N_n(b) = M_{xn}(b) = 0. \tag{5.46}$$

Note that in the latter equation the effective shear resultants N_n and Q_n are used because of the free-edge condition [18]). For several values of the circumferential wavenumber n the axial admittance Y_{an}, defined by

$$Y_{an} = j\omega\,[u_n(a) \cos\alpha - w_n(a) \sin\alpha]/F_{an} \tag{5.47}$$

is calculated as a function of frequency; this yields the resonant ($|Y_{an}| = \infty$) and antiresonant ($|Y_{an}| = 0$) frequencies. However, in this process we assumed that the asymmetrical standing waves were provided by a sinusoidally distributed axial driving force at the inner edge. In practice, these waves will mainly be due to cone inhomogeneities **), and the relatively rigid inner edge will not in effect be deformable. Since the inner edge is not deformed at the antiresonant frequencies ($|Y_{an}| = 0$), the natural frequencies for asymmetric vibrations excited by inhomogeneities on a cone with a rigid inner edge will be the above-mentioned asymmetric antiresonant frequencies.

Figure 5.26 shows these natural frequencies f_{nm} for cone 52.1 plotted as a function of n, indicating the number of nodal diameters of the asymmetric mode. The value of m indicates the number of nodal circles without that on the inner edge. On the ordinate ($n = 0$) the symmetric bending antiresonant frequencies are encountered. Asymmetric natural frequencies appear at much lower frequencies. For cone 52.1 the lowest asymmetric natural frequency lies at about

*) Note that this condition cannot be represented by a rigid massless ring at the inner edge (see sec. 5.4) since the axial displacement varies with $\cos(n\theta)$.

**) An exception occurs if cone and voice-coil axis are misaligned; then the inner edge is submitted to a bending moment varying with $\cos\theta$.

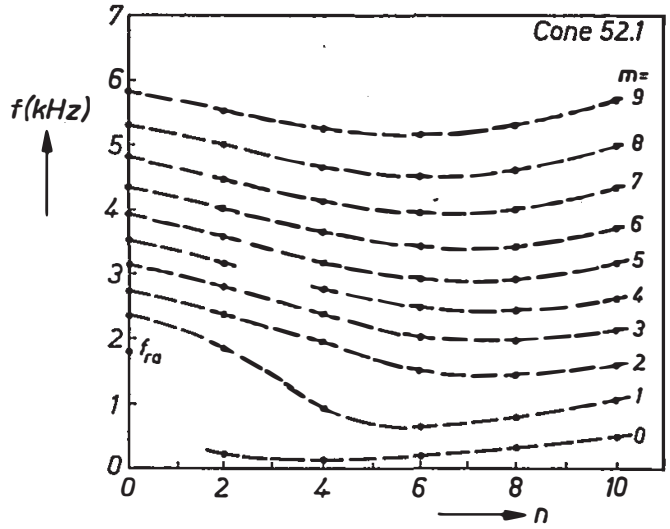

Fig. 5.26. Calculated natural frequencies for asymmetric bending vibrations of cone 52.1 with a clamped inner edge; n is the number of nodal diameters, m the number of nodal circles (excluding the one at the inner edge).

120 Hz. The cone then shows an asymmetric vibration pattern with four nodal diameters, one nodal circle at the inner edge and an antinode at the outer edge. When the driving frequency is raised, many natural frequencies are passed; inhomogeneities will excite asymmetric vibration patterns with a certain number of nodal diameters that changes with frequency. Asymmetric vibrations will not be discussed in any further detail since their influence on the sound radiation is negligible (chapter 6). Further approximative calculations on asymmetric vibrations of cones can be found inter alia in ref. 21.

5.12. Measurements

Measurements have been carried out on a few cones mainly to verify the foregoing calculations. These measurements comprise the recording of the motional impedance as a function of frequency and the holographic visualization of vibration patterns.

5.12.1. *Comparison of calculated and measured motional impedances*

The motional impedance of three plastic (CAB*)) truncated loudspeaker cones was measured as a function of frequencywith the circuit shown in fig. 3.3. These cones differ in several parameters (table 5-VI), but have other parameters in common (table 5-VII).

The value of Young's modulus E was obtained experimentally from the following adjustment procedure applied to cone 60.2e. The first bending anti-resonant frequency f'_{ba1} was calculated for an arbitrary value E' of Young's modulus and $\delta = 0$. Then f_{ba1} was measured from the recorded motional

*) CAB stands for cellulose-aceto-butyrate.

TABLE 5-VI
Cones 50.5e, 60.2e and 70.3e

	α (°)	h (mm)	M_c/M_d
cone 50.5e	50	0·27	0·24
cone 60.2e	60	0·26	0·28
cone 70.3e	70	0·28	0·28

TABLE 5-VII
Cones 50.5e, 60.2e and 70.3e

geometry	material (CAB)
inner-edge radius $R_a = 17$ mm outer-edge radius $R_b = 83$ mm	Young's modulus $E = 2{\cdot}2 \cdot 10^9$ N/m² mass density $\varrho = 1160$ kg/m³ Poisson's ratio $\nu \approx 0{\cdot}34$ loss factor $\delta \approx 0{\cdot}06$

impedance (fig. 5.27*a*). Since all resonant and antiresonant frequencies are proportional to the square root of Young's modulus, E was found from

$$E = \left(\frac{f_{ba1}}{f'_{ba1}}\right)^2 E', \tag{5.48}$$

where the influence of δ on the measured value of f_{ba1} is neglected.

Finally, the motional impedance was recorded as a function of frequency for the cone vibrating in vacuum (100 Pa) without outer suspension. Of course the above procedure could also be applied to the first longitudinal antiresonant frequency, but the minimum in the measured curve at the latter frequency is broader, which leads to a less accurate value of E.

The motional impedance is calculated using the equation

$$|Z_{mot}| = (B\,l)^2\,|Y_{tot}| \tag{5.49}$$

where Y_{tot} follows from eq. (5.40). The value of the electromechanical conversion factor $(B\,l)^2$ of the driving system is obtained with eq. (3.7a) by measuring the motional impedance of cone 60.2e at 200 Hz. We find

$$(B\,l)^2 = 20 \text{ Wb}^2/\text{m}^2.$$

Since the same electrodynamic driving system is used in all measurements, this value is maintained in all subsequent calculations.

The measured frequency characteristics of $|Z_{mot}|$ of the above experimental

TABLE 5-VIII
Cones 50.5, 60.2 and 70.3

	α (°)	h (mm)	M_c/M_d
cone 50.5	50	0·23	0·24
cone 60.2	60	0·26	0·28
cone 70.3	70	0·1	0·28

TABLE 5-IX
Cones 50.5, 60.2, and 70.3

geometry	material
inner-edge radius $R_a = 17$ mm outer-edge radius $R_b = 83$ mm	Young's modulus $E = 2{\cdot}2 \cdot 10^9$ N/m² mass density $\varrho = 1160$ kg/m³ Poisson's ratio $\nu = 0{\cdot}3$ loss factor $\delta = 0{\cdot}1$

cones are compared with the calculated curves of the cones 50.5, 60.2 and 70.3 (see table 5-VIII); the latter cones have the parameters of table 5-IX in common. As these cones will also be used to compare calculated and measured radiation characteristics in chapter 6, the theoretical loss factor δ is taken higher than the measured value to account for additional rim and radiation damping, as explained in sec. 4.7.4. The difference between the theoretical and measured Poisson's ratios has a negligible influence; a theoretical value $\nu = 0{\cdot}3$ is taken because the $Z_a(f)$ characteristics of cones 50.3 and 70.2 have already been calculated with this value *). The latter cones only differ from cones 50.5 and 70.3 in their values of E and ϱ. Therefore the $Z_a(f)$ characteristics of the latter cones can easily be obtained from the characteristics of cones 50.3 and 70.2 already calculated (figs 5.13, 5.16), since all frequencies are proportional to $c = (E/\varrho)^{1/2}$ and Z_a is proportional to ϱc. The remaining difference in thickness between the calculated and measured 50° and 70° cones is of minor importance, as shown in sec. 5.7.1. Although the theoretical and experimental cone masses differ, the measured ratio M_c/M_d is constantly used in the calculations in order to keep the influence of M_c on the shape of the characteristics equal.

We will first compare the calculated characteristic of cone 60.2 with the measured curve of cone 60.2e (fig. 5.27*a*) because these cones only differ in their values of ν and δ. In the following graphs the calculated curves are dashed. The drawn curve of fig. 5.27*a*, measured in vacuum, shows a peak at the fun-

*) In view of the large computing times required, computations carried out previously are used as much as possible.

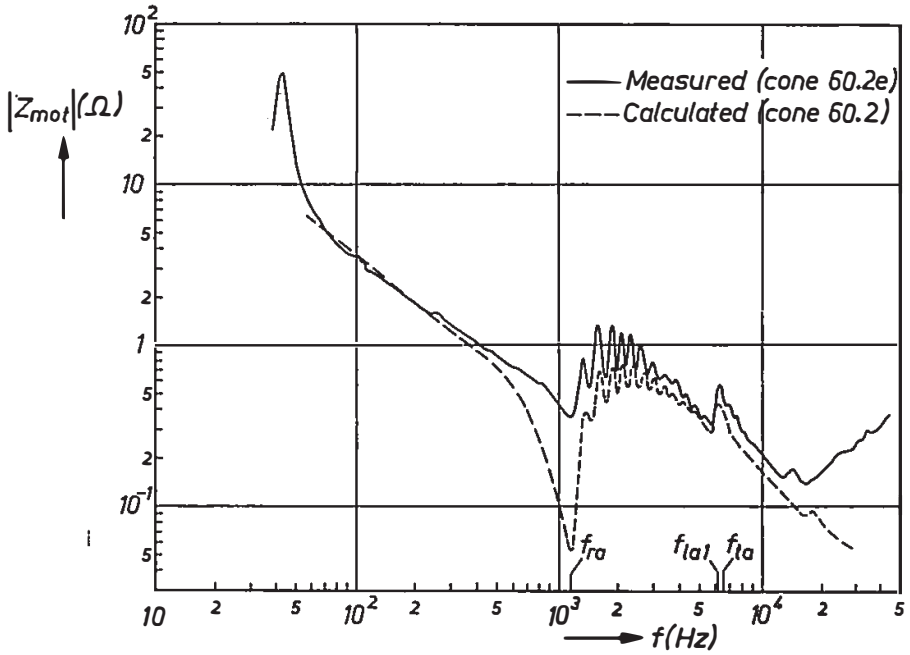

Fig. 5.27*a*. Calculated (cone 60.2, dashed) and measured (cone 60.2e, drawn curve) frequency characteristics of the motional impedance $|Z_{mot}|$ in vacuum.

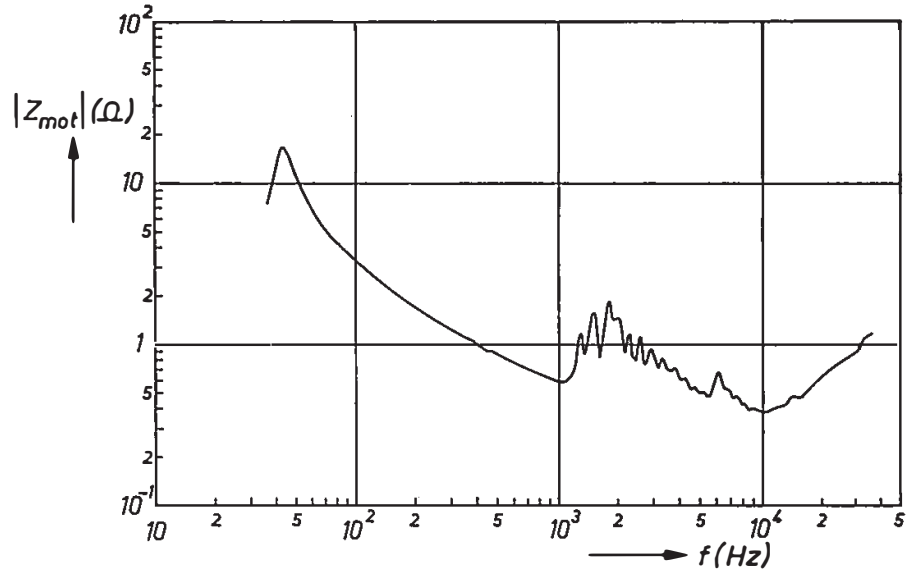

Fig. 5.27*b*. Measured frequency characteristic of the motional impedance of cone 60.2e vibrating in air.

damental resonant frequency f_0 ($\approx$ 40 Hz) of the loudspeaker mass-spring system (eq.(3.4)). Above f_0, calculated and measured curves decrease with increasing frequency (eq.(3.7a)). The measured minimum at f_{ra} is less deep than the calculated one, presumably because the inner edge is not completely rigid. The amplitudes of the oscillations above f_{ra} (fine structure) in the calculated curve are somewhat smaller because of the assumed higher loss factor.

Table 5-X shows the calculated longitudinal and bending antiresonant frequencies of cone 60.2 for $\delta = M_c = 0$ and the measured values (minima in fig. 5.27*a*) of cone 60.2e. It should be recalled that the calculated and measured values of f_{ba1} were made equal by adjusting the value of E.

TABLE 5-X
Cones 60.2 and 60.2e

	calculated values cone 60.2 (Hz)	measured values cone 60.2e (Hz)	deviation (%)
f_{ra}	1121	1190	6
f_{ba1}	1463	1465	—
f_{ba2}	1733	1730	—
f_{ba3}	2003	2005	—
f_{ba4}	2279	2275	—
f_{ba5}	2576	2579	—
f_{ba6}	2894	2912	1
f_{ba7}	3238	3262	1
f_{ba8}	3607	3685	2
f_{ba9}	4004	4140	3
f_{ba10}	4436	4689	6
f_{ba11}	4915	5288	8
f_{la1}	5800	5808	—

The deviations between calculated and measured values of f_{ba} increase with increasing frequency. They may be caused by the decreasing accuracy of the measuring circuit with increasing frequency, by the fact that Young's modulus of plastics is frequency-dependent and finally by the fact that the antiresonant frequencies are calculated for $\delta = M_c = 0$.

In fig. 5.27*a* as well as in all following figures the indicated values of f_{ra} and f_{la1} are calculated for $M_c = 0$; a nonzero value of M_c shifts the minimum at f_{la1} to a somewhat lower frequency. Just above f_{la1} a maximum appears; this is not a resonance but merely the influence of M_c (at this point the mechanical reactance ωM_c starts to dominate). Deviations between the calculated and measured curves may be caused by differences between the test and the reference loudspeakers (see sec. 3.3). Above 15 kHz the inner edge, not being completely rigid as assumed in the calculations, introduces additional compliance; this causes the measured motional impedance to increase.

Figure 5.27*b* shows the frequency characteristic of the motional impedance of cone 60.2e vibrating in air. The characteristic is not fundamentally different from the one in vacuum, except that all longitudinal and bending resonant and

antiresonant frequencies are decreased by the air-mass loading on the cone surface. This decrease varies from about 8 % at the lower boundary of region II to less than 4 % at the upper boundary of this region. The effect of the radiation damping on the bandwidths of the bending resonances is small because the internal material damping of the plastic is already relatively high.

Figure 5.28 shows the calculated motional impedance of cone 50.5 and the measured characteristic of cone 50.5e. These cones differ in thickness, which

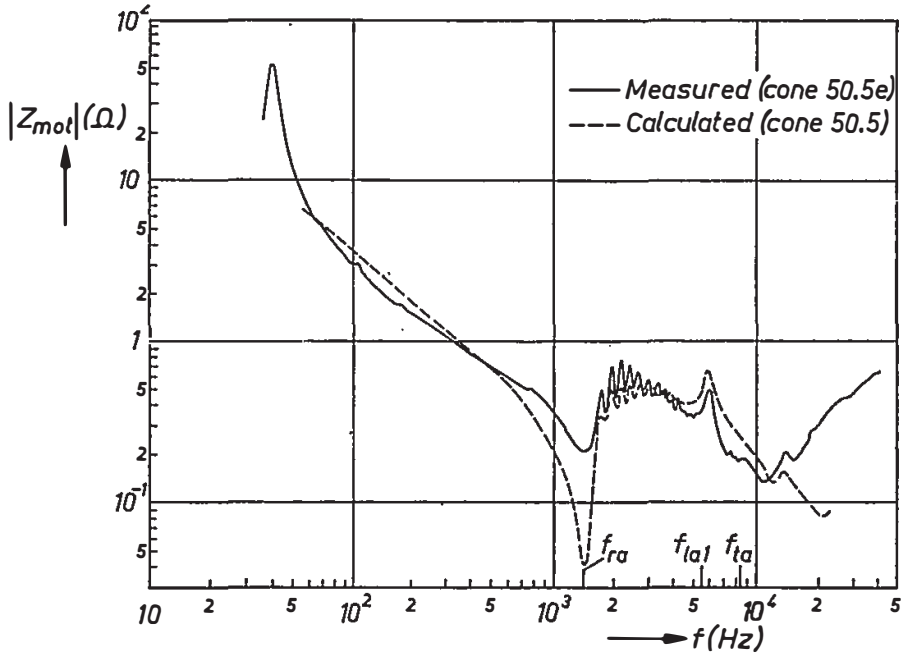

Fig. 5.28. Calculated (cone 50.5, dashed) and measured (cone 50.5e, drawn curve) frequency characteristics of the motional impedance $|Z_{mot}|$ in vacuum.

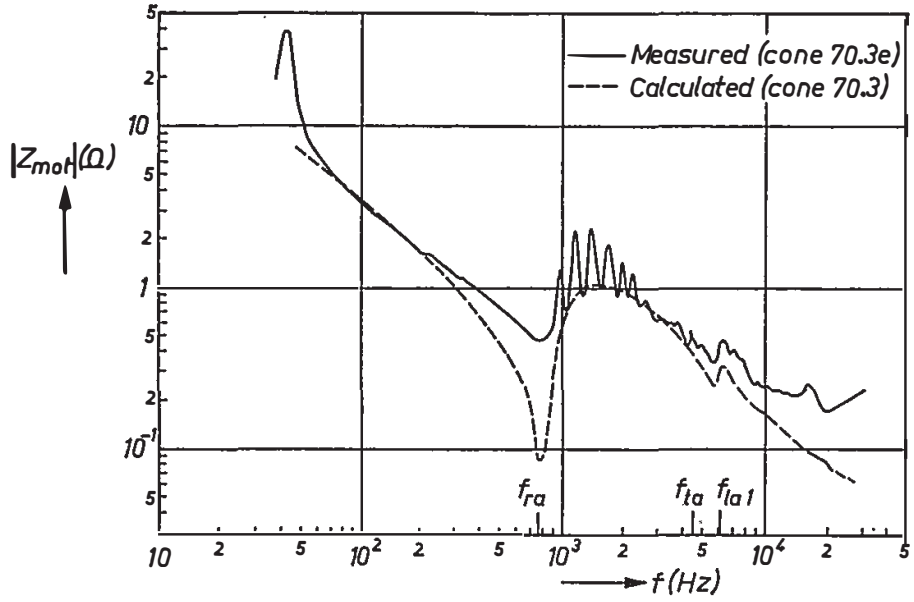

Fig. 5.29. Calculated (cone 70.3, dashed) and measured (cone 70.3e, drawn curve) frequency characteristics of the motional impedance $|Z_{mot}|$ in vacuum. The calculated curve is shifted downward by a factor 2·8 to account for the difference in thickness.

has no influence on the longitudinal antiresonant frequencies and mean shape of the curves. The calculated curve runs somewhat higher than the measured one because of the smaller thickness ($Z_{mot} \propto h$).

Figure 5.29 shows the calculated motional impedance of cone 70.3 divided by a factor of 2·8 and the measured curve of cone 70.3e. The factor 2·8 is introduced to allow easy comparison of both curves; it originates from the smaller thickness h of cone 70.3. The small value of h completely eliminates the fine structure in the calculated curve.

On the basis of the preceding figures it may be concluded that there is good agreement between calculations and measurements. Further, these figures confirm the theoretical conclusion drawn in sec. 5.7.1 that the cone thickness has no influence on the mean shape of the frequency characteristic of the axial admittance (provided that M_c/M_d is kept constant).

5.12.2. *Comparison of calculated and measured vibration patterns*

To compare theory and experiment, cone vibration patterns are visualized holographically by means of the time-average fringe technique (appendix F). Holographic recordings are made of cone 50.2e at a number of frequencies selected on the basis of the measured motional-impedance characteristic (fig. 4.20). The cone, which is given a thin layer of white paint to enhance reflection of the He–Ne laser beam, vibrates without outer suspension in free air. Upon each recording the vibration amplitude is adjusted in such a way that bright and dark parts appear. At bright parts the transverse amplitude is low (nodal line), at grey and black parts it is high, which indicates the positions of antinodes, as explained in appendix F.

Calculated and measured vibration patterns are compared in fig. 5.30. The measured pattern of fig. 5.30*a* at f_{ra} shows that an asymmetric standing-wave pattern with 10 nodal diameters is superimposed upon the symmetric pattern. As the outer edge is approached, black (circular) parts alternate with grey areas; the latter are not nodes but originate from the high vibrational amplitude at the outer edge. Figures 5.30*b* through 5.30*d* were recorded at bending resonant and antiresonant frequencies. These figures clearly show the different pattern of vibration of the inner and the outer cone parts; the transition point is indicated by a dot.

Figure 5.30*e* was calculated and recorded at 6432 Hz, which lies just above

---

Fig. 5.30. Calculated (cone 50.2) and measured (cone 50.2e) vibration patterns at
(*a*) the ring antiresonant frequency $f_{ra} = 1646$ Hz,
(*b*) the second bending resonant frequency $f_{br2} = 2063$ Hz,
(*c*) the second bending antiresonant frequency $f_{ba2} = 2170$ Hz,
(*d*) the third bending resonant frequency $f_{br3} = 2337$ Hz,
(*e*) 6432 Hz (calculated first membrane resonant frequency $f_{mr1} = 6172$ Hz),
(*f*) 8956 Hz (calculated upper boundary of region II $f_{ta} = 8520$ Hz),
(*g*) 13970 Hz (calculated second membrane resonant frequency $f_{mr2} = 13912$ Hz),
(*h*) 25000 Hz (calculated third membrane resonant frequency $f_{mr3} = 22160$ Hz).

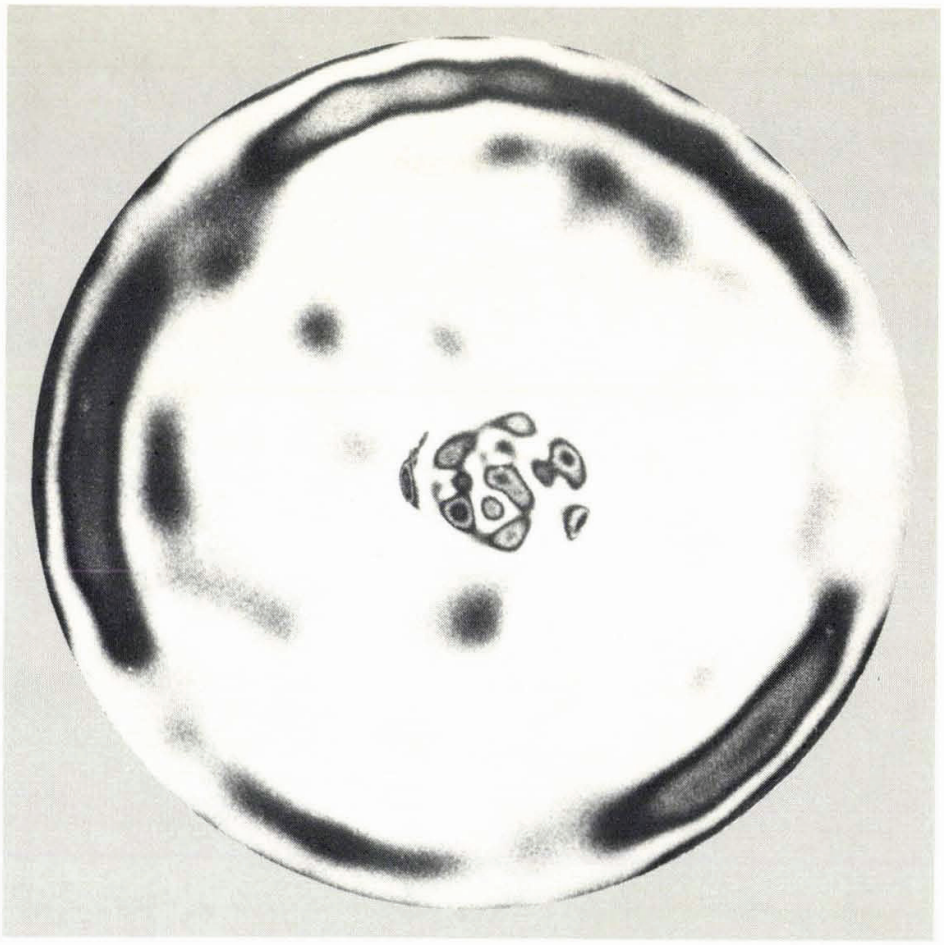

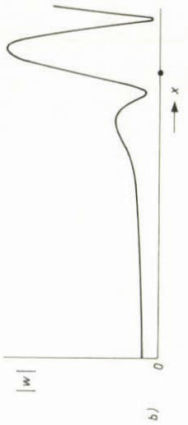
x
|w|
0

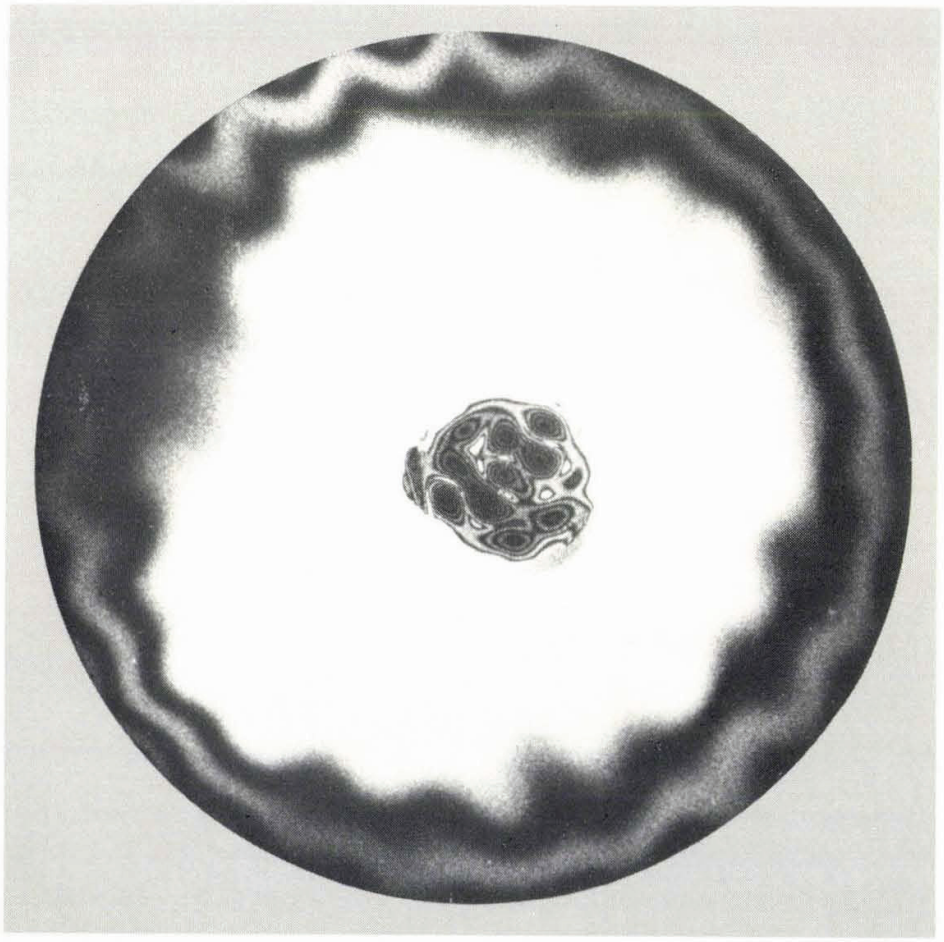


x
|w|
0

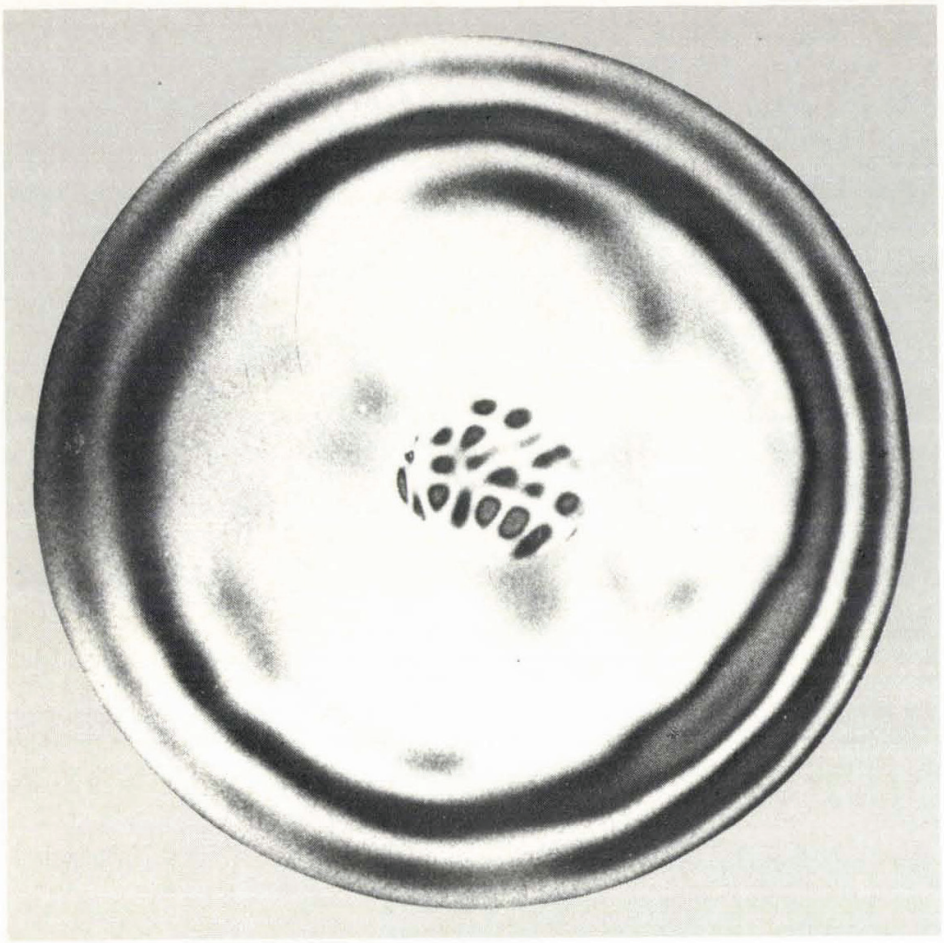

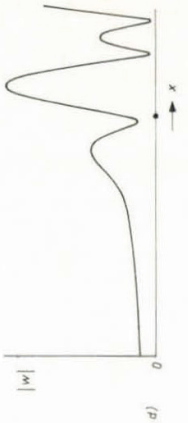
x
|w|
0
d)

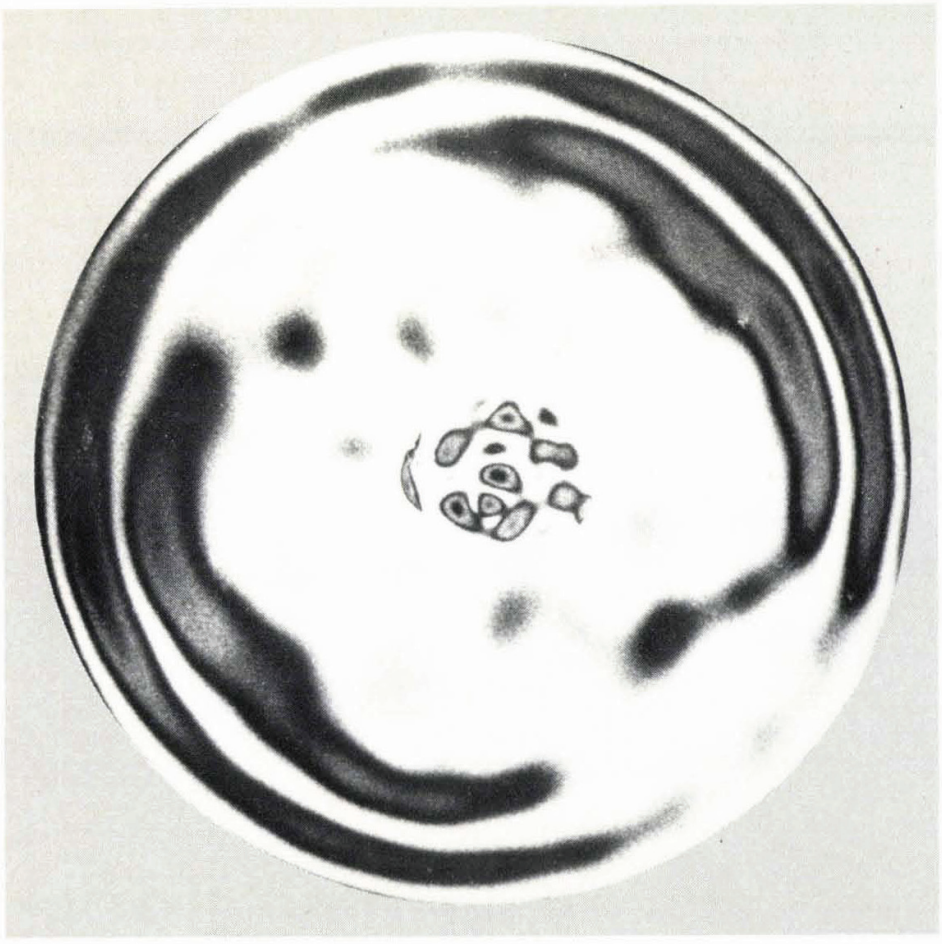


x
|w|
0
c)

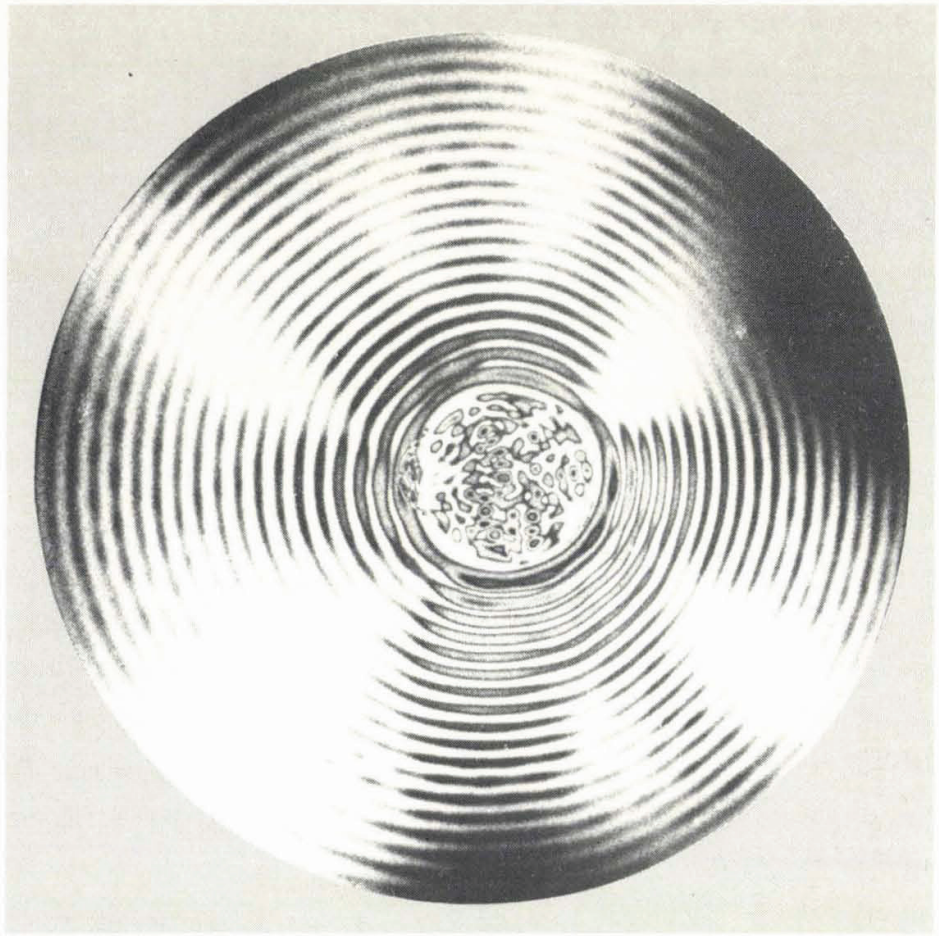

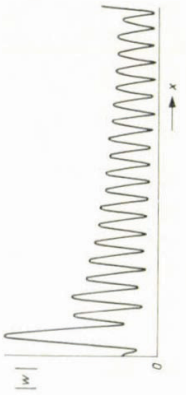
|w|
x
0

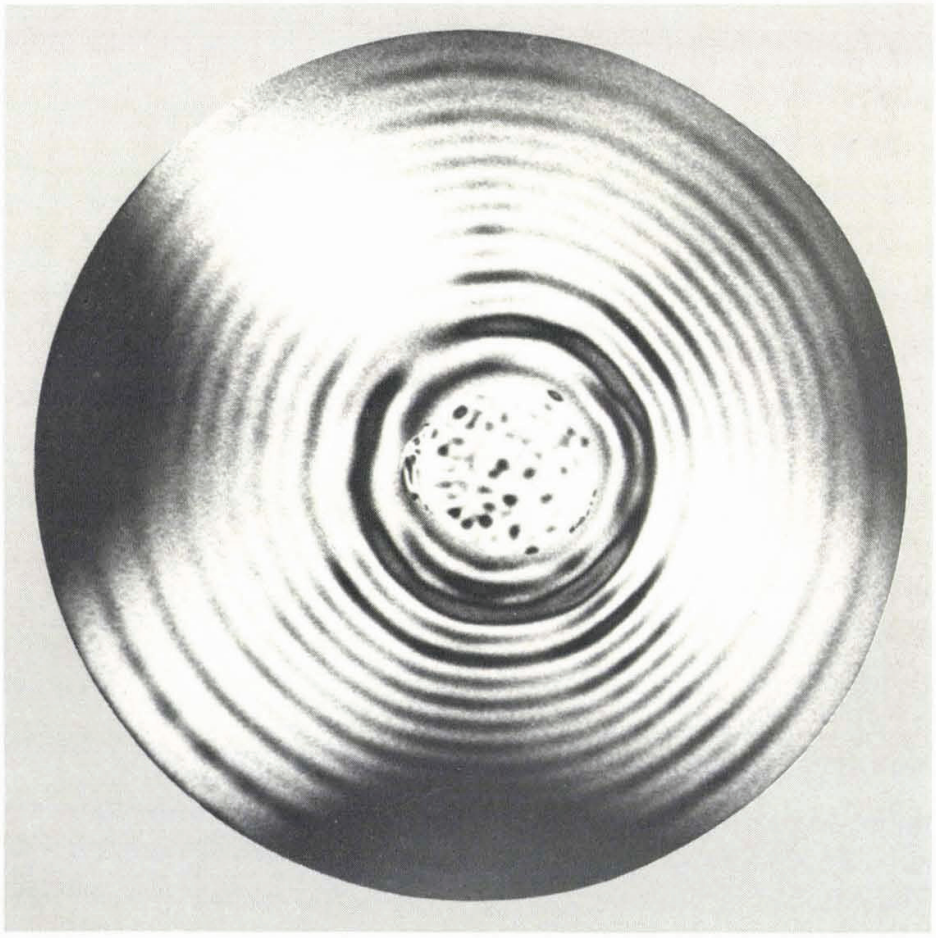

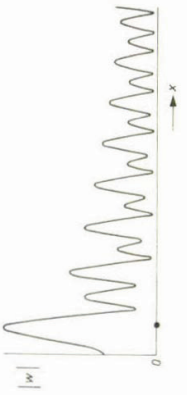
|w|
x
0

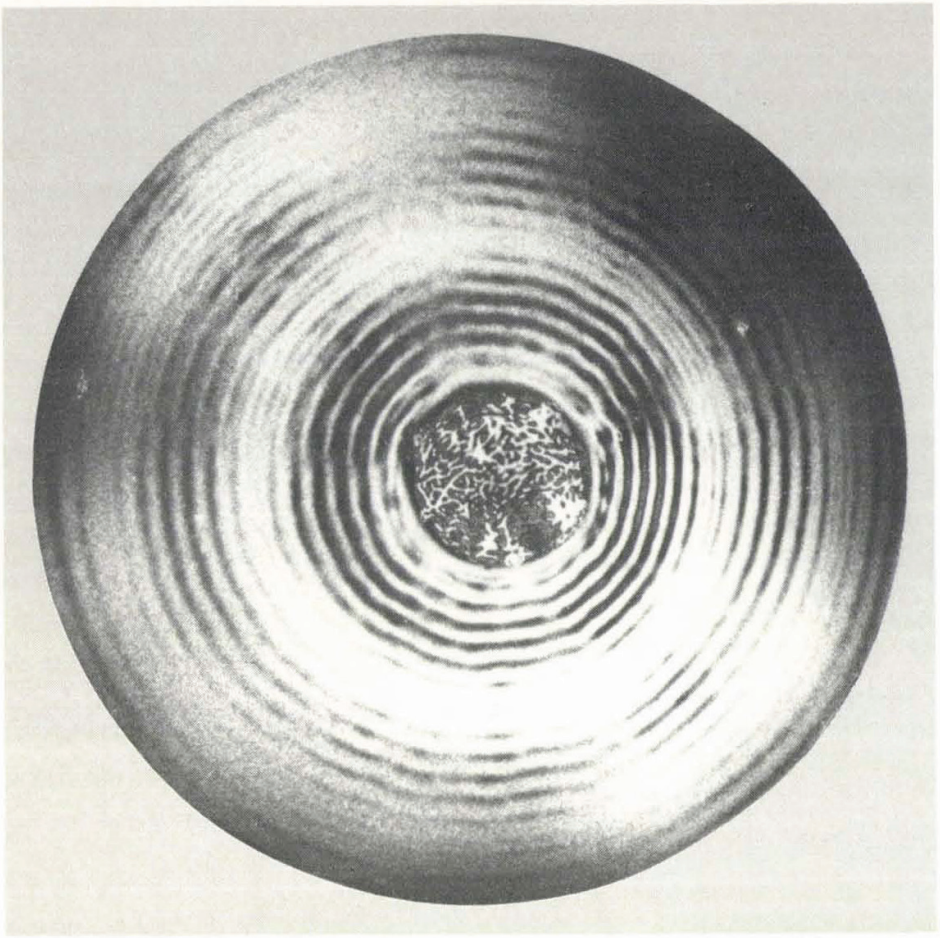

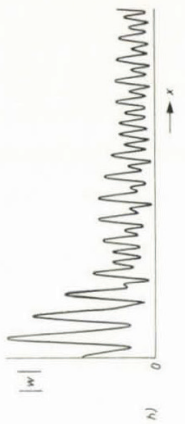

2)

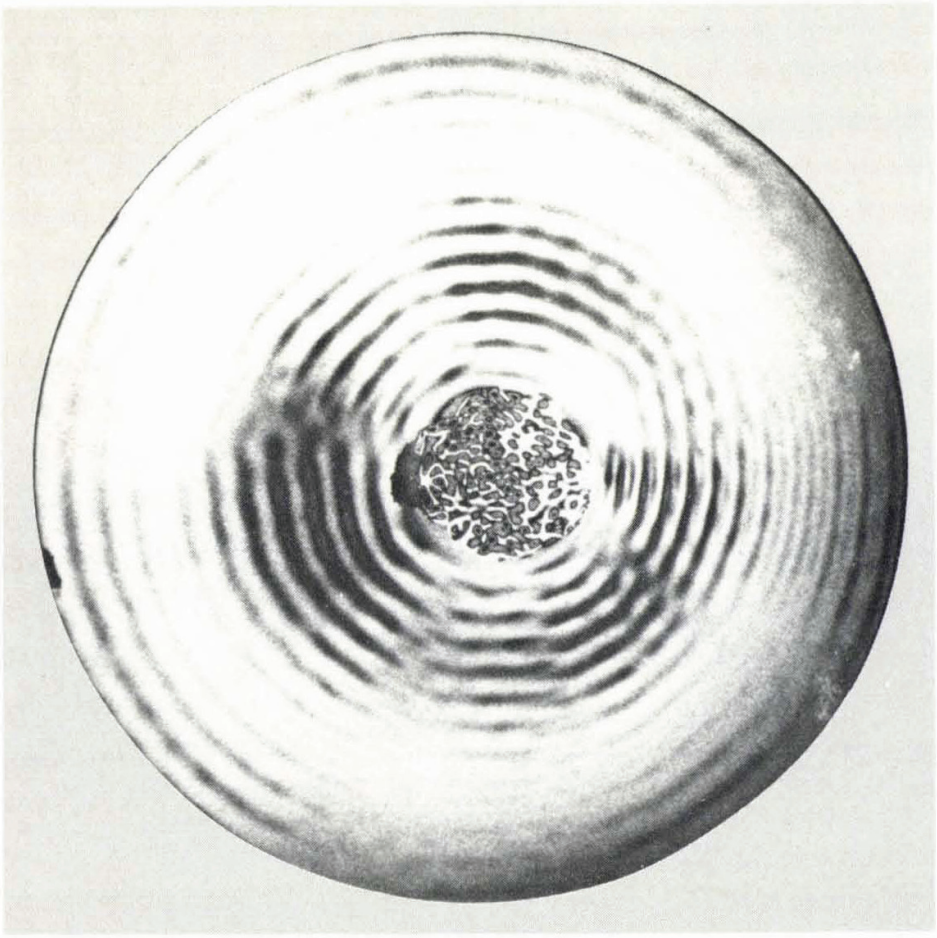

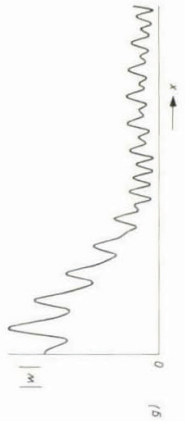

1)

the theoretical value of the first membrane resonant frequency $f_{mr1} = 6172$ Hz. Figure 5.30*f* shows the calculated and measured patterns at 8956 Hz, which is just above $f_{ta} = 8520$ Hz. The cone is fully covered by bending waves. Since the distance between two nodal circles is equal to half the bending wavelength, the average value of the latter can be obtained by dividing the cone meridional length by half the number of nodal circles in the recorded pattern. The value found is 9·5 mm. Using eq. (5.10) for the bending wavelength on a plate we find a 10 per cent lower value.

Figure 5.30*g* shows the calculated and recorded patterns in the neighbourhood of the second membrane resonant frequency f_{mr2}. The longitudinal wave with superimposed bending waves is clearly visible. Since f_{mr2} lies close to the second longitudinal antiresonant frequency, the cone is covered by $\frac{3}{4}$ of a longitudinal wavelength λ_l. From $L = 3\lambda_l/4$ we find $\lambda_l = 115$ mm, whereas for the longitudinal wavelength in an infinite polycarbonate plate at 13970 Hz we calculate $\lambda_l = c_l/f = 109$ mm. The measured pattern of fig. 5.30*h*, recorded at about 25000 Hz, shows the typical vibration at the third membrane resonant frequency. The theoretical value of f_{mr3} lies at 22160 Hz.

The above figures illustrate the satisfactory agreement between calculated

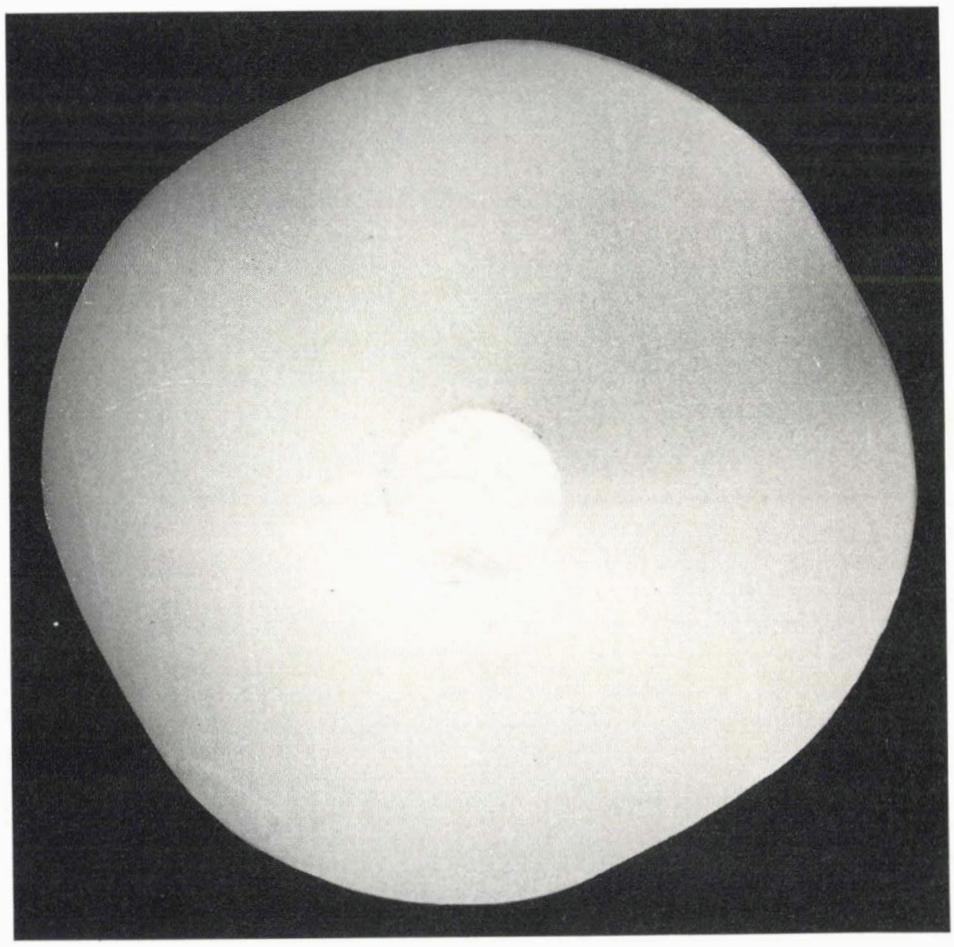

Fig. 5.31. Stroboscopically visualized asymmetric vibration pattern with 2 nodal diameters of cone 50.2e at 130 Hz.

and measured vibration patterns. As discussed in sec. 5.11, asymmetric vibration patterns already appear at relatively low frequencies. This is illustrated by fig. 5.31, which shows the stroboscopically visualized vibration pattern with four nodal diameters of cone 50.2e at 130 Hz.

The inhomogeneities on a paper cone are in general greater and cause a more distorted pattern. Additional distortions of the symmetry may be caused by the outer suspension. This is illustrated in fig. 5.32, which shows the holographically visualized vibration pattern of a complete (i.e. with top) paper cone with paper rim, vibrating in air.

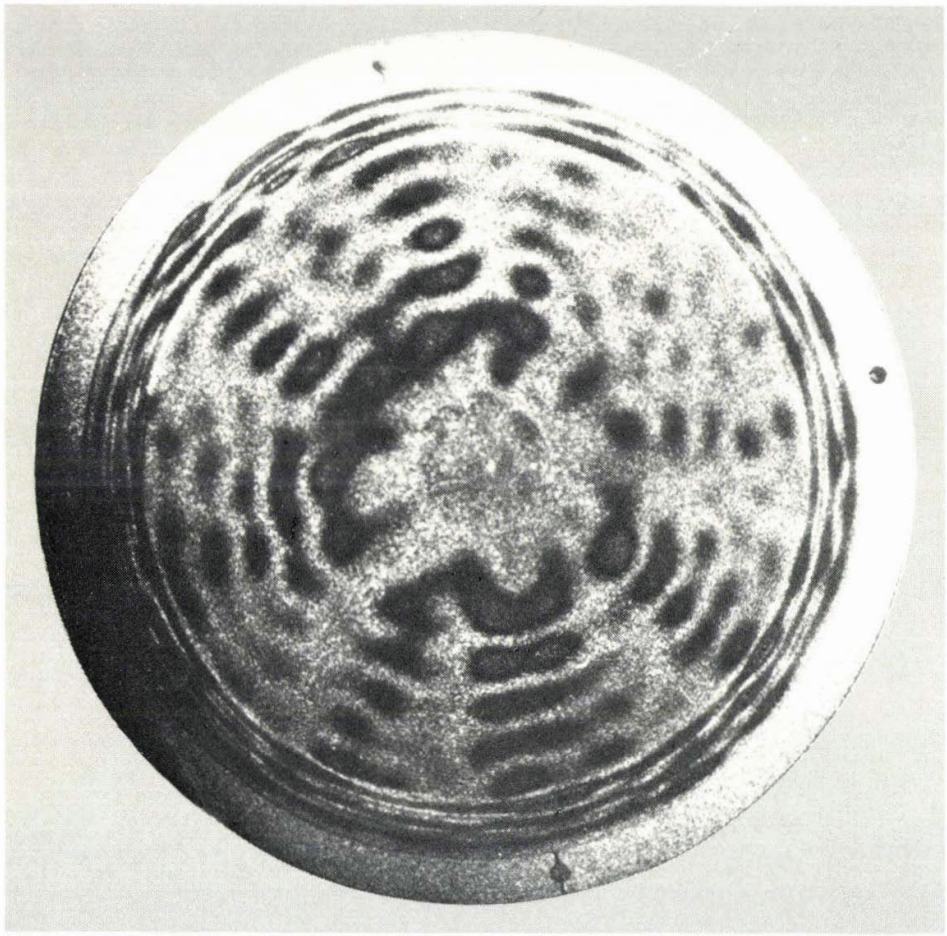

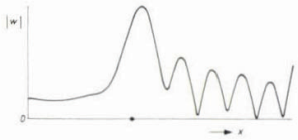

Fig. 5.32. Calculated and measured vibration patterns of a complete paper cone at 5929 Hz. Cone parameters: $\alpha = 52°$, $R_a = 17$ mm, $R_b = 83$ mm, $h = 0{\cdot}36$ mm, $E = 2{\cdot}7 \cdot 10^9$ N/m^2, $\varrho = 420$ kg/m^3, $\nu = 0{\cdot}3$, $\delta = 0{\cdot}04$.

5.13. Conclusion

It has been shown that the introduction of bending stiffness considerably complicates the description of the forced mechanical cone behaviour. On the average, the mechanical admittance at the inner edge shows the same frequency characteristic as the longitudinal admittance calculated with the membrane equations. The difference lies in the appearance of a fine structure above cone break-up ($f > f_{ra}$), caused by bending resonances and antiresonances. Above f_{ra}, the vibration patterns calculated with the general equations may considerably deviate from the membrane patterns. Bending waves appear on the outer cone part and gradually cover the whole cone with increasing frequency. Simultaneously, the inner part of the cone vibrates more or less uniformly while decreasing in area with increasing frequency. The voice-coil mass causes a roll-off of the frequency characteristic of the axial admittance. At the longitudinal resonant frequencies for the radially supported inner edge (in the foregoing briefly called membrane resonant frequencies) all bending action is overshadowed and the transverse displacement pattern is determined by a longitudinal wave with a relatively large wavelength. This pattern can be accurately predicted on the basis of the membrane equations. It has been shown that calculations of motional impedance and vibration patterns agree well with measurements.

6. SOUND RADIATION

6.1. Introduction

The calculation of the sound radiation of a loudspeaker cone in the entire audio region has in the past been regarded as intractable. Therefore approximations have been made, and the most commonly used approximation, to be found in almost any textbook on acoustics, has been to consider the cone as a rigid piston [1,10,25,26]). However, this approximation is very crude in the middle- and high-frequency regions, and it is only at low frequencies that the sound radiation is predicted correctly.

About thirty years ago, two authors [27,28]) discussed the radiation of a rigid cone, and showed that above a certain frequency the rigid-cone radiation substantially deviates from that of the rigid piston. However, at about the same frequency, mechanical waves appear on the cone (cone break-up) which makes the rigid-cone approximation only useful at low frequencies.

It is clear that a description of the mechanical behaviour of the cone must form the basis of a description of its sound radiation. This mechanical behaviour was discussed in chapters 4 and 5. Once the transverse velocity distribution on the cone is known, the sound-pressure and -power responses can be approximated by simple numerical integration. The calculation of this transverse velocity distribution for a sufficient number of frequencies requires a great deal of computer time. In this chapter the aim is therefore to describe and explain the sound radiation on the basis of calculations on a few cones rather than to produce a more or less complete list of tables or graphs to predict the frequency response for any loudspeaker cone used in practice.

The outline of this chapter is as follows. First, in sec. 6.2, basic assumptions and definitions used in the calculation of the sound radiation will be discussed. Then, since the real cone acts as a rigid piston at low frequencies, sound radiation by a rigid piston will be briefly reviewed in sec. 6.3. In sec. 6.4. sound radiation by a rigid cone is calculated, which in the high-frequency region shows typical deviations from radiation by a rigid piston. In sec. 6.5 the sound radiation by a flexible cone is discussed; this section also deals with the influence of the cone geometry and material, and demonstrates the essential influence of the voice-coil mass. In sec. 6.6 calculations are compared with measurements on a few loudspeaker cones. Finally, in sec. 6.7 some essential rules of design are discussed.

6.2. Basic assumptions and definitions

A cross-section of a normal electrodynamic loudspeaker has been shown in fig. 2.1*b*. Its working principle and characteristic properties have been discussed

in chapter 3 and may be found in the textbooks, for example in ref. 41. To allow a proper comparison of the properties of a rigid piston, a rigid cone and a flexible cone and to separate essential from inessential parameters, a number of assumptions will be made, some of which were briefly mentioned in sec. 2.2.

First, all radiators are assumed to vibrate in an infinite rigid baffle. Further, the radiated sound pressure and intensity at a great distance are calculated (far-field or Fraunhofer region). In all radiation calculations reported here, the reaction of the air and the influence of the radiation (formally expressed by the radiation impedance) will be neglected. This may be justified on the basis of the following considerations on the simplest radiator, viz. the flat rigid piston. In the low-frequency region, where the sound wavelength is longer than the radiator circumference, the air reaction is mainly mass-like. This is shown in fig. 6.1

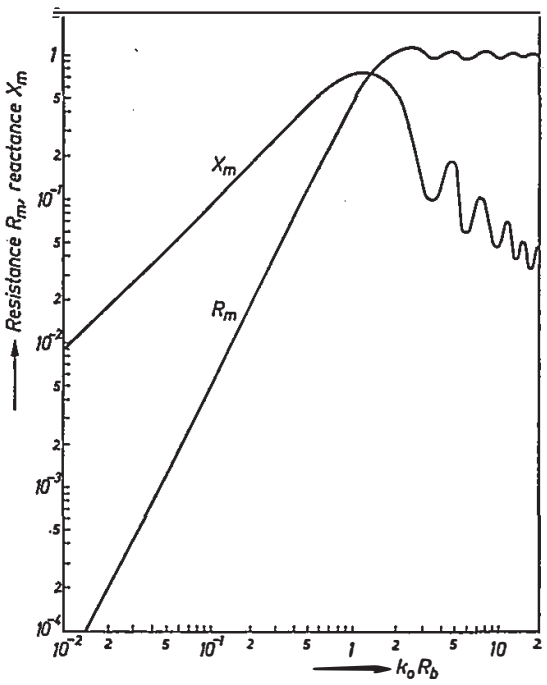

Fig. 6.1. Real part R_m and imaginary part X_m of the normalized mechanical radiation impedance of a rigid piston in an infinite baffle. Normalization factor $\pi R_b^2 \varrho_0 c_0$.

where the real and imaginary parts of the radiation impedance of a rigid piston are plotted as a function of frequency [1]). At low frequencies neglecting this mass is equivalent to assuming too small a value for the piston mass; with a constant driving force the sound pressure and power are frequency-independent and inversely proportional to the total moving mass (sec. 6.3). The above holds equally well for rigid non-plane radiators, for instance cones, because in the frequency region considered only the created volume velocity is of interest and not the shape of the radiator. It should be remarked that in practice the air mass and diaphragm mass of a real loudspeaker may have the same order of magnitude.

In the high-frequency region, where the sound wavelength is shorter than the piston circumference, the reaction of the air on the radiator is resistive; the influence of the air mass decreases rapidly with frequency and can be neglected (fig. 6.1). The mechanical radiation resistance of the piston is in most cases negligible as compared with the mechanical reactance of the piston. The effect of neglecting the radiation impedance on the sound radiation of non-rigid diaphragms is explicitly considered in sec. 6.5.2.

Summarizing the effect of neglecting the air reaction we may conclude that in the low-frequency range the calculated sound pressure and power may be too high. We will accept this discrepancy because we are not primarily concerned with the low-frequency region. Moreover, calculations that account for the effect of the radiation impedance in this region can be found in many textbooks [25,26]).

We will further assume in all cases that the radiator is driven by a sinusoidally alternating axial force F_a the amplitude of which is frequency-independent. In practice this is achieved by supplying the voice coil with a sinusoidal current having a frequency-independent amplitude i. The axial force is then $F_a = B\,l\,i$, where B is the magnetic induction in the air gap of the permanent magnet and l the total length of the voice-coil windings. This assumption rules out the influence of the voice-coil impedance, which considerably simplifies the calculations without loss of generality. A possible frequency dependence of the force can easily be introduced afterwards.

Finally, the frequency of the driving force is assumed to be higher than the fundamental resonant frequency f_0 of the loudspeaker mass-spring system. The well-known influence of the diaphragm suspension can then be neglected.

The sound pressure level L_p is always referred to 20 μPa and the sound power level L_W to 10^{-12} W.

In all radiation calculations the following four acoustic parameters are calculated as a function of frequency: the axial sound-pressure level L_p, the power level L_{W100}, the beam width β and the directivity index DI_{100}. The power level L_{W100} follows from the ratio of the sound power radiated within a space sector with an apex angle of 100 degrees to the reference power of 10^{-12} W. This angle has been chosen because the approximation for the sound pressure (see sec. 6.4) is unrealistic for field points lying outside the space sector bounded by the cone surface and its extension; in this paper we will not consider cones with apex angles smaller than 100 degrees. The beam width β and the directivity index DI_{100} have been defined in sec. 2.5.2.

A simple relation between DI_{100}, L_p and L_{W100} can be derived as follows. Let W be the radiated sound power of a cone within a space angle of 100° and W_p the power (within the same space angle) of a point source creating the same intensity on the cone axis as the cone itself, then it follows that

$$W = \frac{2\pi r^2}{\varrho_0 c_0} \int_0^{50°} \hat{p}^2 \sin \varphi \, d\varphi, \tag{6.1}$$

$$W_p = \frac{2\pi r^2}{\varrho_0 c_0} \int_0^{50°} \hat{p}_{ax}^2 \sin \varphi \, d\varphi, \tag{6.2}$$

where $\hat{p}_{ax}$ is the amplitude of the axial sound pressure created by the cone at a distance r, ϱ_0 is the air mass density and c_0 the sound velocity in air. With the above definition of the directivity index, we find

$$DI_{100} = 10 \lg \left(\frac{(1 - \cos 50°) \hat{p}_{ax}^2}{\int_0^{50°} \hat{p}^2 \sin \varphi \, d\varphi} \right) \tag{6.3}$$

which can be written as

$$DI_{100} = L_p - L_{W100} + 10 \lg (2{\cdot}2 r^2). \tag{6.4a}$$

In the calculations $r = 10$ m is mostly used, so

$$DI_{100} = L_p - L_{W100} + 23{\cdot}4 \text{ dB}. \tag{6.4b}$$

On the basis of the following considerations the sound radiation by asymmetric bending vibrations will be neglected. The bending wavelength λ_B is rather short; azimuthal standing waves already appear at very low frequencies (about 100 Hz for a paper cone of 16 cm diameter). This bending wavelength remains short as compared with the sound wavelength in air λ_0, although λ_B increases with $f^{-1/2}$. The coincidence frequency, at which λ_B becomes equal to λ_0, has an order of magnitude of 10^5 Hz for normal cones. The waves are therefore acoustically short-circuited in the audio region. Moreover, adjacent segments that vibrate in antiphase have equal areas. Therefore, the sound radiation of the bending waves travelling in the azimuthal direction can be neglected as compared with that of the bending waves propagating in the meridional direction. The latter are also acoustically short-circuited, but the vibrating concentric areas are not equal, as will be discussed in sec. 6.5.

6.3. Rigid-piston radiation

One of the simplest approximations that can be made in calculating the loudspeaker sound radiation is the well-known rigid-piston approximation. The loudspeaker cone is then assumed to be a flat rigid piston vibrating in an infinite rigid baffle (fig. 6.2). Simple expressions result for the sound pressure at large distances and the total radiated sound power. As they can be found in almost any textbook on acoustics, we will confine ourselves to simply men-

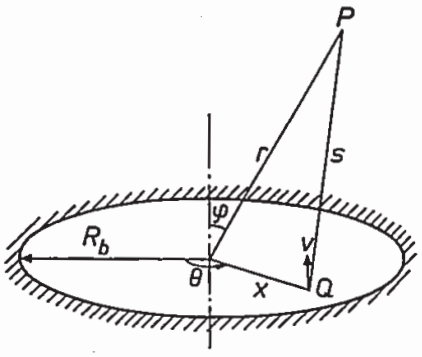

Fig. 6.2. Coordinates of a source point Q on a rigid piston in an infinite baffle and a field point P.

tioning the results. Basic formulas are given in appendix D.

The sound pressure at a distant field point with coordinates (r, φ) (fig. 6.2) is given by

$$p = \frac{\varrho_0}{2\pi r}\frac{F_a S}{M_d}\exp(-j k_0 r)\frac{2 J_1(k_0 R_b \sin\varphi)}{k_0 R_b \sin\varphi} \tag{6.5}$$

where k_0 is the sound wavenumber in air; R_b, M_d and S are respectively the radius, mass and area of the piston. The time factor $\exp(j\omega t)$ has been left out. The amplitude of the axial sound pressure is frequency-independent:

$$\hat{p}_{ax} = \frac{\varrho_0}{2\pi r}\frac{F_a S}{M_d}. \tag{6.6}$$

At low frequencies, where $k_0 R_b \ll 1$, the directivity function

$$2 J_1(k_0 R_b \sin\varphi)/(k_0 R_b \sin\varphi)$$

approaches unity; then sound is radiated uniformly into all directions. In the high-frequency region, where $k_0 R_b \gg 1$, the radiation concentrates in a central beam with small sidelobes.

The radiated sound power (see appendix D) is given by

$$W = \tfrac{1}{2}\varrho_0 c_0 S\left(\frac{F_a}{\omega M_d}\right)^2\left[1 - \frac{J_1(2 k_0 R_b)}{k_0 R_b}\right]. \tag{6.7}$$

At low frequencies, where $k_0 R_b \ll 1$, the function in square brackets may be approximated by $(k_0 R_b)^2/2$, using the series development for the Bessel function. Then eq. (6.7) becomes

$$W = \frac{\varrho_0}{4\pi c_0}\left(\frac{F_a S}{M_d}\right)^2. \tag{6.8}$$

In that region the radiated sound power is frequency-independent. In the high-frequency region ($k_0 R_b \gg 1$) the factor in square brackets approximates to 1 and the sound power decreases with the square of the frequency:

$$W = \tfrac{1}{2} \varrho_0 c_0 S \left(\frac{F_a}{\omega M_d} \right)^2 . \tag{6.9}$$

To illustrate the foregoing the axial sound-pressure level L_p, the power level L_{W100}, the beam width β and the directivity index DI_{100} are calculated as a function of frequency for a piston with an outer radius $R_b = 83$ mm. These frequency characteristics are shown in figs 6.6*a* and *b* (dashed curves). The sound-pressure level L_p is referred to the value given by eq. (6.6); L_{W100} is plotted relative to its value at very low frequencies (eq. (6.8)).

The low- and high-frequency regions of the piston radiation are clearly visible in the characteristic of L_{W100}. The transition between the two regions is marked by the transition frequency f_t at which the asymptotes, given by eqs (6.8) and (6.9), intersect. At the intersection point we have

$$k_0 R_b = 1{\cdot}4, \tag{6.10a}$$

hence

$$f_t = \frac{0{\cdot}7\, c_0}{\pi R_b} . \tag{6.10b}$$

At this frequency the sound wavelength in air λ_0 is approximately equal to the piston circumference. For the piston under consideration, f_t lies at 920 Hz (fig. 6.6*a*).

The quantity describing the directional effect of the radiator is the beam width β. In fig. 6.6*b*, β is shown for the above-mentioned piston parameters (dashed curve). In the high-frequency region the beam becomes very narrow. It follows from eq. (6.4) that the directivity index DI_{100} increases by 6 dB per octave in this region, because L_p is constant and L_{W100} decreases by 6 dB per octave (eq. (6.9)).

In figs 6.6*c*, *d* and *e* the directivity diagrams for the above piston are shown at 1, 5, 10 and 20 kHz (left parts). These figures clearly illustrate the increasing beaming effect of the rigid piston with increasing frequency.

The foregoing is well known and is only intended as a background to the description of the radiation by conical diaphragms.

6.4. Rigid-cone radiation

In this section we will deal with the sound radiation of a rigid cone in an infinite baffle. We will first discuss some alternative methods of calculating the sound radiation by a conical surface (rigid or not). The configuration is shown in fig. 6.3.

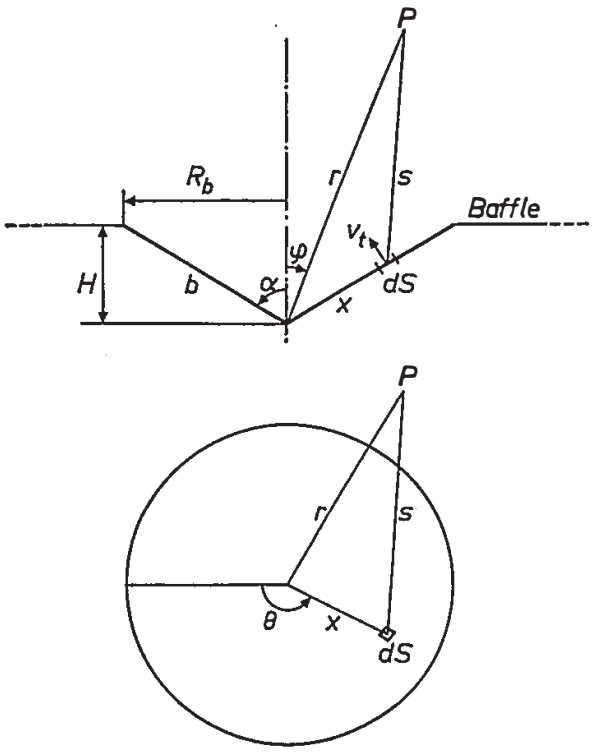

Fig. 6.3. Coordinates of a source point on a rigid cone in an infinite baffle and a field point P. For a flexible cone the same configuration holds, except that the cone is then truncated.

The first method (which will not be used for reasons discussed below) makes use of the specific conical shape of the radiator. The starting point is the Helmholtz integral for the velocity potential ϕ (from which the sound pressure p and particle velocity $\mathbf{v}$ can be derived using the relations $p = j\omega\varrho\phi$ and $\mathbf{v} = -\operatorname{grad}\phi$):

$$\phi(\mathbf{r}) = \int_S \left(G(\mathbf{r} \mid \mathbf{r}_s) \frac{\partial}{\partial n} \phi(\mathbf{r}_s) - \phi(\mathbf{r}_s) \frac{\partial}{\partial n} G(\mathbf{r} \mid \mathbf{r}_s) \right) \mathrm{d}S \tag{6.11}$$

where $\mathbf{r}$ and $\mathbf{r}_s$ are the position vectors of the field point and source point respectively, S is a closed surface around P, and G is Green's function, satisfying the inhomogeneous wave equation

$$(\nabla^2 + k^2)\, G(\mathbf{r} \mid \mathbf{r}_s) = \delta(\mathbf{r} - \mathbf{r}_s). \tag{6.12}$$

Let the closed surface S be composed of the cone surface S_c, the baffle surface and a hemisphere with infinite radius. The problem is then reduced to finding a Green's function G that

— is regular at infinity (i.e. $\lim_{R\to\infty} R\,G = \text{finite}$, where R is the radius of the hemisphere),

— satisfies Sommerfeld's radiation condition

$$\lim_{R\to\infty} R \left(\frac{\partial G}{\partial R} + j k_0 R \right) = 0,$$

— and in our case satisfies $\partial G/\partial n = 0$ on the cone and the baffle.
For this characteristic function G the Helmholtz integral reduces with

$$\partial\phi(r_s)/\partial n = + v_t(r_s) \text{ *)}$$

to

$$\phi(\mathbf{r}) = \int_{S_c} G(\mathbf{r} \mid \mathbf{r}_s)\, v_t(\mathbf{r}_s)\, \mathrm{d}S \tag{6.13}$$

where $v_t(\mathbf{r}_s)$ is the transverse velocity at the source point and the integration must be carried out over the cone surface. For an infinite cone Green's function given above can be expressed by an infinite series [30,31]). For the configuration of fig. 6.3 the construction of Green's function would at least be impractical. This method is therefore rejected.

There exists another class of solution methods that can be applied to radiating surfaces of any shape [32,33]). A common feature of these methods is that first an initially unknown function (source-density distribution or sound pressure on the radiator surface) is numerically determined on the basis of an integral equation, after which the sound pressure in the field point is calculated by numerical quadrature, using the above-mentioned function. However, these methods require long computation times and are therefore not economical. Besides, the relatively high accuracy with which the sound pressure in the field point is calculated is of no use as long as the velocity distribution on the cone is only approximately known.

We will therefore adopt a more approximative method of calculation, in which in eq. (6.11) the Green's function of an infinite plane is used. The fact that this plane has a conical indentation is neglected. This leads to the following expression for the velocity potential $\phi(r)$ at the field point P:

$$\phi(\mathbf{r}) = \int_{S} \frac{\exp(-j\, k_0\, s)}{2\pi\, s}\, v_t(\mathbf{r}_s)\, \mathrm{d}S \tag{6.14}$$

where s is the distance from the surface element $\mathrm{d}S$ to the field point P (fig. 6.3) and $v_t(\mathbf{r}_s)$ is the transverse velocity of $\mathrm{d}S$. When the radiating surface is plane, the equation is rigorously correct [10]). One of the effects of a non-plane radiating surface concerns the relative positions of the surface elements, regarded as point sources; these positions are taken into account by integrating over the radiating surface a function of the distance s. The integral disregards the fact that waves radiated by some part of the non-plane radiator are diffracted by other parts. This secondary diffraction due to the curvature can be neglected if the radiator is only slightly curved. The results obtained with this approximation

*) Note that $v_t(r_s)$ has a direction opposite to the normal n on S_c which points away from the the field point P, hence the plus sign.

will presumably be reasonably accurate for shallow cones (cf. the results for shallow spherical radiators obtained by O'Neil [34]) and Belle [35,36]).

The integral is further processed as follows. For a point in the far field we may write

$$s \approx r - x\,(\cos\alpha\cos\varphi + \sin\alpha\sin\varphi\cos\theta) \tag{6.15}$$

where r is the distance from the origin of the coordinate system to the field point, φ is the angle between the vector $\mathbf{r}$ and the cone axis, x is the distance from the origin to the source element $\mathrm{d}S$ and θ is the azimuthal coordinate of the latter. Approximating s in the denominator of the integrand of eq. (6.14) by r and using $p = j\omega\,\varrho_0\,\phi$ we find for the sound pressure p at the field point:

$$p = j\exp(-jk_0 r)\frac{\varrho_0\,\omega\sin\alpha}{2\pi r}\int_0^b v_t(x)\,x\,\mathrm{d}x\;\times$$

$$\times\int_0^{2\pi}\exp\left[jk_0\,x\,(\cos\alpha\cos\varphi + \sin\alpha\sin\varphi\cos\theta)\right]\mathrm{d}\theta \tag{6.16}$$

where the transverse velocity $v_t(x)$ is assumed to depend on x only (axisymmetric vibration). Carrying out the θ integration we find:

$$p = j\exp(-jk_0 r)\frac{\varrho_0\,\omega\sin\alpha}{r}\;\times$$

$$\times\int_0^b v_t(x)\exp(jk_0\,x\cos\alpha\cos\varphi)\,J_0(k_0\,x\sin\alpha\sin\varphi)\,x\,\mathrm{d}x. \tag{6.17}$$

The latter integral may be evaluated numerically if the velocity distribution $v_t(x)$ on the cone is known. For a rigid cone $v_t(x)$ is easily found; for a flexible cone $v_t(x)$ can be numerically calculated with the mechanical differential equations (chapter 5).

The assumption that the radiation pattern of each source element is not affected by small departures of the radiating surface from a plane certainly will not hold for field points at angles $\varphi > \alpha$. In that case, parts of the cone are screened off. In the calculations we will therefore only consider field points at angles $\varphi < \alpha$, although the directivity diagrams will be drawn up to $\varphi = 90°$. For easy comparison of the radiated sound power L_p of cones with different apex angles we will calculate the radiated power L_{W100} inside an angle of 100 degrees and not consider cones with $\alpha < 50°$.

In the remaining part of this section we will deal with the sound radiation of a rigid cone. Although in practice the cone can only be considered to vibrate rigidly well below cone break-up ($f \ll f_{ra}$), the understanding of the rigid-cone radiation is indispensable for explaining the low-frequency radiation of a flexible cone (see sec. 6.5.3).

Since a rigid cone has a uniform velocity distribution v_t, eq. (6.17) becomes

$$p = j \exp(-j k_0 r) \frac{\varrho_0 \omega v_t \sin\alpha}{r} \times \\ \times \int_0^b \exp(j k_0 x \cos\alpha \cos\varphi) J_0(k_0 x \sin\alpha \sin\varphi) x \, dx. \qquad (6.18)$$

In 1941 Brown [27]) had already calculated the sound pressure on the basis of the above formula for one frequency. In 1945, Bordoni [28]) developed a series expansion for eq. (6.18)*). Both, however, were very brief in their calculations and conclusions.

For a cone driven with a frequency-independent force F_a the transverse velocity v_t becomes

$$v_t = \frac{F_a \sin\alpha}{j\omega M_d}, \qquad (6.19)$$

giving a sound pressure

$$p = \frac{\varrho_0}{r} \frac{F_a \sin^2\alpha}{M_d} \exp(-j k_0 r) \times \\ \times \int_0^b \exp(j k_0 x \cos\alpha \cos\varphi) J_0(k_0 x \sin\alpha \sin\varphi) x \, dx. \qquad (6.20)$$

For field points on the cone axis the integral in eq. (6.20) may be easily evaluated; we find for the amplitude of the axial sound pressure:

$$\hat{p}_{ax} = \frac{\varrho_0}{2\pi r} \frac{F_a S_b}{M_d} \frac{2(2 - 2\cos z - 2z \sin z + z^2)^{1/2}}{z^2}, \qquad (6.21)$$

where $S_b = \pi R_b^2$ is the cone base area and $z = k_0 b \cos\alpha$.

In the low-frequency limit, where $z \to 0$ (which may be effectuated by either increasing the cone angle or decreasing the frequency), the last factor in eq. (6.21) becomes equal to unity and the axial sound pressure for the rigid cone becomes equal to that for the rigid piston (eq. (6.6)):

$$\hat{p}_{ax} = \frac{\varrho_0}{2\pi r} \frac{F_a S_b}{M_d}. \qquad (6.22)$$

For off-axis directions the sound pressure is easily found if $k_0 b \sin\alpha \ll 1$, which is equivalent to $f \ll f_t$, where f_t is the transition frequency for the rigid piston (eq. (6.10b)). In that case we may integrate the series development of the integrand of eq. (6.20) and neglect terms of higher order than 2. Then we arrive at

$$\hat{p} \approx \hat{p}_{ax} [1 - (\tfrac{1}{6} k_0 b \sin\varphi)^2 (11 \sin^2\alpha - 2)]^{1/2}.$$

*) Both authors erroneously took the axial velocity for v_t.

A crude approximation is

$$\hat{p} \approx \hat{p}_{ax}, \qquad f \ll f_t; \tag{6.23}$$

the cone then radiates sound uniformly in all directions.

In the high-frequency limit, when $z \to \infty$, the last factor in eq. (6.21) decreases as $2/z$ and the sound pressure on the axis becomes

$$\hat{p}_{ax} = \frac{\varrho_0}{2\pi r} \frac{F_a S_b}{M_d} \frac{2}{k_0 b \cos \alpha}. \tag{6.24}$$

Low- and high-frequency asymptotes intersect at

$$k_0 b \cos \alpha = 2 \tag{6.25}$$

which may also be written as

$$k_0 H = 2$$

where $H = b \cos \alpha$ is the cone depth. The intersection occurs at a characteristic cone frequency f_c, which divides the sound-pressure response into a low- and a high-frequency region. For f_c it follows that

$$f_c = \frac{c_0}{\pi H} \tag{6.26a}$$

or

$$f_c = \frac{c_0 \tan \alpha}{\pi R_b}. \tag{6.26b}$$

From eqs (6.10b) and (6.26b) it follows that the characteristic cone frequency f_c lies above the transition frequency for the rigid piston f_t if $\alpha > 35°$, which is nearly always the case in practice.

Figure 6.4 shows the axial sound-pressure level as a function of $k_0 b \cos \alpha$

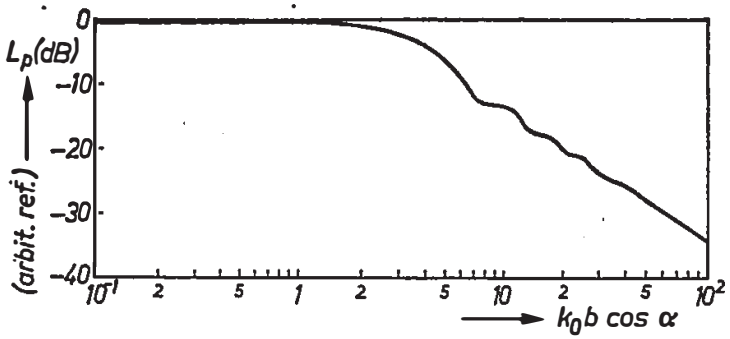

Fig. 6.4. Calculated sound-pressure level L_p of a rigid cone as a function of the dimensionless frequency parameter $k_0 b \cos \alpha$.

(in fact this means that the last factor in eq. (6.21) is plotted as a function of frequency).

The foregoing may be interpreted as follows. For low frequencies the cone acts as a point source; the conical shape has no influence. For high frequencies where $k_0 H \gg 2$, the axial sound pressure decreases with frequency and cone depth H. In that case many sound wavelengths λ_0 fit between cone top and base. Waves radiated by different concentric cone areas no longer arrive in phase at the field point, thus decreasing the sound pressure.

This will be illustrated with fig. 6.5*a*. Let the cone be divided into concentric areas S_i whose mean distances to the (distant) field point on the axis differ by half a wavelength in air. Then waves from neighbouring areas arrive in anti-phase at the field point. Since the sound pressure is proportional to each radiating area, the total sound pressure at the field point will be

$$p \propto S_1 - S_2 + S_3 - \ldots . \tag{6.27}$$

The outer radius of the nth area S_n being equal to $n\,(\lambda_0/2)\tan\alpha$, it follows that

$$S_n \propto \left(n\frac{\lambda_0}{2}\right)^2 - \left((n-1)\frac{\lambda_0}{2}\right)^2 \tag{6.28}$$

and we find for the alternating series eq. (6.27):

$$p \propto N\,\lambda_0^2 \tag{6.29}$$

where N is the number of wavelengths on the cone depth H: $N\,\lambda_0 = H$. We find

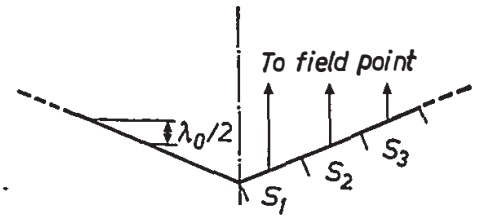

Fig. 6.5*a*. Illustration of the axial sound radiation of a rigid cone by concentric conical rings at high frequencies ($f > f_c$).

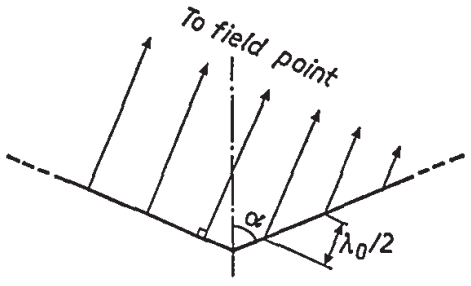

Fig. 6.5*b*. Illustration of the origin of a sidelobe in the directivity diagram of a rigid cone at $90 - \alpha$ degrees.

$$p \propto \lambda_0$$

or

$$p \propto 1/f, \tag{6.30}$$

which shows the typical frequency dependence of the sound pressure in the high-frequency region for the rigid cone.

If the cone depth H is decreased by increasing the apex angle α, the transition frequency f_c increases according to eq. (6.26a). In the limit, when $\alpha \to \pi/2$, f_c tends to infinity and the axial pressure becomes frequency-independent at all frequencies, in accordance with the rigid-piston radiation.

The off-axis sound pressure and the beam width β must be calculated by numerical evaluation of eq. (6.20). The sound-power level L_{W100} is calculated by numerically integrating the intensity over a space angle of 100 degrees. The directivity index DI_{100} is then found with eq. (6.4b).

In order to demonstrate the difference between the rigid cone and the piston we calculated the axial sound-pressure level L_p, the sound-power level L_{W100}, the beam width β and the directivity index DI_{100} for a rigid cone with a semi-apex angle $\alpha = 50°$ and an outer radius $R_b = 83$ mm; the same values were used for the rigid piston discussed in the preceding section. The results are shown in fig. 6.6*a* (drawn curves). As remarked before, L_p is frequency-independent at low frequencies and equal to L_p of the rigid piston. Above f_c (1580 Hz) L_p starts to decrease as $1/f$. The sound-power level L_{W100} starts to decrease at a somewhat lower frequency in the neighbourhood of the piston transition frequency $f_t = 920$ Hz. Because in the high-frequency region the sound powers in both cases are about equal whereas the axial sound pressures are not, we may conclude that for off-axis points, L_p of the cone must on the average be higher than L_p of the piston. This is illustrated in fig. 6.6*b* which shows that the directivity index DI_{100} of the cone is relatively small and on the average almost frequency-independent, indicating a relatively high off-axis radiation. This is further illustrated by directivity diagrams.

The figures 6.6*c*, *d* and *e* show the directivity diagrams for the rigid cone (right parts) at various frequencies. At 1 kHz the radiation is practically uniform and equal in both cases. At 5 kHz, the cone shows a broad sidelobe normal to the cone axis ($\varphi = 40°$); this direction is indicated by an arrow. At higher frequencies this sidelobe becomes the principle sidelobe and is now more pronounced, which is illustrated by the directivity diagrams of figs 6.6*d* and *e*, calculated for 10 and 20 kHz respectively.

The cause of the big sidelobe at $90 - \alpha$ degrees can easily be explained: at wavelengths smaller than the dimensions of the radiating surface, the radiation normal to the latter becomes very high. This is illustrated in fig. 6.5*b* where concentric parts with mutual spacing $\lambda_0/2$ on the left cone side radiate waves which arrive in phase at the field point. The contribution from the right cone

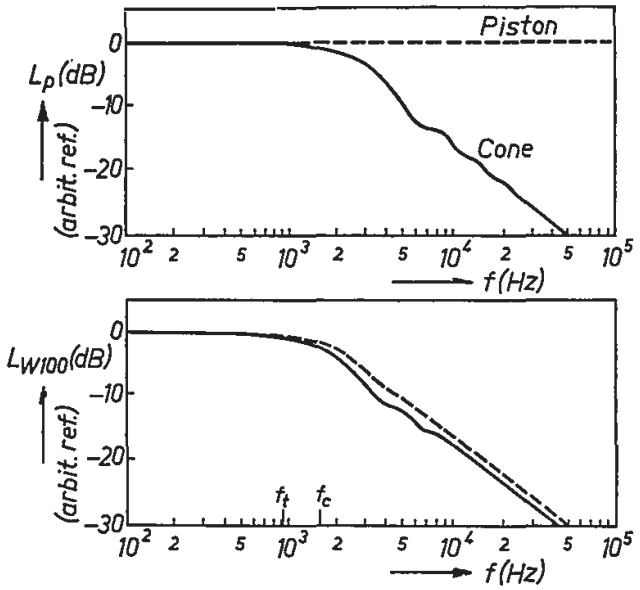

Fig. 6.6*a*. Calculated pressure and power responses of a piston (dashed) and a rigid cone with $\alpha = 50°$ (drawn curves), both with $R_b = 83$ mm.

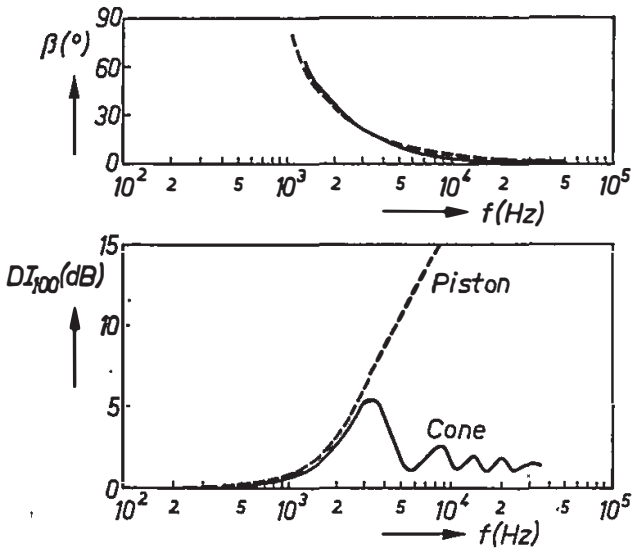

Fig. 6.6*b*. Calculated frequency characteristics of the beam width ϱ and the directivity index DI_{100} of the rigid piston (dashed) and the rigid cone (drawn curves) of fig. 6.6*a*.

side is relatively low. The result is a sidelobe which may even exceed the axial lobe (fig. 6.6*e*).

The power level L_{W100} of the cone is about 2 dB lower than that of the piston in the high-frequency region (fig. 6.6*a*). One cause is the fact that the intensity at $\varphi = 50°$, which is the boundary value for the integration over a space angle of 100°, is much higher for the cone than for the piston. It is interesting to calculate the sound power radiated by a piston and by a cone into a semi-space. The result (fig. 6.6*f*) shows that the difference between the piston and cone powers is somewhat smaller than the difference between L_{W100} for the two radiators. The remaining difference of about 1 dB may be attributed to the

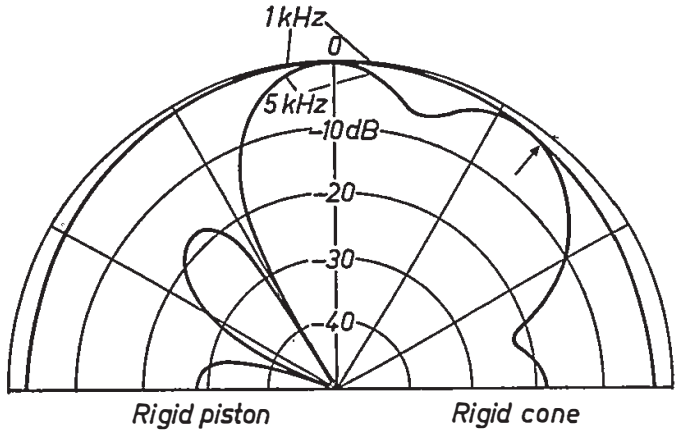

Fig. 6.6*c*. Calculated directivity diagrams of the rigid piston (left) and the rigid cone (right) of fig. 6.6*a* at 1 and 5 kHz.

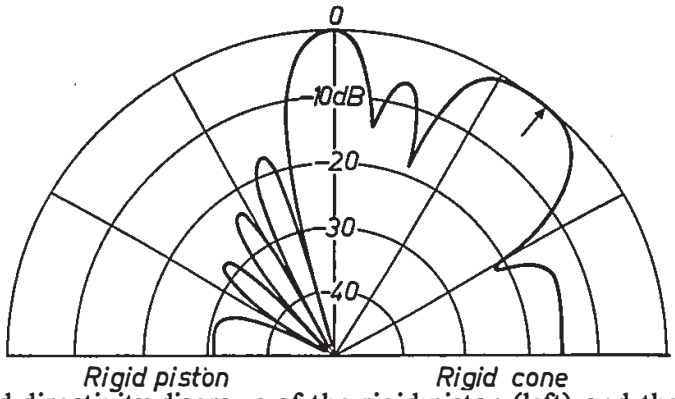

Fig. 6.6*d*. Calculated directivity diagrams of the rigid piston (left) and the rigid cone (right) of fig. 6.6*a* at 10 kHz.

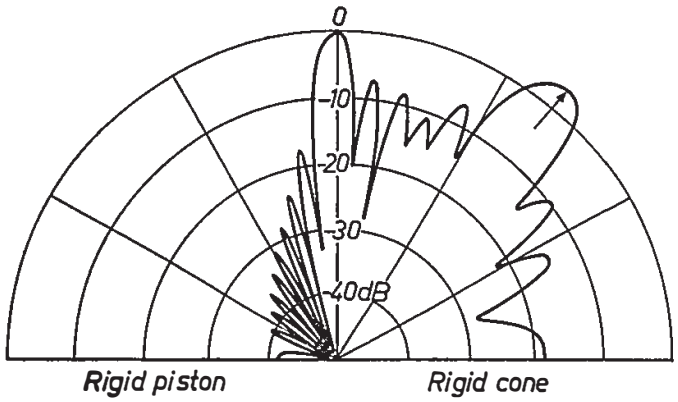

Fig. 6.6*e*. Calculated directivity diagrams of the rigid piston (left) and the rigid cone (right) of fig. 6.6*a* at 20 kHz.

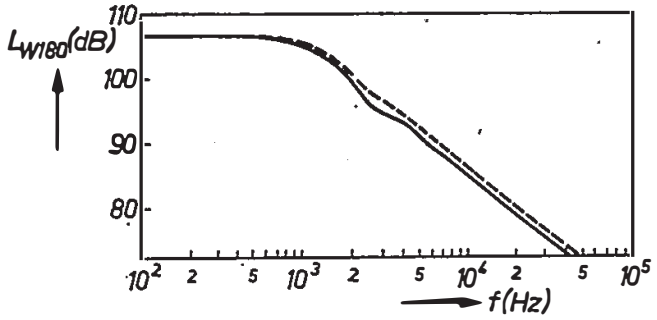

Fig. 6.6*f*. Calculated frequency characteristics of the sound power radiated into semi-space of the rigid piston (dashed) and the rigid cone (drawn curve) of fig. 6.6*a*.

approximative character of the solution for field points in the shadow region (i.e. $\varphi > \alpha$).

The beam widths β of the rigid piston and the rigid cone do not differ much (fig. 6.6*b*). It must be remembered, though, that β is the width of the central beam; the directivity diagram of the cone is as a whole much wider than that of the piston.

6.5. Flexible-cone radiation

6.5.1. *Introduction*

The sound radiation of a flexible cone is greatly influenced by the fact that above cone break-up the transverse velocity of the cone surface is no longer uniform. This transverse velocity may be created by longitudinal as well as bending waves. In a certain frequency region (region II), they even appear simultaneously: a longitudinal wave at the cone top, bending waves at the cone base. The sound radiation of a flexible cone can only be calculated numerically, although approximate analytical descriptions can be given in the low- and high-frequency regions (secs 6.5.3 and 6.5.4).

First of all it will be shown why the air reaction on the cone vibrations can be neglected. In secs 6.5.5, 6.5.6 and 6.5.7, the sound radiation of a number of cones will be discussed and the influence of the geometry and material parameters of the cone will be considered. In sec. 6.5.9, finally, it will be shown that voice-coil mass has a considerable influence on the sound radiation in the high-frequency region.

6.5.2. *Description of the problem*

The sound radiation of a flexible cone may be calculated in the same way as that of a rigid cone. First, the transverse (axisymmetric) velocity $v_t(x)$ is computed for a number of points on the cone and for various frequencies, using the general differential equations described in the preceding chapter. Then the integral for the sound pressure eq. (6.17) is numerically evaluated for these frequencies. Lastly the beam width β, the sound power L_{W100} and the directivity index DI_{100} are calculated as described in the foregoing section. In these numerical calculations the sound radiation of a truncated cone is considered (i.e. $v_t = 0$ for $x < a$). The influence of a rigid cone top ($0 \leqslant x < a$) will be discussed in sec. 6.5.8.

The velocity distribution $v_t(x)$ is calculated for a cone vibrating in vacuum. This means that the air reaction on the velocity distribution is neglected. Some justification for this at first sight crude approximation is offered by Lax [37]), who calculated the effect of the radiation on a circular plate. It is shown by him that for

$$\frac{\varrho_0 R_b}{\varrho h} < 1$$

where R_b is the plate radius, the shift in resonant frequencies and the change in shape of the four lowest modes due to the reaction of the air on the plate is negligible. Further, the air influence tends to decrease with increasing mode number. Substituting normal loudspeaker parameters ($R_b/h = 200$, $\varrho = 500$ kg/m³ for paper cones) we arrive at

$$\frac{\varrho_0 R_b}{\varrho h} \approx 0{\cdot}5.$$

Hence, the neglect of the air reaction would be justified if the cone were a flat plate. We do not expect, however, a fundamentally different air reaction in the case of the cone, especially not in the high-frequency region, where the cone behaves as a flat plate.

It is also shown in ref. 37 that the effect of the radiation damping on the sharpness of the plate resonances is not negligible. Of course the additional effect of the radiation damping decreases with increasing loss factor of the radiator material. In the preceding chapter it was shown experimentally that the reactive part of the radiation impedance reduced the antiresonant frequencies by a few per cent. In the following calculations the influence of the reactive part of the radiation impedance is neglected; the influence of the resistive part is accounted for in an approximative way: the internal material damping is taken higher ($\delta = 0{\cdot}1$) than the value encountered in practice ($\delta \approx 0{\cdot}04$ for normal cone paper).

Before carrying out specific numerical calculations we will first modify somewhat the radiation integral eq. (6.17). At the inner edge, the axial admittance Y_a is defined by

$$Y_a = \frac{v_a(a)}{F_a} \tag{6.31}$$

where $v_a(a)$ is the axial velocity at the inner edge and F_a is the applied axial force. Let $v_t(x)$ be the transverse velocity distribution on the cone; then we have

$$v_t(a) = v_a(a) \sin \alpha, \tag{6.32}$$

which may be written as

$$v_t(a) = Y_a F_a \sin \alpha. \tag{6.33}$$

Introducing $V_t(x)$ as the transverse velocity at the point x divided by $v_t(a)$:

$$V_t(x) = \frac{v_t(x)}{v_t(a)} \tag{6.34}$$

it follows that

$$v_t(x) = Y_a F_a V_t(x) \sin \alpha \tag{6.35}$$

and

$$V_t(a) = 1. \tag{6.36}$$

Substituting eq. (6.35) in eq. (6.17) we arrive at

$$p = j \exp(-j k_0 r) \frac{\varrho_0}{r} \omega Y_a F_a \sin^2 \alpha \times$$

$$\times \int_a^b V_t(x) \exp(j k_0 x \cos \alpha \cos \varphi) J_0(k_0 x \sin \alpha \sin \varphi) x \, dx \tag{6.37}$$

and for the axial value of p we find

$$p_{ax} = j \exp(-j k_0 r) \frac{\varrho_0}{r} \omega Y_a F_a \sin^2 \alpha \int_a^b V_t(x) \exp(j k_0 x \cos \alpha) x \, dx. \tag{6.38}$$

Hence

$$\hat{p}_{ax} = \frac{\varrho_0}{r} \omega F_a \sin^2 \alpha \left| Y_a \int_a^b V_t(x) \exp(j k_0 x \cos \alpha) x \, dx \right| \tag{6.39}$$

which can also be written as

$$\hat{p}_{ax} = \frac{\varrho_0}{r} \frac{F_a \tan^2 \alpha}{2\pi R_a \varrho h} k_1 \left| y_a \int_a^b V_t(x) \exp(j k_0 x \cos \alpha) x \, dx \right|, \tag{6.40}$$

where y_a is the reduced axial admittance, defined by eq. (5.35).

The radiated sound power within a space angle of 100 degrees is given by

$$W_{100} = \frac{\pi r^2}{\varrho_0 c_0} \int_0^{50°} \hat{p}^2 \sin \varphi \, d\varphi. \tag{6.41}$$

On the basis of eq. (6.39) we may roughly predict the sound-pressure response as follows. For low frequencies (region I) the cone oscillates more or less rigidly, hence $V_t(x) \approx 1$. If $k_0 b \cos \alpha \ll 1$, the integral becomes approximately equal to $(b^2 - a^2)/2$, independent of φ. The radiation will be uniform and the sound pressure and sound power will be frequency-independent, because $|Y_a|$ is inversely proportional to the frequency. This low-frequency radiation will be further discussed in the next section.

For high frequencies (region III) the velocity distribution $V_t(x)$ is in general

determined by bending waves. For normal loudspeaker cones the bending wavelength λ_B is much smaller than the sound wavelength in air λ_0. Hence, the bending waves are acoustically short-circuited and their sound radiation depends only on the geometric mean volume velocity created by these waves. This is expressed by the integral in eq. (6.39) whose integrand is a highly oscillating function of x. The resultant mean volume velocity and consequently the sound radiation will be small. In the middle-frequency region (region II) the sound radiation is difficult to predict, because the inner part of the cone oscillates more or less rigidly and contributes a great deal to the sound radiation, whereas the outer part of the cone shows acoustically short-circuited bending waves which radiate little sound. The radiation in this region will therefore be discussed on the basis of numerical examples in subsequent sections. Note that the sound pressure is directly proportional to Y_a and hence to Y_l: the peaks and dips in Y_a will also show up in the sound-pressure response (except the dip at f_{ra}, as explained in the next section). Before carrying out numerical computations of eqs (6.37) and (6.41), we will first take a closer look at the sound radiation in the low- and high-frequency regions.

6.5.3. *Radiation in the low-frequency region*

It has been shown in chapter 5 that cone break-up, which is synonymous with the appearance of axisymmetric bending waves on the cone, starts at the ring antiresonant frequency f_{ra}, which can be approximated by (see sec. 4.4)

$$f_{ra} \approx \frac{c \cos \alpha}{2\pi R_b}. \tag{6.42}$$

By definition the low-frequency region (region I) is given by $f < f_{tb}$ or, approximately,

$$f < f_{ra}. \tag{6.43}$$

The sound radiation in this region can be described by the rigid-cone approximation. For the sound-power characteristic even the rigid-piston approximation can be used in view of the small difference between the rigid piston and rigid cone (fig. 6.6*a*). At very low frequencies, the radiated axial sound pressure and sound power are frequency-independent and given by eqs (6.6) and (6.8).

Let us first consider the sound-power response, which shows a 6-dB roll-off above f_t. At f_{ra} the sound power rises again, because of cone break-up (shown later). Therefore, if $f_t < f_{ra}$, a dip will appear between f_t and f_{ra} in the power response. This dip will not appear if $f_t > f_{ra}$, from which we find with eqs (6.10*b*) and (6.42)

$$\cos \alpha < 1{\cdot}4 \frac{c_0}{c}. \tag{6.44}$$

For normal paper cones with $c = 2700$ m/s, we find that this dip will not appear

if $\alpha > 80°$. Since in practice nearly all semi-apex angles are smaller than 80°, we will find a dip in the frequency characteristic of L_{W100}. The depth of this dip increases with increasing spacing between f_t and f_{ra}; for a paper cone with $\alpha = 70°$ and $c = 2700$ m/s, we find $f_t = \frac{1}{2} f_{ra}$ and the dip will be relatively small (≈ 3 dB). Besides α we can also vary c; if c decreases, eq. (6.44) will be satisfied at smaller cone angles. This will be illustrated in sec. 6.5.7.

The axial sound-pressure response is not influenced by the transition frequency f_t, but by the characteristic cone frequency f_c (eq. (6.26b)) above which L_p of the rigid cone shows a 6-dB roll-off. At f_{ra} the pressure response rises again (cone break-up). If $f_c < f_{ra}$, a dip will appear in the pressure response. This dip does not appear if $f_c > f_{ra}$, or according to eqs (6.26b) and (6.42) if

$$\sin \alpha > \left[\left(\frac{c_0}{c} \right)^2 + 1 \right]^{1/2} - \frac{c_0}{c}. \tag{6.45}$$

For a paper cone with $c = 2700$ m/s, eq. (6.45) is satisfied if $\alpha > 60°$, which is the case for many practical loudspeaker cones.

The requirement $f_c > f_{ra}$ for avoiding a dip is not stringent; even if $f_c = \frac{1}{2} f_{ra}$ the dip is hardly noticeable (fig. 6.14*b*, upper graph). This is due to the fact that in the neighbourhood of f_{ra} the outer-edge amplitude $w(b)$ becomes higher than the amplitude w_r of a rigid cone (see fig. 4.8*a*). The inner-edge amplitude is relatively small. Because the outer cone area, where $w(x) > w_r$, is much larger than the inner cone area, where $w(x) < w_r$, the total volume velocity will be higher than that of the rigid cone. To a certain extent this compensates for the roll-off above f_c predicted by the rigid-cone approximation. A possible dip may be eliminated by decreasing c or increasing α.

We may summarize the sound radiation of the flexible cone in the low-frequency region as follows. The (axial) sound-pressure and sound-power responses are well described by the rigid-piston approximation, provided f_c lies above cone break-up ($f_c > f_{ra}$). If $f_c \ll f_{ra}$, the sound-pressure response must be described by the rigid-cone approximation in the interval $f_c < f < f_{ra}$. The foregoing will be further illustrated on the basis of specific numerical examples in subsequent sections.

6.5.4. *Radiation in the high-frequency region*

In this section we derive an approximate expression (of limited practical value) for the axial sound pressure at high frequencies, i.e. for $f \gg f_{ta}$.

Now, as far as the radiation of sound is concerned, surfaces with dimensions large with respect to wavelength (the bending wavelength in this case) tend to behave as infinite plates when considered per unit area and on averaging over frequency. A case to the point is the sound transmission through walls at high frequencies where identical results are obtained for an infinite wall with travel-

ling waves only [42]) and a finite wall with standing waves only [43]). The resonances occurring in the latter case apparently average out.

Assuming that the above holds for the loudspeaker cone for the frequencies under consideration we introduce a reduced transverse velocity distribution of the travelling-wave type:

$$V_t(x) = \frac{H_0^{(2)}(k_B\, x)}{H_0^{(2)}(k_B\, a)} \tag{6.46}$$

where $H_0^{(2)}$ is the zero-order Hankel function of the second kind and k_B the bending wavenumber. With eq. (6.39) we find for the modulus $\hat{p}_{ax}$ of the axial sound pressure:

$$\hat{p}_{ax} = \frac{\varrho_0}{r}\, \omega\, F_a \left| Y_a\, I_1 \right| \sin^2 \alpha \tag{6.47}$$

where

$$I_1 = \frac{1}{H_0^{(2)}(k_B\, a)} \int_a^b H_0^{(2)}(k_B\, x) \exp\left(j\, k_0\, x \cos\alpha\right) x\, \mathrm{d}x. \tag{6.48}$$

From $f \gg f_{ta}$ it follows

$$k_B\, a \gg 1, \tag{6.49}$$

provided $h\ (\tan\alpha)/a\ \sqrt{12} < 1$ (see eqs (4.12), (5.7)). The latter inequality is nearly always satisfied in practice. As the argument of the Hankel function is always much larger than unity, we replace it by its asymptotic expansion:

$$H_0^{(2)}(t) \approx \left(\frac{2}{\pi\, t}\right)^{1/2} \exp\left[-j\,(t - \pi/4)\right], \qquad t \gg 1. \tag{6.50}$$

Then the assumed velocity distribution (eq. (6.46)) becomes

$$V_t(x) \approx \left(\frac{a}{x}\right)^{1/2} \exp\left[-j\, k_B\,(x - a)\right],$$

in accordance with the asymptotic bending solution given by Ross [4]). Thus:

$$I_1 \approx a^{1/2} \exp\left(j\, k_B\, a\right) \int_a^b x^{1/2} \exp\left[-j\, x\,(k_B - k_0 \cos\alpha)\right] \mathrm{d}x$$

$$= a^{1/2} \exp\left(j\, k_B\, a\right) \int_a^b x^{1/2} \exp\left[-j\, k_B\, x(1 - q)\right] \mathrm{d}x \tag{6.51}$$

where

$$q = \frac{k_0}{k_B} \cos\alpha. \tag{6.52}$$

Assuming

$$f \ll f_{co} \text{ *)} \tag{6.53}$$

we see that

$$q \ll 1. \tag{6.54}$$

Introducing

$$k_B x = t,$$

$$\left(\frac{2(1-q)}{\pi} k_B x\right)^{1/2} = s,$$

we now rewrite eq. (6.51):

$$\begin{aligned} I_1 &= \left(\frac{a}{k_B{}^3}\right)^{1/2} \exp(j k_B a) \int_{k_B a}^{k_B b} t^{1/2} \exp[-j(1-q)t]\,\mathrm{d}t \\ &= j\left(\frac{a}{k_B{}^3}\right)^{1/2} \frac{\exp(j k_B a)}{1-q} \left(t^{1/2} \exp[-j(1-q)t] \Big|_{k_B a}^{k_B b} - I_2 \right) \end{aligned} \tag{6.55}$$

where

$$I_2 = \left(\frac{\pi}{2(1-q)}\right)^{1/2} \int_{s_1}^{s_2} \exp\left(-j\frac{\pi}{2} s^2\right) \mathrm{d}s,$$

$$s_1 = \left(\frac{2(1-q)}{\pi} k_B a\right)^{1/2}, \qquad s_2 = \left(\frac{2(1-q)}{\pi} k_B b\right)^{1/2}. \tag{6.56}$$

Now I_2 reduces to (see eqs 7.3.1, 7.3.2, 7.3.9, 7.3.10, 7.3.27, 7.3.28 in ref. 38):

$$\begin{aligned} I_2 = \left(\frac{\pi}{2(1-q)}\right)^{1/2} \{ &[jf(s_2) - g(s_2)] \exp[-j(1-q) k_B b] + \\ &- [jf(s_1) - g(s_1)] \exp[-j(1-q) k_B a] \}, \end{aligned}$$

where

$$\begin{aligned} f(s) &= \frac{1}{\pi s}\left(1 - \frac{3}{(\pi s^2)^2} \cdots\right), \\ g(s) &= \frac{1}{\pi s}\left(\frac{1}{\pi s^2} \cdots\right). \end{aligned} \tag{6.57}$$

*) At the coincidence frequency f_{co} the bending wavenumber k_B becomes equal to the sound wavenumber in air k_0; for bending waves on an infinite plate [9]) $f_{co} = c_0{}^2/2\pi\gamma^2$. For practical loudspeaker cones we find $f_{co} \approx 10^5$ Hz.

On considering eqs (6.55), (6.56), (6.57) in conjunction with eq. (6.49) we see that, in the present order of approximation, I_2 may be neglected in eq. (6.55). Thus

$$I_1 = \frac{j a^{1/2}}{(1-q)\, k_B} \exp(j k_B a)\{b^{1/2} \exp[-j(1-q) k_B b] - a^{1/2} \exp[-j(1-q) k_B a]\}$$

and

$$|I_1| = \frac{a^{1/2}}{(1-q)\, k_B} \{b + a - 2\,(a\,b)^{1/2} \cos[(1-q)\, k_B\,(b-a)]\}^{1/2}. \tag{6.58}$$

In order to find the frequency average of $|I_1|$ we determine

$$I_3 = \frac{1}{\pi} \int_0^{\pi} [b + a - 2(a\,b)^{1/2} \cos\theta]^{1/2}\, \mathrm{d}\theta. \tag{6.59}$$

Substituting

$$\theta = \pi - 2\varphi$$

and assuming

$$b \gg a \tag{6.60}$$

we find that (see eqs 17.3.3, 17.3.12 in ref. 38)

$$I_3 = \frac{2}{\pi} (\sqrt{b} + \sqrt{a}) \int_0^{\pi/2} [1 - 4\,(a\,b)^{1/2} \sin^2\varphi/(\sqrt{b} + \sqrt{a})^2]^{1/2}\, \mathrm{d}\varphi$$

$$= \frac{2}{\pi} (\sqrt{b} + \sqrt{a})\, E\,[4\,(a\,b)^{1/2}/(\sqrt{b} + \sqrt{a})^2]$$

$$\approx \frac{2}{\pi} (\sqrt{b} + \sqrt{a})\, [1 - (a\,b)^{1/2}/(\sqrt{b} + \sqrt{a})^2 \ldots]$$

$$= \frac{2}{\pi} \frac{b^{3/2} - a^{3/2}}{b-a} \approx \frac{2}{\pi} \sqrt{b}. \tag{6.61}$$

Neglecting q with respect to unity eqs (6.58), (6.59) and (6.61) now yield the following relation for the frequency average $\langle |I_1| \rangle$:

$$\langle |I_1| \rangle \approx \frac{2}{\pi\, k_B} (a\,b)^{1/2}. \tag{6.62}$$

Using eq. (6.47) we find the following approximation for the frequency average of the amplitude of the axial sound pressure:

$$\langle \hat{p}_{ax} \rangle \approx \frac{2\varrho_0}{\pi r} \gamma F_a (\omega a b)^{1/2} \langle |Y_a| \rangle \sin^2 \alpha. \tag{6.63}$$

In region III, for semi-apex angles α not near 90°, the frequency average of $|Y_a|$ is given by eq. (5.38):

$$\langle |Y_a| \rangle = Y_{tc} / \cos^2 \alpha.$$

Using eq. (5.8) we find

$$\langle \hat{p}_{ax} \rangle \approx \frac{\varrho_0}{12^{1/4} \pi^2 r} \left(\frac{k_1 b}{h a} \right)^{1/2} \frac{F_a \tan^2 \alpha}{\varrho \sin \alpha}. \tag{6.64}$$

It is expedient to normalize the above value of $\langle \hat{p}_{ax} \rangle$ with respect to the sound pressure $\hat{p}_0$ at low frequencies (eq. (6.22)) *):

$$\left\langle \frac{\hat{p}_{ax}}{\hat{p}_0} \right\rangle \approx \frac{2}{12^{1/4} \pi \cos^2 \alpha} \left(k_1 b \frac{h}{a} \right)^{1/2} \tag{6.65a}$$

which can also be written as

$$\left\langle \frac{\hat{p}_{ax}}{\hat{p}_0} \right\rangle \approx \frac{2}{12^{1/4} \pi} \left(\frac{f}{f_{ta}} \frac{R_b}{R_a} \frac{h}{R_a \cos^3 \alpha} \right)^{1/2}, \tag{6.65b}$$

where a factor $(1 - \nu^2)^{1/2}$ is omitted. Note that the frequency average of the normalized axial sound pressure increases by 3 dB per octave. Further, it increases relatively fast with increasing α.

The above approximations hold for frequencies in the interval

$$f_{ta} \ll f \ll f_{co}, \tag{6.66}$$

which interval in practice usually lies above the region for which the loudspeaker is designed. Therefore, the practical value of eq. (6.65) is limited. An impression of the value of the normalized mean pressure may be obtained by substituting the following practical values: $\alpha = 60°$, $R_b/R_a = 5$ and $h/R_a = 25 \cdot 10^{-3}$; we find

$$\left\langle \frac{\hat{p}_{ax}}{\hat{p}_0} \right\rangle \approx 0{\cdot}6$$

at $f = 3 f_{ta}$. For the cones numbered 50.1 and 70.2, whose numerically calculated frequency characteristics will be discussed elsewhere, we find a normalized frequency-average sound pressure of 0·2 and 0·5 respectively at $f = 3 f_{ta}$.

*) Equation (6.22) holds for a complete cone but is a fair approximation for the truncated cone if $a \ll b$, which is assumed here (eq. (6.60)).

We may conclude that for frequencies well above f_{ta} (but below f_{co}) the mean value of the axial sound-pressure level increases by 3 dB per octave. This increase is caused by the fact that the ratio of the bending wavelength λ_B to the sound wavelength in air λ_0 increases by $\sqrt{f}$: with increasing frequency the bending waves become acoustically less short-circuited and radiate more sound. The pressure level at a constant frequency strongly increases with α. Since in region II only the outer part of the cone ($x > x_t$) is covered by acoustically short-circuited bending waves, whereas the wavelength on the inner part of the cone is relatively large, we may expect that on the average the sound pressure in region II will be higher than that in region III. In the next sections the above conclusions will be illustrated by numerical calculations.

6.5.5. *A typical example*

In this section all characteristic phenomena encountered in the sound radiation of flexible cones will be discussed on the basis of the numerical evaluation of eqs (6.37) and (6.41) for cone 50.3 (cone parameters in table 5-I) and for a great number of frequencies (about 50). The frequencies are chosen in such a way that the frequency characteristics of the mechanical and acoustical variables can be drawn with sufficient accuracy. In all cases, the calculation of the mechanical variables (axial admittance and transverse displacement pattern) requires a computer time (about 2 minutes for each frequency with an IBM 370/168 computer) which is much longer than that needed for the evaluation of the acoustic variables.

The voice-coil mass will always be neglected. The amplitude of the axial driving force F_a is assumed to be 1 N. The frequency characteristic of the axial admittance of this cone, shown in fig. 5.13, was discussed in sec. 5.7.

Figure 6.7*a* shows the calculated axial sound-pressure level L_p at a distance of 10 metres from the cone top (if not stated otherwise this value will always be taken), the radiated sound-power level L_{W100}, the beam width β and the directivity index DI_{100} of cone 50.3. Comparing fig. 6.7*a* with fig. 6.6*a* for the rigid piston and rigid cone we make the following observations.

Below f_{ra} (1840 Hz) the sound radiation of both the flexible and the rigid cone is practically piston-like. However, at $f_c = 1580$ Hz, L_p of the rigid cone starts to decrease. Because $|y_a|$ becomes minimum at $f_{ra} = 1840$ Hz, we expect a corresponding dip in the flexible-cone response, but this does not appear, owing to the increasing transverse amplitude $w(b)$ at the outer edge, as explained in sec. 6.5.3.

Although $f_c < f_{ra}$, no rigid-cone roll-off appears above f_c because f_c and f_{ra} lie relatively close together (sec. 6.5.3). In region II ($f_{tb} \leqslant f \leqslant f_{ta}$) the sound radiation is predominantly controlled by the more or less uniformly vibrating inner part of the cone; the acoustically short-circuited bending waves on the outer part of the cone radiate little sound. In this region, cone 50.3 shows a

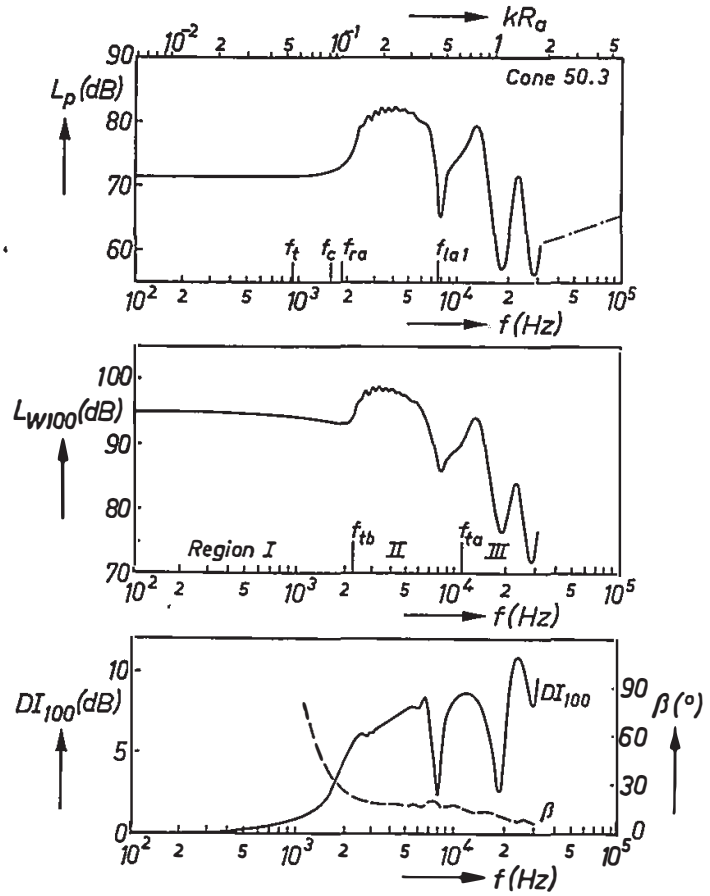

Fig. 6.7*a*. Calculated frequency characteristics of cone 50.3.

broad maximum with a superimposed fine structure (bending resonances and antiresonances) followed by a deep minimum at the first longitudinal antiresonant frequency $f_{la1} = 7513$ Hz where $|y_a|$ becomes minimum (fig. 5.13). In the high-frequency region (region III, $f > f_{ta}$) the pressure response shows the same oscillating character as the frequency characteristic of $|y_a|$: peaks and dips appear at longitudinal resonant and antiresonant frequencies (eq. (6.40)). However, the mean value of L_p decreases with increasing frequency to the level predicted by the high-frequency approximation (eq. (6.65)). If L_p had been calculated for higher frequencies than those plotted in fig. 6.7*a* the mean value of L_p would be shown to rise again, as explained in sec. 6.5.4. The high-frequency approximation eq. (6.65) is represented by the dash-dotted line.

The power response of cone 50.3 is shown by the middle graph of fig. 6.7*a*. Below f_t the response is practically frequency-independent, as predicted by the low-frequency approximation (sec. 6.5.3). A roll-off starts at f_t with a faint minimum at f_{ra}, as was also explained in sec. 6.5.3. On the average the power response has roughly the same shape as the pressure response, although the

former does not have such a high maximum in region II but has a steeper mean slope in region III than the latter. Both differences indicate a main lobe in the axial direction.

Above f_{ra} the beam width β of a flexible cone (bottom picture) is greater than that of the rigid piston and rigid cone (cf. fig. 6.6*b*). This is due to the wave motion of the cone surface, which smooths the directivity diagram.

The directivity index DI_{100} is relatively low below cone break-up ($f < f_{ra}$); in this frequency region it is about equal to that of the rigid piston and the rigid cone. Above f_{ra}, however, the slope is much less than that of the rigid piston, because in region II the radiating area decreases with increasing frequency and in region III bending waves, which radiate sound in all directions, cover the entire cone. Compared with the rigid cone, DI_{100} of the flexible cone is in general higher, because the former radiates a great deal of energy normal to its surface.

Minima in the DI_{100} characteristic occur at the axial membrane resonant frequencies (7968 and 17960 Hz); as will be explained below, they indicate a broad sidelobe at these frequencies.

Figures 6.7*b* and *c* illustrate the shape of the directivity pattern in the various frequency regions. At 1 kHz (region I) the radiation is practically uniform; at 5 and 10 kHz (region II) a main axial lobe appears; at 20 kHz (region III) this lobe has become narrower and a broad sidelobe normal to the cone surface shows up.

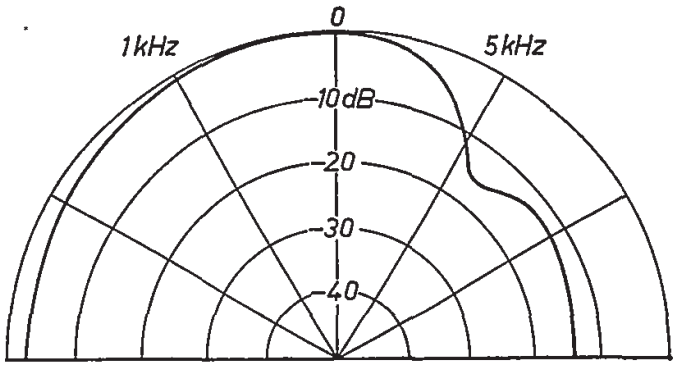

Fig. 6.7*b*. Calculated directivity diagrams of cone 50.3 at 1 kHz (left) and 5 kHz (right).

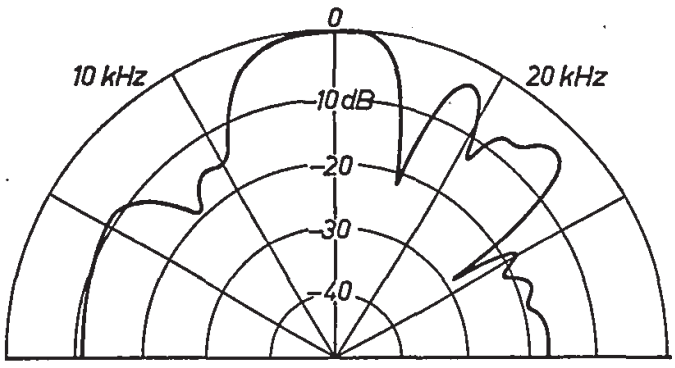

Fig. 6.7*c*. Calculated directivity diagrams of cone 50.3 at 10 kHz (left) and 20 kHz (right).

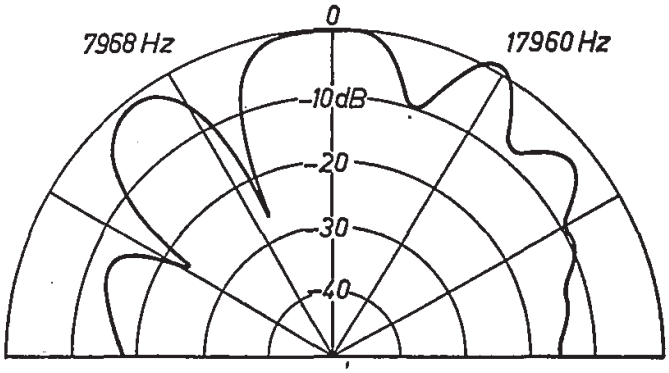

Fig. 6.7*d*. Calculated directivity diagrams of cone 50.3 at the first (left) and second (right) membrane resonant frequencies.

Pronounced sidelobes appear at the membrane resonant frequencies f_{mr}. At these frequencies (about 7968, 17960, 28610 Hz for cone 50.3) the entire cone comes into pure membrane resonant conditions, which overshadow all bending effects (sec. 5.8). At least, this occurs in the absence of internal losses. Because the wavelength λ_1 of the longitudinal waves is three to four times longer than λ_0, much sound is radiated normal to the cone surface. It may even occur that the sound pressure radiated in axial direction becomes smaller than that radiated in directions approximately normal to the cone surface. In that case the minima in the frequency characteristic of the axial sound-pressure level L_p at the longitudinal antiresonant frequencies f_{lan} may be further lowered (as discussed in sec. 4.7.3, f_{mrn} approaches f_{lan} with increasing n).

In the presence of internal damping the longitudinal resonance cannot fully build up, because the reflected longitudinal wave is damped. In that case, bending waves with $\lambda_B \ll \lambda_0$ are superimposed upon the longitudinal wave (figs 5.22*a* and *b*) which somewhat flatten the sidelobe. This blurring effect increases with increasing δ, owing to the decreasing longitudinal-wave amplitude. Nevertheless, even for $\delta = 0{\cdot}1$ strong sidelobes exist, as the directivity patterns at the first and second membrane resonant frequencies show (fig. 6.7*d*).

6.5.6. *Influence of the cone geometry*

In the next sections the influence of the cone geometrical parameters h, R_b and α on the sound radiation will be discussed on the basis of numerical examples.

6.5.6.1. Influence of the cone thickness

Figure 6.8 shows the calculated frequency characteristics of cone 50.1, which has the same parameters as cone 50.3 except that the thickness is reduced from 0·23 to 0·1 mm. This reduction in thickness eliminates the fine structure, as explained in sec. 5.7.1 (cf. figs 6.7*a*, 6.8). The mean shapes of the characteristics are approximately equal.

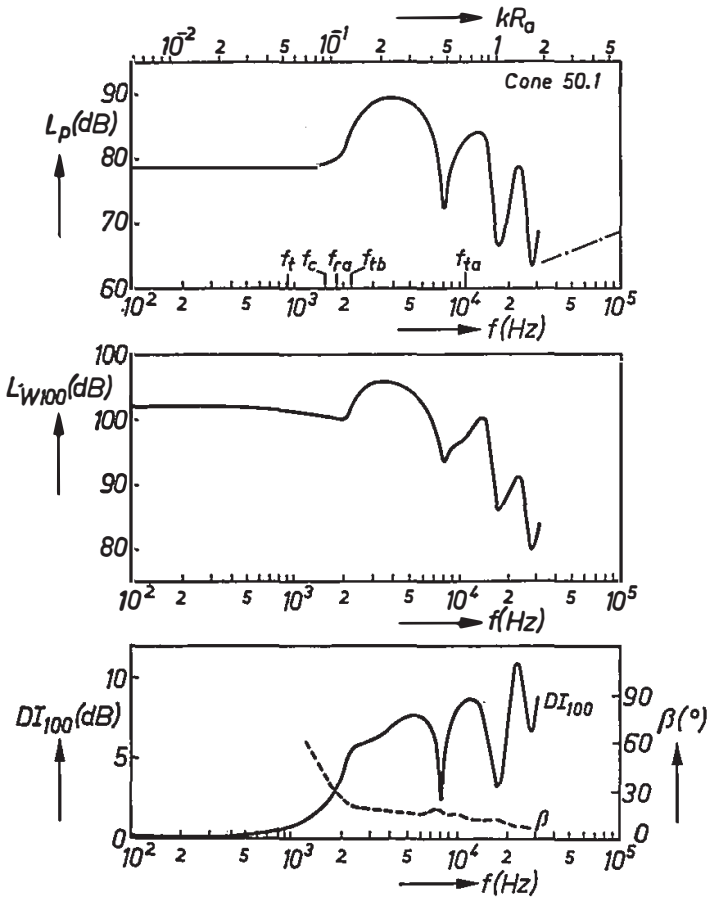

Fig. 6.8. Calculated frequency characteristics of cone 50.1.

At low frequencies, the L_p and L_{W100} characteristics are shifted upwards by 7·2 dB relative to those of cone 50.3 because of the difference in cone mass.

In the high-frequency region ($f > f_{ta}$) the L_p characteristic decreases, as discussed in sec. 6.5.5; if L_p is calculated for higher frequencies than those shown in fig. 6.8 we would find an average value lying below that for cone 50.3 (fig. 6.7*a*). The high-frequency approximation is again represented by the dash-dotted line.

The characteristics of the directivity index DI_{100} and the beam width β of the cones 50.1 and 50.3 are also practically equal. This is trivial in the low-frequency region; in the high-frequency region the directivity patterns are the same because in both cases the bending waves are acoustically well short-circuited.

In all subsequent calculations the thickness h will be taken as 0·1 mm to eliminate the fine structure. In this way the number of frequencies at which the mechanical variables have to be calculated can be reduced from at least 50 to about 30, which considerably shortens the computer time required.

6.5.6.2. Influence of the outer-edge radius

In this section the influence of a variation of the outer-edge radius R_b will be discussed. It was shown in chapter 4 that the ring antiresonant frequency f_{ra} is

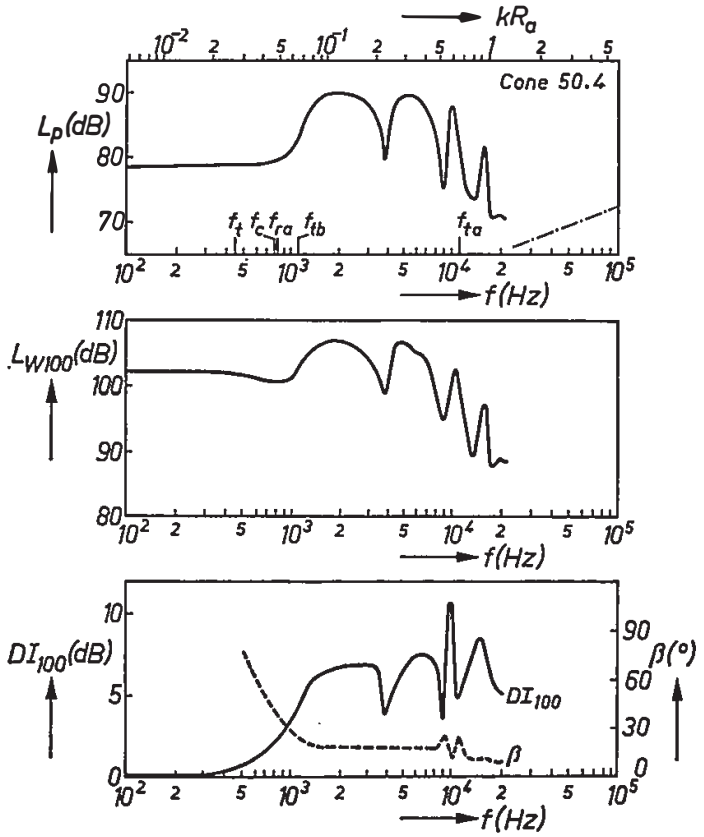

Fig. 6.9. Calculated frequency characteristics of cone 50.4.

inversely proportional to R_b (eq. (6.42)); the same holds for the characteristic cone frequency f_c (eq. (6.26b)). Therefore, a variation of R_b will not change the ratio of these frequencies, and the shape of the L_p response up to f_{ra} will be independent of R_b. The longitudinal resonant and antiresonant frequencies are inversely proportional to the meridional cone length $L = b - a$. If $b \gg a$, L is approximately proportional to R_b. Hence, the longitudinal resonant and antiresonant frequencies are also inversely proportional to R_b. Therefore, an increase of R_b means a shifting of the whole frequency response to lower frequencies. This is illustrated in the following example.

The outer radius R_b of cone 50.1 is doubled, which leads to cone 50.4 (cone parameters in table 5-IV). The frequency characteristic of the axial admittance of this cone, shown in fig. 5.17, was discussed in sec. 5.7.3.

Figure 6.9 shows the calculated acoustic performance of cone 50.4. As compared with cone 50.1, all characteristic frequencies are approximately halved and the curves are shifted to the lower side of the spectrum. In the low-frequency region the values of L_p and L_{W100} are equal in both cases, because the ratio of the cone base area S_b to the cone mass M_d remains practically *) unchanged (eq. (6.22)).

The foregoing is well illustrated by fig. 6.10, in which the frequency charac-

*) Remember that M_d is the mass of the truncated flexible cone.

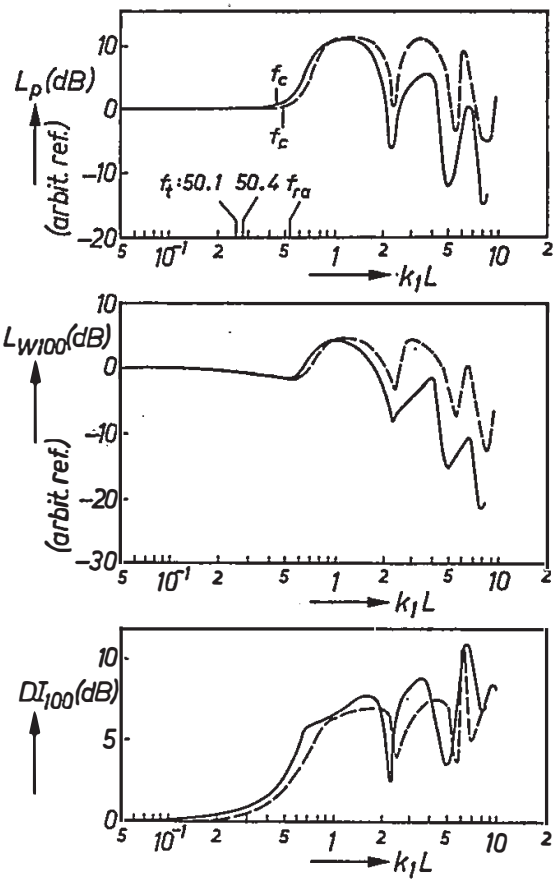

Fig. 6.10. Comparison of the calculated frequency characteristics of the cones 50.1 (drawn curves) and 50.4 (dashed).

teristics of L_p, L_{W100} and DI_{100} of the cones 50.1 and 50.4 are plotted as a function of the dimensionless frequency parameter k_1L. The value of L_p and L_{W100} are taken relative to the low-frequency value. Note that in the high-frequency region the mean values of L_p and L_{W100} of cone 50.4 are higher than those of cone 50.1. According to the high-frequency approximation eq. (6.65) (which cannot be used rigorously in the region considered), this difference should be about 3 dB.

6.5.6.3. Influence of the apex angle

The influence of a variation of the apex angle is demonstrated by comparing the frequency characteristics of cone 50.1 ($\alpha = 50°$) with those of cone 60.1 ($\alpha = 60°$) and cone 70.2 ($\alpha = 70°$). The other geometrical and material parameters of these cones are equal and given in tables 4-I, 5-II and 5-III.

We will first discuss cone 60.1. The frequency characteristic of the axial admittance was shown in fig. 5.15 and discussed in sec. 5.7.2. The frequency characteristics of the acoustic output of cone 60.1 are shown in fig. 6.11. Compared with cone 50.1 the values of L_p and L_{W100} have increased by about 1 dB because of the smaller cone mass. Region II is shifted to lower frequencies and the broad maximum has decreased in height. In the high-frequency region the

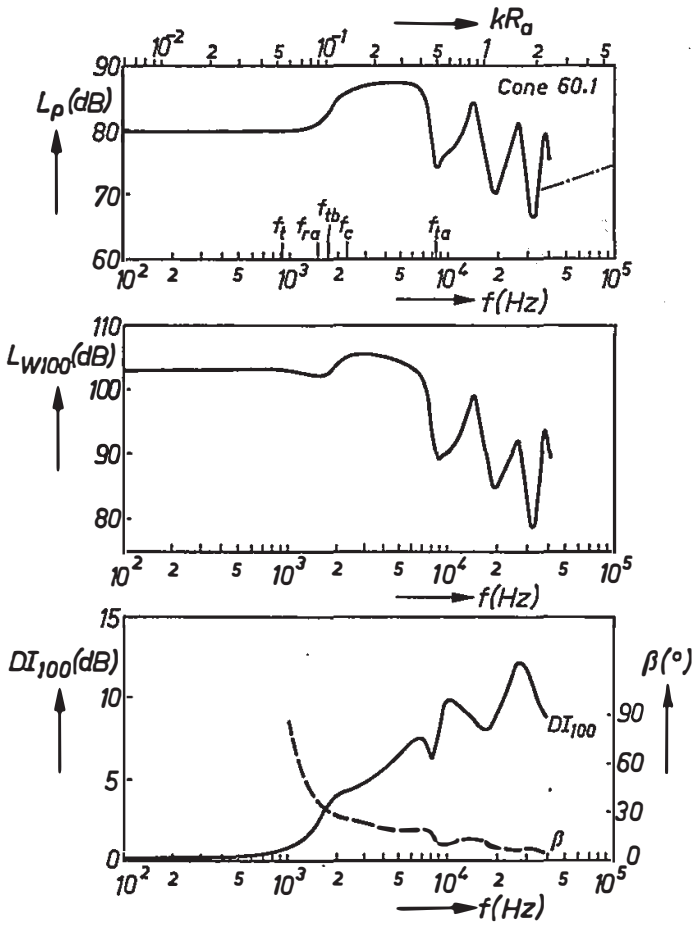

Fig. 6.11. Calculated frequency characteristics of cone 60.1.

longitudinal resonant and antiresonant frequencies are shifted slightly upwards. The DI_{100} characteristic of cone 60.1 runs higher in this region.

The above applies equally well to cone 70.2, the frequency characteristics of which are shown in fig. 6.12. Note the pronounced maximum at $f_{rr} = 6500$ Hz; the broad maximum in region II has still further decreased, although the $|Y_a|$ characteristics run higher for larger α (cf. figs 5.14, 5.15 and 5.16). This is explained as follows. As stated previously, in region II only the inner part of the cone radiates effectively. An increase in apex angle reduces this inner part because $x_t \propto 1/\tan \alpha$ (eq. (4.10)). This decreases L_p and L_{W100} in the lower part of region II.

The influence of a variation of the apex angle is more clearly illustrated by fig. 6.13, in which the frequency characteristics of the cones 50.1, 60.1 and 70.2 are plotted as a function of the dimensionless frequency parameter $k_1 L$. In this way the differences in the higher longitudinal resonant and antiresonant frequencies are eliminated. This figure clearly illustrates the effects of an increasing α, viz.

(1) the decrease of f_{ra},

(2) the decrease of L_p, L_{W100} and DI_{100} in region II,

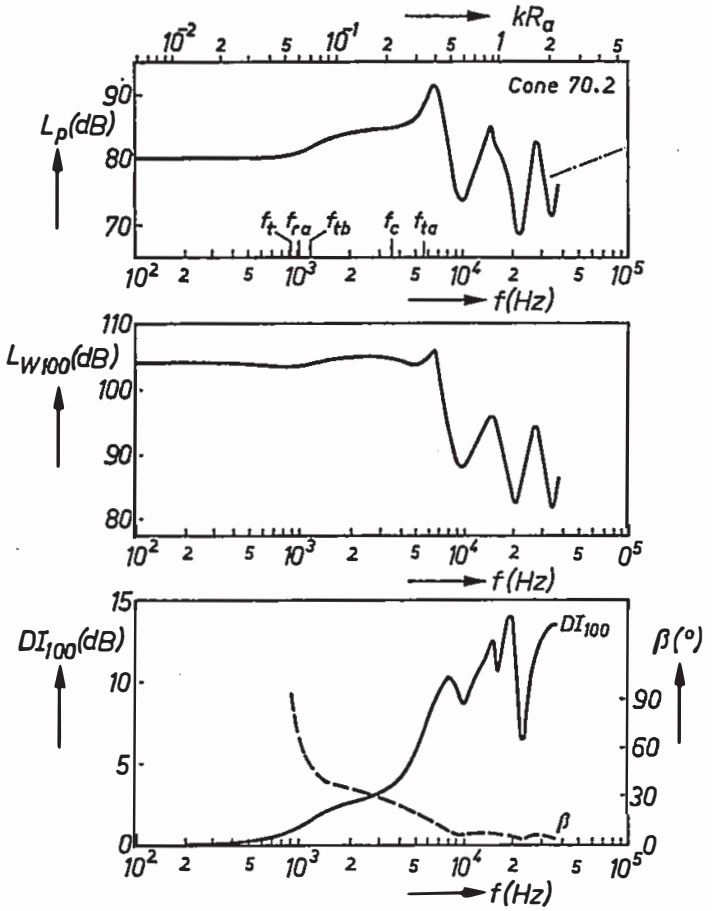

Fig. 6.12. Calculated frequency characteristics of cone 70.2.

(3) the increase of the mean value of L_p and DI_{100} for the highest frequencies (in accordance with eq. (6.65)). In this region DI_{100} increases because the sidelobe normal to the cone surface shifts closer to the cone axis with increasing α.

6.5.7. *Influence of the cone material*

In this section, the influence of the cone material will be described. The cone material is determined by Young's modulus E, the mass per unit volume ϱ, Poisson's ratio ν and the internal loss factor δ. The influence of δ on the mechanical cone behaviour has been discussed in sec. 5.7; an increase in δ smooths the peaks and dips in the frequency characteristic of $|Y_a|$; the same occurs in the frequency characteristics of the acoustic quantities. This will not be further illustrated. Poisson's ratio ν has in general a negligible influence; only the lower axial membrane resonant frequencies depend to a certain extent on its value (eq. (4.63)).

A rough estimate of the influence of the remaining material parameters E and ϱ can be given on the basis of eq. (6.39). The positions of the peaks and dips in the pressure and the power responses are proportional to $c = (E/\varrho)^{1/2}$. At low frequencies the axial admittance $|Y_a|$ is proportional to $1/\varrho$ (eq. (5.28)). At

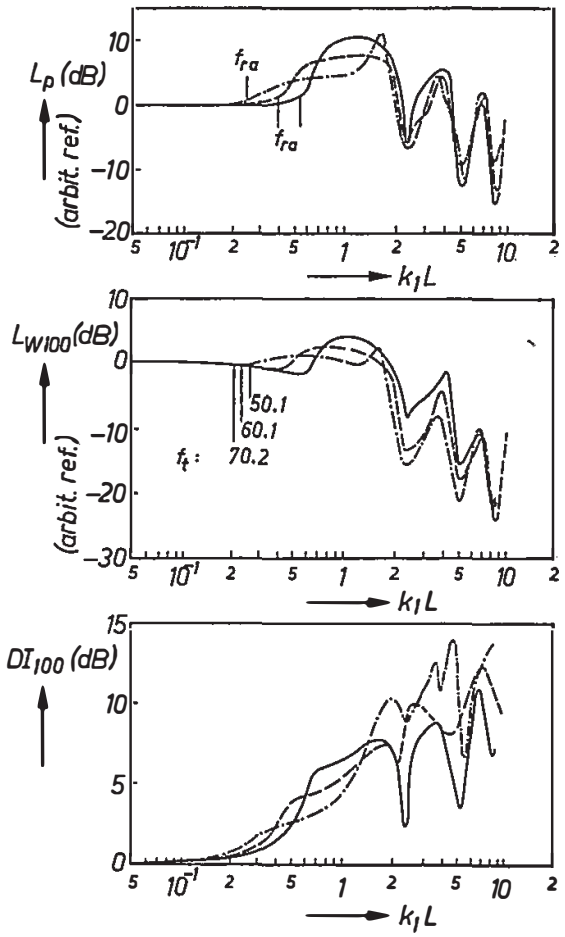

Fig. 6.13. Comparison of the calculated frequency characteristics of three cones with different apex angles: ——— cone 50.1, - - - - cone 60.1, - · - · - · - cone 70.2.

high frequencies the frequency average of $|Y_a|$ is determined by Y_{tc} (eq. (5.38)) and is consequently proportional to $1/\varrho c$. The reduced velocity distribution $V_t(x)$ is influenced by c.

The above is illustrated in figs 6.14*a* and *b* which show the frequency characteristics of the acoustic performance of cone 50.1 if its specific mass density is increased and decreased by a factor of 4 respectively. Compared with fig. 6.8 the resonant and antiresonant frequencies as well as the transition frequencies f_{tb} and f_{ta} are halved and doubled. The frequencies f_t and f_c remain unchanged.

In the low-frequency region the values of L_p and L_{W100} in figs 6.14*a* and *b* differ by 24 dB. Owing to the high value of c in fig. 6.14*b*, the characteristic cone frequency f_c falls well below cone break-up, which causes a faint minimum at f_{ra} in the L_p characteristic. In the L_{W100} characteristic a clear dip occurs at f_{ra}, as discussed in sec. 6.5.3. In the power response of fig. 6.14*a* this dip has completely disappeared, since $f_{ra} \approx f_t$ here.

In the mid-frequency region (region II) the broad maximum decreases with decreasing c, since this region shifts to lower frequencies. This enhances the acoustic short-circuit of the inner cone part, which is responsible for the radiation in this region.

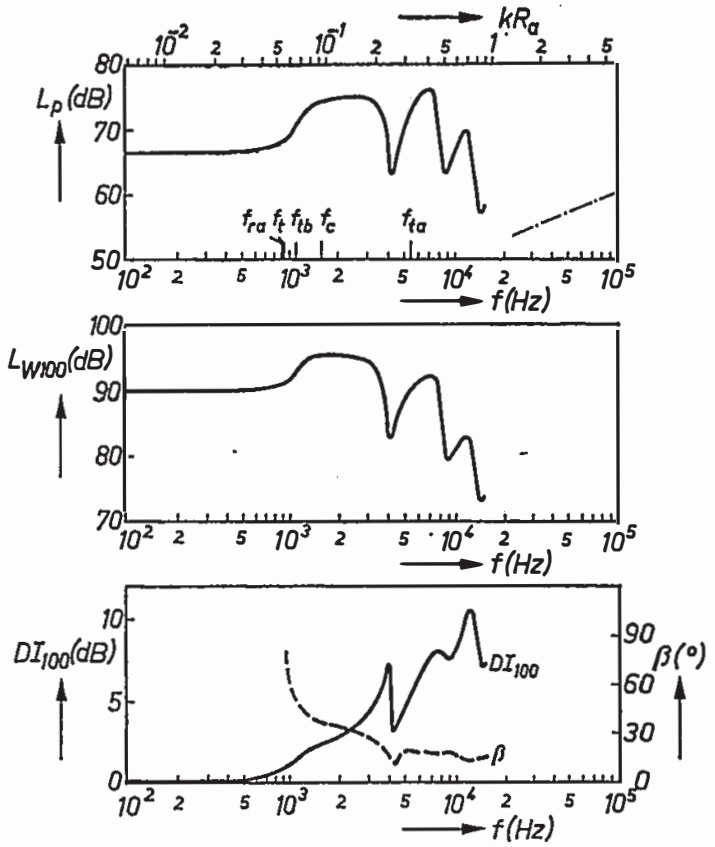

Fig. 6.14*a*. Calculated frequency characteristics of cone 50.1 with a mass density $\varrho = 2400\ \mathrm{kg/m^3}$.

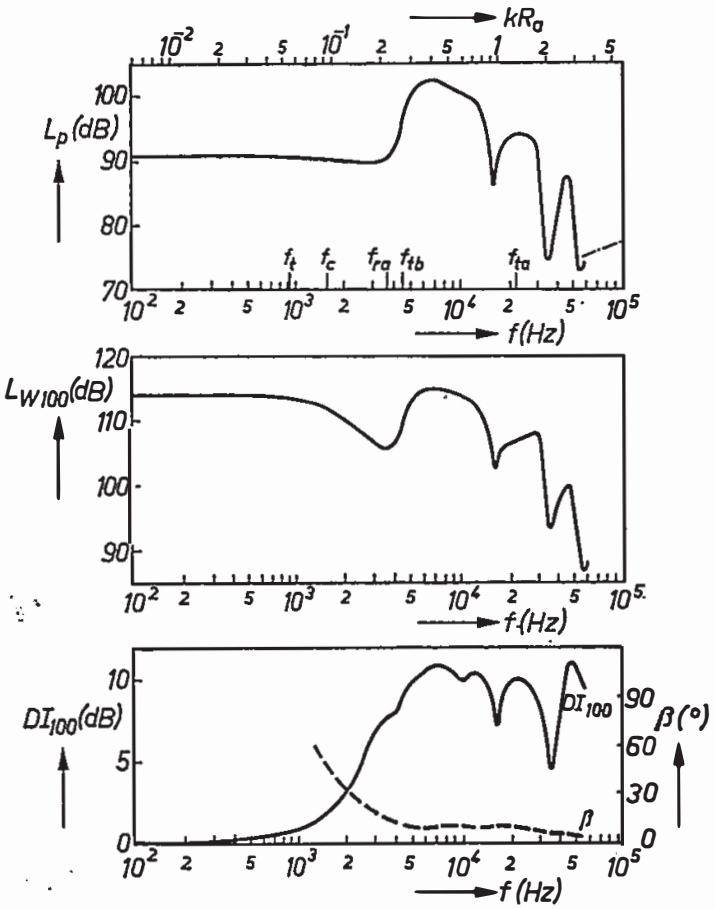

Fig. 6.14*b*. Calculated frequency characteristics of cone 50.1 with a mass density $\varrho = 150\ \mathrm{kg/m^3}$.

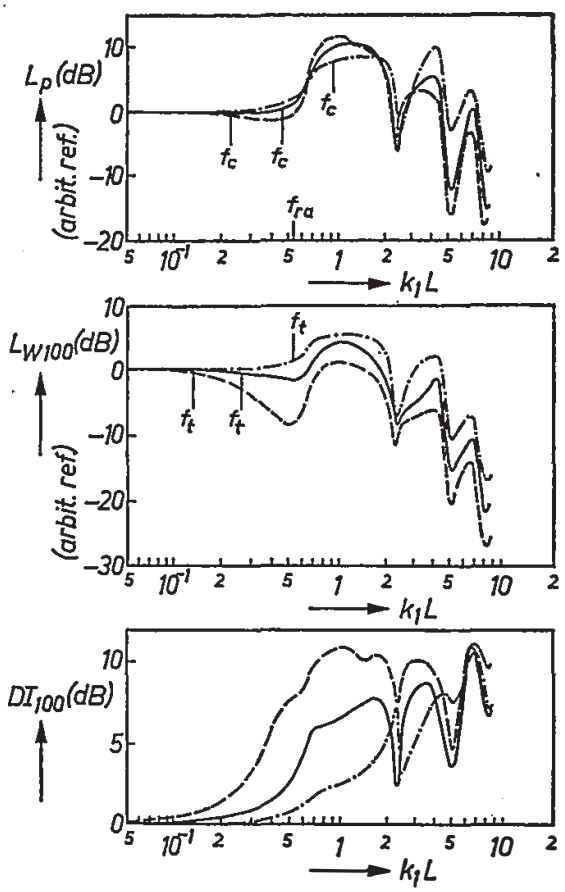

Fig. 6.15. Comparison of the calculated frequency characteristics of cone 50.1 with different mass densities ϱ: - - - - 150 kg/m^3, ——— 600 kg/m^3, - · - · - · - 2400 kg/m^3.

In the high-frequency region the influence of a variation of ϱ can be better illustrated with the aid of fig. 6.15, where k_1L is used as the independent variable. Since L_p and L_{W100} are proportional to $1/\varrho$ at low frequencies and to $1/\sqrt{\varrho}$ at high frequencies, a normalization relative to the low-frequency value means a 6-dB decrease at high values of k_1L when ϱ decreases by a factor of 4. In these normalized characteristics the dips at high values of k_1L remain at rest, which proves that these dips are determined mechanically.

According to the high-frequency approximation eq. (6.65a) the normalized characteristics should have the same mean value. This is not the case; the reason may be that the condition $f \gg f_{ta}$ is not fully satisfied at the frequencies considered.

The DI_{100} characteristics of fig. 6.15 show the increasing acoustic short-circuit in regions I and II as ϱ increases. In the high-frequency region, there is not much difference because in all cases the bending waves are well short-circuited.

In the foregoing, the influence of a variation of the mass density ϱ was discussed. The influence of a variation of Young's modulus E on the frequency characteristics of L_p and L_{W100} can now be easily predicted. At low frequencies the influence is small: dips may appear at f_{ra}. At high frequencies the influence

of E on L_p and L_{W100} is the same as that of ϱ. The positions of the peaks and dips, being proportional to c, show the inverse dependence on E as compared with ϱ.

6.5.8. *Influence of a rigid cone top*

In the preceding calculations the interval $0 \leqslant x < a$ was assumed to radiate no sound. However, in practice the cone is either complete or it is truncated and provided with a dust cap. If this part is relatively rigid, it may considerably contribute to the sound radiation in the high-frequency region.

This is shown by fig. 6.16 where L_p, L_{W100} and DI_{100} are plotted as functions of $k_1 L$ for the cones 50.1, 60.1 and 70.2 with a massless rigid conically shaped top having the same apex angle as the cone. These characteristics should be compared with those of fig. 6.13. The additional cone top has little influence in the low-frequency region, at least if $b \gg a$. In the high-frequency region, however, the top contributes considerably to the sound radiation. It increases the radiation in the direction normal to the cone surface and therefore lowers the DI_{100} curves, which may even become negative. This occurs in the case of cone

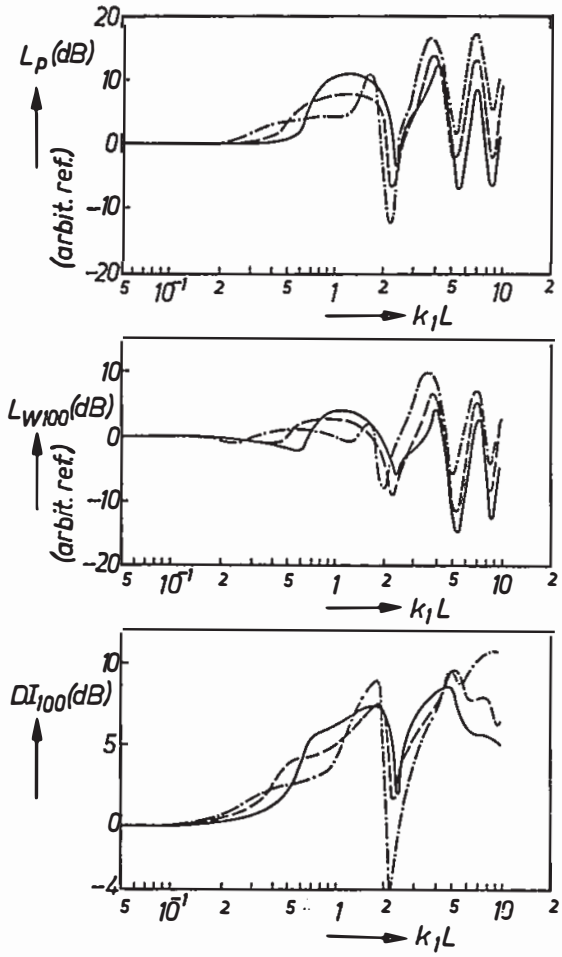

Fig. 6.16. Comparison of the calculated frequency characteristics of three cones with a rigid conical top: ——— cone 50.1, - - - - cone 60.1, - · - · - · - cone 70.2.

70.2 at the first membrane resonant frequency ($k_1 L = 2{\cdot}1$), at which there is already a big sidelobe for the truncated cone. Of course, in practice the contribution of the cone top is not as extreme as shown in fig. 6.16 because it is not completely rigid. This section only serves an illustrative purpose. In the following we will again consider the sound radiation of truncated cones.

6.5.9. *Influence of the voice-coil mass*

In the preceding radiation calculations the mass of the voice coil and of the other parts attached to the inner cone edge (suspension, dust cap) was not taken into account. The influence of this additional mass (briefly called M_c in the following) on the frequency characteristic of the mechanical impedance was discussed in sec. 5.10 and illustrated in figs 5.23, 5.24 and 5.25. In the latter section it was shown that above the frequency at which $|Z_a|$ and ωM_c become equal the additional mass completely changes the shape of the frequency characteristic of the axial admittance: the total admittance $|Y_{tot}|$ decreases with $1/f$ (fig. 5.25). Below the mentioned frequency, the $|Y_a|$ characteristic is only shifted downwards without a change of the shape. The same effects can be observed in the frequency characteristics of the acoustic quantities, which will now be discussed.

In the presence of a voice-coil mass the total axial impedance becomes

$$Z_{tot} = Z_a + j\omega M_c. \tag{5.40}$$

Calling $v_t(x)$ the transverse velocity distribution on the cone for $M_c = 0$, we find for the velocity distribution $v_t'(x)$ in the presence of M_c:

$$v_t'(x) = \frac{Z_a}{Z_a + j\omega M_c} v_t(x). \tag{6.67}$$

The reduced velocity distribution $V_t(x)$ is not influenced by M_c:

$$V_t'(x) = \frac{v_t'(x)}{v_t'(a)} = \frac{v_t(x)}{v_t(a)} = V_t(x). \tag{6.68}$$

This means that the absolute value of the axial sound pressure now becomes

$$\hat{p}'_{ax} = \frac{\varrho_0}{r} \omega F_a \left| Y_{tot} I_1 \right| \sin^2 \alpha \tag{6.69}$$

where the integral

$$I_1 = \int_a^b V_t(x) \exp(j k_0 x \cos \alpha)\, x \, dx$$

is not changed by the introduction of M_c, and Y_{tot} is the inverse of Z_{tot}, given by eq. (5.40). Hence, the axial sound pressure $\hat{p}'_{ax}$ and sound power W'_{100} of a cone with an additional voice-coil mass are related to $\hat{p}_{ax}$ and W_{100} of the same cone with $M_c = 0$ by the expression

$$\frac{\hat{p}'_{ax}}{\hat{p}_{ax}} = \frac{W'_{100}}{W_{100}} = \left|\frac{Y_{tot}}{Y_a}\right| = \left|\frac{Z_a}{Z_a + j\omega M_c}\right|. \tag{6.70}$$

For frequencies at which

$$\omega M_c \gg |Z_a| \tag{6.71}$$

we find

$$\frac{\hat{p}'_{ax}}{\hat{p}_{ax}} = \frac{W'_{100}}{W_{100}} \approx \left|\frac{Z_a}{\omega M_c}\right|. \tag{6.72}$$

Because eq. (6.71) is usually satisfied in the high-frequency region, in which $\hat{p}_{ax}$ already decreases, this roll-off is further steepened by M_c.

Condition (6.71) can be further elaborated by introducing the mean value of $|Z_a|$ in the high-frequency region:

$$\langle |Z_a| \rangle = 2\pi R_a \varrho h c_1 \cos^2 \alpha \tag{6.73}$$

which follows from eqs (5.38) and (4.46).

Substituting eq. (6.73) into eq. (6.71) we find as an approximative expression for the frequency region in which the voice-coil mass steepens the roll-off:

$$f > f_{ta} \frac{M_d}{M_c} \left(\frac{R_a}{R_b}\right)^2 \sin 2\alpha. \tag{6.74}$$

Equation (6.72) then becomes

$$\frac{\hat{p}'_{ax}}{\hat{p}_{ax}} = \frac{W'_{100}}{W_{100}} \approx \frac{f_{ta}}{f} \frac{M_d}{M_c} \left(\frac{R_a}{R_b}\right)^2 \sin 2\alpha. \tag{6.75}$$

In the derivation of eqs (6.74) and (6.75) a factor $(1 - \nu^2)^{1/2}$ is omitted, while the cone mass M_d is approximated by

$$M_d \approx \pi R_b^2 \varrho h / \sin \alpha \tag{6.76}$$

which is valid for $b^2 \gg a^2$.

In the vicinity of f_{ta} the pressure and power characteristics decrease in any case so that f_{ta} can roughly be considered as the upper limit of the loudspeaker response. This upper limit is not shifted downwards by the voice-coil mass if

$$\frac{M_c}{M_d} < \left(\frac{R_a}{R_b}\right)^2 \sin 2\alpha. \tag{6.77}$$

For a cone with $\alpha = 60°$ and $R_b/R_a = 5$ we find $M_c < 0{\cdot}03\ M_d$, which is too low to be of any value in practice. The latter condition might be satisfied by taking an exceptionally heavy cone as compared with the voice coil; however, this would greatly reduce the pressure and power levels and hence the efficiency of the loudspeaker.

In practice, the dip in the pressure and power characteristics that occurs in any loudspeaker at the first longitudinal antiresonant frequency f_{la1} will usually be inacceptable. Then the upper limit of the frequency response of a loudspeaker is in fact formed by f_{la1}. If $f_{la1} < f_{ta}$ the ratio of the voice-coil mass to the cone mass may therefore be somewhat higher. In practice this ratio is mostly higher than 0·1 and the upper frequency limit is usually decreased by the voice-coil mass. On the other hand the bandwidth of a given loudspeaker can be increased by making the ratio M_c/M_d as small as possible *). This can be achieved by minimizing the voice-coil mass or by making the cone heavy. Of course the latter cannot be done without loss of efficiency.

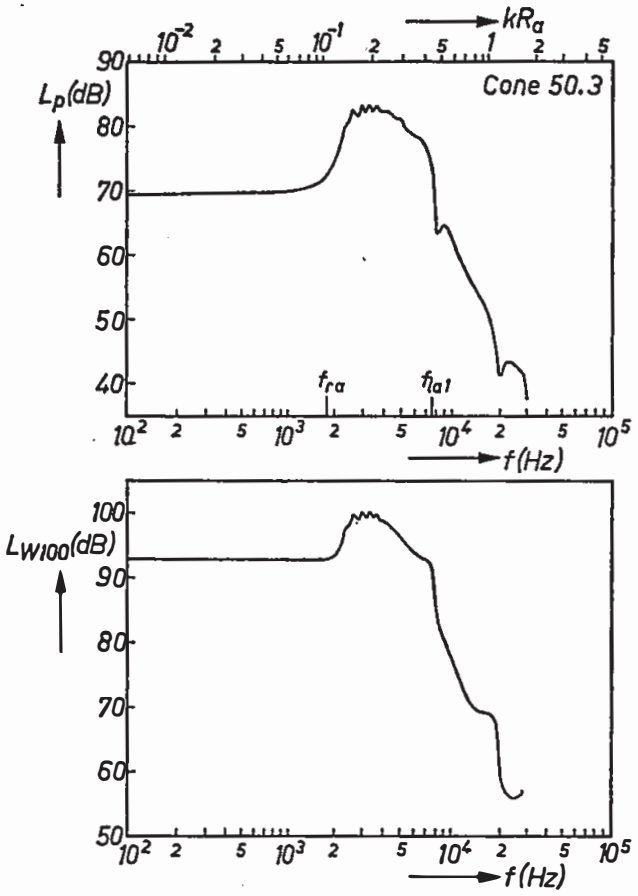

Fig. 6.17*a*. Calculated pressure and power responses of cone 50.3 with a voice-coil mass $M_c = M_d/4$.

*) For maximum efficiency of the electro-acoustical conversion below cone break-up, the voice-coil mass M_c should be equal to the sum of the cone mass M_d and the mass of the air load $8\ \varrho_0\ R_b^3/3$ [41]).

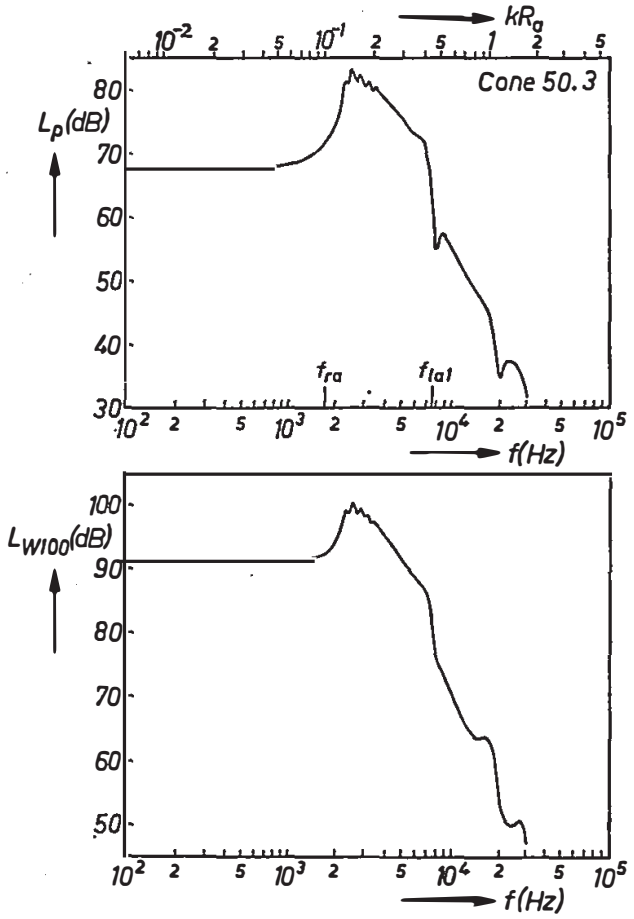

Fig. 6.17*b*. Calculated pressure and power responses of cone 50.3 with a voice-coil mass $M_c = M_d/2$.

Figures 6.17*a* and *b* show the pressure and power responses of cone 50.3 with an additional voice-coil mass M_c equal to one fourth and to one half of the cone mass M_d respectively. In the low-frequency region, the pressure and power levels are lower than those of fig. 6.7*a*, because of the increase of the total mass. The upper limit of the frequency response is in both cases formed by the first longitudinal antiresonant frequency, where a very steep roll-off occurs. Because the reduced transverse velocity distribution $V_t(x)$ is not influenced by M_c, the frequency characteristic of the directivity index is not changed; for cone 50.3 it is shown in fig. 6.7*a*.

6.6. Measurements

Measurements have been carried out for two reasons. First, to verify experimentally the preceding calculations the calculated and measured frequency

characteristics of three plastic cones are compared with each other in sec. 6.6.1. Secondly, it is shown in sec. 6.6.2 on the basis of the measured frequency responses of four commercial loudspeakers that the rough shape of these responses can be explained on the basis of a few easily obtainable characteristic frequencies. In all figures the indicated positions of f_{ra}, f_{la1}, f_t and f_{ta} are calculated for the case $M_c = 0$ (the influence of M_c on f_{ra} and f_{la1} is comparatively small).

6.6.1. *Comparison of calculated and measured acoustical behaviour*

The preceding calculations are experimentally verified by acoustical measurements on the three plastic loudspeaker cones 50.5e, 60.2e and 70.3e, whose geometry and material parameters have been given in tables 5-VI and 5-VII. To prevent acoustic short-circuit a textile disc of negligible weight and stiffness was attached in the plane of the inner edge of these truncated cones. The measured frequency characteristics will be compared with the calculated ones of cones 50.5, 60.2 and 70.3, which have the same values of R_a, R_b, E, ϱ and M_c/M_d as the above experimental cones (see tables 5-VIII and 5-IX). The thickness h of the cones 50.5 and 70.3 is smaller than that of their corresponding experimental specimens (50.5e and 70.3e). The theoretical value of the loss factor δ is taken higher than the experimental value to account for radiation and rim damping.

The measurements are carried out as follows. First, the frequency characteristic of the axial sound-pressure level L_p is measured for the unbaffled cones without outer suspension in an anechoic chamber (driving current $i_{\text{eff}} = 100$ mA, microphone distance $r = 0{\cdot}5$ m). This is done to show the influence of the outer suspension which is attached afterwards; moreover, most frequency characteristics are given for an unbaffled cone in practice. Because a baffle is always assumed in the calculations, calculations and measurements deviate considerably in the low-frequency region. The free responses should therefore only be considered as an illustration and a reference for the understanding of other unbaffled characteristics. Subsequently the cone is provided with a rubber outer suspension of 5 g and placed in an acoustic box of 100 l. This box is attached to the middle of a square baffle ($1{\cdot}5 \times 1{\cdot}5$ m^2), which should approximate to the infinite baffle assumed in the calculations. The axial sound-pressure level is then again recorded with $i_{\text{eff}} = 300$ mA and $r = 1$ m.

The sound-power level L_{W100}, the directivity index DI_{100} and the beam width β are measured as follows. Ten microphones are distributed with equal mutual spacings over 50 degrees of a circle (fig. 6.18). The loudspeaker is fed with a signal current of 200 mA. For a number of discrete frequencies, the sound-pressure levels of the microphones are stored on paper tape, which is used as input for a computer program. With the latter, L_{W100} is calculated by

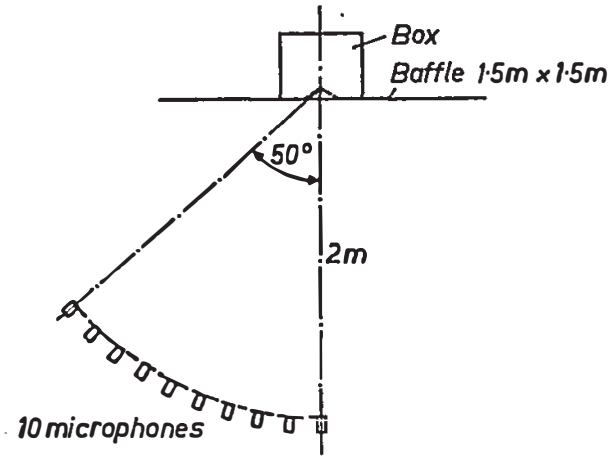

Fig. 6.18. Set-up for the measurement of the sound-power level L_{W100}, the directivity index DI_{100} and the beam width β.

numerical integration; DI_{100} is calculated using eq. (6.4). With the same program, β is calculated by inverse linear interpolation.

At each frequency, the acoustic parameters are determined as the mean value of two measurements by each microphone; the second measurement is carried out after rotating the loudspeaker by 180 degrees about its own axis. This is done to compensate for measuring errors caused by possible azimuthal asymmetries in the directivity diagram.

It was remarked above that there is a mass difference (caused by the difference in h) between the experimental cones 50.5e and 70.3e and the cones 50.5 and 70.3 on which the calculations are carried out. The degree of correction for this mass difference is obtained in the calculations by making the applied force per unit mass equal to the value in the experiment. In all figures the calculated curves are shown dashed, whereas the measured curves are represented by drawn curves.

Figure 6.19*a* shows the calculated and measured frequency characteristics of cones 50.5 and 50.5e respectively, both with $M_c = 0{\cdot}24\, M_d$. The upper figure shows the measured response of the unbaffled cone, which of course greatly deviates from the calculated curve in the low-frequency region (acoustic short-circuit). A deep minimum occurs at $f^- = 1500$ Hz, where the sound wave radiated by the front of the cone arrives in the measuring point in antiphase with the wave emanating from the back of the cone. This pronounced dip only occurs if the cone vibrates more or less uniformly at f^-. This is indeed the case for cone 50.5e, for which $f^- \approx f_{ra}$.

If we assume that the value of f^- is independent of the apex angle, the cones 60.2e and 70.3e would also show a dip at 1500 Hz. However, this dip does not appear since for these cones $f_{ra} < 1500$ Hz (cf. figs 6.20*a*, 6.21*a*, upper figures). At $f^+ \approx 1000$ Hz the waves from the back of the cones arrive in phase with

those from the front and cause a higher pressure level L_p than the theoretical level for the baffled cones.

For frequencies much higher than $f_t = 920$ Hz, a baffle has not much influence: the sound wavelength λ_0 has become so small that the cone acts as its own baffle (remember that mainly the inner part of the cone provides the sound radiation in region II). At these frequencies there is a satisfactory agreement between the calculated and measured curves.

It should be noted that the loss factor of the measured cone is lower than that assumed in the calculations; this causes the measured response to be more spiky. In the high-frequency region the measured curve runs higher than the calculated one. A possible cause may be the fact that the voice-coil cylinder is not completely rigid and the inner edge of the cone may vibrate with significant amplitudes in other directions than the axial one. This may lead to a higher motional impedance (see fig. 5.28) and a higher sound pressure.

The lower part of fig. 6.19*a* shows the calculated response of cone 50.5 and the measured response of cone 50.5e in the above-mentioned box-baffle system. The fundamental loudspeaker resonant frequency f_0 is about 40 Hz, below which L_p decreases by 12 dB per octave with decreasing frequency [1]). The baffle-box system causes a diffraction dip at 300 Hz at which a great deal of sound is radiated into an off-axis direction. At low frequencies ($f < f_{ra}$) the measured curve runs higher than the calculated curve because of the radiation of the outer suspension. Above cone break-up this suspension contributes little to the sound radiation. Because of its relatively high damping it smooths the response slightly (this is more clearly visible in fig. 6.20*a*). As discussed in sec. 6.5.3, no dip appears at f_{ra}. At the first membrane resonant frequency f_{mr1} ($\approx$ 7000 Hz), which lies just above f_{la1}, a deep minimum appears in both measured responses: much sound is radiated in off-axis directions. This minimum does not appear in the calculated response owing to the assumed high value of the internal loss factor (sec. 6.5.5). The upper frequency limit lies at f_{la1}.

Figure 6.19*b* shows the calculated and measured sound-power responses of the present cones. The power is measured at discrete frequencies (centre frequencies of the standard one-third-octave bands); the measured values are indicated by dots and interconnected by a drawn curve. Here too, the measured response runs higher than the calculated response for $f < f_{ra}$ because of the rim radiation. The baffle dip at 300 Hz in L_p does not appear in L_{W100}: the baffle-box diffraction causes a broad sidelobe which, in the integral of L_{W100}, compensates for the pressure minimum in the axial direction. The upper limit of the power response also lies at f_{la1}. The deep minimum in L_p at f_{mr1} does not appear in L_{W100} because of the broad sidelobe at this frequency.

Calculated and measured frequency plots of the directivity index DI_{100} are shown in the upper graph in fig. 6.19*c*. The broad sidelobe at 300 Hz causes a high negative value of DI_{100}. For the same reason a minimum appears at f_{mr1}.

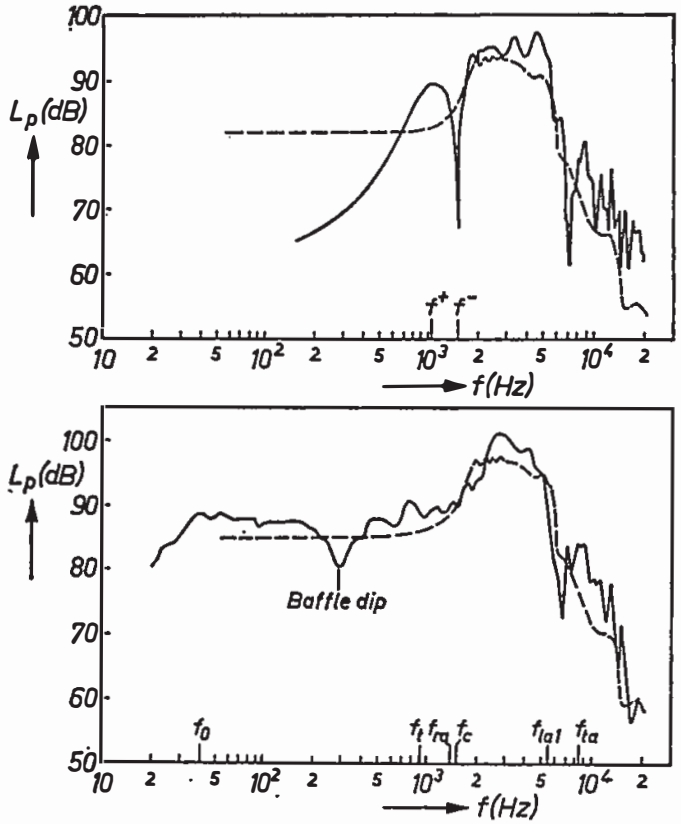

Fig. 6.19*a*. Calculated pressure response of cone 50.5 (dashed); measured pressure response (drawn curves) of cone 50.5e unbaffled (upper figure) and in baffle-box system (lower figure).

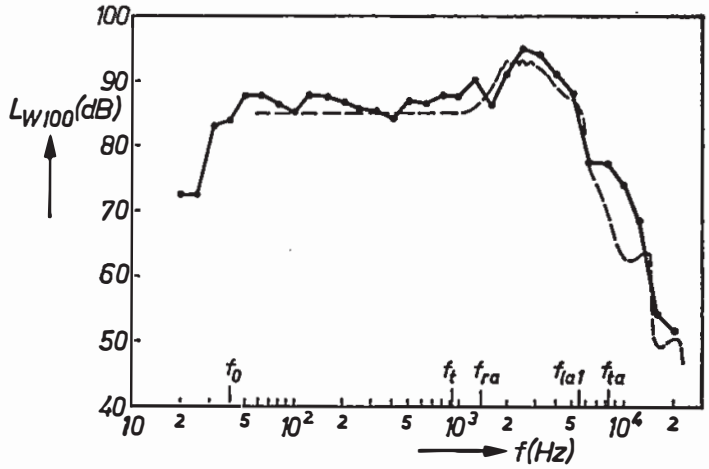

Fig. 6.19*b*. Calculated power response of cone 50.5 (dashed); measured power response of cone 50.5e (drawn curve).

The lower graph of fig. 6.19*c* shows the calculated and measured beam widths β versus frequency.

Calculated and measured directivity diagrams at four frequencies are shown in figs 6.19*d* and *e*. Note that for angles greater than 50 degrees and high fre-

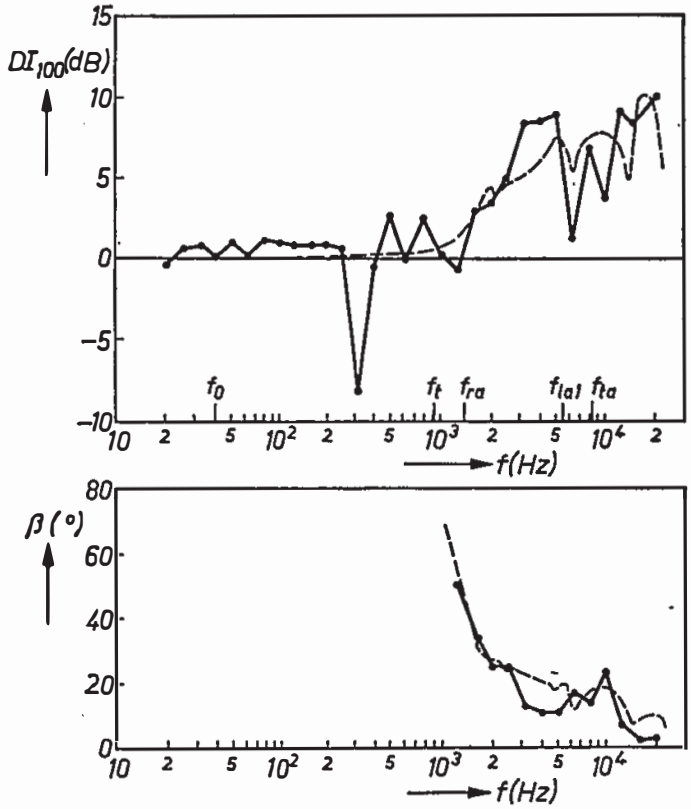

Fig. 6.19*c*. Calculated frequency characteristics of the directivity index DI_{100} and the beam width β of cone 50.5 (dashed); measured characteristics of cone 50.5e (drawn curves).

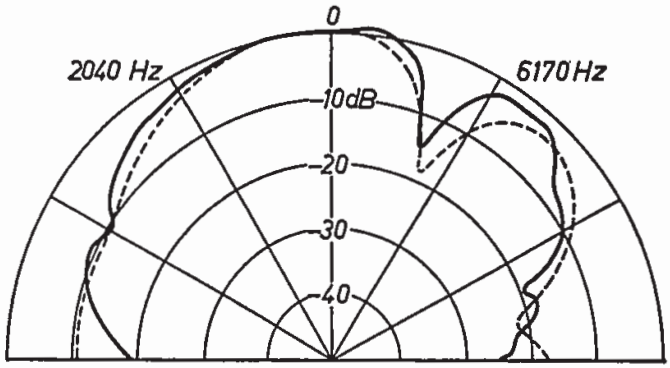

Fig. 6.19*d*. Calculated (cone 50.5, dashed) and measured (cone 50.5e, drawn curve) directivity diagrams at 2040 Hz (left) and 6170 Hz (right).

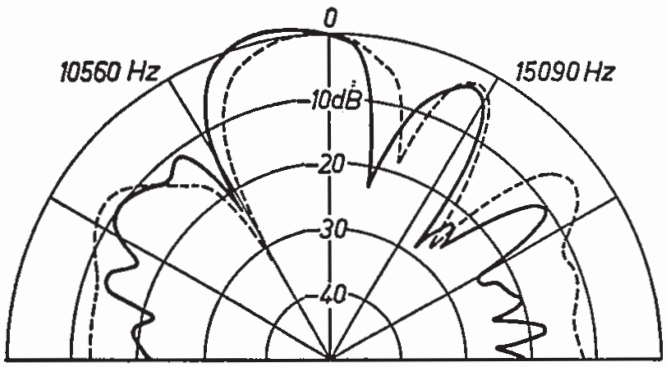

Fig. 6.19*e*. Calculated (cone 50.5, dashed) and measured (cone 50.5e, drawn curve) directivity diagrams at 10560 Hz (left) and 15090 Hz (right).

quencies the measured pressure level runs lower than the calculated curve (screening-off effect).

Figures 6.20*a*, *b* and *c* show the calculated and measured frequency characteristics of cones 60.2 and 60.2e. The frequency characteristics of cones 60.2 do not show fundamental differences from those of cones 50.5. Note that the maximum in region II is less high and that the responses start to roll off at a

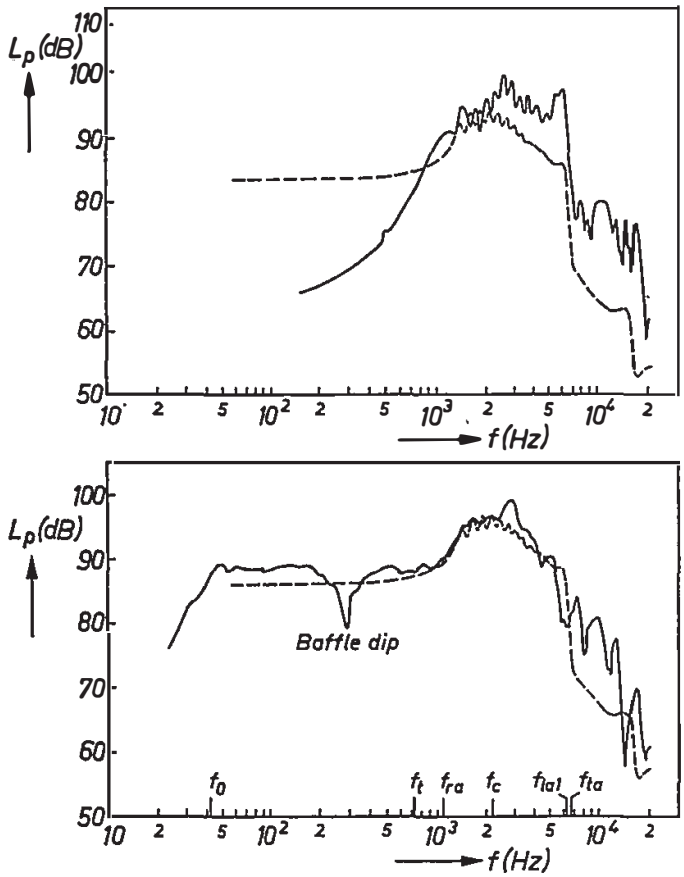

Fig. 6.20*a*. Calculated pressure response of cone 60.2 (dashed); measured pressure response (drawn curves) of cone 60.2e unbaffled (upper figure) and in baffle-box system (lower figure).

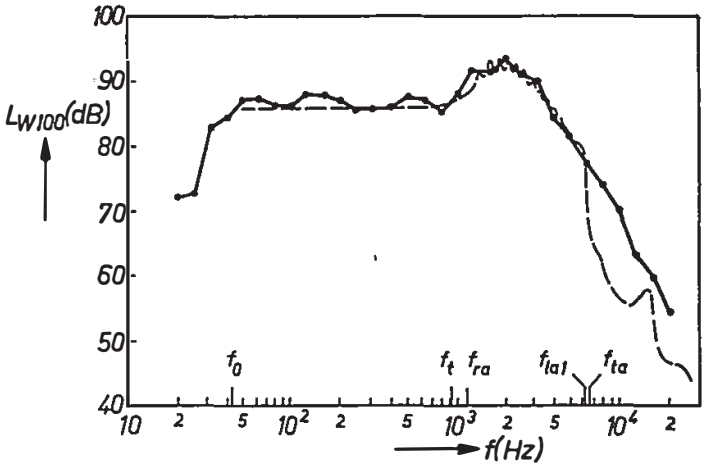

Fig. 6.20*b*. Calculated power response of cone 60.2 (dashed); measured power response of cone 60.2e (drawn curve).

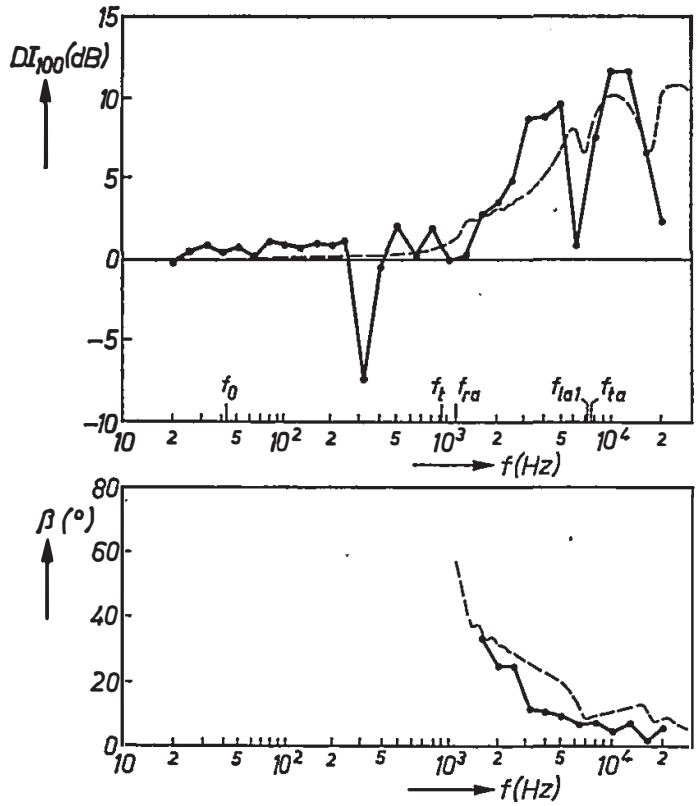

Fig. 6.20*c*. Calculated frequency characteristics of the directivity index DI_{100} and the beam width β of cone 60.2 (dashed); measured characteristics of cone 60.2e (drawn curves).

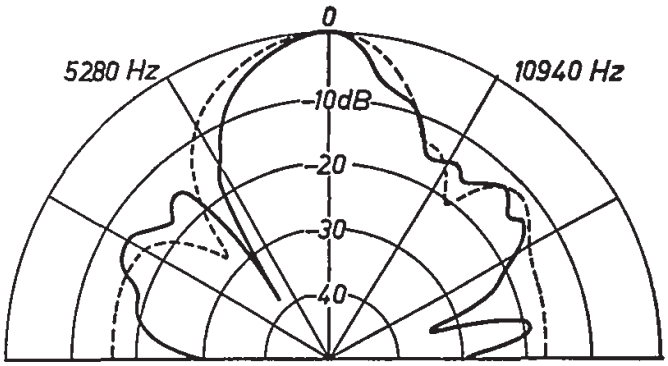

Fig. 6.20*d*. Calculated (cone 60.2, dashed) and measured (cone 60.2e, drawn curve) directivity diagrams at 5280 Hz (left) and 10940 Hz (right).

somewhat lower frequency than cone 50.5e (influence of M_c/M_d). Figure 6.20*d* illustrates the satisfactory agreement of the calculated and measured directivity diagrams at two frequencies.

The above remarks hold equally well for figs 6.21*a*, *b* and *c*, showing the calculated characteristics of cone 70.3 and the measured curves of cone 70.3e. The calculated pressure response is a good approximation of the mean measured curve (fig. 6.21*a*, lower graph). Note the pronounced measured bending resonances and antiresonances, compared with the other cones (as shown in sec. 5.6.2 the spacing between these bending resonances and antiresonances increases with increasing α). Bending resonances and antiresonances do not

appear in the calculated curve as the value of h is too small. The maximum in region II is lower than that of the foregoing cones. The relatively small value of f_{ta} causes a smaller bandwidth as compared with the other cones. In the high-frequency region ($f > f_{ta}$), the measured pressure and power responses run

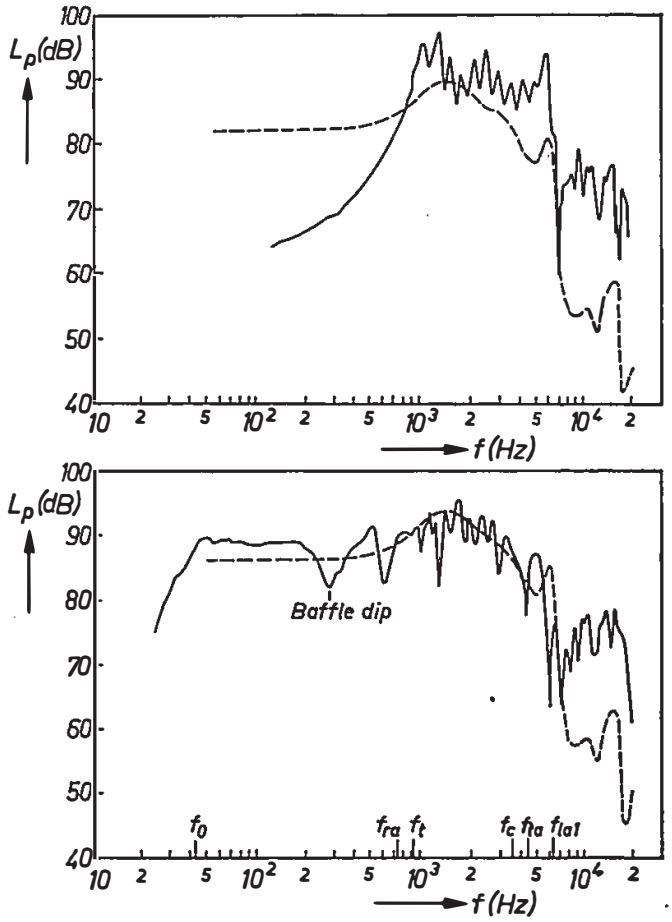

Fig. 6.21*a*. Calculated pressure response of cone 70.3 (dashed); measured pressure response (drawn curves) of cone 70.3e unbaffled (upper figure) and in baffle-box system (lower figure).

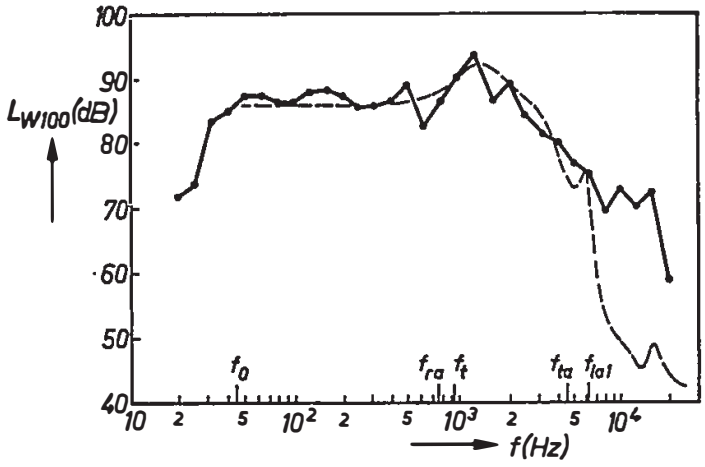

Fig. 6.21*b*. Calculated power response of cone 70.3 (dashed); measured power response of cone 70.3e (drawn curve).

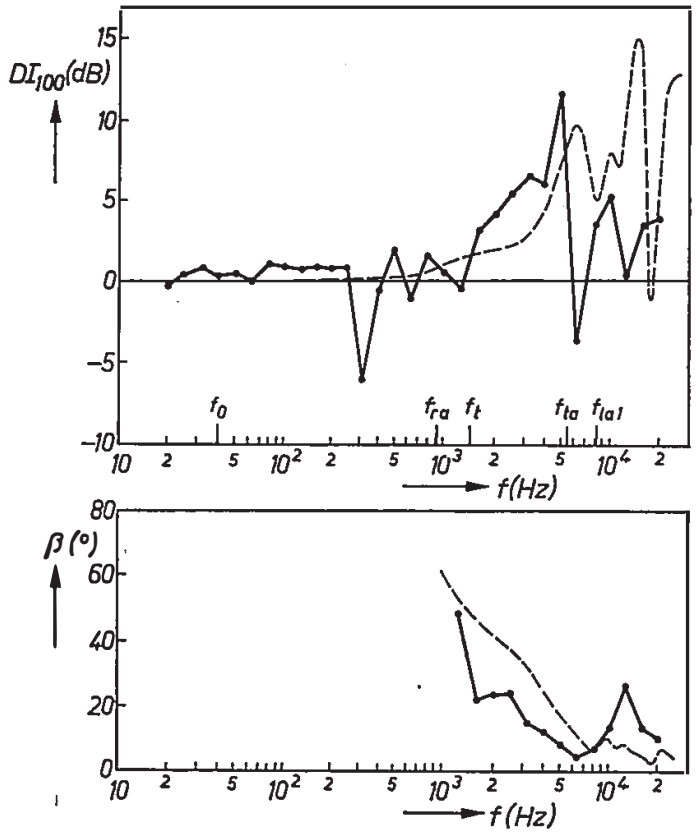

Fig. 6.21*c*. Calculated frequency characteristics of the directivity index DI_{100} and the beam width β of cone 70.3 (dashed); measured characteristics of cone 70.3e (drawn curves).

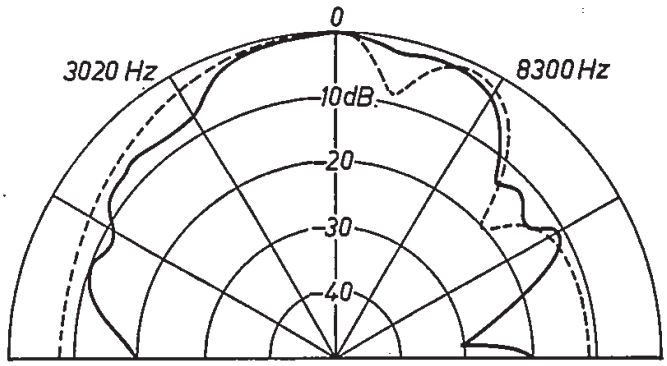

Fig. 6.21*d*. Calculated (cone 70.3, dashed) and measured (cone 70.3e, drawn curve) directivity diagrams at 3020 Hz (left) and 8300 Hz (right).

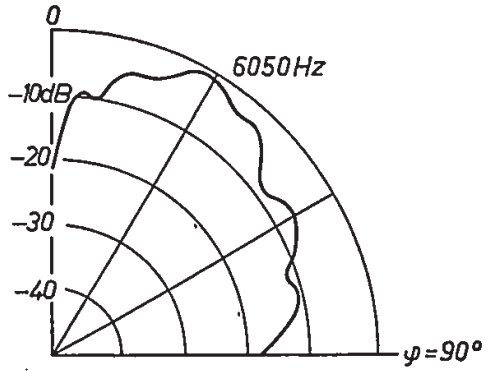

Fig. 6.21*e*. Measured directivity diagram of cone 70.3e at the first membrane resonant frequency $f_{mr1} = 6050$ Hz.

higher than the calculated curves; here the difference in h causes a considerable error (see eq. (6.65)) in addition to the previously mentioned effects.

Calculated and measured directivity diagrams are shown in fig. 6.21*d*. Figure 6.21*e* shows the measured directivity diagram at the first membrane resonant frequency (6050 Hz); a deep minimum in the axial direction appears, as explained in sec. 6.5.5.

The above comparison of calculations and measurements shows that pressure and power responses as well as directivity diagrams can be calculated with acceptable accuracy, at least below f_{la1}. Besides, measurements confirm the conclusion that the upper limit of pressure and power responses lies at most at the lower one of f_{la1} and f_{ta}.

The pronounced off-axis radiation at the membrane resonant frequencies is further illustrated on the basis of measurements on the polycarbonate cone 50.2e. The frequency response of the latter, shown in fig. 6.22*a*, closely resembles that of cone 50.5e (fig. 6.19*a*), except that cone 50.2e has a smaller internal loss factor, which causes a more distinct fine structure in region II. The directivity

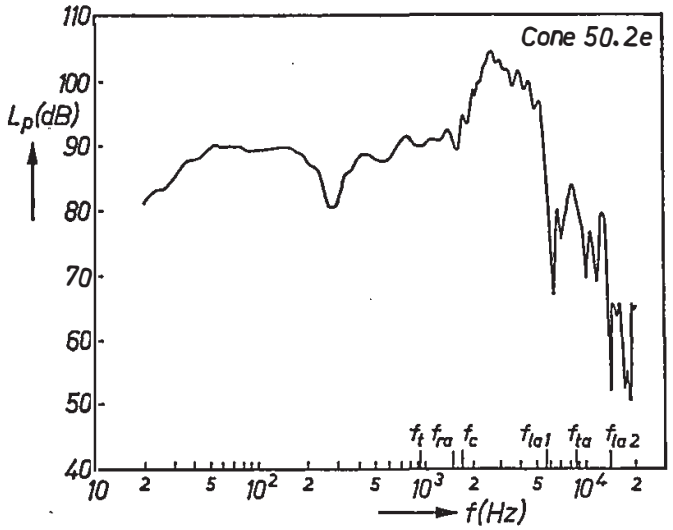

Fig. 6.22*a*. Measured pressure response of cone 50.2e in baffle-box system.

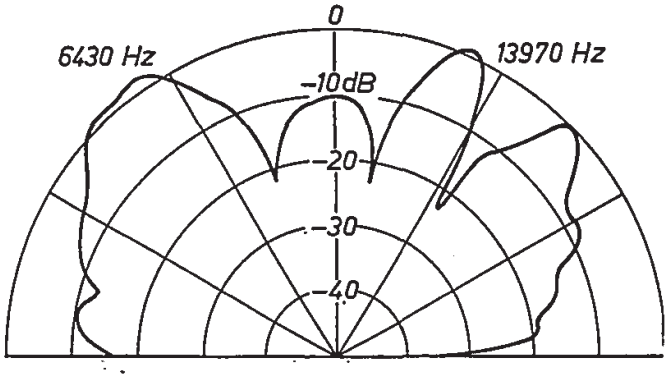

Fig. 6.22*b*. Measured directivity diagrams at the membrane resonant frequencies f_{mr1} = 6430 Hz and f_{mr2} = 13970 Hz of cone 50.2e.

diagrams at the first and second membrane resonant frequencies are shown in fig. 6.22*b* (vibration patterns at these frequencies are shown in figs 5.30*e* and *g*). Note the relatively small axial values, which further deepen the already existing dips at f_{la1} and f_{la2} in the frequency characteristic of the axial sound pressure (fig. 6.22*a*).

6.6.2. *Pressure responses of four commercial loudspeakers*

In this section it will be shown that the rough shape of the frequency response can be explained without carrying out extensive numerical calculations. In fact, only the relative positions of the following frequencies must be known: f_t, f_c, f_{ta}, f_{ra} and f_{la1}. The first-mentioned three frequencies follow directly from eqs (6.10b), (6.26) and (4.12) respectively, whereas f_{ra} may be approximated by eq. (6.42). However. in the following, f_{ra} and f_{la1} are graphically determined from fig. 5.9*b*. In the figures discussed below, f_{tb} is not indicated, it lies just above f_{ra}.

The above-mentioned frequencies are indicated in the measured sound-pressure response of four loudspeakers, which are ranked according to their value of M_c/M_d (see table 6-I).

TABLE 6-I

type	R_b (mm)	R_a (mm)	M_c/M_d	fig. 6.23
AD8065/W8	75	12·7	1	*a*
AD5080/X8	44	9·4	0·7	*b*
AD7080/X8	61	9·4	0·4	*c*
AD8080/X8	79	9·4	0·2	*d*

The total mass of voice coil, voice-coil cylinder and dust cap is M_c; M_d is the cone mass plus outer suspension mass if the latter is made of paper (last-mentioned three types), for the woofer (first-mentioned type) M_d is the cone mass without the mass of the (heavy) rubber rim. All cones have a semi-apex angle of 60°; for the determination of f_{ra}, f_{la1} and f_{ta} we have taken $c = 2700$ m/s.

Figures 6.23*a* to 6.23*d* show the measured pressure responses of the unbaffled loudspeakers. These curves are recorded with a constant-voltage drive $e_{\text{eff}} = 0{\cdot}63$ V, except for the response of the woofer (fig. 6.23*a*) where $e_{\text{eff}} = 2{\cdot}4$ V is used. In all cases f_c lies just above f_{ra} ($f_c \approx 1{\cdot}1 f_{ra}$), so no dip will appear in the pressure response of the baffled loudspeakers (f_c is not indicated). On the other hand, $f_t \approx 0{\cdot}5 f_{ra}$ for all cones; this will cause a dip at f_{ra} in the power response of the baffled loudspeakers.

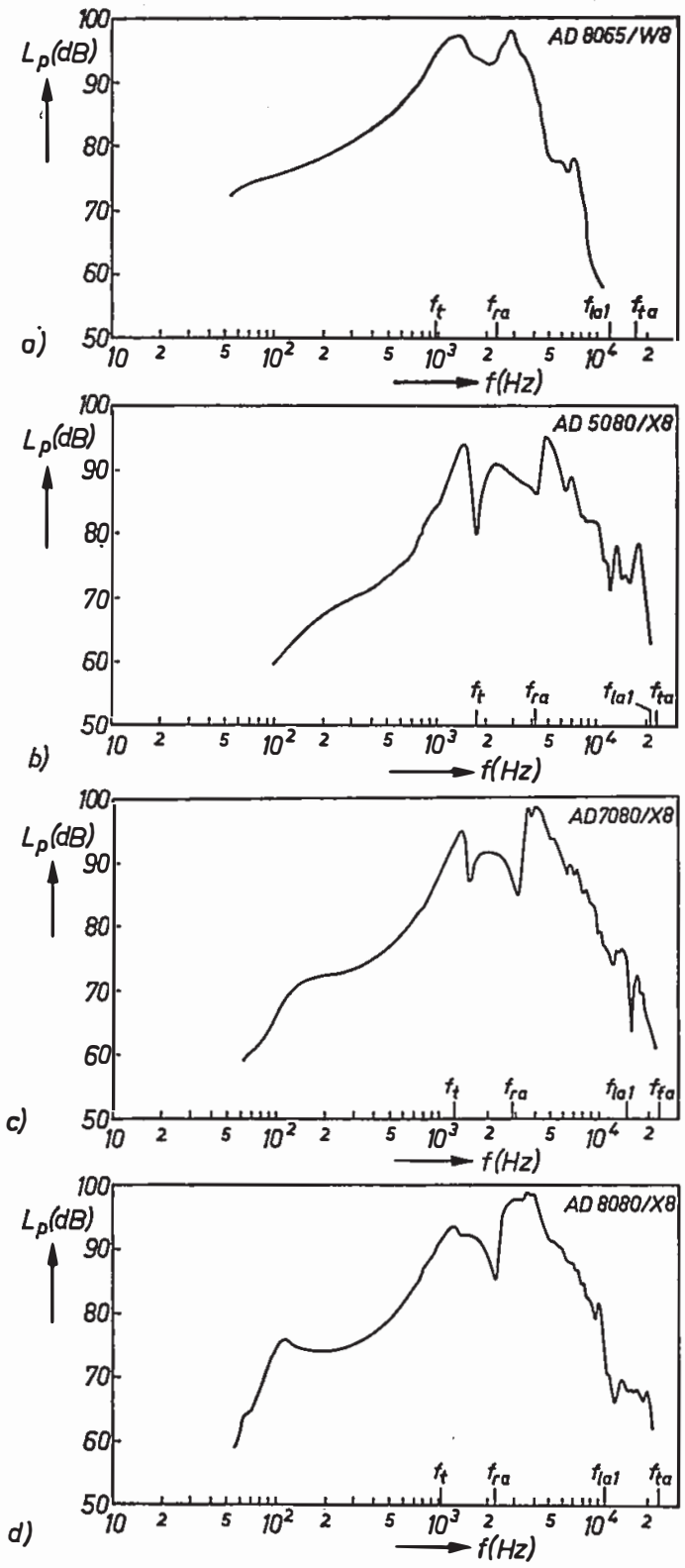

Fig. 6.23. Measured pressure responses of four unbaffled commercial (Philips) loudspeakers. The indicated values of f_t, f_{ra}, f_{la1} and f_{ta} are calculated; in all cases $f_c \approx 1{\cdot}1\, f_{ra}$.
(*a*) AD 8065/W8 (woofer), (*b*) AD 5080/X8 (standard), (*c*) AD 7080/X8 (standard), (*d*) AD 8080/X8 (standard).

At low frequencies the responses increase with increasing frequency, as is well known. After this low-frequency rise we encounter a maximum caused by the waves from the front and the back of the cone arriving in phase in the measuring point ($f^+ \approx 1200$ Hz in figs 6.23*a* and *d*). At about 1500 Hz in figs 6.23*b* and *c* a rim resonance (a pronounced peak directly followed by a dip) is superimposed on this maximum. There the outer suspension comes into a resonant condition: with increasing frequency it first vigorously vibrates in phase and then in antiphase with the practically uniformly oscillating cone (the proximity of f_t is sheer coincidence).

The maximum at f^+ is followed by a roll-off caused by the partial mutual compensation of the waves emanating from the front and the back of the cone. Though in all cases cone break-up starts at a sufficiently *) high frequency, pronounced dips at a certain frequency f^- (as in fig. 6.19*a*, upper graph) do not show up. This is probably due to the fact that the present cones are provided with an outer suspension that may vibrate in a phase different from that of the cone, thus blurring the above compensation effect.

At f_{ra} a relatively sharp rise occurs, followed by a fast roll-off. The frequency at which this roll-off starts depends on M_c/M_d (sec. 6.5.9). The woofer (fig. 6.23*a*) has a relatively high value of M_c/M_d; the response first shows a small peak just above f_{ra} (remainder of the broad maximum in region II for $M_c = 0$) and is then practically cut off (this "early" roll-off is of course no disadvantage for a woofer).

Figures 6.23*a* through 6.23*d* show that with decreasing M_c/M_d the maximum just above f_{ra} first increases in height and then broadens. Even the value $M_c/M_d = 0{\cdot}2$ is still too high to prevent an early roll-off caused by the voice-coil mass (fig. 6.23*d*), in accordance with the calculations made in sec. 6.5.9.

6.7. Design rules

In practice a flat pressure and power response, a large bandwidth and a high efficiency cannot be achieved simultaneously. Hence, the design of a loudspeaker cone is a matter of compromise. First we will discuss how a flat pressure and power response can be realized (sec. 6.7.1). In sec. 6.7.2, the emphasis is placed upon the creation of the largest possible bandwidth. It is assumed that the longitudinal wave velocity c in the cone material is known. Further the outer-edge radius R_b is determined by the required sound power and maximum voice-coil excursion below cone break-up **). The rigid-piston transition frequency f_t follows from eq. (6.10b).

*) Assuming that f^- is proportional to R_b and measuring $f^- = 1500$ Hz for $R_b = 83$ mm (fig. 6.19*a*) we find for the cones in this section $f^- < f_{ra}$.

**) Usually R_b is directly related to the loudspeaker functioning as a low-, middle- or high-frequency radiator.

6.7.1. *Realization of a flat pressure and power response*

To avoid a dip at f_{ra} in the sound-power response, f_{ra} should not lie too far above f_t. If we take for instance $f_{ra} < 2 f_t$, the apex angle is determined by eqs (6.10b) and (6.42): $\cos \alpha < 2{\cdot}8\, c_0/c$. For a paper cone with $c = 2700$ m/s we find $\alpha > 70°$. This range of α corresponds at the same time to a low maximum in region II, as required for a flat response.

To allow easy elimination of the fine structure we take α as small as possible. If α is chosen in this way a dip at f_{ra} in the sound-pressure response caused by a rigid-cone roll-off cannot occur, since f_c is higher than f_t (sec. 6.5.3).

The inner-edge radius R_a determines f_{ta1} and f_{ta}; the lower of these frequencies sets the upper limit for the pressure and power responses, at least if $M_c = 0$. On the basis of the foregoing we take $f_{ta1} \leqslant f_{ta}$. The value of kR_a at f_{ta} is determined by the upper boundary of region II (fig. 4.19*a*). The intersection of this horizontal line with the f_{ta1} curve in fig. 4.19*b* determines the minimum value of R_b/R_a.

The pressure and power responses usually start to roll off at a lower frequency than f_{ta} or f_{ta1}, because of the influence of the voice-coil mass. Hence M_c/M_d should be chosen as small as possible to obtain a high upper frequency limit.

The cone thickness h can be determined experimentally after the determination of the other geometrical parameters. For a paper cone a first trial value of $h = R_b/200$ can be taken. If a fine structure appears, either the internal or the rim damping must be increased or h must be decreased. The latter, however, reduces M_c/M_d. Further, too small a thickness may increase the harmonic distortion as the vibrational amplitudes may exceed the linear range. As long as the efficiency of the electro-acoustical conversion is of secondary importance, the thickness should be taken as great as possible. The elimination of the fine structure *) in the above example of a paper cone with a relatively high value of α will not be easy. One remedy may be the use of a highly damping rim. If it introduces insufficient damping the cone may be covered by a damping layer (which, of course can also be applied to the rim). Further, c can be made lower to reduce the spacing between the bending resonant and antiresonant frequencies. If c is made lower by increasing the mass density, M_c/M_d is reduced, which may increase the upper frequency limit.

6.7.2. *Realization of a large bandwidth*

As discussed in sec. 6.5.9, a prerequisite for obtaining a large bandwidth is to

*) The elimination of the fine structure also prevents undesired oscillations (ringing) caused by bending resonances after the application of a transient input signal to the voice coil. However, after an input pulse even a loudspeaker with a frequency response like that of fig. 6.23*a* (in which the fine structure is practically eliminated) will show decaying oscillations with frequencies corresponding to the maxima in the response. They are caused by the loudspeaker acting as a filter to an applied signal.

have the smallest possible value of M_c/M_d. In general this means a heavy cone and consequently a low efficiency. If the dips in the responses at f_{ra} and f_{la1} are allowed we should choose a small value of α and take c as large as possible *). Then f_{ra}, f_{la1} as well as f_{ta} shift upwards (figs 4.19*a* and *b*). If only a dip in the power response at f_{ra} is allowed, we should take $f_{la1} \approx f_{ta}$; this likewise results in a relatively small value of α (e.g. 50°); R_b/R_a follows from the intersection of the f_{ta} and f_{la1} curves in figs. 4.19*a* and *b*. The small value of α results in a relatively high maximum in region II. The thickness is again chosen in such a way that the fine structure is eliminated.

6.7.3. *Realization of a high efficiency*

It is well known how the efficiency below cone break-up may be optimized [1,41]). A high efficiency above cone break-up usually demands other measures. The cone weight should be as small as possible (small $\varrho\, h$). Therefore the voice-coil mass will determine the upper limit of the pressure and power responses, and the bandwidth will be small. A high maximum above cone break-up can be obtained by taking a small value of α. If a dip in the pressure response at f_{ra} is not allowed, Young's modulus E should be adapted in such a way that $f_{ra} < 2f_c$.

6.8. Conclusion

The sound radiation of a flexible cone may be summarized as follows. Below cone break-up the flexible cone can be approximated by the rigid piston. Above cone break-up the radiation is provided by the inner part of the cone, which decreases in area with increasing frequency; this causes a broad maximum in the pressure and power responses. The bending waves on the outer part radiate little sound. At high frequencies ($f > f_{ta}$) bending waves cover the entire cone; then the average pressure and power responses decrease with increasing frequency. The upper limit of the responses lies at the lower of f_{ta} and the first longitudinal antiresonant frequency f_{la1}. In practice, however, the upper frequency limit of the responses is lowered by the voice-coil mass. Longitudinal effects play an important role in the sound radiation: the axial admittance Y_a, which is a measure of the vibration amplitude, is determined by the longitudinal admittance Y_l; above cone break-up the radiation is provided by a longitudinal wave on the inner cone part; peaks and dips in the responses are caused by longitudinal resonances and antiresonances.

The bandwidth of a loudspeaker in which cone break-up occurs appropriately is larger than that of a rigid cone or a rigid piston. From this point of view it is therefore quite wrong to make the cone as rigid as possible, for instance by using expanded plastics or sandwich constructions. Apart from that,

*) If the voice-coil mass causes a roll-off below f_{la1}, an increase of c does not lead to an increase of the bandwidth as long as M_c/M_d is not decreased at the same time.

because of the high bending stiffness of a rigid cone, the fine structure will then consist of pronounced peaks and dips which are very difficult to eliminate.

The directivity diagram of the flexible cone is in general wider than that of the rigid piston. At the membrane resonant frequencies, which lie just above the longitudinal antiresonant frequencies, a broad sidelobe appears which may be accompanied by an axial minimum. This further deepens the minima in the axial response caused by the longitudinal antiresonant frequencies.

In the foregoing, it has been implicitly explained why a cone is preferable to a plate. For the cone the bending waves only appear above f_{ra} and on a limited (outer) part of the cone. The relatively stiff inner part takes care of the sound radiation: the cone exhibits a "prolonged rigid-piston action" with the advantage that the "piston" area decreases with increasing frequency. For the plate, acoustically short-circuited bending waves appear at a much lower frequency and cover the whole plate, resulting in a low sound-pressure response with pronounced peaks and dips.

The preceding conclusions also hold to a certain extent for slightly flared (i.e. horn-shaped) diaphragms. For such a diaphragm, α increases with the meridional coordinate. The ring antiresonant frequency f_{ra} of a flared diaphragm is in general lower than that of a conical diaphragm with the same inner- and outer-edge radii and depths because the local value of α at the outer edge of the flared diaphragm is larger than that of the cone (f_{ra} lies just below f_{tb} which is proportional to cos α, see eq. (4.11)). Therefore the flared diaphragm has a less high maximum in region II than the cone. The longitudinal antiresonant frequencies of the flared diaphragm are somewhat lower than those of a conical diaphragm because the former has a larger meridional (arc) length L than the latter.

We may summarize the main conclusions as follows.

(1) Pressure and power responses as well as directivity diagrams of a loudspeaker cone can be calculated with acceptable accuracy.

(2) The shape of the pressure- and power-reponse curves can be easily understood on the basis of the ratio of voice-coil mass to cone mass and five easily obtainable characteristic frequencies f_t, f_c, f_{ra}, f_{la1} and f_{ta}.

(3) The bandwidth of the power response of a flexible cone can be larger than that of a rigid cone or a rigid piston.

(4) In practice the voice-coil mass causes a roll-off in the pressure and power responses, thus limiting the loudspeaker bandwidth; to obtain a high upper frequency limit the ratio of voice-coil mass to cone mass should be made as small as possible.

(5) The reaction of the cone to the voice-coil force is mainly determined by the mechanical impedance in the longitudinal (i.e. meridional) direction.

(6) The influence of asymmetrical cone vibrations on the acoustical performance of the loudspeaker is negligible.

APPENDIX A

Differential equations for the mechanical cone behaviour

It was discussed in chapters 4 and 5 that the mechanical cone behaviour can be described by a system of m simultaneous first-order linear differential equations which can be written as

$$\frac{\mathrm{d}y(x)}{\mathrm{d}x} = A(x)\, y(x) \tag{A.1}$$

where $y(x)$ is an m-dimensional vector containing the fundamental variables and $A(x)$ is an (m, m) matrix. This system is subjected to $m/2$ boundary conditions at either edge of the cone and it is numerically solved with the method of direct integration (appendix B).

For the lossless conical membrane $m = 2$; the membrane equations comprise the following fundamental variables:

$$y(x) = \begin{bmatrix} u \\ N_x \end{bmatrix} \tag{A.2}$$

whereas the matrix $A(x)$ is given by

$$\begin{aligned} A(1,1) &= -\nu\, g/x, \\ A(1,2) &= (1 - \nu^2\, g)/Eh, \\ A(2,1) &= E\, h\, (g - k^2\, x^2)/x^2, \\ A(2,2) &= (-1 + \nu\, g)/x, \end{aligned} \tag{A.3}$$

where the factor g is given by eq. (4.7). Internal material damping is introduced by means of a complex Young's modulus, the differential equations are found by replacing E by $E\,(1 + j\delta)$ in the above lossless equations. All fundamental variables then become complex and are provided with indices 1 and 2 to indicate the real and imaginary parts. For the conical membrane we then have $m = 4$, and eq. (A.1) is determined by

$$y(x) = \begin{bmatrix} u_1 \\ u_2 \\ N_{x1} \\ N_{x2} \end{bmatrix} \tag{A.4}$$

and

$$\begin{aligned} A(1,1) &= A(2,2) = -\nu\, g_1/x, \\ A(1,2) &= -A(2,1) = -A(3,4) = A(4,3) = \nu\, g_2/x, \\ A(1,3) &= A(2,4) = (1 - \nu^2\, g_1 - \delta\, \nu^2\, g_2)/E\, h, \\ A(1,4) &= -A(2,3) = (\delta - \delta\, \nu^2\, g_1 + \nu^2\, g_2)/E\, h, \\ A(3,1) &= A(4,2) = E\, h\, (g_1 - \delta\, g_2 - k^2\, x^2)/x^2, \\ A(3,2) &= -A(4,1) = -E\, h\, (\delta\, g_1 + g_2)/x^2, \\ A(3,3) &= A(4,4) = (\nu\, g_1 - 1)/x, \end{aligned} \tag{A.5}$$

where g_1 and g_2 are given by eqs (4.66a) and (4.66b) and powers of δ higher than unity are neglected with respect to 1.

For axisymmetric vibrations with inclusion of bending effects but without internal losses (general equations) $m = 6$, and the system of differential equations is determined by the following fundamental variables:

$$y(x) = \begin{bmatrix} w \\ u \\ \beta_x \\ Q \\ N_x \\ M_x \end{bmatrix}. \tag{A.6}$$

The (6, 6) matrix $A(x)$ can be derived from that given in ref. 16; if we assume that

$$\frac{h^2 \cos^2 \alpha}{12 R_a^2} \ll 1 \tag{A.7}$$

we find the following nonzero elements of $A(x)$:

$$\begin{aligned}
&A(1, 3) = -A(6, 4) = -1, \\
&A(2, 1) = -A(4, 5) = -\nu \cot \alpha / x, \\
&A(2, 2) = A(3, 3) = -\nu/x, \\
&A(2, 5) = (1 - \nu^2)/E h, \\
&A(3, 6) = 12 (1 - \nu^2)/E h^3, \\
&A(4, 1) = E h (\cot^2 \alpha - k^2 x^2)/x^2, \\
&A(4, 2) = A(5, 1) = E h \cot \alpha / x^2, \\
&A(4, 4) = -1/x, \\
&A(5, 2) = E h (1 - k^2 x^2)/x^2, \\
&A(5, 5) = A(6, 6) = -(1 - \nu)/x, \\
&A(6, 3) = E h^3 (1 - k^2 x^2)/12 x^2.
\end{aligned} \tag{A.8}$$

In the presence of internal losses $m = 12$; then $y(x)$ is given by

$$y(x) = \begin{bmatrix} w_1 \\ w_2 \\ u_1 \\ u_2 \\ \beta_{x1} \\ \beta_{x2} \\ Q_1 \\ Q_2 \\ N_{x1} \\ N_{x2} \\ M_{x1} \\ M_{x2} \end{bmatrix} \tag{A.9}$$

and the (12, 12) matrix $A(x)$ has the following nonzero elements:

$$
\begin{aligned}
A(1,5) &= A(2,6) &&= -A(11,7) = -A(12,8) = -1,\\
A(3,1) &= A(4,2) &&= -A(7,9) = -A(8,10) = -\nu \cot\alpha/x,\\
A(3,3) &= A(4,4) &&= A(5,5) = A(6,6) = -\nu/x,\\
A(3,9) &= A(4,10) &&= (1-\nu^2)/Eh,\\
A(3,10) &= -A(4,9) &&= \delta\,(1-\nu^2)/Eh,\\
A(5,11) &= A(6,12) &&= 12\,(1-\nu^2)/Eh^3,\\
A(5,12) &= -A(6,11) &&= 12\,\delta\,(1-\nu^2)/Eh^3,\\
A(7,1) &= A(8,2) &&= Eh\,(\cot^2\alpha - k^2x^2)/x^2,\\
A(7,2) &= -A(8,1) &&= -\delta\,Eh\cot^2\alpha/x^2,\\
A(7,3) &= A(8,4) &&= A(9,1) = A(10,2) = Eh\cot\alpha/x^2,\\
A(7,4) &= -A(8,3) &&= A(9,2) = -A(10,1) = -\delta\,Eh\cot\alpha/x^2,\\
A(7,7) &= A(8,8) &&= -1/x,\\
A(9,3) &= A(10,4) &&= Eh\,(1-k^2x^2)/x^2,\\
A(9,4) &= -A(10,3) &&= -\delta\,Eh/x^2,\\
A(9,9) &= A(10,10) &&= A(11,11) = A(12,12) = -(1-\nu)/x,\\
A(11,5) &= A(12,6) &&= Eh^3\,(1-k^2x^2)/12\,x^2,\\
A(11,6) &= -A(12,5) &&= -\delta\,Eh^3/12\,x^2.
\end{aligned}
\tag{A.10}
$$

In these equations δ^2 and higher orders of δ are neglected with respect to 1.

Finally, for asymmetric vibrations without internal losses the fundamental variables which are assumed to be separable in the form given by eq. (5.1) are the following eight:

$$
y(x) = \begin{bmatrix} w_n \\ u_n \\ v_n \\ \beta_{xn} \\ Q_n \\ N_{xn} \\ N_n \\ M_{xn} \end{bmatrix}. \tag{A.11}
$$

The (8, 8) matrix $A(x)$ has the following nonzero elements, which follow from those given by Kalnins [15]) under the assumptions

$$
\frac{h^2\cos^2\alpha}{12\,R_a^2} \ll 1, \qquad \frac{n^2h^2}{12\,R_a^2} \ll 1:
$$

$$A(1,4) = -A(8,5) = -1,$$
$$A(2,1) = -A(5,6) = -\nu \cot \alpha/x,$$
$$A(2,2) = \quad A(4,4) = -\nu/x,$$
$$A(2,3) = -A(7,6) = -\nu\, t/x,$$
$$A(2,6) = (1-\nu^2)/E\,h,$$
$$A(3,1) = -A(5,7) = t\,h^2 \cot \alpha/6\,x^3,$$
$$A(3,2) = -A(6,7) = t/x,$$
$$A(3,3) = -A(5,5) = 1/x,$$
$$A(3,4) = -A(8,7) = t\,h^2 \cot \alpha/6\,x^2,$$
$$A(3,7) = 2\,(1+\nu)/E\,h,$$
$$A(4,1) = -A(5,8) = -\nu\, t^2/x^2,$$
$$A(4,3) = -A(7,8) = -\nu\, t \cot \alpha/x^2,$$
$$A(4,8) = 12\,(1-\nu^2)/E\,h^3,$$
$$A(5,1) = E\,h\left[\frac{t^2\,h^2}{12\,x^2}\left(t^2 + \frac{2}{1+\nu}\right) + \cot^2\alpha - k^2\,x^2\right]\Big/x^2,$$
$$A(5,2) = \quad A(6,1) = E\,h \cot \alpha/x^2 \sin \alpha,$$
$$A(5,3) = \quad A(7,1) = t\,E\,h \cot \alpha\,(1-k^2\,h^2/12)/x^2,$$
$$A(5,4) = \quad A(8,1) = t^2\,(3+\nu)\,E\,h^3/12\,x^3\,(1+\nu),$$
$$A(6,2) = E\,h\,[1-k^2\,x^2 + t^2\,h^2 \cos^2 \alpha/24\,(1+\nu)]/x^2,$$
$$A(6,3) = A(7,2) = t\,E\,h/x^2,$$
$$A(6,4) = A(8,2) = -t^2\,E\,h^3 \cot \alpha/12\,(1+\nu)\,x^3,$$
$$A(6,6) = A(8,8) = -\,(1-\nu)/x,$$
$$A(7,3) = E\,h\,(t^2 - k^2\,x^2)/x^2,$$
$$A(7,4) = A(8,3) = t\,(2+\nu)\,E\,h^3 \cot \alpha/12\,(1+\nu)\,x^3,$$
$$A(7,7) = -2/x,$$
$$A(8,4) = E\,h^3\,[1-k^2\,x^2 + 2\,t^2/(1+\nu)]/12\,x^2,$$

where $t = n/\sin \alpha$.

APPENDIX B

Description of the numerical method for the solution of a system of simultaneous differential equations

B.1. *Introduction*

In the past, various methods have been employed for the numerical solution of the equations that describe the static and dynamic behaviour of shells of revolution. A short survey with additional references is given in ref. 24. We have selected the direct-integration method [14,15]), in which the shell boundary-value problem is reduced to an initial-value problem involving simultaneous first-order differential equations which are integrated numerically. An advantage of this method is that it permits a selection of an optimum step size of integration at each step according to the desired accuracy of the solution. A further advantage is that it can be applied to an arbitrary number m of first-order differential equations; the computer program remains basically unchanged. In this way the cone membrane equations (chapter 4) have been solved for zero and nonzero values of the internal loss factor ($m = 2$ and 4 respectively); in chapter 5 the general equations including bending effects have been solved ($m = 6$ and 12 respectively). In the latter chapter the antiresonant frequencies for asymmetric vibration ($m = 8$) were determined with the same program.

In comparison with other methods the direct-integration method is rather slow if it is used for the determination of the shell natural frequencies [14]); the latter have literally to be searched for. However, this disadvantage does not apply here since for calculating the sound radiation we want forced-displacement patterns in the presence of internal losses rather than natural frequencies. However, with direct integration it appears that a total loss of accuracy results if the length of the integration interval is increased beyond a certain critical value [15]). This disadvantage of the direct-integration approach is avoided by dividing the shell into segments.

The method is applicable to any two-point boundary-value problem governed by a system of m first-order linear ordinary differential equations with $m/2$ boundary conditions at either end of the interval. Kalnins [14]) shows that the boundary-value problem of a rotationally symmetric shell can be stated in this form. The resulting equations allow arbitrary meridional variation (including discontinuities) in Young's modulus, Poisson's ratio, radii of curvature and thickness. The method of solution consists of the following steps. First the two-point boundary-value problem is reduced to a series of initial-value problems. These are directly integrated over preselected segments of the total interval. After integration, continuity requirements on all variables are written

at the end points of the segments. They constitute a system of linear matrix equations, which is solved by means of Gaussian elimination.

In the next subsection the method of solution is explained for the case where the shell is not subdivided into segments; this is followed by a discussion of a multisegment shell. Further details can be found in ref. 14.

B.2. *Method of solution for a one-segment shell*

The fundamental variables (sec. 5.2) which appear in the governing system of differential equations are represented by an m-dimensional vector $y(x)$. If no external loads are present, the mechanical behaviour is determined by a system of m homogeneous first-order linear differential equations:

$$\frac{dy(x)}{dx} = A(x)\, y(x), \tag{B.1}$$

where the (m, m) matrix $A(x)$ was given in appendix A. In the presence of external loads on the cone surface (a case not dealt with in this thesis) an inhomogeneous $(m, 1)$ matrix $B(x)$ would appear at the inner edge. This additional term would require the determination of a particular solution which can easily be obtained [14]). There are $m/2$ boundary conditions at either edge. The solution of eq. (B.1) can be written as

$$y(x) = W(x)\, C, \tag{B.2}$$

where $W(x)$ is an (m, m) matrix whose columns represent m linearly independent solutions of the homogeneous governing equations and C is a column matrix of m arbitrary constants. The m linearly independent solutions are obtained by solving the homogeneous system subjected to m linearly independent initial conditions at $x = a$. If the initial conditions are independent, then the solutions will be independent for all values of x in the interval (a, b). To reduce the boundary-value problem to an initial-value problem we proceed as follows. At $x = a$ eq. (B.2) becomes:

$$y(a) = W(a)\, C\,, \tag{B.3}$$

so

$$C = W^{-1}(a)\, y(a). \tag{B.4}$$

Substituting C in eq. (B.2) leads to

$$y(x) = W(x)\, W^{-1}(a)\, y(a). \tag{B.5}$$

Define

$$Y(x) = W(x)\, W^{-1}(a), \tag{B.6}$$

then eq. (B.6) becomes

$$y(x) = Y(x)\, y(a) \tag{B.7}$$

with

$$Y(a) = I, \tag{B.8}$$

where I is the unit matrix. Substituting eq. (B.7) into the system of differential equations (B.1) we find that the original boundary-value problem is reduced to m initial-value problems given by

$$\frac{\mathrm{d}Y(x)}{\mathrm{d}x} = A(x)\, Y(x), \tag{B.9}$$

$$Y(a) = I. \tag{B.10}$$

Equation (B.9) is numerically integrated with a fifth-order Runge–Kutta method [29]). In this way the matrix $Y(b)$ at the end of the integration interval is determined. At $x = b$ eq. (B.7) becomes

$$y(b) = Y(b)\, y(a). \tag{B.11}$$

Equation (B.1) constitutes a system of m linear algebraic equations with m unknowns, half of the elements of $y(a)$ and $y(b)$ being known in terms of boundary conditions. After solution of this system, $y(a)$ is fully known and the solution at any value of x may be calculated using eq. (B.7), provided the value of $Y(x)$ is stored at that particular value of x during integration.

B.3. *Method of solution for a multisegment shell.*

If the length of the interval (a, b) is increased, complete loss of accuracy occurs beyond a certain critical value. This is caused by the fact that with increasing value of b the elements of $Y(b)$ rapidly increase in magnitude; then $Y(b)$ becomes bad-conditioned and while solving eq. (B.9) small errors in $Y(b)$ may lead to totally wrong results. This difficulty can be avoided by dividing the shell into segments and restarting the integration process at the beginning of each segment. Continuity requirements at the interconnection points lead to linear algebraic equations which can be easily solved. The above is carried out as follows.

Let the shell be divided into M segments denoted by S_i in which $x_i \leqslant x \leqslant x_{i+1}$ where $i = 1, 2, \ldots, M$. The shell edges are now denoted by x_1 and x_{M+1} (fig. B.1). The matrices $Y(x)$ are now determined on each segment:

$$\frac{\mathrm{d}Y_i(x)}{\mathrm{d}x} = A(x)\, Y_i(x), \tag{B.12}$$

$$Y_i(x_i) = I. \tag{B.13}$$

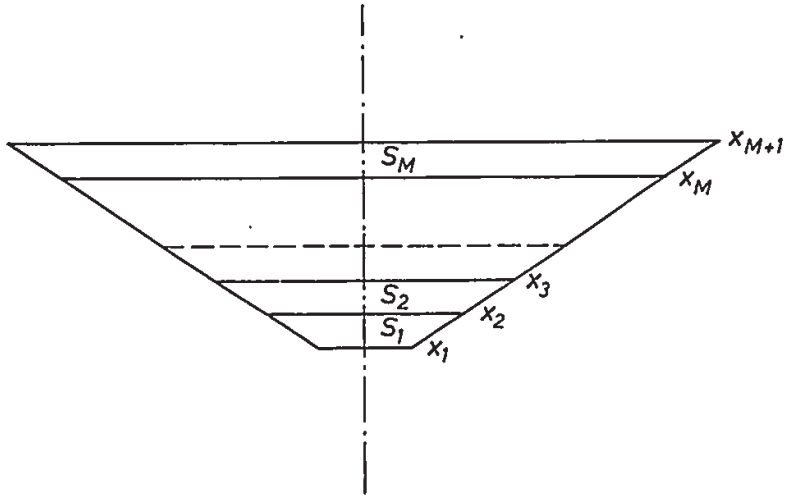

Fig. B.1. Notation for the division of a cone into segments.

By numerical integration Y_i is determined at the end points of each segment. The solution on each segment is

$$y(x) = Y_i(x)\, y(x_i), \tag{B.14}$$

where $x_i \leqslant x \leqslant x_{i+1}$. Requiring continuity of $y(x)$ at all points x_i we arrive at the following M matrix equations:

$$y(x_{i+1}) = Y_i(x_{i+1})\, y(x_i). \tag{B.15}$$

Assume that at the inner edge the first $m/2$ elements of $y(x_1)$ denoted by $y_1(x_1)$ are known and the remaining $m/2$ elements denoted by $y_2(x_1)$ are unknown. At the outer edge $y_1(x_{M+1})$ is the unknown and $y_2(x_{M+1})$ the known half of $y(x_{M+1})$. The continuity equations (B.15) are rewritten as a partitioned matrix product of the form

$$\begin{bmatrix} y_1(x_{i+1}) \\ \\ y_2(x_{i+1}) \end{bmatrix} = \begin{bmatrix} Y_i^1(x_{i+1}) & Y_i^2(x_{i+1}) \\ \\ Y_i^3(x_{i+1}) & Y_i^4(x_{i+1}) \end{bmatrix} \begin{bmatrix} y_1(x_i) \\ \\ y_2(x_i) \end{bmatrix} \tag{B.16}$$

which turns into a pair of equations

$$\begin{aligned} y_1(x_{i+1}) &= Y_i^1\, y_1(x_i) + Y_i^2\, y_2(x_i), \\ y_2(x_{i+1}) &= Y_i^3\, y_1(x_i) + Y_i^4\, y_2(x_i), \end{aligned} \tag{B.17}$$

where the matrices $Y_i^j(x_{i+1})$, $j = 1$ to 4 are abbreviated by Y_i^j. The result is a simultaneous system of $2M$ linear matrix equations in which Y_i^j are known coefficients; the $(m/2, 1)$ matrices $y_1(x_i)$ and $y_2(x_i)$ are unknown. Since $y_1(x_1)$ and $y_2(x_{M+1})$ are known there are $2M$ unknowns: $y_1(x_i)$ with $i = 2, 3, \ldots, M+1$ and $y_2(x_i)$ with $i = 1, 2, \ldots, M$. By means of Gaussian elimination the system of eqs (B.17) is brought to the form

$$\begin{bmatrix} E_1 & -I & 0 & 0 & \vdots & 0 & 0 \\ 0 & C_1 & -I & 0 & \vdots & 0 & 0 \\ 0 & 0 & E_2 & -I & \vdots & 0 & 0 \\ 0 & 0 & 0 & C_2 & \vdots & 0 & 0 \\ \cdots & \cdots & \cdots & \cdots & \vdots & \cdots & \cdots \\ & & & & \vdots & & \\ \cdots & \cdots & \cdots & \cdots & \vdots & \cdots & \cdots \\ 0 & 0 & 0 & 0 & \vdots & E_M & -I \\ 0 & 0 & 0 & 0 & \vdots & 0 & C_M \end{bmatrix} \begin{bmatrix} y_2(x_1) \\ y_1(x_2) \\ y_2(x_2) \\ y_1(x_3) \\ \cdots \\ \\ \cdots \\ y_2(x_M) \\ y_1(x_{M+1}) \end{bmatrix} = \begin{bmatrix} A_1 \\ B_1 \\ A_2 \\ B_2 \\ \cdots \\ \\ \cdots \\ A_M \\ B_M \end{bmatrix} \tag{B.18}$$

where the $(m/2, m/2)$ matrices E_1 and C_1 are defined by

$$E_1 = Y_1^{\,2}, \tag{B.19}$$

$$C_1 = Y_1^{\,4}\, E_1^{\,-1}; \tag{B.20}$$

$i = 2, 3, \ldots, M$:

$$E_i = Y_i^{\,2}\, Y_i^{\,1}\, C_{i-1}^{\,-1}, \tag{B.21}$$

$$C_i = (Y_i^{\,4} + Y_i^{\,3}\, C_{i-1}^{\,-1})\, E_i^{\,-1}. \tag{B.22}$$

The $(m/2, 1)$ matrices A_i and B_i are given by

$$A_1 = -Y_1^{\,1}\, y_1(x_1), \tag{B.23}$$

$$B_1 = -Y_1^{\,3}\, y_1(x_1) - Y_1^{\,4}\, E_1^{\,-1}\, A_1; \tag{B.24}$$

$i = 2, 3, \ldots, M-1$:

$$A_i = -Y_i^{\,1}\, C_{i-1}^{\,-1}\, B_{i-1}, \tag{B.25}$$

$$B_i = -Y_i^{\,3}\, C_{i-1}^{\,-1}\, B_{i-1} - C_i\, A_i. \tag{B.26}$$

For the Mth segment:

$$A_M = -Y_M^{\,1}\, C_{M-1}^{\,-1}\, B_{M-1}, \tag{B.27}$$

$$B_M = y_2(x_{M+1}) - Y_M^{\,3}\, C_{M-1}^{\,-1}\, B_{M-1} - C_M\, A_M. \tag{B.28}$$

By means of eqs (B.19) to (B.28) the unknowns are obtained by

$$y_1(x_{M+1}) = C_M^{\,-1}\, B_M, \tag{B.29}$$

$$y_2(x_M) = E_M^{\,-1}\, [y_1(x_{M+1}) + A_M], \tag{B.30}$$

and for $i = 1, 2, \ldots, M-1$:

$$y_1(x_{M-i+1}) = C_{M-i}^{\,-1}\, [y_2(x_{M-i+1}) + B_{M-i}], \tag{B.31}$$

$$y_2(x_{M-i}) = E_{M-i}^{\,-1}\, [y_1(x_{M-i+1}) + A_{M-i}]. \tag{B.32}$$

Equations (B.19) to (B.32) should be evaluated in succession, because each equation involves the result obtained by the preceding equation. If the fundamental variables $y(x)$ are desired at more points than at the ends of the segments, they can be obtained from eq. (B.14) provided that the values of $Y_i(x)$ at these points are stored during integration.

The elements of $y(x)$ are the fundamental variables; for the membrane equations $y(x)$ is given by

$$y(x) = \begin{bmatrix} y_1 \\ \cdots\cdots \\ y_2 \end{bmatrix} = \begin{bmatrix} u \\ \cdots\cdots \\ N_x \end{bmatrix}; \tag{B.33}$$

for the general axisymmetric equations we have

$$y(x) = \begin{bmatrix} y_1 \\ \cdots\cdots \\ y_2 \end{bmatrix} = \begin{bmatrix} w \\ u \\ \beta_x \\ \cdots\cdots \\ Q \\ N_x \\ M_x \end{bmatrix}, \tag{B.34}$$

whereas for asymmetric vibrations

$$y(x) = \begin{bmatrix} y_1 \\ \cdots\cdots \\ y_2 \end{bmatrix} = \begin{bmatrix} w_n \\ u_n \\ v_n \\ \beta_{xn} \\ \cdots\cdots\cdots \\ Q_n \\ N_{xn} \\ N_n \\ M_{xn} \end{bmatrix}. \tag{B.35}$$

The boundary conditions at the free outer edge are in all cases readily expressed in these fundamental variables (eqs (4.18), (5.13), (5.46)):

$$y_2(x_{M+1}) = 0. \tag{B.36}$$

In the general case, the axially driven inner edge is radially supported; hence the boundary conditions at x_1 (eqs (5.12) and (5.42) through (5.45)) are linear combinations of the fundamental variables $y(x)$. Therefore new variables $\psi(x)$ are introduced, on the first segment only, by means of a simple transformation

$$\psi(x) = T_1\, y(x) \tag{B.37}$$

where T_1 is an (m, m) nonsingular matrix constructed in such a way that the first half of $\psi(x_1)$, denoted by $\psi_1(x_1)$, is known (see below). Hence, at the end of the first segment the fundamental variables are determined by

$$y(x_2) = \Psi(x_2)\,\psi(x_1) \tag{B.38}$$

where

$$\Psi(x_2) = Y_1(x_2)\,T^{-1}. \tag{B.39}$$

Comparing eq. (B.38) with eq. (B.14) we find that in eqs (B.19), (B.20), (B.23), (B.24) and (B.32) $Y_1{}^j$ must be replaced by Ψ^j, $y_1(x_1)$ by $\psi_1(x_1)$, and $y_2(x_1)$ by $\psi_2(x_1)$. Then, after evaluation of all eqs (B.19) through (B.32), the latter equation yields the value of $\psi_2(x_1)$; the fundamental variables at x_1 are then found by inverse transformation of eq. (B.37).

The transformation matrix T_1 is constructed by choosing the elements of $\psi(x)$ on the basis of the boundary conditions at the inner edge. In the case of the longitudinally driven conical membrane we take for the first element of $\psi(x_1)$ the longitudinal driving force F_t at the inner edge and for the second element the longitudinal displacement $u(x_1)$:

$$\psi(x_1) = \begin{bmatrix} F_t \\ u(x_1) \end{bmatrix}. \tag{B.40}$$

From eqs (4.17), (B.33) and (B.37) we find

$$T_1 = \begin{bmatrix} 0 & 2\pi R_a \\ 1 & 0 \end{bmatrix}. \tag{B.41}$$

If we take $F_t = 1\,\mathrm{N}$, the first half of $\psi(x_1)$ is known, as required:

$$\psi_1(x_1) = 1. \tag{B.42}$$

In the case of axisymmetric vibration including bending, we define $\psi(x_1)$ as follows:

$$\psi(x_1) = \begin{bmatrix} 2\pi R_a\,[Q(x_1)\sin\alpha - N_x(x_1)\cos\alpha] \\ w(x_1)\cos\alpha + u(x_1)\sin\alpha \\ \beta_x(x_1) \\ -w(x_1)\sin\alpha + u(x_1)\cos\alpha \\ N_x(x_1) \\ M_x(x_1) \end{bmatrix} \tag{B.43}$$

of which the first half is known:

$$\psi_1(x_1) = \begin{bmatrix} 1 \\ 0 \\ 0 \end{bmatrix}. \tag{B.44}$$

The first element of $\psi(x_1)$ is the axially applied driving force F_a at the inner edge (eq. (5.12c)) and we take $F_a = 1\,\mathrm{N}$. The second element is the inner-edge displacement normal to the cone axis which must be zero (eq. (5.12a)). The third element is the angle of rotation at the inner edge, put equal to zero (eq. (5.12b)). The fourth element is the axial inner-edge displacement needed to compute the axial admittance Y_a; since $F_a = 1\,\mathrm{N}$ it follows that Y_a is numerically equal to $j\omega$ times the value of this fourth element. With eqs (B.34), (B.37) and (B.43) we find the following nonzero elements of the (6, 6) matrix T_1:

$$\begin{aligned} T_1(1,4) &= 2\pi R_a \sin\alpha, \\ T_1(1,5) &= -2\pi R_a \cos\alpha, \\ T_1(2,1) &= T_1(4,2) = \cos\alpha, \\ T_1(2,2) &= -T_1(4,1) = \sin\alpha, \\ T_1(3,3) &= T_1(5,5) = T_1(6,6) = 1. \end{aligned} \tag{B.45}$$

In the case of asymmetric vibration including bending, $\psi(x_1)$ differs only slightly from eq. (B.43):

$$\psi(x_1) = \begin{bmatrix} 2\pi R_a\,[Q_{xn}(x_1)\sin\alpha - N_{xn}(x_1)\cos\alpha] \\ w_n(x_1)\cos\alpha + u_n(x_1)\sin\alpha \\ v_n(x_1) \\ \beta_{xn}(x_1) \\ -w_n(x_1)\sin\alpha + u_n(x_1)\cos\alpha \\ N_{xn}(x_1) \\ N_n(x_1) \\ M_{xn}(x_1) \end{bmatrix}. \tag{B.46}$$

The transformation matrix T_1 follows from eqs (B.35) and (B.37); it has the following nonzero elements:

$$\begin{aligned} T_1(1,5) &= 2\pi R_a \sin\alpha, \\ T_1(1,6) &= -2\pi R_a \cos\alpha, \\ T_1(2,1) &= T_1(5,2) = \cos\alpha, \\ T_1(2,2) &= -T_1(5,1) = \sin\alpha, \\ T_1(3,3) &= T_1(4,4) = T_1(6,6) = T_1(7,7) = T_1(8,8) = 1. \end{aligned} \tag{B.47}$$

From the boundary conditions eqs (5.42) to (5.45) it follows for the upper half of $\psi(x_1)$:

$$\psi_1(x_1) = \begin{bmatrix} 1 \\ 0 \\ 0 \\ 0 \end{bmatrix} \tag{B.48}$$

where again the amplitude of the driving force in eq. (5.41) is taken 1N. Of course the above transformation procedure can also be applied to the outer edge if the latter is submitted to boundary conditions different from those previously assumed.

APPENDIX C

Strain-energy coefficient

The strain-energy coefficient, primarily introduced by Kalnins [15]) for the classification of modes, is defined as the ratio of the strain energy V_B due to bending to the total strain energy of the cone:

$$\eta = \frac{V_B}{V_s + V_B}, \tag{C.1}$$

where V_s is the strain energy due to stretching of the middle surface. In the absence of internal losses we find for symmetric vibrations [18]):

$$V_s = \frac{\pi E h \sin \alpha}{1 - \nu^2} \int_a^b (\varepsilon_x^2 + \varepsilon_\theta^2 + 2 \nu \varepsilon_x \varepsilon_\theta)\, x \, \mathrm{d}x, \tag{C.2}$$

$$V_B = \frac{\pi E h^2 \sin \alpha}{12 (1 - \nu^2)} \int_a^b (\varkappa_x^2 + \varkappa_\theta^2 + 2 \nu \varkappa_x \varkappa_\theta)\, x \, \mathrm{d}x. \tag{C.3}$$

For the strains ε_x, ε_θ and the changes of curvature $\varkappa_x$, $\varkappa_\theta$ the following relations hold:

$$\begin{aligned} \varepsilon_x &= \frac{\mathrm{d}u}{\mathrm{d}x}, \\ \varepsilon_\theta &= (u + w \cot \alpha)/x, \\ \varkappa_x &= \frac{\mathrm{d}\beta_x}{\mathrm{d}x}, \\ \varkappa_\theta &= \beta_x/x. \end{aligned} \tag{C.4}$$

The derivatives of the fundamental variables in the above equations can be written as a linear combination of these fundamental variables (eqs (A.1), (A.6) and (A.8)); we find

$$\begin{aligned} \varepsilon_x &= -\nu (u + w \cot \alpha)/x + (1 - \nu^2) N_x/E h, \\ \varepsilon_\theta &= (u + w \cot \alpha)/x, \\ \varkappa_x &= -\nu \beta_x/x + 12 (1 - \nu^2) M_x/E h^3, \\ \varkappa_\theta &= \beta_x/x. \end{aligned} \tag{C.5}$$

The right-hand sides of these equations are calculated simultaneously with the numerical determination of the solution $y(x_l)$ of the general symmetric differential equations at the end points of each segment (appendix B). The integrals (C.2) and (C.3) are then determined using Simpson's rule.

APPENDIX D

Basic formulas for the rigid-piston radiation

The calculation of the sound radiation of a rigid circular piston vibrating in an infinite rigid baffle can be found in many textbooks on acoustics, e.g. in refs 10 and 26. The result for the sound pressure at a distant field point with coordinates r, φ (see fig. 6.2) is

$$p = j\exp(-j\,k_0\,r)\frac{\varrho_0\,\omega\,v_t\,S}{2\pi\,r}\,\frac{2J_1(k_0\,R_b\sin\varphi)}{k_0\,R_b\sin\varphi} \tag{D.1}$$

where k_0 is the sound wavenumber in air, ϱ_0 the air mass density, ω the angular frequency, v_t, R_b, S the transverse velocity, the radius and the area of the piston respectively.

The sound intensity at the distant field point is

$$I = \hat{p}^2/2\varrho_0 c_0 \tag{D.2}$$

where c_0 is the sound velocity in air and $\hat{p}$ the amplitude of the sound pressure.

The sound power radiated into semi-space is found by integrating the intensity over the hemi-spherical surface with radius r; the result is

$$W = \tfrac{1}{2}\,\varrho_0\,c_0\,v_t^{\,2}\,S\left(1 - \frac{J_1(2\,k_0\,R_b)}{k_0\,R_b}\right). \tag{D.3}$$

In this thesis the radiating diaphragm is assumed to be driven by a sinusoidal axial force of which the amplitude F_a is frequency-independent. We will only consider frequencies lying above the fundamental resonant frequency f_0 of the mass-spring system formed by the total moving mass and the suspension. The motion is therefore essentially mass-controlled and we find for the piston velocity v_t according to Newton's law:

$$v_t = F_a/j\omega M_d \tag{D.4}$$

where M_d is the diaphragm or piston mass. Substituting eq. (D.4) into eq. (D.1), we find

$$p = \frac{\varrho_0}{2\pi\,r}\,\frac{F_a\,S}{M_d}\,\frac{2J_1(k_0\,R_b\sin\varphi)}{k_0\,R_b\sin\varphi}\exp(-j\,k_0\,r). \tag{D.5}$$

The amplitude of the axial sound pressure then becomes frequency-independent:

$$\hat{p}_{ax} = \frac{\varrho_0}{2\pi\,r}\,\frac{F_a\,S}{M_d}. \tag{D.6}$$

The sound power radiated by the mass-controlled piston is

$$W = \tfrac{1}{2}\,\varrho_0\,c_0\,S\left(\frac{F_a}{\omega\,M_d}\right)^2\left(1 - \frac{J_1(2\,k_0\,R_b)}{k_0\,R_b}\right). \tag{D.7}$$

APPENDIX E

Measuring circuit for the motional impedance

The block diagram (fig. 3.3) of the measuring circuit for the motional impedance was discussed in sec. 3.3. It consists of standard electronic parts with circuit diagrams which are not likely to cause difficulties. As an example the circuit diagram of the summation network is shown in fig. E.1; the voltage followers provide the high input impedance of the network and deliver their output signals to a conventional adder with unity gain. The circuit diagram of the current source (fig. E.2) is likewise conventional, and can supply a maximum current of 40 mA. For B (fig. 3.3) any operational amplifier with a power stage can in principle be used.

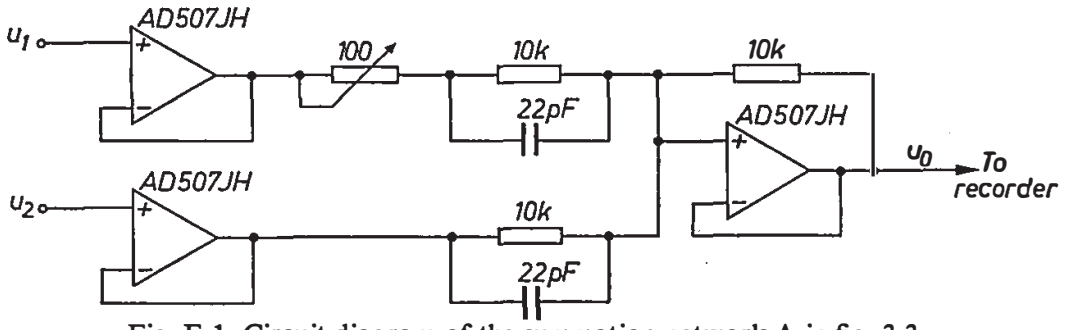

Fig. E.1. Circuit diagram of the summation network A in fig. 3.3.

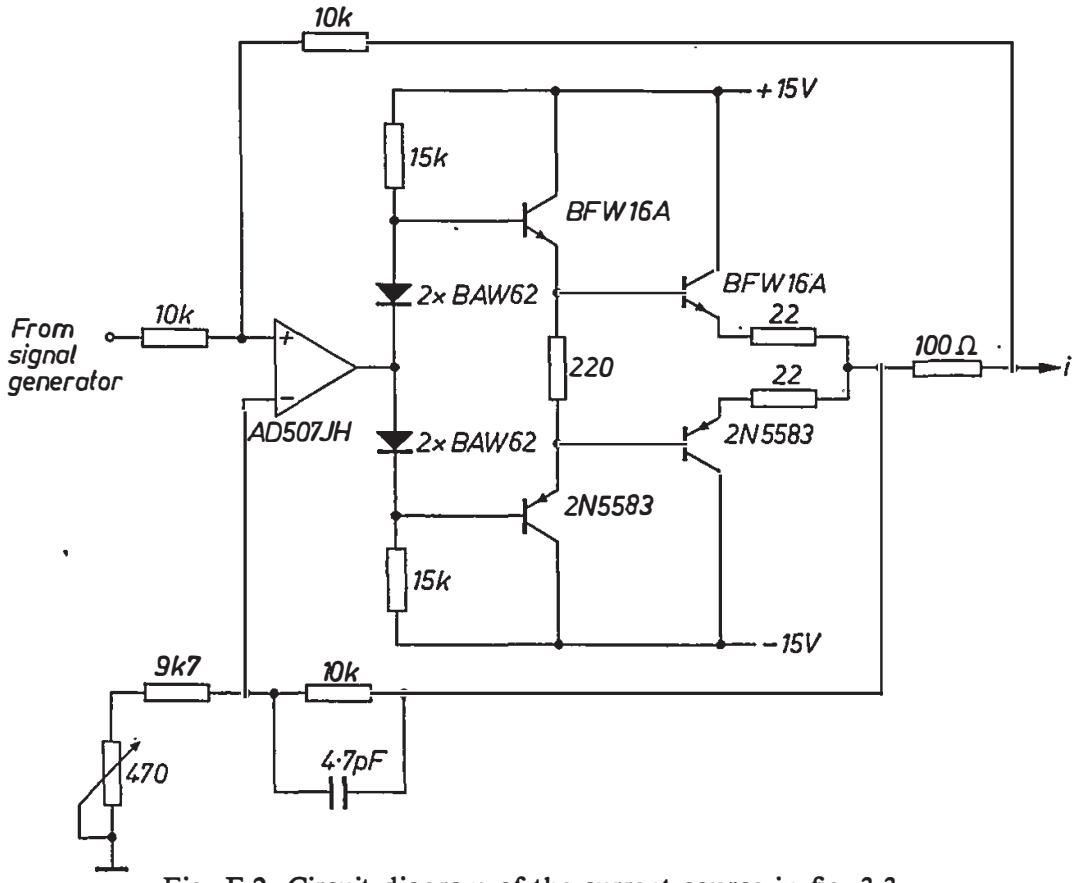

Fig. E.2. Circuit diagram of the current source in fig. 3.3.

APPENDIX F

Time-average fringe holography

Cone vibration patterns shown in sec. 5.12.2 are recorded holographically by means of the time-average fringe technique. A short description of this method will be given below. Further details can be found in the extensive literature on the subject [22,23]).

The optical set-up is sketched in fig. F.1. The beam of a 50-mW helium–neon laser is split into an object beam and a reference beam. The object beam illuminates the sinusoidally vibrating loudspeaker diaphragm. Part of the reflected light falls on a photographic plate, which at the same time is illuminated by the reference beam. The intensity of the latter is adjusted to about four times the intensity of the reflected light from the cone. Thus an interference pattern is created and recorded by the photographic plate during a time much longer than the cone vibration period (in practice several seconds). After development, the photographic plate — now called hologram — is replaced in its original position and illuminated only by the reference beam at full strength (fig. F.2). In this way an infinite number of exposures of the continually vibrating cone, recorded by the hologram, are now reconstructed and interfere with one

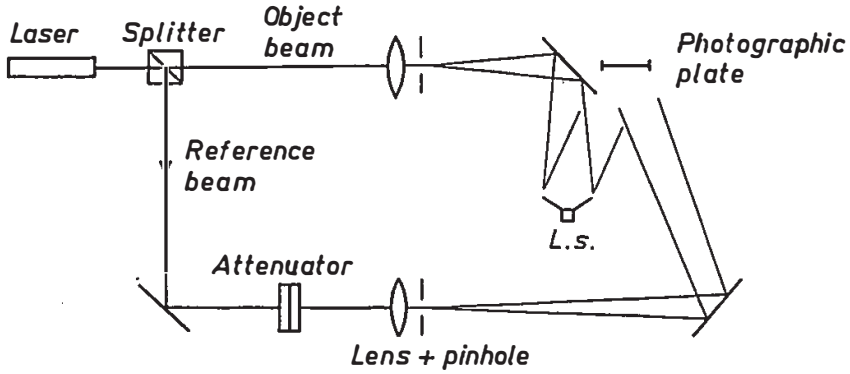

Fig. F.1. Set-up for time-average fringe holography.

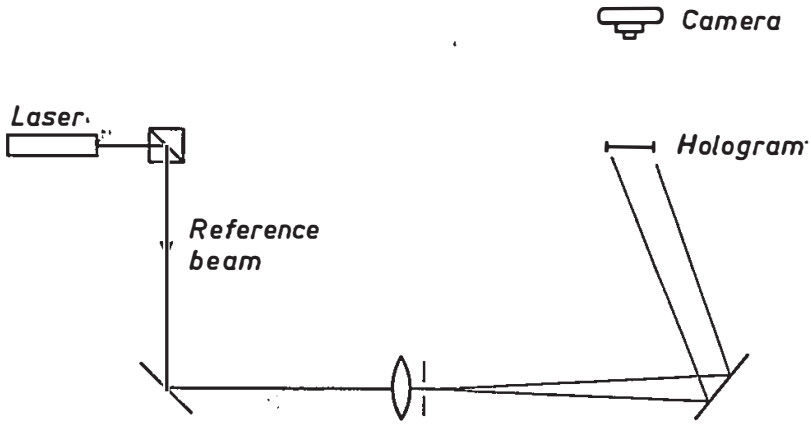

Fig. F.2. Reconstruction of a vibration pattern.

another. Hence, fringes appear at places where the cone has a certain vibrational amplitude; cone parts at rest are normally reconstructed. The reconstructed image of the cone with the superimposed fringes can be photographed normally.

It can be shown [22]) that the intensity of the reconstructed image is proportional to $J_0^2(\varphi)$, where J_0 is the zero-order Bessel function of the first kind and φ the amplitude of the phase shift of the object beam caused by a transverse cone displacement w. It can be shown that

$$\varphi = 2\pi w (\cos \varphi_1 + \cos \varphi_2)/\lambda$$

where φ_1 is the angle between the direction of the object beam and the surface normal, φ_2 the angle between the direction of the photographic plate and the

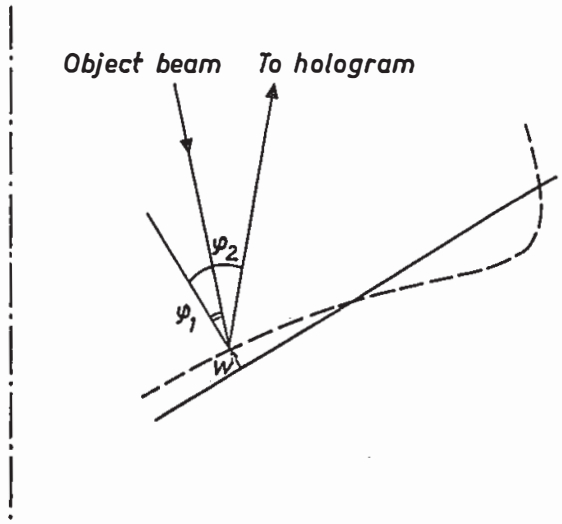

Fig. F.3. Detail of fig. F.1 showing the directions of the illuminating beam and the photographic plate.

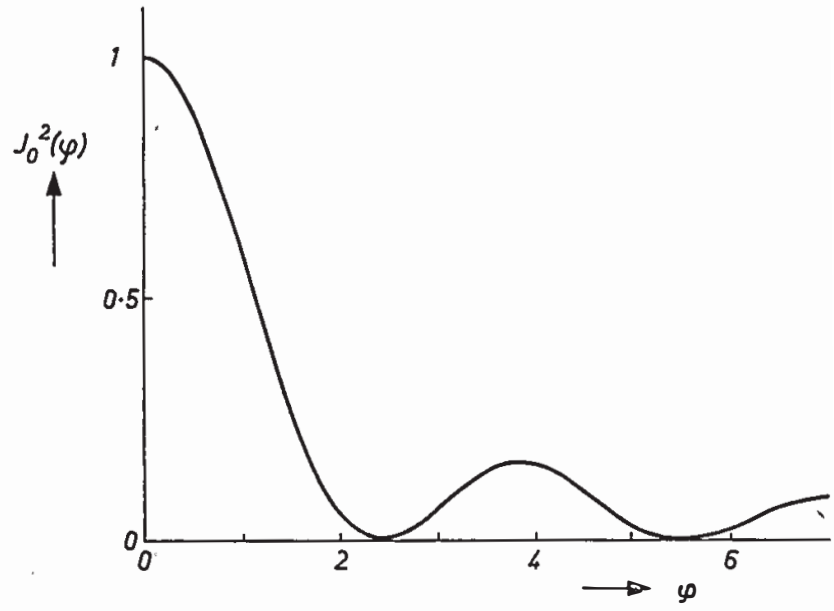

Fig. F.4. Intensity of the reconstructed image as a function of the amplitude of the phase shift φ produced by the cone vibration.

surface normal (fig. F.3), and λ the wavelength of the laser light (632·8 nm). Figure F.4 shows J_0^2 (φ) versus φ. Cone parts at rest are reconstructed with full intensity ($\varphi = 0$). When going from a node to an antinode, φ increases and the intensity becomes zero at the roots of the Bessel function. In this way fringes (black lines) appear on the reconstructed image. The transverse amplitude at these fringes can be found with the above equation. The intensity between the fringes is lower than the intensity of cone parts at rest (see e.g. fig. 5.30*a*).

APPENDIX G

List of cones used in the calculations and measurements

The cones are numbered according to their value of the semi-apex angle α; the last digit is an ordinal number. The experimental cones are indicated by the letter *e*.

	geometry				material				
	semi-apex angle	inner-edge radius	outer-edge radius	thickness	Young's modulus	mass density	Poisson's ratio	loss factor	
cone number	α (°)	R_a (mm)	R_b (mm)	h (mm)	E (. 10^9 N/m²)	ϱ (kg/m³)	ν	δ	
50.1	50	17	83	0·1	2	600	0·3	0·1	
50.2e	50	17	83	0·23	2·4	1200	0·35	0·014	polycarbonate
50.3	50	17	83	0·23	2	600	0·3	0·1	
50.4	50	17	166	0·1	2	600	0·3	0·1	
50.5	50	17	83	0·23	2·2	1160	0·3	0·1	
50.5e	50	17	83	0·27	2·2	1160	0·34	0·06	CAB*)
52.1	52	17	83	0·3	2	600	0·3	0	
60.1	60	17	83	0·1	2	600	0·3	0·1	
60.2	60	17	83	0·26	2·2	1160	0·3	0·1	
60.2e	60	17	83	0·26	2·2	1160	0·34	0·06	CAB
70.1	70	17	98	0·1	2	600	0·3	0·1	
70.2	70	17	83	0·1	2	600	0·3	0·1	
70.3	70	17	83	0·1	2·2	1160	0·3	0·1	
70.3e	70	17	83	0·28	2·2	1160	0·34	0·06	CAB

*) Cellulose-aceto-butyrate.

List of symbols

$A(x)$	(m, m) matrix, denoting the coefficients of the differential equations for the mechanical cone behaviour (see appendix A)
a	meridional coordinate of the inner edge
b	meridional coordinate of the outer edge
B	magnetic induction in the air gap
c	$= (E/\varrho)^{1/2}$ longitudinal-wave velocity in a bar
c_0	sound velocity in air
c_1	$= c/(1 - \nu^2)^{1/2}$ longitudinal-wave velocity in a flat plate
c_B	bending-wave velocity (eq. (5.9))
C_{is}	compliance of the inner suspension (spider)
C_{os}	compliance of the outer suspension (rim)
C_{tot}	total compliance of inner and outer suspensions
DI_{100}	directivity index (eq. (6.3))
E	Young's modulus
f	frequency
f^+, f^-	frequency at which the sound pressure radiated by the back of an unbaffled loudspeaker arrives in phase and in antiphase with that emanating from the front (sec. 6.6.1)
f_0	fundamental resonant frequency of the loudspeaker mass-spring system (eq. (3.4))
f_c	characteristic cone frequency (eq. (6.26))
f_{co}	coincidence frequency (definition in sec. 6.5.4)
f_{lan}	nth longitudinal antiresonant frequency (approximation given by eq. (4.51))
f_{lrn}	nth longitudinal resonant frequency (approximation given by eq. (4.49))
f_{mrn}	nth axial membrane resonant frequency (see secs 4.7.3 and 5.8)
f_{ra}	ring antiresonant frequency (sec. 4.4)
f_{rr}	ring resonant frequency (sec. 4.4)
f_t	transition frequency for the rigid piston (eq. (6.10b))
f_{ta}	upper limit of the cone transition region (eq. (4.12))
f_{tb}	lower limit of the cone transition region (eq. (4.11))
F_a	applied axial force at the inner edge
h	cone thickness
H	cone height (fig. 6.3)
i	voice-coil current
I	sound intensity
k	$= \omega/c$, longitudinal wavenumber in a bar
k_1	$= \omega/c_1$, longitudinal wavenumber in a flat plate
k_B	$= \omega/c_B$, bending wavenumber

k_0	$= \omega/c_0$, sound wavenumber in air
K	$= E\,h/(1 - \nu^2)$ extensional stiffness
l	length of voice-coil windings
L	$= b - a$, meridional cone length
L_c	inductance of blocked voice coil
L_{W100}	sound-power level within a space angle of 100° (sec. 6.2)
m	number of differential equations; number of nodal circles
M	number of segments (sec. B.3)
M_c	voice-coil mass (including the mass of voice-coil cylinder and dust cap or cone top)
M_d	diaphragm mass
M_{tot}	$= M_c + M_d$ total moving mass
$M_x, M_\theta, M_{\theta x}$	moment resultants (fig. 5.1)
n	number of nodal diameters
N	$= N_{\theta x} + M_{\theta x} \cot \alpha/x$, effective tangential shear resultant (ref. 18)
$N_x, N_\theta, N_{\theta x}$	stress resultants (fig. 5.1)
p	sound pressure
$\hat{p}$	amplitude of the sound pressure
Q	$= Q_x + \dfrac{1}{x \sin \alpha} \dfrac{\partial M_{\theta x}}{\partial \theta}$ effective transverse shear resultant (ref. 18)
Q_x, Q_θ	transverse shear resultants (fig. 5.1)
r	distance from axis of symmetry; distance of field point from cone top or piston centre
r_2	radius of curvature (fig. 4.1*a*)
R_a	inner-edge radius
R_b	outer-edge radius
R_c	resistance of the blocked voice coil
R_{is}	mechanical resistance of the inner suspension
R_{os}	mechanical resistance of the outer suspension.
R_2	$= R_a/\cos \alpha$, radius of curvature at the inner edge
S	piston area
S_b	$= \pi R_b^2$, cone base area
$T_1(x)$	(m, m) transformation matrix (eq. (B.37))
u	cone displacement in the meridional direction (fig. 5.1)
v	cone displacement in the azimuthal direction (fig. 5.1)
v_a	axial velocity (fig. 5.3*a*)
v_l	longitudinal velocity (fig. 5.3*a*)
v_t	transverse velocity (fig. 5.3*a*)
V_t	reduced transverse velocity (eq. (6.34))
w	cone displacement in the transverse direction (fig. 5.1)
W	acoustic power

x	meridional coordinate
x_t	meridional coordinate of the transition point (eq. (4.10))
$Y(x)$	(m, m) matrix whose columns are the linearly independent solutions of the mechanical differential equations (eq. (B.7))
$Y_i^j(x)$	$(m/2, m/2)$ matrix, i identifies segment S_i, j denotes the quadrant of the partitioned matrix $Y(x)$ (eq. (B.16))
$Y_{a,t,l}$	axial, transverse and longitudinal admittances at the inner edge (see definition of $Z_{a,t,l} = 1/Y_{a,t,l}$, eqs (5.14) and (5.15))
y_a	$= Y_a \cos^2 \alpha / Y_{lc}$, reduced axial admittance at the inner edge (eq. (5.35))
y_l	$= Y_l / Y_{lc}$, reduced longitudinal admittance at the inner edge (eq. (4.53))
Y_{lc}	characteristic longitudinal admittance of a single-ended infinite plate (eq. (4.46))
Y_{tot}	total axial admittance of cone and voice coil (see definition of $Z_{\text{tot}} = 1/Y_{\text{tot}}$, eq. (5.40))
$Z_{a,t,l}$	axial, transverse and longitudinal impedances at the inner edge (eqs (5.14) and (5.15))
Z_e	electrical impedance between voice-coil terminals (eq. (3.1))
Z_{lc}	characteristic longitudinal impedance of a single-ended infinite plate (see definition of $Y_{lc} = 1/Z_{lc}$, eq. (4.46))
Z_{mot}	motional impedance (eq. (3.2))
Z_{tc}	characteristic transverse impedance of a single-ended infinite plate (eq. (5.22))
Z_r	electrical impedance of a reference loudspeaker with a blocked voice coil (eq. (3.10))
α	semi-apex angle
β	beam width (definition in sec. 2.5.2)
β_x	angle of rotation in the meridional direction
β_θ	angle of rotation in the azimuthal direction
γ	bending constant (eq. (5.8))
δ	internal loss factor of the cone material
θ	azimuthal coordinate (fig. 6.3)
λ_0	sound wavelength in air
λ_1	longitudinal wavelength in an infinite plate
λ_B	bending wavelength in an infinite plate (eq. (5.10))
ν	Poisson's ratio
ϱ	specific mass density of the cone material
ϱ_0	air mass density
φ	angle between cone axis and field-point direction (fig. 6.3)
ω	angular frequency

REFERENCES

[1]) L. L. Beranek, Acoustics, McGraw-Hill, New York, 1954.
[2]) T. Nimura, E. Matsui, K. Shibayama and K. Kido, Rep. Res. Inst. El. Comm. (Japan) 3, 55, 1951.
[3]) T. Nimura and K. Shibayama, Rep. Res. Inst. Tohoku Univ. B3, 189, 1952.
[4]) E. W. Ross Jr., J. Appl. Mech. 33, 85, 1966.
[5]) E. W. Ross Jr., J. Math. Phys. 45, 335, 1966.
[6]) E. W. Ross Jr. and W. T. Matthews, J. Appl. Mech. 34, 73, 1967.
[7]) J. C. Snowdon, Vibration and shock in damped mechanical systems, Wiley, New York, 1968.
[8]) E. H. Love, A treatise on the mathematical theory of elasticity, Cambridge, 1927.
[9]) E. Skudrzyk, Simple and complex vibratory systems, Pennsylvania Univ. Press, London, 1968.
[10]) E. Skudrzyk, The foundations of acoustics, Springer, New York, 1971.
[11]) N. W. McLachlan, Loudspeakers, Oxford Univ. Press, 1934.
[12]) E. Reissner, Am. J. Math. 63, 177, 1941.
[13]) J. E. Goldberg, J. L. Bogdanoff and L. Marcus, J. Acoust. Soc. Am. 32, 738, 1960.
[14]) A. Kalnins, J. Appl. Mech. 31, 467, 1964.
[15]) A. Kalnins, J. Acoust. Soc. Am. 36, 74, 1964.
[16]) A. Kalnins, J. Acoust. Soc. Am. 36, 1355, 1964.
[17]) A. Kalnins, Appl. Mech. Rev. 18, 867, 1965.
[18]) V. V. Novozhilov, The theory of thin shells, Noordhoff Ltd., Groningen, 1959.
[19]) R. F. Hartung and W. A. Loden, J. Spacecraft Rock. 7, 1153, 1970.
[20]) R. N. Arnold and G. B. Warburton, Proc. Roy. Soc. A197, 238, 1949.
[21]) P. Seide, Isr. J. Techn. 3, 50, 1965.
[22]) R. L. Powell and K. A. Stetson, J. Opt. Soc. Am. 55, 612 and 1593, 1965.
[23]) G. Groh, VDI-Ber. 135, 145, 1969.
[24]) H. M. Adelman, D. S. Catherines and W. C. Walton, Jr., NASA TN D-4972, jan. 1969.
[25]) P. M. Morse, Vibration and sound, McGraw-Hill, New York, 1948.
[26]) P. M. Morse and K. U. Ingard, Theoretical acoustics, McGraw-Hill, New York, 1968.
[27]) W. N. Brown Jr., J. Acoust. Soc. Am. 13, 20, 1941.
[28]) P. G. Bordoni, J. Acoust. Soc. Am. 17, 123, 1945.
[29]) J. A. Zonneveld, Automatic numerical integration, Math. Centr. Tracts nr. 8, Math. Centre Amsterdam, 1964.
[30]) N. Marcuvitz, Comm. Pure Appl. Math. 4, 263, 1951.
[31]) O. N. Loginova, Radio Eng. Electron. Phys. 14, 514, 1969.
[32]) H. A. Schenk, J. Acoust. Soc. Am. 44, 41, 1968.
[33]) G. Chertock, J. Acoust. Soc. Am. 47, 387, 1970.
[34]) H. T. O'Neil, J. Acoust. Soc. Am. 21, 516, 1949.
[35]) T. S. Belle, Sov. Phys. Ac. 14, 296, 1969.
[36]) T. S. Belle, Sov. Phys. Ac. 15, 296, 1970.
[37]) M. Lax, J. Acoust. Soc. Am. 16, 5, 1944.
[38]) M. Abramowitz and I. A. Stegun, Handbook of mathematical functions, Dover Publ., New York, 1965.
[39]) P. M. Morse and H. Feshbach, Methods of theoretical physics, McGraw-Hill, New York, 1953.
[40]) L. Cremer, M. Heckl and E. E. Ungar, Structure-borne sound, Springer, Berlin, 1973.
[41]) H. F. Olson, Acoustical engineering, Van Nostrand, London, 1957.
[42]) L. Cremer and M. Heckl, Körperschall, Springer, Berlin, 1967, p. 491.
[43]) R. Josse and C. Lamure, Acustica 14, 266, 1964.

On the Calculation of the Axisymmetric Modes and Frequencies of Conical Shells

JOHN E. GOLDBERG AND JOHN L. BOGDANOFF
Purdue University, Lafayette, Indiana

AND

LEE MARCUS
Allison Division, General Motors Corporation, Indianapolis, Indiana

(Received December 1, 1959)

A numerical method is presented for determining the axisymmetric modes of vibration and natural frequencies of thin conical shells such as loudspeaker cones. Assuming the applicability of the classical theory of thin shells, the pertinent differential equations are presented in a form which is well-suited to numerical integration on an electronic digital computer. The method may be used also to determine the impedance of the cone at other than the natural frequencies, and to calculate the mechanical impedance of the assembly comprising the cone and the voice coil. Results are shown, by a numerical example, to compare favorably with a previously available method based upon the use of power series.

INTRODUCTION

THE most common type of loudspeaker in general use consists essentially of a truncated circular conical shell of rather large apical angle, driven by a voice coil which is suspended in a magnetic field. The voice coil is wound upon a cylindrical tube which, together with a flat diaphragm or closure, is attached integrally and coaxially to the small end of the truncated cone. At the large end, the edge of the cone is turned outward to form a flange, usually containing one or more concentric corrugations and attached to a rigid frame.

In selecting or designing a loudspeaker of this type, information on the natural frequencies and natural modes is necessary. The response and mode shape assumed by the cone at other frequencies within the operating range are also important in the calculation of the acoustical impedance of the speaker. Unfortunately, simple solutions to the problems of vibrating conical shells have not been available, and it has been necessary in loudspeaker applications to replace the cone by a rigid circular disk[1] or equivalent piston[2] for the purpose of calculating the acoustical impedance.

In the general case of vibration of conical shells, two fundamentally different configurations are possible: mode shapes having nodal lines coincident with generators, and mode shapes having concentric circular nodal lines. Combinations of the two are, of course, also possible. The radial nodes are associated with essentially pure bending and do not require significant extension of the median surface. The axisymmetric modes, having circular nodal lines, require both bending and extension, the latter particularly in the circumferential direction.

It has been observed[3] that the increased rigidity obtained at the edge of the cone by bending the edge to form a flange which is attached, in turn, to the speaker frame suppresses the radial modes. The axisymmetric modes therefore are particularly important in loudspeaker design and selection.

A solution to the problem of axisymmetric oscillation of thin conical shells was obtained by Goldberg[4] in the form of power series involving three parameters determined by the geometry of the cone, the mechanical properties of the material and the frequency. The solution gives the response of the cone to a harmonic forcing function of prescribed amplitude and frequency applied at one end of the cone, and can be used also to determine the natural frequencies since the mechanical impedance of a simple cone drops to zero or becomes infinite at the natural frequencies, depending upon the end constraints.

The purpose of the present paper is to describe a purely numerical method of solution of problems of axisymmetric vibration of conical shells and to display and discuss some results obtained by this method. These results have been obtained on an electronic digital computer.

Equations are presented in a form which is particularly convenient for numerical integration. The equations are valid not only for uniform shells but also for shells in which the thickness and mechanical properties may vary in the direction of the generator. In the form given, the equations presuppose that the material is isotropic and obeys Hooke's law, and that the other assumptions of classical shell theory are not violated. Obviously, these restrictions may be relaxed somewhat if appropriate modifications are made to the equations.

[1] N. W. McLachlan, *Loud Speakers* (Oxford University Press, London, 1934) p. 8.

[2] I. B. Crandall, *Theory of Vibrating Systems and Sound* (D. Van Nostrand and Company, New York, 1927), pp. 29, 36. See also, by L. L. Beranek, *Acoustic Measurements* (John Wiley and Sons, Inc., New York, 1949), p. 22.

[3] See reference 1, pp. 307, 308.

[4] John E. Goldberg, "Axisymmetric oscillation of conical shells," *Proceedings of the IXth International Congress of Applied Mechanics*, Brussels, 1956.

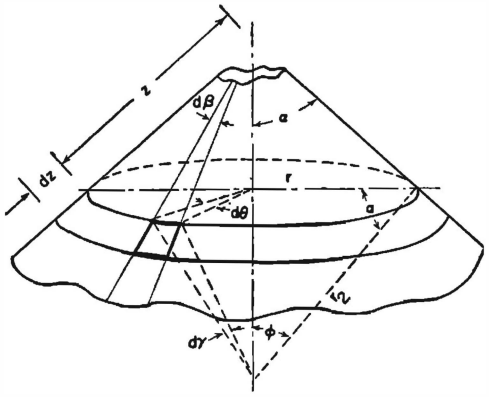

FIG. 1. Median surface of conical shell and generic element.

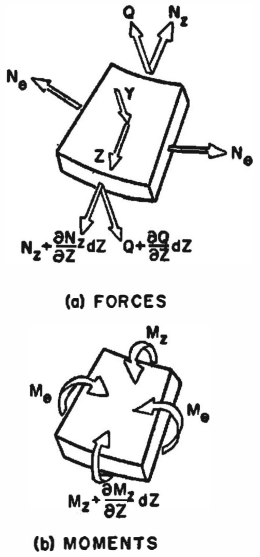

FIG. 2. Element of shell showing positive directions of applied loads and internal forces and moments.

EQUATIONS FOR AXISYMMETRIC PROBLEMS OF CONICAL SHELLS

The shell and coordinates are shown in Fig. 1. The generic element of the shell and the forces acting upon the element are shown in Fig. 2. The lateral boundaries of the element lie in meridional planes with an included angle $d\theta$. The upper and lower boundaries lie on coaxial cones which are orthogonal to the median surface of the shell.

By virtue of symmetry about the axis of the cone, the internal and external forces and displacements are independent of the coordinate θ, and depend only upon the coordinate z, measured along the generator from the apex of the cone. Because of symmetry, there are no shearing forces at the lateral boundaries of the element, and there are no tangential shearing forces on the upper and lower edges of the element. The edges of the element are thus seen to be subjected to membrane forces N_z and N_θ in the direction of the generator and in the circumferential direction, bending moments M_z and M_θ in the corresponding directions, and normal shears Q at only the upper and lower edges. These internal loads are per unit length of edge of element. The element is also subjected to distributed loadings Y and Z per unit area of the median surface applied in the directions of the normal and of the generator. The distributed loads may include acoustical or aerodynamic loading.

Consideration of the equilibrium of the element leads to the following equation of motion[5]:

$$\begin{aligned}
&\frac{\partial}{\partial z}(zN_z)-N_\theta+zZ=z\rho h\frac{\partial^2 v}{\partial t^2},\\
&\frac{\partial}{\partial z}(zQ)-N_\theta\cot\alpha+zY=z\rho h\frac{\partial^2 w}{\partial t^2},\\
&\frac{\partial}{\partial z}(zM_z)-M_\theta-zQ=0,
\end{aligned}\tag{1}$$

where v=displacement in the direction of the generator, positive in the direction of positive z, w=displacement normal to the surface, positive inward, ρ=density.

With the usual assumptions of thin shell theory[4,5] the relations between the internal forces and the displacements of the median surface are:

$$\begin{aligned}
N_z&=\frac{Eh}{1-\mu^2}\left[\frac{\partial v}{\partial z}+\mu\left(\frac{v}{z}-\frac{w}{z}\cot\alpha\right)\right],\\
N_\theta&=\frac{Eh}{1-\mu^2}\left(\frac{v}{z}-\frac{w}{z}\cot\alpha+\mu\frac{\partial v}{\partial z}\right),\\
M_z&=-D\left(\frac{\partial^2 w}{\partial z^2}+\frac{\mu}{z}\frac{\partial w}{\partial z}\right),\\
M_\theta&=-D\left(\frac{1}{z}\frac{\partial w}{\partial z}+\mu\frac{\partial^2 w}{\partial z^2}\right),\\
Q&=-D\left(\frac{\partial^3 w}{\partial z^3}+\frac{1}{z}\frac{\partial^2 w}{\partial z^2}-\frac{1}{z^2}\frac{\partial w}{\partial z}\right),
\end{aligned}\tag{2}$$

where E=modulus of elasticity, h=thickness, μ=Poisson's ratio, and $D=(Eh^3)/[12(1-\mu^2)]$.

If the distributed loadings and the edge loadings fluctuate harmonically with time at a circular frequency p,

$$\begin{aligned}
Y(z,t)&=\bar{Y}(z)\cos pt,\\
Z(z,t)&=\bar{Z}(z)\cos pt, \text{ etc.}
\end{aligned}\tag{3}$$

the solution to Eqs. (1) and (2) may be taken in the form

$$\begin{aligned}
v(z,t)&=V(z)\cos pt,\\
w(z,t)&=W(z)\cos pt,\\
M_z(z,t)&=\bar{M}_z(z)\cos pt,\\
M_\theta(z,t)&=\bar{M}_\theta(z)\cos pt,\\
N_z(z,t)&=\bar{N}_z(z)\cos pt,\\
N_\theta(z,t)&=\bar{N}_\theta(z)\cos pt,\\
Q(z,t)&=\bar{Q}(z)\cos pt.
\end{aligned}\tag{4}$$

[5] Goldberg, Bogdanoff, and Marcus, "Analysis of conical shells by electronic computer," presented at National Meeting of American Society of Civil Engineers, Cleveland, Ohio, May, 1959.

Substitution of Eqs. (3) and (4) into Eqs. (1) and (2) and simple algebraic manipulation yield the following system of six first-order differential equations in the amplitudes of the displacements and forces:

$$\frac{dW}{dz}=S,$$

$$\frac{dS}{dz}=\frac{\bar{M}_z}{D}-\frac{\mu}{z}S,$$

$$\frac{d\bar{M}_z}{dz}=-\frac{1-\mu}{z}\bar{M}_z-\frac{(1-\mu^2)D}{z^2}S+\bar{Q}, \tag{5}$$

$$\frac{d\bar{Q}}{dz}=-\frac{\bar{Q}}{z}-\frac{Eh}{z}\cot\alpha(V-W\cot\alpha)-\frac{\mu\cot\alpha}{z}\bar{N}_z-Y-p^2\rho hW,$$

$$\frac{d\bar{N}_z}{dz}=\frac{Eh}{z}(V-W\cot\alpha)-\frac{1-\mu}{z}\bar{N}_z-Z-p^2\rho hV,$$

$$\frac{dV}{dz}=\frac{1-\mu^2}{Eh}\bar{N}_z-\frac{\mu}{z}(V-W\cot\alpha).$$

The dependent variable S which appears in the first of Eqs. (5) is seen to be simply the local amplitude of slope in the meridional direction, and is introduced to permit (5) to be stated completely as a set of first-order differential equations for the purpose of numerical integration by a suitable technique.

For a specified value of the circular frequency p and with V and Z expressed as functions of z or of V and W, Eq. (5) may be integrated in a straightforward manner by numerical methods, subject to appropriate boundary conditions. For example, the boundary equations at the outer edge may be formulated in terms of the elastic constants of the outer suspension. If the impedance of the cone is the major consideration, the boundary conditions at the inner edge may be taken as the amplitudes associated with a unit axial displacement of the voice coil at the specified frequency. After integrating Eq. (5) so that the boundary conditions are satisfied, the amplitude of the axial force applied at the inner edge may be calculated. If this is done for several values of the frequency, a curve of impedance vs frequency may be drawn. Subject to the accuracy of the numerical methods which have been employed, the zeros of this curve are the values of the natural frequencies for the condition of a "guided" inner end or voice coil—that is, the inner end is free only to move axially. The infinities of this curve are the approximate values of the natural frequencies for the condition of a rigidly constrained or built-in inner end. Furthermore, the values of frequency for which the total axial force at the inner edge is equal to the corresponding inertia force of the voice coil assembly are the natural frequencies of the system consisting of conical shell and voice coil. If only the natural frequencies and mode shapes are being sought, the integration may be started directly with the appropriate geometrical or natural initial conditions.

Alternatively, as will be discussed later, one may take the determinant of the coefficients of the arbitrary constants in the three outer boundary equations as a measure of the error of the trial value of the frequency. Frequencies for which the value of the determinant becomes zero are the approximate natural frequencies of the cone.

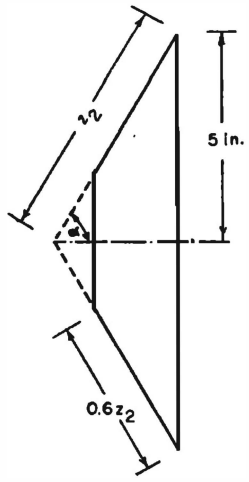

FIG. 3. Illustrative example.

NUMERICAL ANALYSIS

The equations of motion (5) of the differential element of the shell constitute a set of six first-order linear differential equations of the form

$$\frac{dYi}{dz}=\sum_{j=1}^{6}a_{ij}Y_j \quad i=1, 2, 3, \cdots, 6, \tag{6}$$

for which, in general, three initial conditions have been prescribed. In order to perform the numerical integration, the problem is transformed from a two-point boundary value problem to an initial value problem. This is accomplished by introducing six linear transformations of the form

$$Y_i(z)=\alpha_i(z)\bar{N}_{z,a}+\beta_i(z)\bar{M}_{z,a}+\gamma_i(z)\bar{Q}_{,a}, \tag{7}$$

where $\bar{N}_{z,a}$, $\bar{M}_{z,a}$, $\bar{Q}_{,a}$ essentially are three arbitrary and previously uncommitted constants and represent the values of $\bar{N}_z$, $\bar{M}_z$, and $\bar{Q}$ at $z=a$. By use of Eq. (7) along with the appropriate initial conditions, the initial values of the new dependent variables become known in terms of the arbitrary constants.

Through the substitution of Eq. (7) into Eq. (6) and equating coefficients of the arbitrary constants,

three sets of differential equations are formed:

$$\frac{d\alpha_i}{dz} = \sum_{j=1}^{6} a_{ij}\alpha_j$$

$$\frac{d\beta_i}{dz} = \sum_{j=1}^{6} a_{ij}\beta_j \quad i=1, 2, 3, \cdots, 6. \tag{8}$$

$$\frac{d\gamma_i}{dz} = \sum_{j=1}^{6} a_{ij}\gamma_j$$

The three sets of differential equations (8) are integrated numerically by an appropriate technique, such as the fourth-order Runge-Kutta method, from the inner edge at $z=a$ to the outer edge at $z=b$, for an assigned value of the frequency, p.

Substituting the transformation equations (7) into the boundary equations at the outer edge and using the numerical values of the functions α_i, β_i, γ_i $(i=1, 2, \cdots, 6)$ at $z=b$ yields three linear equations in the arbitrary constants $\bar{N}_{z,a}$, $\bar{M}_{z,a}$, and $\bar{Q}_{,a}$.

If one is seeking a natural frequency and has begun the integrations for a trial value of the frequency with the proper boundary conditions at $z=a$, the determinant of the coefficients of the arbitrary constants in the three outer boundary equations becomes a measure of the error of the trial value of the frequency. If a correct value of p were used, the value of this determinant would be zero. Thus, letting ϵ be the value of the determinant, a plot of ϵ vs p can be constructed for a set of trial values of the frequency. The zeros of this curve are the approximate values of the natural frequencies.

Alternatively, as suggested in the previous section, if one is seeking a natural frequency and has begun the integrations with possible displacements of arbitrary magnitude at $z=a$, but with the axial force undefined, the outer boundary equations may be solved for the arbitrary constants. These constants are then used to determine the forces at the inner edge of the cone. The resultant force in the axial direction may be calculated and a plot of this resultant force vs frequency may be constructed. The zeros of this curve are the natural frequencies of the cone when there is no constraint against axial displacement at $z=a$. The infinities of this curve are the natural frequencies when the inner edge is rigidly constrained against axial displacement, i.e., is "built-in" with respect to axial displacement.

The frequencies of the cone when connected to a voice coil or other mass can also be determined from the latter curve. If m is the mass of the voice coil and the integration is made for an axial displacement of unit magnitude, the natural frequencies are those frequencies for which the resultant force is equal to mp^2.

ILLUSTRATIVE EXAMPLE

As an illustrative example, the lower axisymmetrical natural frequencies and mode shapes of the uniform cone shown in Fig. 3 were computed. Calculations for this cone previously have been made[4] by the series method and the results obtained by the two methods are compared.

The fundamental data for this cone are: $\alpha=60°$, $h=0.025$ in., $E=150{,}000$ psi, $\mu=0.25$, $\rho=30\times10^{-6}$ slug per in.^{3} The cone was assumed to be free at the outer edge and clamped at the inner edge.

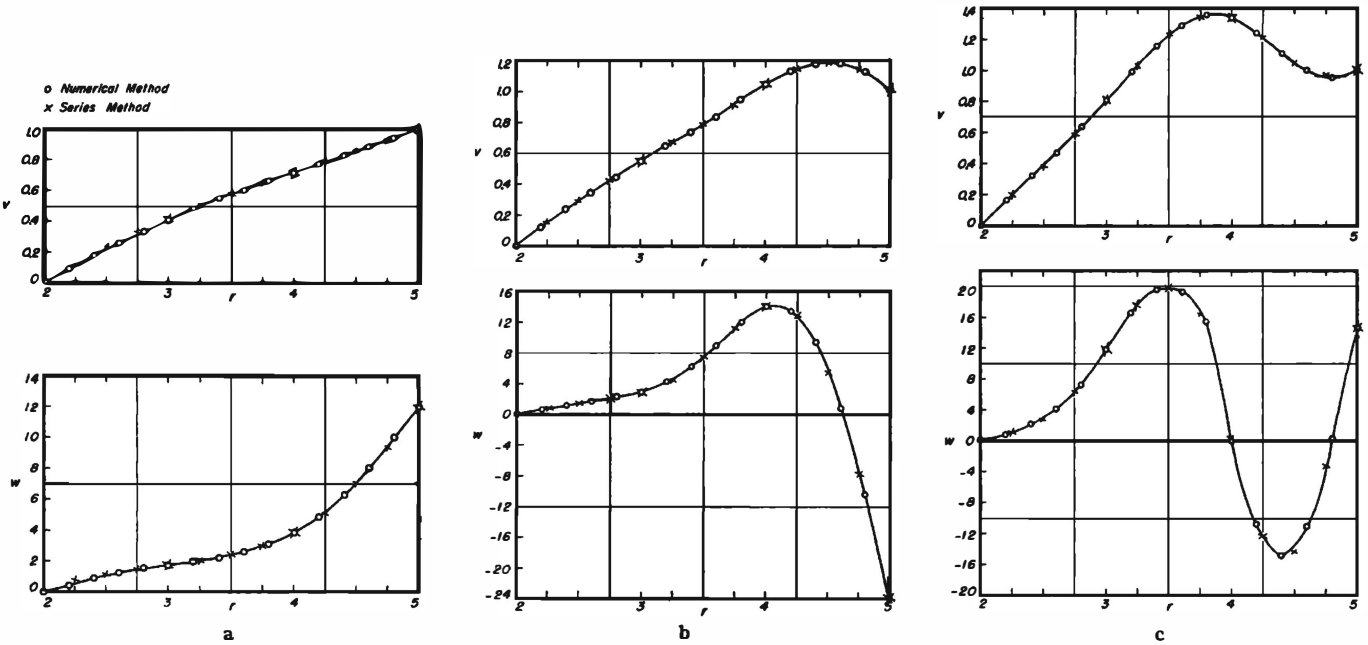

FIG. 4 (a) Mode shape at fundamental frequency; (b) mode shape at second natural frequency; (c) mode shape at third natural frequency.

TABLE I. Calculated frequency, cps.

Mode	Numerical method	Series method
1st	1072	1071
2nd	1315	1315
3rd	1611	1610

The values of the three lowest frequencies were found essentially by a trial-and-error technique as indicated in the previous sections. A trial value of the frequency was chosen and the equations integrated with initial values of the dependent variables satisfying the initial boundary conditions. A measure of the amount by which the terminal boundary conditions were not satisfied was determined. Successive runs were made until a value of the frequency was found which substantially satisfied the complete set of boundary conditions, i.e., the value of the measure vanished.

The equations were integrated by the Runge-Kutta fourth-order process, using fifteen equal intervals to represent the total length of the generator. From the results which have been obtained, it is seen that this number of divisions gives excellent results for the first three frequencies and modes. Useful results doubtless would be obtained for the fourth natural frequency and fourth mode with the same number of intervals, but somewhat more dependable results would be obtained for the fourth and higher orders of vibration if a greater number of intervals were used.

The three lowest apparent natural frequencies of axisymmetric vibration of the shell shown in Fig. 3 with the boundary conditions previously mentioned, computed by the numerical method using only fifteen intervals, are listed in Table I. For comparison, the frequencies computed by the series method[4] are also listed. It is seen that the agreement between the calculated frequencies as obtained by the two methods is excellent.

The mode shapes computed by the numerical method are shown in Fig. 4. The mode shapes have been normalized so that the displacement v at the outer edge in the direction of the generator has a unit amplitude. For comparison, the amplitudes as computed by the series method are also shown on these figures, and it is seen that the agreement between the results obtained by the two methods is again excellent.

Analysis of Shells of Revolution Subjected to Symmetrical and Nonsymmetrical Loads[1]

A. KALNINS
Assistant Professor
of Engineering and Applied Science,
Yale University,
New Haven, Conn.
Mem. ASME

The boundary-value problem of deformation of a rotationally symmetric shell is stated in terms of a new system of first-order ordinary differential equations which can be derived for any consistent linear bending theory of shells. The dependent variables contained in this system of equations are those quantities which appear in the natural boundary conditions on a rotationally symmetric edge of a shell of revolution. A numerical method of solution which combines the advantages of both the direct integration and the finite-difference approach is developed for the analysis of rotationally symmetric shells. This method eliminates the loss of accuracy encountered in the usual application of the direct integration approach to the analysis of shells. For the purpose of illustration, stresses and displacements of a pressurized torus are calculated and detailed numerical results are presented.

THE shell of revolution is an important structural element, and the literature devoted to its analysis is extensive. With regard to axisymmetric deformation, various methods have been employed to obtain solutions of the bending theory of shells of revolution by means of the H. Reissner-Meissner equations. For example, Naghdi and DeSilva [1][2] use asymptotic integration; Lohmann [2], Münz [3], Klingbeil [4], employ a direct numerical integration approach; Galletly, et al. [5] find the solution for an ellipsoidal shell of revolution by both the finite-difference and the Runge-Kutta method; and Penny [6], Radkowski, et al. [7], and Sepetoski, et al. [8] utilize the finite-difference technique. A number of additional references which deal with the solution of the H. Reissner-Meissner equations can be found in the papers cited.

For problems of bending in the absence of axial symmetry, a reduction of the governing equations of arbitrary shells of revolution to a system of four second-order differential equations involving four unknowns has been carried out by Budiansky and Radkowski [9]. A method for obtaining the solution of these equations is given in [9] which is an extension of that employed in [7] and [8]. Furthermore, treatments of nonsymmetric deformation of shells of revolution are found in papers by Goldberg and Bogdanoff [10], where a system of first-order differential equations for conical shells is derived, and by Steele [11] and Schile [12], where solutions of certain types are considered by means of asymptotic integration.

Among the papers which employ numerical analysis, two dif-

[1] National Science Foundation Grant No. 23922, Report No. 3, July, 1963.

[2] Numbers in brackets designate References at end of paper.

Presented at the Summer Conference of the Applied Mechanics Division, Boulder, Colo., June 9–11, 1964, of THE AMERICAN SOCIETY OF MECHANICAL ENGINEERS.

Discussion of this paper should be addressed to the Editorial Department, ASME, United Engineering Center, 345 East 47th Street, New York, N. Y. 10017, and will be accepted until October 10, 1964. Discussion received after the closing date will be returned. Manuscript received by ASME Applied Mechanics Division, July 31, 1963. Paper No. 64—APM-33.

Nomenclature

ϕ, θ, ζ = coordinates of a point of shell
s = distance measured from an arbitrary origin along meridian in positive direction of ϕ
$\mathbf{t}_\phi, \mathbf{t}_\theta, \mathbf{n}$ = unit vectors tangent to coordinate curves (see Fig. 1)
R_ϕ, R_θ = principal radii of curvature of middle surface
r = distance of a point on middle surface from axis of symmetry
E = Young's modulus
ν = Poisson's ratio
h = thickness of shell
α = coefficient of thermal expansion
$D = Eh^3/[12(1 - \nu^2)]$
$K = Eh/(1 - \nu^2)$
u_ϕ, u_θ, w = components of displacement of middle surface
β_ϕ, β_θ = angle of rotation of normal
p_ϕ, p_θ, p = components of mechanical surface loads
m_ϕ, m_θ = components of moment of surface loads
T, T_0, T_1 = temperature increment and temperature resultants
$N_\phi, N_\theta, N_{\theta\phi}$ = membrane stress resultants
$M_\phi, M_\theta, M_{\theta\phi}$ = moment resultants
Q_ϕ, Q_θ = transverse-shear resultants
N, Q = effective-shear resultants
$J = 1/R_\phi + \sin\phi/r$
$U = 1/R_\phi + \nu \sin\phi/r$
$H = 1/R_\phi - \sin\phi/r$
n = integer, designating nth Fourier component
β = length factor
$( )_{,x}$ = derivative with respect to any coordinate
m = order of system of equations
M = number of segments
x = independent variable, either ϕ or s
x_i = end point of segment
$y(x)$ = $(m, 1)$ matrix, fundamental variables
$A(x)$ = (m, m) matrix, coefficients of differential equations
$B(x)$ = $(m, 1)$ matrix, nonhomogeneous coefficients
$Y(x)$ = (m, m) matrix, homogeneous solutions
$Z(x)$ = $(m, 1)$ matrix, nonhomogeneous solutions
C = $(m, 1)$ matrix, arbitrary constants
I = unit matrix

ferent methods of solution of the boundary-value problem of deformation of shells must be recognized; i.e., the direct integration [2–5] and the finite difference approach [5–9]. While the direct integration approach has certain important advantages, it also has a serious disadvantage; i.e., when the length of the shell is increased, a loss of accuracy invariably results. This phenomenon was clearly pointed out in [8]. The loss of accuracy does not result from accumulative errors in integration, but it is caused by the subtraction of almost equal numbers in the process of determination of the unknown boundary values. It follows that for every set of geometric and material parameters of the shell there is a critical length beyond which the solution loses all accuracy. The advantage of the finite-difference approach over direct integration is that it can avoid such a loss of accuracy. It is concluded from [8] that if the solution of the system of algebraic equations, which result from the finite-difference equations, is obtained by means of Gaussian elimination, then no loss of accuracy is experienced if the length of the shell is increased.

This paper is concerned with the general problem of deformation of thin, elastic shells of revolution, symmetrically or nonsymmetrically loaded, and with the development of a numerical method of its solution, which employs the direct integration technique, but eliminates the loss of accuracy owing to the length of the shell. The method developed here is applicable to any two-point boundary-value problem which is governed within an interval by a system of m first-order linear ordinary differential equations together with $m/2$ boundary conditions prescribed at each end of the interval. It is shown that the boundary-value problem of a rotationally symmetric shell can be stated in this form for any consistent linear bending theory of shells in terms of those quantities which appear in the natural boundary conditions on a rotationally symmetric edge.

The method of this paper offers definite advantages over the finite-difference approach. The main advantages are: (a) It can be applied conveniently to a large system of first-order differential equations, and (b) it permits an automatic selection of an optimum step size of integration at each step according to the desired accuracy of the solution. The first point means that the equations of the theory of shells of revolution, characterized in terms of first-order differential equations, can be integrated directly, and further reduction of the equations to a smaller number of unknowns is not necessary. The second point seems to be of great importance if a truly general method is desired which is expected to hold for arbitrary loads, shell configurations, thickness, and so on. With the finite-difference approach, a meaningful *a priori* estimate of the step size is often difficult, if not impossible, especially when rapid changes and discontinuities in the shell parameters are encountered. If a predictor-corrector direct integration approach is employed with the method of this paper, then the step size can be selected automatically at each step which ensures a prescribed accuracy of the solution and optimum efficiency in the calculation.

The method given in this paper can be divided into two parts: (a) Direct integration of $m + 1$ initial value problems over preselected segments of the total interval, and (b) the use of Gaussian elimination for the solution of the resulting system of matrix equations. The first part of this method is a generalization of that which is employed over the whole interval in [2–5]. Here, however, the initial value problems are defined over segments of the total interval, the lengths of which are within the range of the applicability of the direct integration approach. After the initial value problems are integrated over these segments, continuity conditions on all variables are written at the endpoints of the segments, and they constitute a simultaneous system of linear matrix equations. This system of matrix equations is then solved directly by means of Gaussian elimination. The result is that the direct integration method is employed and at the same time there is no loss of accuracy because the lengths of the segments are selected in such a way that the solutions of the initial value problems are kept sufficiently small. A convenient parameter is given from which the appropriate lengths of the segments can be estimated easily.

In the application of this method to the analysis of rotationally symmetric shells, the boundary-value problem is formulated in terms of first-order ordinary differential equations. For this purpose, starting with the equations of the linear classical bending theory of shells in which the thermal effects are included, first a system of equations is derived in the form of eight partial differential equations involving eight unknowns in such a manner that the system of equations contains no derivatives of the material parameters, thickness, or principal radii of curvature. The absence of the derivatives in the coefficients of the differential equations permits the calculation of the coefficients at a point without regard to the values of the shell parameters at preceding or following points. Then, assuming separability with respect to the independent variables, the desired system of eight first-order ordinary differential equations is obtained which together with the boundary conditions on two edges of the shell constitute a two-point boundary-value problem. The derived system of equations is applicable to rotationally symmetric shells with arbitrary meridional variations (including discontinuities) in Young's modulus, Poisson's ratio, radii of curvature, thickness, and coefficient of thermal expansion. While such a system of equations is derived in this paper only for one version of the classical theory of shells, it can be derived in the same way for all other consistent linear bending theories of shells, including those which account for the dynamic effects, transverse shear deformation, nonhomogeneity, and anisotropy.

Finally, with the use of the method and the equations given in this paper, stresses and displacements are calculated in a thin-walled torus subjected to internal pressure. The solution shows that the meridional membrane stress is almost identical to that predicted by membrane theory, but that the bending stresses even for a relatively thin torus may not be negligible.

Geometry and Basic Equations

The position of a point of a shell of revolution is given by the coordinates θ, ϕ, ζ measured along the triplet of unit vectors $\mathbf{t}_\theta$, $\mathbf{t}_\phi$, $\mathbf{n}$, respectively, as shown in Fig. 1. The shape of the shell is determined by specifying the two principal radii of curvature R_ϕ, R_θ of the middle surface as functions of ϕ. Instead of R_θ, it is convenient to use the distance r from a point on the middle surface to the z-axis; from Fig. 1 it follows that

$$r = R_\theta \sin \phi \tag{1}$$

If the generating curve of the middle surface is given by $r = r(z)$, then

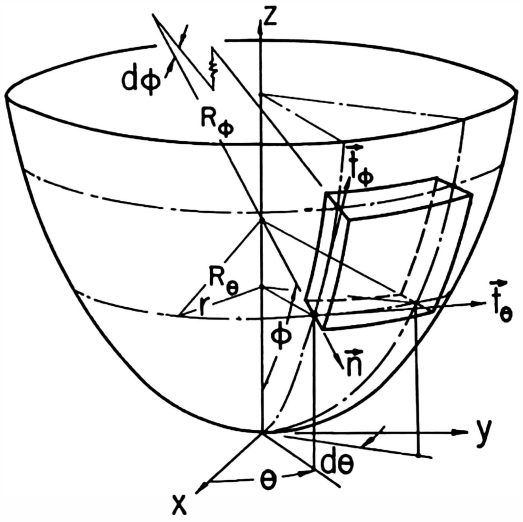

Fig. 1 Element of a shell of revolution

$$R_\phi = -\left[1 + \left(\frac{dr}{dz}\right)^2\right]^{3/2} \Big/ \frac{d^2r}{dz^2}$$
$$R_\theta = r\left[1 + \left(\frac{dr}{dz}\right)^2\right]^{1/2} \tag{2}$$

The following analysis requires frequent differentiation of r (or R_θ) with respect to ϕ, and it is convenient to express this derivative by the Codazzi relation

$$\frac{dr}{d\phi} = R_\phi \cos\phi \tag{3}$$

The displacement components of the middle surface of the shell and the rotations of the normal are defined by the expression of the displacement vector $\mathbf{U}$ of the form

$$\mathbf{U} = (u_\phi + \zeta\beta_\phi)\mathbf{t}_\phi + (u_\theta + \zeta\beta_\theta)\mathbf{t}_\theta + w\mathbf{n} \tag{4a}$$

The shell is subjected to the mechanical load vector $\mathbf{p}$, which is measured as force per unit area of the middle surface and written as

$$\mathbf{p} = p_\phi\mathbf{t}_\phi + p_\theta\mathbf{t}_\theta + p\mathbf{n} \tag{4b}$$

and the moment vector $\mathbf{m}$, which is measured as moment per unit area and given by

$$\mathbf{m} = -m_\theta\mathbf{t}_\phi + m_\phi\mathbf{t}_\theta \tag{4c}$$

With reference to Fig. 1, equations (4) serve the purpose for establishing the positive directions of the components of the displacement and mechanical load vectors.

The temperature distribution in the shell caused by some thermal loads is accounted for in the usual manner by means of the integrated temperature effect of the form

$$T_0(\phi, \theta) = \frac{1}{h}\int_{-\frac{h}{2}}^{\frac{h}{2}} T(\phi, \theta, \zeta)d\zeta \tag{5a}$$

$$T_1(\phi, \theta) = \frac{12}{h^3}\int_{-\frac{h}{2}}^{\frac{h}{2}} \zeta T(\phi, \theta, \zeta)d\zeta \tag{5b}$$

The derivation of a new set of equations carried out in the next section is based on a linear classical theory of shells given by Reissner [13]. When referred to arbitrary shells of revolution, the governing system of equations of [13] can be written in the following form. Equations of equilibrium:

$$N_{\theta,\theta} + \frac{r}{R_\phi}N_{\phi\theta,\phi} + 2\cos\phi\, N_{\theta\phi} + Q_\theta \sin\phi + rp_\theta = 0 \tag{6a}$$

$$N_{\theta\phi,\theta} + \frac{r}{R_\phi}N_{\phi,\phi} + (N_\phi - N_\theta)\cos\phi + \frac{r}{R_\phi}Q_\phi + rp_\phi = 0 \tag{6b}$$

$$Q_{\theta,\theta} + \frac{r}{R_\phi}Q_{\phi,\phi} + Q_\phi\cos\phi - N_\theta\sin\phi - \frac{r}{R_\phi}N_\phi + rp = 0 \tag{7}$$

$$M_{\theta,\theta} + \frac{r}{R_\phi}M_{\phi\theta,\phi} + 2\cos\phi\, M_{\theta\phi} - rQ_\theta + rm_\theta = 0 \tag{8a}$$

$$M_{\theta\phi,\theta} + \frac{r}{R_\phi}M_{\phi,\phi} + (M_\phi - M_\theta)\cos\phi - rQ_\phi + rm_\phi = 0 \tag{8b}$$

Stress-strain relations:

$$N_\theta = K(\epsilon_\theta + \nu\epsilon_\phi) - (1+\nu)\alpha KT_0 \tag{9a}$$

$$N_\phi = K(\epsilon_\phi + \gamma\epsilon_\theta) - (1+\nu)\alpha KT_0 \tag{9b}$$

$$N_{\theta\phi} = N_{\phi\theta} = (1-\nu)K\epsilon_{\theta\phi} \tag{9c}$$

$$M_\theta = D(\kappa_\theta + \nu\kappa_\phi) - (1+\nu)\alpha DT_1 \tag{10a}$$

$$M_\phi = D(\kappa_\phi + \nu\kappa_\theta) - (1+\nu)\alpha DT_1 \tag{10b}$$

$$M_{\theta\phi} = M_{\phi\theta} = (1-\nu)D\kappa_{\theta\phi} \tag{10c}$$

Strain-displacement relations:

$$\epsilon_\theta = \frac{1}{r}(u_{\theta,\theta} + u_\phi\cos\phi + w\sin\phi) \tag{11a}$$

$$\epsilon_\phi = \frac{1}{R_\phi}(u_{\phi,\phi} + w) \tag{11b}$$

$$2\epsilon_{\theta\phi} = \frac{1}{r}(u_{\phi,\theta} - u_\theta\cos\phi) + \frac{1}{R_\phi}u_{\theta,\phi} \tag{11c}$$

$$\kappa_\theta = \frac{1}{r}(\beta_{\theta,\theta} + \beta_\phi\cos\phi) \tag{12a}$$

$$\kappa_\phi = \frac{1}{R_\phi}\beta_{\phi,\phi} \tag{12b}$$

$$2\kappa_{\theta\phi} = \frac{1}{r}(\beta_{\phi,\theta} - \beta_\theta\cos\phi) + \frac{1}{R_\phi}\beta_{\theta,\phi} \tag{12c}$$

$$\beta_\theta = -\frac{1}{r}w_{,\theta} + \frac{\sin\phi}{r}u_\theta \tag{13a}$$

$$\beta_\phi = -\frac{1}{R_\phi}w_{,\phi} + \frac{1}{R_\phi}u_\phi \tag{13b}$$

The positive directions of the stress resultants in the foregoing equations are the same as the corresponding stresses on the edge of the shell. The definitions of the stress resultants are found in [13].

The order of the system of equations (6)–(13) is eight with respect to ϕ, and consequently it is possible to reduce (6)–(13) to eight first-order differential equations which involve eight unknowns. If the eight unknowns are those quantities which enter into the natural boundary conditions at the edge ϕ = const, then the boundary-value problem of a rotationally symmetric shell can be completely stated in terms of these unknowns. For this reason, the eight differential equations, derived in the following sections, and the eight unknowns are called the fundamental set of equations and the fundamental variables, respectively.

Derivation of Fundamental Set of Equations

According to the classical theory of shells, the quantities which appear in the natural boundary conditions on a rotationally symmetric edge of a shell of revolution include the effective shear resultants N and Q defined by

$$N = N_{\theta\phi} + \frac{\sin\phi}{r}M_{\theta\phi} \tag{14a}$$

$$Q = Q_\phi + \frac{1}{r}M_{\theta\phi,\theta} \tag{14b}$$

Thus, the fundamental variables, which are consistent with the theory of [13], are the four generalized displacements w, u_ϕ, u_θ, β_ϕ, and the four generalized forces Q, N_ϕ, N, and M_ϕ.

In the derivation of the fundamental equations, it is more convenient to employ the distance s, measured along the meridian of the shell, rather than the angular coordinate ϕ. However, after the equations are derived, the problem can again be easily formulated in terms of ϕ by means of the relation

$$\frac{1}{R_\phi}\frac{\partial}{\partial\phi} = \frac{\partial}{\partial s}$$

As a preliminary step, it is necessary to express N_θ, M_θ, $M_{\theta\phi}$ in terms of the fundamental variables. From (9a) it follows that

$$N_\theta = \nu N_\phi + K\frac{1-\nu^2}{r}(w\sin\phi + u_{\theta,\theta} + u_\phi\cos\phi) - \alpha K(1-\nu^2)T_0 \quad (15)$$

and from (10a) that

$$M_\theta = \nu M_\phi + D\frac{1-\nu^2}{r}\left(-\frac{1}{r}w_{,\theta\theta} + \frac{\sin\phi}{r}u_{\theta,\theta} + \beta_\phi\cos\phi\right) - \alpha D(1-\nu^2)T_1 \quad (16)$$

Elimination of $u_{\theta,s}$ and $w_{,\theta s}$ from equation (12c) leads to an expression for $M_{\theta\phi}$ in the form

$$M_{\theta\phi} = LD\frac{1-\nu}{2r}\left[2\beta_{\phi,\theta} + \frac{2\cos\phi}{r}w_{,\theta} + Hu_\theta\cos\phi - Ju_{\phi,\theta}\right] + \frac{LD}{K}\frac{\sin\phi}{r}N \quad (17)$$

where

$$L = \frac{1}{1 + \dfrac{\sin^2\phi}{r^2}\dfrac{D}{K}}$$

In the derivation of the four equations of the fundamental set which involve the derivatives of the stress resultants with respect to s, the use of (14) is essential. Elimination of Q_θ from (6a) and (8a) by means of (14a) leads to

$$N_{,s} = H\frac{\cos\phi}{r}M_{\theta\phi} - \frac{2\cos\phi}{r}N - \frac{1}{r}N_{\theta,\theta} - \frac{\sin\phi}{r^2}M_{\theta,\theta} - p_\theta - \frac{\sin\phi}{r}m_\theta \quad (18)$$

Similarly, elimination of Q_θ from (7) and (8a) gives

$$Q_{,s} = -\frac{2\cos\phi}{r^2}M_{\theta\phi,\theta} - \frac{\cos\phi}{r}Q + \frac{\sin\phi}{r}N_\theta + \frac{1}{R_\phi}N_\phi - \frac{1}{r^2}M_{\theta,\theta\theta} - p - \frac{1}{r}m_{\theta,\theta} \quad (19)$$

Solving (6b) from $N_{\phi,s}$ there results

$$N_{\phi,s} = -\frac{1}{r}N_{,\theta} + \frac{1}{r}JM_{\theta\phi,\theta} + \frac{\cos\phi}{r}(N_\theta - N_\phi) - \frac{1}{R_\phi}Q - p_\phi \quad (20)$$

and it follows from (8b) that

$$M_{\phi,s} = -\frac{2}{r}M_{\theta\phi,\theta} + \frac{\cos\phi}{r}(M_\theta - M_\phi) + Q - m_\phi \quad (21)$$

Wherever necessary, $N_{\theta\phi}$ and Q_ϕ were eliminated with the use of (14).

The fundamental set of equations consists of (18)–(21), where N_θ, M_θ, $M_{\theta\phi}$ can be replaced directly in terms of the fundamental variables by means of (15)–(17), and four additional equations involving the derivatives of w, u_ϕ, u_θ, β_ϕ with respect to s, which are obtained from (13b), (11c), (11b), (12b), respectively. Finally, the system of eight differential equations that governs the deformation of a shell of revolution can be expressed in terms of the eight fundamental variables and written as

$$w_{,s} = \frac{1}{R_\phi}u_\phi - \beta_\phi \quad (22a)$$

$$u_{\phi,s} = -Uw - \frac{\nu\cos\phi}{r}u_\phi - \frac{\nu}{r}u_{\theta,\theta} + \frac{1}{K}N_\phi + \alpha(1+\nu)T_0 \quad (22b)$$

$$u_{\theta,s} = -\frac{LD\sin 2\phi}{Kr^3}w_{,\theta} - \frac{1}{r}\left(1 - \frac{LDJ\sin\phi}{Kr}\right)u_{\phi,\theta} + \frac{\cos\phi}{r}\left(1 - \frac{LDH\sin\phi}{Kr}\right)u_\theta - \frac{2LD\sin\phi}{Kr^2}\beta_{\phi,\theta} + \frac{2}{(1-\nu)K}\left(1 - \frac{LD\sin^2\phi}{Kr^2}\right)N \quad (22c)$$

$$\beta_{\phi,s} = \frac{\nu}{r^2}w_{,\theta\theta} - \frac{\nu\sin\phi}{r^2}u_{\theta,\theta} - \frac{\nu\cos\phi}{r}\beta_\phi + \frac{1}{D}M_\phi + \alpha(1+\nu)T_1 \quad (22d)$$

$$Q_{,s} = \frac{1-\nu}{r^4}\left[D(1+\nu)\frac{\partial^4}{\partial\theta^4} - 2LD\cos^2\phi\frac{\partial^2}{\partial\theta^2} + (1+\nu)Kr^2\sin^2\phi\right]w + (1-\nu)\frac{\cos\phi}{r^2}\left[\frac{1}{r}LDJ\frac{\partial^2}{\partial\theta^2} + (1+\nu)K\sin\phi\right]u_\phi - \frac{1-\nu}{r^2}\left[\frac{1}{r}LDH\cos^2\phi - (1+\nu)K\sin\phi + D(1+\nu)\frac{\sin\phi}{r^2}\frac{\partial^2}{\partial\theta^2}\right]u_{\theta,\theta} - D(1-\nu)\frac{\cos\phi}{r^3}(1+\nu+2L)\beta_{\phi,\theta\theta} + UN_\phi - \frac{\nu}{r^2}M_{\phi,\theta\theta} - \frac{LD\sin 2\phi}{Kr^3}N_{,\theta} - \frac{\cos\phi}{r}Q - p - \frac{1}{r}m_{\theta,\theta} - \alpha(1-\nu^2)\frac{1}{r}\left(K\sin\phi\,T_0 - \frac{1}{r}DT_{1,\theta\theta}\right) \quad (22e)$$

$$N_{\phi,s} = (1-\nu)\frac{\cos\phi}{r^2}\left[\frac{1}{r}LDJ\frac{\partial^2}{\partial\theta^2} + (1+\nu)K\sin\phi\right]w + \frac{1-\nu}{r^2}\left[(1+\nu)K\cos^2\phi - \tfrac{1}{2}LDJ^2\frac{\partial^2}{\partial\theta^2}\right]u_\phi + (1-\nu)\frac{\cos\phi}{r^2}\left[\tfrac{1}{2}LDJH + (1+\nu)K\right]u_{\theta,\theta} + JLD\frac{1-\nu}{r^2}\beta_{\phi,\theta\theta} - \frac{1}{R_\phi}Q - (1-\nu)\frac{\cos\phi}{r}N_\phi - \frac{1}{r}\left(1 - \frac{LDJ\sin\phi}{Kr}\right)N_{,\theta} - p_\phi - \alpha(1-\nu^2)K\frac{\cos\phi}{r}T_0 \quad (22f)$$

$$N_{,s} = \frac{1-\nu}{r^2}\left[HLD\frac{\cos^2\phi}{r} - (1+\nu)K\sin\phi + (1+\nu)D\frac{\sin\phi}{r^2}\frac{\partial^2}{\partial\theta^2}\right]w_{,\theta} - (1-\nu)\frac{\cos\phi}{r^2}\left[\tfrac{1}{2}LDJH + (1+\nu)K\right]u_{\phi,\theta} + \frac{1-\nu}{r^2}\left[\tfrac{1}{2}LDH^2\cos^2\phi - (1+\nu)\left(K + \frac{D\sin^2\phi}{r^2}\right)\frac{\partial^2}{\partial\theta^2}\right]u_\theta - D(1-\nu)\frac{\cos\phi}{r^2}\left[(1+\nu)\frac{\sin\phi}{r} - LH\right]\beta_{\phi,\theta} - \frac{\nu}{r}N_{\phi,\theta}$$

$$-\frac{\cos\phi}{r}\left(2-\frac{LDH\sin\phi}{Kr}\right)N-\frac{\nu\sin\phi}{r^2}M_{\phi,\theta}-p_\theta-\frac{\sin\phi}{r}m_\theta$$
$$+\alpha(1-\nu^2)\frac{1}{r}\left(KT_{0,\theta}+D\frac{\sin\phi}{r}T_{1,\theta}\right) \quad (22g)$$

$$M_{\phi,s}=-(1-\nu)D\frac{\cos\phi}{r^3}(1+\nu+2L)w_{,\theta\theta}+LDJ\frac{1-\nu}{r^2}u_{\phi,\theta\theta}$$
$$+D(1-\nu)\frac{\cos\phi}{r^2}\left[(1+\nu)\frac{\sin\phi}{r}-HL\right]u_{\theta,\theta}$$
$$+D\frac{1-\nu}{r^2}\left[(1+\nu)\cos^2\phi-2L\frac{\partial^2}{\partial\theta^2}\right]\beta_\phi+Q-\frac{2LD\sin\phi}{Kr^2}N_{,\theta}$$
$$-(1-\nu)\frac{\cos\phi}{r}M_\phi-m_\phi-\alpha(1-\nu^2)D\frac{\cos\phi}{r}T_1 \quad (22h)$$

Equations (22), (14), and (15) to (17) determine all unknown variables except Q_θ which can be found from (8a) and written in the form

$$Q_\theta=\frac{1}{r}M_{\theta,\theta}+M_{\theta\phi,s}+\frac{2\cos\phi}{r}M_{\theta\phi}+m_\theta \quad (23)$$

By calculating $M_{\theta\phi,s}$ from (17) and making use of (16), it is possible to express Q_θ directly in terms of the fundamental variables. This expression is lengthy and contains
s of the shell parameters. Since Q_θ does not enter into any boundary conditions on the edge s = const, it is preferable to calculate Q_θ as the last unknown directly from (23). The derivative of $M_{\theta\phi}$ can be easily obtained by numerical differentiation.

The procedure for the derivation of an equivalent set of equations for other linear classical theories of isotropic shells is identical to that given before. For general anisotropic and/or nonhomogeneous shells of revolution with rotationally symmetric properties, the fundamental set of equations is derived in the same way as (22) except that (9) and (10) must be replaced by the appropriate stress-strain relations given, for example, by Ambartsumyan [14]. Otherwise, the derivation is straightforward. For the improved theory of shells, such as the one given by Naghdi [15], in which the effects of transverse-shear deformation are accounted for, the following ten fundamental variables are required: $w, u_\phi, u_\theta, \beta_\phi, \beta_\theta, Q_\phi, N_\phi, N_{\phi\theta}, M_\phi, M_{\phi\theta}$. Since now Q_ϕ and Q_θ appear in (13), the elimination of Q_θ from (6a), (7), (8a), is done by means of (13a). The required equations for the derivatives of the generalized forces are obtained directly from the five equations of equilibrium (6), (7), (8). The remaining five equations are derived by following a procedure similar to that of the foregoing.

Fundamental Equations for Separable Solutions

For shells of revolution which consist of complete latitude circles, the surface loads are periodic with respect to θ period of 2π, and they can be assumed to be of the form

$$\{p_\phi, p, m_\phi\}=\{p_{\phi n}, p_n, m_{\phi n}\}\begin{Bmatrix}\cos n\theta\\ \sin n\end{Bmatrix} \quad (24a)$$

$$\{T_0, T_1\}=\{T_{0n}, T_{1n}\}\begin{Bmatrix}\cos n\theta\\ \sin n\theta\end{Bmatrix} \quad (24b)$$

$$\{p_\theta, m_\theta\}=\{p_{\theta n}, m_{\theta n}\}\begin{Bmatrix}\sin n\theta\\ \cos n\theta\end{Bmatrix} \quad (24c)$$

where the variables with subscripts n depend only on s, and each integral value of n in (24) can be regarded as one Fourier component in a general Fourier series expansion of arbitrary periodic surface loads.

Separable solutions of (22), corresponding to the value of n in (24), are then obtained in the form

$$\{w, u_\phi, \beta_\phi\}=\{w_n, u_{\phi n}, \beta_{\phi n}\}\begin{Bmatrix}\cos n\theta\\ \sin n\theta\end{Bmatrix} \quad (25a)$$

$$\{N_\phi, M_\phi, Q\}=\{N_{\phi n}, M_{\phi n}, Q_n\}\begin{Bmatrix}\cos n\theta\\ \sin n\theta\end{Bmatrix} \quad (25b)$$

$$\{u_\theta, N\}=\{u_{\theta n}, N_n\}\begin{Bmatrix}\sin n\theta\\ \cos n\theta\end{Bmatrix} \quad (25c)$$

The s-dependent coefficients with subscripts n on the right-hand side of (25) are governed by a system of equations which is obtained from (22) and, after using the assumption that the shell is thin,[3] can be written as

$$w_{n,s}=\frac{1}{R_\phi}u_{\phi n}-\beta_{\phi n} \quad (26a)$$

$$u_{\phi n,s}=-Uw_n-\frac{\nu\cos\phi}{r}u_{\phi n}\mp\frac{\nu n}{r}u_{\theta n}+\frac{1}{K}N_{\phi n}+\alpha(1+\nu)T_{0n} \quad (26b)$$

$$u_{\theta n,s}=\pm\frac{D\sin 2\phi}{Kr^3}w_n\pm\frac{n}{r}u_{\phi n}+\frac{\cos\phi}{r}u_{\theta n}\pm\frac{2Dn\sin\phi}{Kr^2}\beta_{\phi n}+\frac{2}{(1-\nu)K}N \quad (26c)$$

$$\beta_{\phi n,s}=-\frac{\nu n^2}{r^2}w_n\mp\frac{\nu n\sin\phi}{r^2}u_{\theta n}-\frac{\nu\cos\phi}{r}\beta_{\phi n}+\frac{1}{D}M_{\phi n}+\alpha(1+\nu)T_{1n} \quad (26d)$$

$$Q_{n,s}=\frac{1-\nu}{r^4}[(1+\nu)n^4D+2n^2D\cos^2\phi+(1+\nu)Kr^2\sin^2\phi]w_n+(1-\nu)\frac{\cos\phi}{r^2}\left[(1+\nu)K\sin\phi-\frac{n^2}{r}DJ\right]u_{\phi n}$$
$$\pm\frac{(1-\nu)n}{r^2}\left[(1+\nu)D\frac{n^2}{r^2}\sin\phi+(1+\nu)K\sin\phi\right]u_{\theta n}+n^2(1-\nu)(3+\nu)D\frac{\cos\phi}{r^3}\beta_{\phi n}-\frac{\cos\phi}{r}Q_n+UN_{\phi n}$$
$$\mp\frac{nD\sin 2\phi}{Kr^3}N_n+\frac{\nu n^2}{r^2}M_{\phi n}-p_n\mp\frac{n}{r}m_{\theta n}-\alpha(1-\nu^2)\frac{1}{r}\left(K\sin\phi\,T_{0n}+D\frac{n^2}{r}T_{1n}\right) \quad (26e)$$

$$N_{\phi n,s}=(1-\nu)\frac{\cos\phi}{r^2}\left[(1+\nu)K\sin\phi-\frac{n^2}{r}JD\right]w_n+\frac{1-\nu}{r^2}\left[(1+\nu)K\cos^2\phi+\frac{n^2}{2}DJ^2\right]u_{\phi n}$$
$$\pm\frac{(1-\nu^2)nK\cos\phi}{r^2}u_{\theta n}-\frac{n^2(1-\nu)}{r^2}DJ\beta_{\phi n}-\frac{1}{R_\phi}Q_n-(1-\nu)\frac{\cos\phi}{r}N_{\phi n}\mp\frac{n}{r}N_n$$

[3] In the derivation of the system of equations (6)–(13) the assumption is made that the shell is sufficiently thin, so that $1+h^2/12R^2\approx 1$, where R denotes the minimum principal radius of curvature. This same approximation is used to obtain the following equations from (22).

$$- p_{\phi n} - \alpha(1 - \nu^2)K \frac{\cos \phi}{r} T_{0n} \quad (26f)$$

$$N_{n,s} = \pm \frac{n(1 - \nu)}{r^2} \left[(1 + \nu)D \frac{n^2}{r^2} \sin \phi + (1 + \nu)K \sin \phi \right] w_n$$
$$\pm \frac{(1 - \nu^2)nK \cos \phi}{r^2} u_{\phi n} + \frac{n^2(1 - \nu^2)K}{r^2} u_{\theta n}$$
$$\pm nD \frac{1 - \nu}{r^2} \cos \phi \left[(1 + \nu) \frac{\sin \phi}{r} - H \right] \beta_{\phi n}$$
$$\pm n \frac{\nu}{r} N_{\phi n} - \frac{2 \cos \phi}{r} N_n$$
$$\pm \frac{\nu n \sin \phi}{r^2} M_{\phi n} - p_{\theta n} - \frac{\sin \phi}{r} m_{\theta n}$$
$$\mp \alpha(1 - \nu^2) \frac{1}{r} \left(KT_{0n} + D \frac{\sin \phi}{r} T_{1n} \right) \quad (26g)$$

$$M_{\phi n,s} = n^2(1 - \nu)(3 + \nu)D \frac{\cos \phi}{r^3} w_n - n^2 \frac{1 - \nu}{r^2} JDu_{\phi n}$$
$$\pm nD \frac{1 - \nu}{r^2} \cos \phi \left[(1 + \nu) \frac{\sin \phi}{r} - H \right] u_{\theta n}$$
$$+ D \frac{1 - \nu}{r^2} [(1 + \nu) \cos^2 \phi + 2n^2] \beta_{\phi n} + Q \mp \frac{2nD \sin \phi}{Kr^2} N_n$$
$$- (1 - \nu) \frac{\cos \phi}{r} M_{\phi n} - m_{\phi n} - \alpha(1 - \nu^2)D \frac{\cos \phi}{r} T_{1n} \quad (26h)$$

The double signs in (26) correspond to the top or bottom trigonometric function employed in (24) and (25).

The quantities which are not included in the fundamental variables can be expressed by means of separation of variables by

$$\{N_\theta, M_\theta, Q_\phi\} = \{N_{\theta n}, M_{\theta n}, Q_{\phi n}\} \begin{Bmatrix} \cos n\theta \\ \sin n\theta \end{Bmatrix} \quad (27a)$$

$$\{N_{\theta\phi}, M_{\theta\phi}, Q_\theta\} = \{N_{\theta\phi n}, M_{\theta\phi n}, Q_{\theta n}\} \begin{Bmatrix} \sin n\theta \\ \cos n\theta \end{Bmatrix} \quad (27b)$$

where the s-dependent coefficients with subscripts n must satisfy a set of equations obtained from equations (14)–(17) and (23) in the form

$$N_{\theta n} = \nu N_{\phi n} + (1 - \nu^2) \frac{K}{r^2} (w_n \sin \phi + u_{\phi n} \cos \phi \pm n u_{\theta n}) - \alpha(1 - \nu^2)KT_{0n} \quad (28a)$$

$$M_{\theta n} = \nu M_{\phi n} + (1 - \nu^2) \frac{D}{r} \left(\frac{n^2}{r} w_n + \beta_{\phi n} \cos \phi \pm n \frac{\sin \phi}{r} u_{\theta n} \right) - \alpha(1 - \nu^2)DT_{1n} \quad (28b)$$

$$M_{\theta\phi n} = D \frac{1 - \nu}{2r} \left(\mp \frac{2n \cos \phi}{r} w_n \pm nJu_{\phi n} + H \cos \phi u_{\theta n} \mp 2n\beta_{\phi n} \right) + \frac{D}{K} \frac{\sin \phi}{r} N_n \quad (28c)$$

$$Q_{\theta n} = \mp \frac{n}{r} M_{\theta n} + M_{\theta\phi n,s} + \frac{2 \cos \phi}{r} M_{\theta\phi n} + m_{\theta n} \quad (28d)$$

$$N_{\theta\phi n} = N_n - \frac{\sin \phi}{r} M_{\theta\phi n} \quad (28e)$$

$$Q_{\phi n} = Q_n \mp \frac{n}{r} M_{\theta\phi n} \quad (28f)$$

The double signs again correspond to the top or bottom trigonometric function employed in (24), (25), and (27).

The remainder of this paper is concerned with the solution of the system of equations (26), subject to the boundary conditions on two edges s = const. It should be noted that after the expansion of the loads in Fourier series, the solution to (26) is obtained for each integral value of n separately, and then the solutions are superimposed to form a Fourier series expansion for the unknown variables.

Reduction to Initial Value Problems

This section is concerned with the reduction of a two-point boundary-value problem governed by

$$\frac{dy(x)}{dx} = A(x)y(x) + B(x) \quad (29a)$$

to a series of initial-value problems. In (29a), $y(x)$ is an $(m, 1)$ matrix which represents m unknown functions; x is the independent variable; $A(x)$ denotes the (m, m) coefficient matrix; and $B(x)$ is the $(m, 1)$ matrix of the nonhomogeneous terms. The elements of $A(x)$ and $B(x)$ are given piecewise continuous functions of x. The object is to determine $y(x)$ in the interval $a \leq x \leq b$ subject to m boundary conditions stated in terms of linear combinations of $y(a)$ and $y(b)$ in the form

$$F_a y(a) + F_b y(b) = G \quad (29b)$$

where F_a, F_b are (m, m) matrices and G is an $(m, 1)$ matrix, which are known from the statement of the boundary conditions of the problem. It should be clear that the governing system of equations (26) derived in the preceding section is stated in the form of (29a), and that the appropriate boundary conditions for a shell of revolution can be expressed in the form of (29b).

Let the complete solution of (29a) be written as

$$y(x) = Y(x)C + Z(x) \quad (30)$$

where the $(m, 1)$ matrix C represents m arbitrary constants, and $Y(x)$ is an (m, m) and $Z(x)$ an $(m, 1)$ matrix which are defined as the homogeneous and particular solutions of (29a) in the form

$$\frac{dY(x)}{dx} = A(x)Y(x) \quad (31a)$$

$$\frac{dZ(x)}{dx} = A(x)Z(x) + B(x) \quad (31b)$$

The initial conditions for determining $Y(x)$ and $Z(x)$ are

$$Y(a) = I \quad (32a)$$

$$Z(a) = 0 \quad (32b)$$

where I is the unit matrix.

Evaluation of (30) at $x = a$ leads at once, in view of (32a, b), to $C = y(a)$, and then (30) at $x = b$ can be written as

$$y(b) = Y(b)y(a) + Z(b) \quad (33)$$

Together with (29b), equation (33) constitutes a system of $2m$ linear algebraic equations from which the $2m$ unknowns, $y(a)$ and $y(b)$, are determined. Once $y(a)$ is known, the solution at any value of x is obtained from (30) provided that the values of $Y(x)$ and $Z(x)$ at that particular x are stored. This completes the reduction of a two-point boundary-value problem defined by (29) to $m + 1$ initial-value problems given by (31, 32).

As stated in the introduction, the solution for shells obtained by means of this procedure suffers a complete loss of accuracy at some critical length of the interval. The reason for this phenomenon can be seen clearly from (33). When the initial-value problems defined by (31, 32) are solved with the use of the equa-

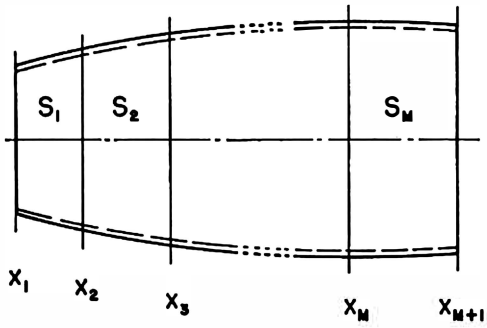

Fig. 2 Notation for division of total interval into segments

tions (26) for shells of revolution, it is observed that the elements of $Y(x)$ and $Z(x)$ increase in magnitude in such a way that if the length is increased by any factor n, then these solutions increase in magnitude approximately exponentially with n.

Consider, for example, the axisymmetric case when the deformation in the shell is caused by some prescribed edge conditions at $x = a$, say, by $M_\phi(a) = 1$ and $N_\phi(a) = Q(a) = 0$. It is reasonable to expect that the corresponding solutions at $x = b$ become smaller and smaller when the interval (a, b) is increased in length. The connection between $y(b)$ and $y(a)$ is given by the matrix equation (33) with the following magnitudes of the elements: $y(b)$-small, $Y(b)$-large, $y(a)$-unity. Clearly, the only way that the matrix product of (33) can give small values of $y(b)$ is that a number of significant digits of the large values of $Y(b)$ subtract out. When the length of the interval is increased, $Y(b)$ increase, while $y(b)$ decrease, and invariably all accuracy is lost at some critical length because all significant digits of $Y(b)$ in (33) are lost. This simple example serves as an illustration for the loss of accuracy encountered in the analysis of shells if the foregoing reduction technique is employed.

A convenient length factor, defined by

$$\beta = l[3(1 - \nu^2)]^{1/4}/(Rh)^{1/2} \tag{34}$$

where l is the length of the meridian of the shell and R is a minimum radius of curvature, can be used for an approximate estimate of the critical length of the shell. If the solutions $Y(x)$ and $Z(x)$ are obtained with a six-digit accuracy, then the foregoing procedure gives good results in the range $\beta \leq 3 - 5$.

However, the loss of accuracy of the solution can be avoided and shells of revolution with much larger values of β can be analyzed by means of the direct integration technique if the multisegment method given in the next section is employed.

Multisegment Method of Integration

Let the shell be divided into M-segments (denoted by S_i, where $i = 1, 2, \ldots, M$) of arbitrary length in each of which $\beta \leq 3$. Denote the coordinates of the ends of the segments by $x = x_i$, where the left-hand edge of the shell is at $x = x_1$ and the right-hand edge is at $x = x_{M+1}$, as shown in Fig. 2. In analogy to (30), the solution in the total interval $x_1 \leq x \leq x_{M+1}$ now can be written as

$$y(x) = Y_i(x)y(x_i) + Z_i(x) \tag{35}$$

where $Y_i(x)$ and $Z_i(x)$ denote the matrices corresponding to $Y(x)$ and $Z(x)$ in each segment $S_i(x_i \leq x \leq x_{i+1})$ and are given by

$$\frac{dY_i(x)}{dx} = A(x)Y_i(x) \tag{36a}$$

$$Y_i(x_i) = I \tag{36b}$$

$$\frac{dZ_i(x)}{dx} = A(x)Z_i(x) + B(x) \tag{36c}$$

$$Z_i(x_i) = 0 \tag{36d}$$

Requiring continuity of all elements of $y(x)$ at the points x_i, $i = 2, 3, \ldots, M + 1$, the following M-matrix equations are obtained from (35):

$$y(x_{i+1}) = Y_i(x_{i+1})y(x_i) + Z_i(x_{i+1}) \tag{37}$$

where $i = 1, 2, \ldots, M$. Equations (37) involve $M + 1$ unknown $(m, 1)$ matrices: $y(x_i)$, $i = 1, 2, \ldots, M + 1$. However, if the quantities prescribed at the edges of the shell are the fundamental variables, then the total number of unknowns is reduced by m, because $m/2$ elements of $y(x_1)$ and $m/2$ elements of $y(x_{M+1})$ are known. The same is true if the boundary conditions are stated in terms of linear combinations of the fundamental variables in the form of (29b). In this case, $y(x_1)$ and $y(x_{M+1})$ should be premultiplied by nonsingular (m, m) transformation matrices F_1 and F_{M+1}, respectively, so that the elements of the products contain the quantities prescribed at each edge. After eliminating $y(x_1)$ and $y(x_{M+1})$ from (37) by means of these products, it is concluded that (37) will retain its form if, after integration and before substitution into (37), $Y_1(x_2)$ is postmultiplied by F_1^{-1}, while $Y_M(x_{M+1})$ and $Z_M(x_{M+1})$ are premultiplied by F_{M+1}. In the following, it will be regarded that this transformation is carried out and that $y(x_1)$ and $y(x_{M+1})$ contain among their elements those quantities which are prescribed at $x = x_1$ and $x = x_{M+1}$, respectively.

Thus for all boundary conditions in the form of (29b), the system of M matrix equations (37) involves exactly M times m unknowns, and formally it can be solved by any method which is applicable to a large number of equations. However, the success of the procedure given in this paper lies in the application of Gaussian elimination directly on the matrix equations (37).

First a rearrangement of elements is performed. Since those $m/2$ elements of $y(x_1)$ and $y(x_{M+1})$ which are known through the boundary conditions can be any $m/2$ of the m-elements, it is necessary to rearrange the rows of $y(x_1)$ and $y(x_{M+1})$ so that the known elements are separated from the unknown elements. It is assumed here that the first $m/2$ elements of $y(x_1)$, denoted by $y_1(x_1)$, are known and that the last $m/2$ elements, denoted by $y_2(x_1)$, are unknown. On the other hand, $y_1(x_{M+1})$ are the unknown and $y_2(x_{M+1})$ are the known elements of $y(x_{M+1})$. Since the order of the variables in the column matrix $y(x)$ is arbitrary, it should be emphasized that this separation of elements does not involve any restriction on the boundary conditions, and that any natural boundary condition in the form of (29b) can be prescribed at each edge. The separation is achieved by a simple rearrangement of the columns of $Y_1(x_2)$ and the rows of $Y_M(x_{M+1})$ and $Z_M(x_{M+1})$ after integrating the initial-value problems defined by (36) to the ends of the segments S_1 and S_M and multiplying by F_1^{-1} and F_{M+1} as stated in the foregoing.

Once it is established which parts of $y(x_1)$ and $y(x_{M+1})$ are known, the continuity conditions (37) are rewritten as a partitioned matrix product of the form

$$\begin{bmatrix} y_1(x_{i+1}) \\ \hline y_2(x_{i+1}) \end{bmatrix} = \begin{bmatrix} Y_i^1(x_{i+1}) & Y_i^2(x_{i+1}) \\ \hline Y_i^3(x_{i+1}) & Y_i^4(x_{i+1}) \end{bmatrix} \begin{bmatrix} y_1(x_i) \\ \hline y_2(x_i) \end{bmatrix} + \begin{bmatrix} Z_i^1(x_{i+1}) \\ \hline Z_i^2(x_{i+1}) \end{bmatrix} \tag{38}$$

so that each of the equations (37) turns into a pair of equations, given by

$$\begin{aligned} Y_i^1(x_{i+1})y_1(x_i) + Y_i^2(x_{i+1})y_2(x_i) - y_1(x_{i+1}) &= -Z_i^1(x_{i+1}) \\ Y_i^3(x_{i+1})y_1(x_i) + Y_i^4(x_{i+1})y_2(x_i) - y_2(x_{i+1}) &= -Z_i^2(x_{i+1}) \end{aligned} \tag{39}$$

The result is a simultaneous system of $2M$ linear matrix equations, in which the known coefficients $Y_i^j(x_{i+1})$ and $Z_i^j(x_{i+1})$ are $(m/2, m/2)$ and $(m/2, 1)$ matrices, respectively, and the unknowns $y_j(x_i)$ are $(m/2, 1)$ matrices. Since $y_1(x_1)$ and $y_2(x_{M+1})$ are known, there are exactly $2M$ unknowns: $y_1(x_i)$, with $i = 2, 3, \ldots, M + 1$, and $y_2(x_i)$, with $i = 1, 2, \ldots, M$.

By means of Gaussian elimination, the system of equations (39) is first brought to the form

$$\left[\begin{array}{cccc:cc} E_1 & -I & 0 & 0 & 0 & 0 \\ 0 & C_1 & -I & 0 & 0 & 0 \\ 0 & 0 & E_2 & -I & 0 & 0 \\ 0 & 0 & 0 & C_2 & -I & 0 \\ \hdashline 0 & 0 & 0 & 0 & E_M & -I \\ 0 & 0 & 0 & 0 & 0 & C_M \end{array}\right] \left[\begin{array}{c} y_2(x_1) \\ y_1(x_2) \\ y_2(x_2) \\ y_1(x_M) \\ \hdashline y_2(x_M) \\ y_1(x_{M+1}) \end{array}\right] = \left[\begin{array}{c} A_1 \\ B_1 \\ A_2 \\ B_2 \\ \hdashline A_M \\ B_M \end{array}\right] \tag{40}$$

where the dots indicate the triangularized equations (39) with $i = 3, 4, \ldots, M-1$. The $(m/2, m/2)$ matrices E_1, C_1 are defined by

$$E_1 = Y_1^2 \tag{41a}$$

$$C_1 = Y_1^4 E_1^{-1} \tag{41b}$$

and for $i = 2, 3, \ldots, M$

$$E_i = Y_i^2 + Y_i^1 C_{i-1}^{-1} \tag{41c}$$

$$C_i = (Y_i^4 + Y_i^3 C_{i-1}^{-1}) E_i^{-1} \tag{41d}$$

The $(m/2, 1)$ matrices A_i, B_i are given by

$$A_1 = -Z_1^1 - Y_1^1 y_1(x_1) \tag{42a}$$

$$B_1 = -Z_1^2 - Y_1^3 y_1(x_1) - Y_1^4 E_1^{-1} A_1 \tag{42b}$$

and for $i = 2, 3, \ldots, M-1$

$$A_i = -Z_i^1 - Y_i^1 C_{i-1}^{-1} B_{i-1} \tag{42c}$$

$$B_i = -Z_i^2 - Y_i^3 C_{i-1}^{-1} B_{i-1} - (Y_i^4 + Y_i^3 C_{i-1}^{-1}) E_i^{-1} A_i \tag{42d}$$

Finally, for the Mth segment

$$A_M = -Z_M^1 - Y_M^1 C_{M-1}^{-1} B_{M-1} \tag{42e}$$

$$B_M = y_2(x_{M+1}) - Z_M^2 - Y_M^3 C_{M-1}^{-1} B_{M-1} - (Y_M^4 + Y_M^3 C_{M-1}^{-1}) E_M^{-1} A_M \tag{42f}$$

For brevity, in place of $Y_i^j(x_{i+1})$ and $Z_i^j(x_{i+1})$, the symbols Y_i^j and Z_i^j have been used.

By means of (41) and (42), the unknowns of (39) are obtained by

$$y_1(x_{M+1}) = C_M^{-1} B_M \tag{43a}$$

$$y_2(x_M) = E_M^{-1}[y_1(x_{M+1}) + A_M] \tag{43b}$$

and for $i = 1, 2, \ldots, M-1$

$$y_1(x_{M-i+1}) = C_{M-1}^{-1}[y_2(x_{M-i+1}) + B_{M-i}] \tag{43c}$$

$$y_2(x_{M-i}) = E_{M-i}^{-1}[y_1(x_{M-i+1}) + A_{M-i}] \tag{43d}$$

It should be noted that (41)-(43) must be evaluated in succession, because each equation involves the result obtained by the preceding equation.

Once all the unknowns $y(x_i)$ are found, the fundamental variables are determined from (35) at any value of x at which the solutions $Y_i(x)$ and $Z_i(x)$ are stored during the integration of the initial-value problems of (36). The integration of (36) can be accomplished by means of any of the standard direct integration methods.

On the basis of the system of equations (26) given in an earlier section and the method of solution developed in the last two sections, the author has prepared a computer program[4] which has been applied to many shell configurations having large values of β and successfully tested against known results. One example of a pressurized torus with $\beta = 57$ is presented in the next section.

The program admits arbitrary meridional variations, including discontinuities, in all shell parameters. It also admits ring loads in the form of prescribed values of N_ϕ, M_ϕ, N, or Q at any value of ϕ on the shell. Such loads introduce discontinuities in the solution for the corresponding stress resultants, and they can be represented at every x_i by an $(m, 1)$ discontinuity matrix which is simply added to the matrix $Z_i(x_{i+1})$ on the right-hand side of (37). This feature is of great value if shell joints are considered. Any discontinuity, either in geometry or in loads, is easily handled by requiring that the end point of a segment coincides with the location of the discontinuity. Since integration is restarted at the beginning of each segment, the precise effect of the discontinuity is obtained. The program outputs all fundamental variables at a number of desired points within each segment, and it also computes the values of $y(x_i)$ twice; once from (43) and then from (35). If a certain number of significant figures of these values match, then the continuity conditions are known to be satisfied to the same number of figures. In this way, a convenient error estimate of the solution is obtained for every case.

[4] The program was written and all calculations were carried out by the author on the IBM 709 computer at the Yale Computer Center. The direct integration of (36) is performed by means of the Adams predictor-corrector method, which selects an optimum step size at every step according to a prescribed accuracy.

Example: Pressurized Torus

In this section the stresses and displacements are determined in a complete torus subjected to a constant internal pressure. It is well known that the solution of this problem, when obtained by means of the linear membrane theory of shells, has a discontinuity in the displacement field. It has been shown by Jordan [16] and by Sanders and Liepins [17] that a satisfactory solution with regard to the displacement field for a sufficiently thin shell can be obtained if the nonlinear membrane theory of shells is employed. Subsequently, Reissner [18] established bounds on certain parameters which show when the nonlinear membrane and when the linear bending theory is applicable. It seems worthwhile to give here the solution for a pressurized torus as predicted by the linear bending theory.

The geometry of the torus is shown in Fig. 3. With regard to the quantities employed in equations (26), the two necessary parameters for a torus are given as

$$R_\phi = b \tag{44a}$$

$$r = a + b \sin \phi \tag{44b}$$

Because of symmetry with respect to the plane XX, Fig. 3, the

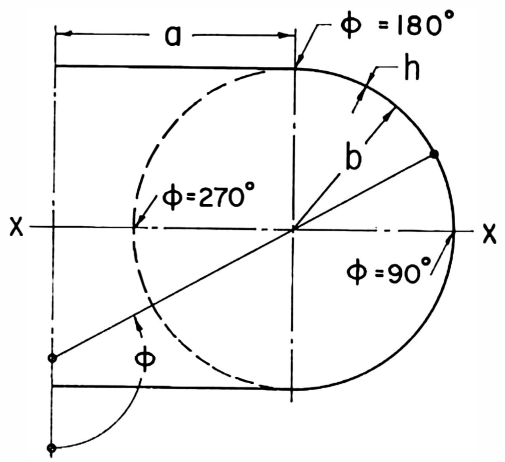

Fig. 3 Geometry of torus considered in example

Table 1 Stresses and displacements of a pressurized torus; $pb/Eh = 0.002$, $a/b = 1.5$, $\nu = 0.3$

h/b / ϕ	$\sigma_{\phi m}/E \times 10^3$	$(\sigma_{\phi b}/E) \times 10^4$			$(w/b) \times 10^3$		
	0.005	0.05	0.02	0.005	0.05	0.02	0.005
90	1.601	−0.063	−0.031	−0.016	1.249	1.284	1.298
108	1.613	−0.188	−0.093	−0.019	1.261	1.315	1.328
126	1.650	−0.886	−0.123	−0.030	1.359	1.393	1.427
144	1.720	−1.915	−0.908	−0.020	1.786	1.597	1.625
162	1.832	−0.895	−1.378	−0.910	2.820	2.580	2.159
171	1.906	1.002	0.168	−0.605	3.467	3.493	3.297
180	1.990	3.089	2.277	1.482	3.994	4.334	4.815
184.5	2.042	3.890	3.035	1.968	4.150	4.576	5.248
189	2.104	4.270	3.119	1.520	4.208	4.637	5.151
193.5	2.175	4.178	2.580	0.530	4.156	4.509	4.693
198	2.254	3.610	1.589	−0.274	3.998	4.221	4.162
216	2.642	−0.587	−0.957	−0.079	2.652	2.527	2.481
234	3.168	−1.245	−0.291	−0.066	1.273	1.269	1.269
252	3.730	−0.717	−0.344	−0.077	0.416	0.417	0.414
270	3 997	−0.824	−0.331	−0.081	0.103	0.101	0.100

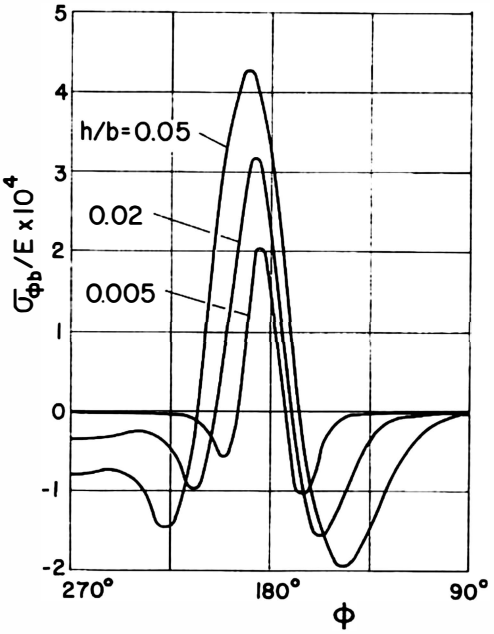

Fig. 4 Meridional bending stress $\sigma_{\phi b}$ at outer fiber versus meridional coordinate ϕ

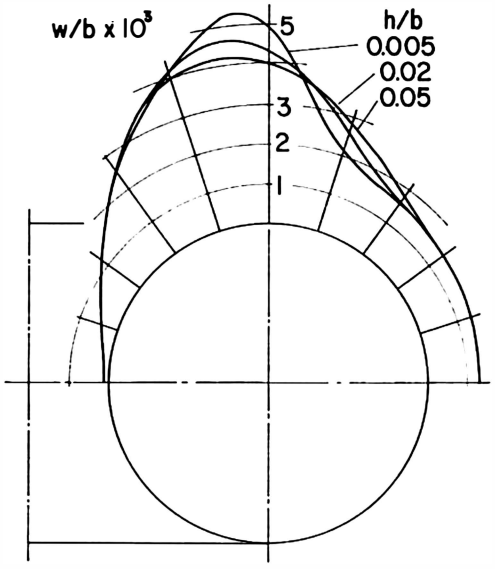

Fig. 5 Normal displacement w versus ϕ showing deformed section

integration of the initial-value problems is carried out from $\phi = 90°$ to $\phi = 270°$, and the boundary conditions at these endpoints are $u_\phi = \beta_\phi = Q = 0$. For the purpose of comparison with the results of [16] and [17], the load parameter is chosen as $pb/Eh = 0.002$ and $a/b = 1.5$.

The numerical values of the normal displacement, meridional membrane stress $\sigma_{\phi m} = N_\phi/h$, and meridional bending stress $\sigma_{\phi b} = 6M_\phi/h^2$ at $\zeta = h/2$ for a pressurized torus are shown in Table 1 and in Figs. 4 and 5. These results were taken from the output of the computer program prepared for an arbitrary shell of revolution after prescribing the geometric parameters as given by (44). The meridional membrane stress distribution agrees very well with that obtained in [17] by means of the membrane theory of shells and it shows only a small variation with h/b. The deformed shapes of the cross section of the torus shown in Fig. 5 for three values of h/b are in qualitative agreement with those given in [16] and [17], but their quantitative agreement cannot be expected because the values of h/b used in this example are outside the range where the bending effects are negligible. This is confirmed by the examination of the bending stresses shown in Fig. 4. The maximum value of $\sigma_{\phi b}$ occurs at $\phi = 189°$ for $h/b = 0.05$ and at $\phi = 184.5°$ for $h/b = 0.005$, which are also the points of maximum normal displacement and curvature as seen in Fig. 5. The comparison of the membrane and the maximum bending stress at various values of h/b is shown in Table 2.

Table 2 Maximum meridional bending stress and meridional membrane stress at $\phi = \phi_0$

h/b	0.05	0.02	0.005
ϕ_0	189°	189°	184.5°
$(\sigma_{\phi m}/E) \times 10^3$	2.053	2.082	2.042
$(\sigma_{\phi b}/E) \times 10^3$	0.427	0.312	0.197
$100\ (\sigma_{\phi b}/\sigma_{\phi m})$	20.8	15.0	9.6

It is of significance to note that even for the thickness ratio $h/b = 0.005$, which for many applications would be regarded as small, the maximum bending stress is about 10 percent of the membrane stress at the same point. Such effects of bending in a torus were previously noted by Clark [19], and they are also in agreement with the statement made by Goldenveizer [20] that when the middle surface touches a closed-plane curve, which in a torus corresponds to $\phi = 180°$, then in the vicinity of this curve bending stresses should be expected and the membrane theory is not applicable.

The boundary layer shown in Fig. 4 is also in agreement with the conclusions reached in [18] to the effect that when μ and ρ given by

$$\mu = [12(1 - \nu^2)]^{1/2}(b/a)(b/h)$$

$$\rho = 12(1 - \nu^2)(p/E)(b/h)^3$$

are large compared to unity, then a boundary layer in the neighborhood of $\phi = 180°$ should be anticipated. For the present example, μ ranges from 44 to 440 and ρ from 9 to 874. However, since p is the only load parameter of the problem, the solutions shown in Figs. 4 and 5 are proportional to p, and the boundary layer remains unaffected if p alone is varied. Of course, for very large values of p the deformation of the torus may exceed the limits of a linear theory which according to [18] restrict ρ to the range $\rho \ll \mu^{2/3}$.

Acknowledgments

This research has been supported by the National Science Foundation Grant #23922. Many ideas leading to this paper originated from the consulting work performed by the author for the United Technology Center, Sunnyvale, California. The author wishes to thank the staff of the Applied Mechanics Department of UTC for many illuminating discussions concerning this subject.

References

1 P. M. Naghdi and C. N. DeSilva, "Deformation of Elastic Ellipsoidal Shells of Revolution," *Proceedings of the Second U. S. National Congress of Applied Mechanics*, 1954, pp. 333–343.

2 W. Lohmann, "Beitrag zur Integration der Reissner-Meissnerschen Schalengleichung für Behälter unter konstantem Innerdruck," *Ingenieur-Archiv*, vol. 6, 1935, pp. 338–346.

3 H. Münz, "Ein Integrationsverfahren für die Berechnung der Biegespannungen achsensymmetrischer Schalen unter achsensymmetrischer Belastung," *Ingenieur-Archiv*, vol. 19, 1951, pp. 103–117, 255–270.

4 E. Klingbeil, "Zur Theorie der Rotationsschalen vom Standpunkt numerischer Rechnungen," *Ingenieur-Archiv*, vol. 27, 1959, pp. 242–249.

5 G. D. Galletly, W. T. Kyner, and C. E. Moller, "Numerical Methods and the Bending of Ellipsoidal Shells," *Journal of the Society of Industrial and Applied Mathematics*, vol. 9, 1961, pp. 489–513.

6 R. K. Penny, "Symmetric Bending of the General Shell of Revolution by Finite Difference Method," *Journal of Mechanical Engineering Science*, vol. 3, 1961, pp. 369–377.

7 P. P. Radkowski, R. M. Davis, and M. R. Bolduc, "Numerical Analysis of Equations of Thin Shells of Revolution," *American Rocket Society Journal*, vol. 32, 1962, pp. 36–41.

8 W. K. Sepetoski, C. E. Pearson, I. W. Dingwell, and A. W. Adkins, "A Digital Computer Program for the General Axially Symmetric Thin-Shell Problem," JOURNAL OF APPLIED MECHANICS, vol. 29, TRANS. ASME, vol. 84, Series E, 1962, pp. 655–661.

9 B. Budiansky and P. P. Radkowski, "Numerical Analysis of Unsymmetrical Bending of Shells of Revolution," *AIAA Journal*, vol. 1, 1963, pp. 1833–1842.

10 J. E. Goldberg and J. L. Bogdanoff, "Static and Dynamic Analysis of Nonuniform Conical Shells under Symmetrical and Unsymmetrical Conditions," *Proceedings of the Sixth Symposium on Ballistic Missile and Aerospace Technology*, Academic Press, New York, N. Y., vol. 1, 1961, pp. 219–238.

11 C. R. Steele, "Shells of Revolution With Edge Loads of Rapid Circumferential Variation," JOURNAL OF APPLIED MECHANICS, vol. 29, TRANS. ASME, vol. 84, Series E, 1962, pp. 701–707.

12 R. D. Schile, "Asymptotic Solution of Nonshallow Shells of Revolution Subjected to Nonsymmetric Loads," *Journal of the Aerospace Sciences*, vol. 29, 1962, pp. 1375–1379.

13 E. Reissner, "A New Derivation of the Equations for the Deformation of Elastic Shells," *American Journal of Mathematics*, vol. 63, 1941, pp. 177–184.

14 S. A. Ambartsumyan, "Theory of Anisotropic Shells" (in Russian), *Gosudarstvennoye Izdatel'stvo Fiziko-Matematicheskoi Literatury*, Moscow, USSR, 1961, p. 91.

15 P. M. Naghdi, "On the Theory of Thin Elastic Shells," *Quarterly of Applied Mathematics*, vol. 14, 1957, pp. 369–380.

16 P. F. Jordan, "Stresses and Deformations of the Thin-Walled Pressurized Torus," *Journal of the Aerospace Sciences*, vol. 29, 1962, pp. 213–225.

17 J. L. Sanders, Jr., and A. Liepins, "Toroidal Membrane Under Internal Pressure," *AIAA Journal*, vol. 1, 1963, pp. 2105–2110.

18 E. Reissner, "On Stresses and Deformations in Toroidal Shells of Circular Cross Section Which Are Acted Upon by Uniform Normal Pressure," *Quarterly of Applied Mathematics*, vol. 21, 1963, pp. 177–187.

19 R. A. Clark, "On the Theory of Thin Elastic Toroidal Shells," *Journal of Mathematics and Physics*, vol. 29, 1950, pp. 146–178.

20 A. L. Goldenveizer, *Theory of Elastic Thin Shells*, Pergamon Press, New York, N. Y., 1961, p. 480.

Free Vibration of Rotationally Symmetric Shells

A. KALNINS

Department of Engineering and Applied Science, Yale University, New Haven, Connecticut
(Received 16 December 1963)

This paper is concerned with a theoretical investigation of the free vibration of arbitrary shells of revolution by means of the classical bending theory of shells. A method is developed that is applicable to rotationally symmetric shells with meridional variations (including discontinuities) in Young's modulus, Poisson's ratio, radii of curvature, and thickness. By means of the method of this paper, the natural frequencies and the corresponding mode shapes of axisymmetric or nonsymmetric free vibration of rotationally symmetric shells can be obtained without a limitation on the length of the meridian of the shell. To illustrate the application of the method given in this paper to particular shells, some results of free vibration of spherical and conical shells obtained earlier by means of the bending theory are reproduced by the general method of this paper, and a detailed comparison is made. In addition, paraboloidal shells and a sphere–cone shell combination are considered, which have been previously analyzed by means of the inextensional theory of shells, and natural frequencies and mode shapes predicted by the bending theory are given.

SYMBOLS

$A(x)$	(m,m) matrix, denotes coefficients of differential equations
D	$=Eh^3/12(1-\nu^2)$
E	Young's modulus
G	$=1/(1+D\sin^2\phi/Kr^2)$
H	$=1/R_\phi-\sin\phi/r$
I	unit matrix
J	$=1/R_\phi+\sin\phi/r$
K	$=Eh/(1-\nu^2)$
L	some characteristic length of shell
M	number of segments
$M_\phi, M_\theta, M_{\theta\phi}$	moment resultants
N	effective tangential shear resultant
$N_\phi, N_\theta, N_{\theta\phi}$	membrane-stress resultants
P	$=1/R_\phi+\nu\sin\phi/r$
Q	effective transverse-shear resultant
Q_ϕ, Q_θ	transverse-shear resultants
R_ϕ	radius of curvature of meridian
$T(x)$	(m,m) transformation matrix
$U(x)$	(m,m) matrix, related to $Y(x)$
$Y(x)$	(m,m) matrix, denotes homogeneous solutions
$Y_i{}^j(x)$	i identifies segment S_i, j denotes quadrant of partitioned matrix $Y(x)$
a, b	end points of shell
c	$=(E/\rho)^{\frac{1}{2}}$—speed of sound
h	thickness of shell
m	number of first-order differential equations
n	integer, denotes Fourier component
r	distance from axis of symmetry
s	distance along meridian in positive direction of ϕ
t	time
$u(x)$	$(m,1)$ matrix, related to $y(x)$
w, u_ϕ, u_θ	displacements of middle surface in normal, meridional, circumferential direction
x	independent variable, can be ϕ or s
$y(x)$	$(m,1)$ matrix, denotes fundamental variables
$y_j{}^i(x)$	$j=1, 2$ denotes upper and lower half of partitioned $y(x)$; i denotes ith element of each submatrix
β_ϕ	angle of rotation of normal in meridional direction
ϕ	angle between normal and axis of symmetry
ν	Poisson's ratio
ω	circular frequency, rad/sec
ρ	mass density
Ω	$\omega L/c$, nondimensional frequency parameter

INTRODUCTION

IN the analysis of free vibration of a shell of revolution, the natural frequencies of the shell are the roots of a determinant whose elements are related to certain solutions of the homogeneous field equations. These solutions, from which the frequency equation is constructed, are characteristic of a particular shell, and for simple shell configurations, such as cylindrical and spherical shells, they are known hypergeometric functions. However, for more-complicated shells such solutions are not available.

The main purpose of the present paper is to develop a method for the determination of the homogeneous solutions, natural frequencies, and mode shapes of free vibration for arbitrary rotationally symmetric shells by means of the linear-bending theory of shells. The method given here is applicable to any eigenvalue problem that is governed in an interval by a system of m linear homogeneous first-order ordinary differential equations and $m/2$ homogeneous boundary conditions at each end of the interval.

It was shown by the present author[1] that the basic equations of the classical static theory of shells of revolution can be reduced to a system of 8 first-order ordinary differential equations involving 8 unknowns in such a way that no derivatives of the shell properties appear in the coefficients of these equations. For the special case of vibration of a conical shell, a similar system of equations was previously derived by Goldberg and Bogdanoff.[2] The essential point in these derivations is the definition of the 8 variables as exactly those quantities that enter into the appropriate boundary conditions on a rotationally symmetric edge of a shell of revolution.

To obtain a similar system of differential equations for the analysis of free vibration of arbitrary rotationally symmetric shells, the reduction scheme given in Ref. 1 is started from the homogeneous equations of the classical dynamic theory of shells. Again, a system of 8 first-order differential equations results, which together with the boundary conditions constitutes an eigenvalue problem. The solution to this problem is obtained in this paper by means of a multisegment, direct, numerical integration approach, which is an extension to eigenvalue problems of the method used successfully by the author[1] for the analysis of static deformation of shells of revolution.

A part of the method given here is similar to the one used in the analysis of axisymmetric modes of free vibration of relatively short conical shells by Goldberg, Bogdanoff, and Marcus.[3] It turns out that, if the method of Ref. 3 is applied to sufficiently long shells of revolution, then a complete loss of accuracy invariably results in the process of calculation of the natural frequencies and mode shapes. The loss of accuracy is attributed to the subtraction of almost equal numbers, and its cause is explained in detail in this paper. It is also shown in this paper that the loss of accuracy can be avoided and that the natural frequencies and mode shapes of long shells can be obtained if the shell is divided into a number of sufficiently short segments and the numerical integration is carried out over each segment separately. By requiring the continuity of all relevant variables at the end points of the segments, a linear homogeneous system of matrix equations is obtained that possesses a nontrivial solution if the determinant of a certain $(m/2,m/2)$ matrix vanishes. Thus, the free-vibration problem of an arbitrary rotationally symmetric shell is reduced to the determination of the homogeneous solutions for a particular frequency and to the calculation of the value of an $(m/2,m/2)$ determinant.

For the purpose of illustration of the use of the method given in this paper, the natural frequencies and mode shapes of free vibration are investigated for some special cases of rotationally symmetric shells. To demonstrate the accuracy of the method, results are obtained for free vibration of a conical and a spherical shell and compared to those obtained previously by means of the bending theory of shells. Then, the lowest natural frequencies and mode shapes of a paraboloidal shell and a sphere–cone shell combination are calculated and compared to previous results, which have been obtained earlier by means of the inextensional theory of shells.

I. FUNDAMENTAL SYSTEM OF EQUATIONS FOR VIBRATION OF SHELLS OF REVOLUTION

In Ref. 1, the governing system of static equations for shells of revolution is reduced to a system of 8 differential equations that contain 8 unknowns. This system of equations and the unknowns are called the fundamental system and the fundamental variables, respectively, because they are necessary and sufficient for a complete statement of the problem.

In this paper, we are concerned with the fundamental system of equations that is reduced from the dynamic theory of shells of revolution. In the absence of any external loads, the fundamental equations can be written in matrix form:

$$dy(x)/dx = A(x)y(x), \tag{1}$$

[1] A. Kalnins, "Analysis of Shells of Revolution Subjected to Symmetrical and Nonsymmetrical Loads," Paper No. 6 -APM-33, J. Appl. Mech. (to be published).

[2] J. E. Goldberg, and J. L. Bogdanoff, Proc. Symp. Ballistic Missile Aerospace Technol., 6th, 1, 219–238 (1961).

[3] J. E. Goldberg, J. L. Bogdanoff, and L. Marcus, J. Acoust. Soc. Am. 32, 738–742 (1960).

where x is an independent variable, $y(x)$ is a column matrix whose elements represent the m fundamental variables, and $A(x)$ is an (m,m) coefficient matrix whose elements are piecewise continuous known functions of x defined in an interval of x denoted by (a,b). The system of Eqs. (1), together with $m/2$ homogeneous boundary conditions at each end point of the interval ($x=a$ and $x=b$), forms an eigenvalue problem, for which a method of solution is given in the following sections.

It should be noted that the method given in Ref. 1 for static analysis, as well as that in this paper for free vibration, can be conveniently used with any version of the consistent linear shell theories available in the literature, including the anisotropic and the improved theories in which the effects of transverse-shear deformation are accounted for. The differences in these theories are reflected only in the elements of $A(x)$ and the number of the fundamental variables. For example, for nonsymmetric deformation of a shell of revolution for improved theory, $m=10$; for classical theory, $m=8$, while, for axisymmetric deformation for both theories, $m=6$. For brevity, in this paper we consider only the symmetric and nonsymmetric free vibration by means of the classical theory of isotropic rotationally symmetric shells. Extensions are straightforward.

The variables of the classical theory of shells used in this paper are assumed to be separable in the form

$$\left.\begin{matrix} w \\ u_\phi \\ \beta_\phi \\ Q \\ Q_\phi \\ N_\phi \\ N_\theta \\ M_\phi \\ M_\theta \end{matrix}\right\} = \left\{\begin{matrix} w_n \\ u_{\phi n} \\ \beta_{\phi n} \\ Q_n \\ Q_{\phi n} \\ N_{\phi n} \\ N_{\theta n} \\ M_{\phi n} \\ M_{\theta n} \end{matrix}\right\} \cos n\theta \cos\omega t,$$

$$\left.\begin{matrix} u_\theta \\ N \\ N_{\theta\phi} \\ Q_\theta \\ M_{\theta\phi} \end{matrix}\right\} = \left\{\begin{matrix} u_{\theta n} \\ N_n \\ N_{\theta\phi n} \\ Q_{\theta n} \\ M_{\theta\phi n} \end{matrix}\right\} \sin n\theta \cos\omega t.$$

The fundamental variables, in terms of which the problem is stated, are taken as those quantities that appear in the appropriate boundary conditions of the classical theory on an axisymmetric circular edge. Thus, The independent variable x can be regarded as either the angle ϕ between the normal and the axis of symmetry of the shell or the distance s measured along the meridian, as shown in Fig. 1. For some shells (e.g., paraboloidal), ϕ is more convenient, while for shells with straight generators, when ϕ is a constant (e.g., conical), s should be employed. However, the distinction between ϕ and s is necessary only in the derivatives where the transformation $d/ds=(1/R_\phi)d/d\phi$ holds.

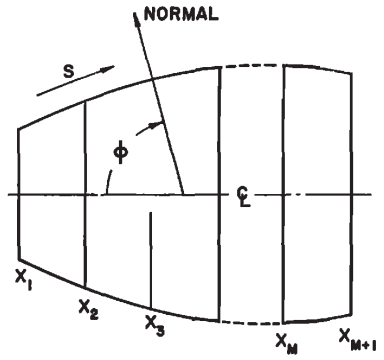

FIG. 1. Coordinates of the shell.

we define the (8,1) matrix $y(x)$ by

$$y(x)=\begin{Bmatrix} w_n(x) \\ u_{\phi n}(x) \\ u_{\theta n}(x) \\ \beta_{\phi n}(x) \\ Q_n(x) \\ N_{\phi n}(x) \\ N_n(x) \\ M_{\phi n}(x). \end{Bmatrix}$$

The fundamental equations for vibration of shells of revolution in the form of Eq. (1) can be derived by following the steps given in Ref. 1. Based on the linear classical theory of shells derived by Reissner,[4] with the inclusion of the effects of translatory and rotatory inertia, the nonzero elements A_{ij} of the coefficient matrix $A(x)$ can be written in the form

$$A_{12}=1/R_\phi, \quad A_{14}=-1,$$

$$A_{21}=-P, \quad A_{22}=-\nu\cos\phi/r, \quad A_{23}=-\nu n/r, \quad A_{26}=1/K,$$

$$A_{31}=nGD\sin 2\phi/Kr^3, \quad A_{32}=n(1-GDJ\sin\phi/Kr)/r,$$

$$A_{33}=(1-GDH\sin\phi/Kr)\cos\phi/r, \quad A_{34}=2nGD\sin\phi/Kr^2,$$

$$A_{37}=2(1-GD\sin^2\phi/Kr^2)/(1-\nu)K,$$

$$A_{41}=-\nu n^2/r^2, \qquad A_{43}=-\nu n\sin\phi/r^2,$$

$$A_{44}=-\nu\cos\phi/r, \quad A_{48}=1/D,$$

$$A_{51}=2n^2GD(1-\nu)\cos^2\phi/r^4+n^4D(1-\nu^2)/r^4 +K(1-\nu^2)\sin^2\phi/r^2-\Omega^2Eh(1+h^2n^2/12r^2)/L^2,$$

$$A_{52}=K(1-\nu^2)\sin 2\phi/2r^2-n^2GDJ(1-\nu)\cos\phi/r^3,$$

[4] E. Reissner, Am. J. Math. **63**, 177–184 (1941).

$$A_{53}=n(1-\nu^2)(K+n^2D/r^2)\sin\phi/r^2 - nGDH(1-\nu)\cos^2\phi/r^3-n\Omega^2Eh^3\sin\phi/12r^2L^2,$$

$$A_{54}=n^2D(1-\nu)(1+\nu+2G)\cos\phi/r^3,$$

$$A_{55}=-\cos\phi/r, \quad A_{56}=P, \quad A_{57}=-A_{31}, \quad A_{58}=-A_{41},$$

$$A_{61}=K(1-\nu^2)\sin2\phi/2r^2-n^2GDJ(1-\nu)\cos\phi/r^3,$$

$$A_{62}=K(1-\nu^2)\cos^2\phi/r^2+n^2GDJ^2(1-\nu)/2r^2-\Omega^2Eh/L^2,$$

$$A_{63}=nK(1-\nu^2)\cos\phi/r^2+nGDJH(1-\nu)\cos\phi/2r^2,$$

$$A_{64}=-n^2GDJ(1-\nu)/r^2, \quad A_{65}=-1/R_\phi,$$

$$A_{66}=-(1-\nu)\cos\phi/r, \quad A_{67}=-n(1-GDJ\sin\phi/Kr),$$

$$A_{71}=A_{53}, \quad A_{72}=A_{63},$$

$$A_{73}=n^2(K+D\sin^2\phi/r^2)(1-\nu^2)/r^2 + GDH^2(1-\nu)\cos^2\phi/2r^2 - \Omega^2Eh(1+h^2\sin^2\phi/12r^2)/L^2,$$

$$A_{74}=-nD(1-\nu)[GH-(1+\nu)\sin\phi/r]\cos\phi/r^2,$$

$$A_{76}=-A_{23}, \quad A_{77}=-(2-GDH\sin\phi/Kr)\cos\phi/r,$$

$$A_{78}=-A_{43},$$

$$A_{81}=A_{54}, \quad A_{82}=A_{64}, \quad A_{83}=A_{74},$$

$$A_{84}=D(1-\nu)[(1+\nu)\cos^2\phi+2n^2G]/r^2-\Omega^2Eh^3/12L^2,$$

$$A_{85}=1, \quad A_{87}=-A_{34}, \quad A_{88}=-(1-\nu)\cos\phi/r.$$

The given coefficients A_{ij} are those which arise when x in Eq. (1) is identified with s. If the independent variable is taken as ϕ, then every element A_{ij} given above must be multiplied by R_ϕ.

The eigenvalue problem as defined above determines the fundamental variables $y(x)$. Other variables are given in terms of $y(x)$ by

$$N_{\theta n}=\nu N_{\phi n}+(1-\nu^2)K(w_n\sin\phi+u_{\phi n}\cos\phi+nu_{\theta n})/r,$$

$$M_{\theta n}=\nu M_{\phi n}+(1-\nu^2) \times D(n^2w_n/r+\beta_{\phi n}\cos\phi+n\sin\phi u_{\theta n}/r)/r,$$

$$M_{\theta\phi n}=D(1-\nu)[-2n\cos\phi w_n/r+nJu_{\phi n} + H\cos\phi u_{\theta n}-2n\beta_{\phi n}]/2r+\sin\phi DN_n/Kr,$$

$$N_{\theta\phi n}=N_n-\sin\phi M_{\theta\phi n}/r,$$

$$Q_{\phi n}=Q_n-nM_{\theta\phi n}/r,$$

$$Q_{\theta n}=-nM_{\theta n}/r+(dM_{\theta\phi n}/ds) + 2\cos\phi M_{\theta\phi n}/r+\Omega^2Eh^3(nw_n+u_{\theta n}\sin\phi)/12rL^2.$$

The method given for static problems in Ref. 1 is equally applicable for finding the forced dynamic response of rotationally symmetric shells to harmonic surface and edge (or ring) loads if the coefficients $A(x)$ derived in Ref. 1 are replaced by those given in this paper. The main purpose of this paper is the development of a method for the analysis of free vibration of rotationally symmetric shells, which is given in the following sections.

II. METHOD OF SOLUTION FOR A ONE-SEGMENT SHELL

In order to find the solution of the system of Eqs. (1), it is desirable to reduce the system of differential equations to one equation and one unknown. This has been accomplished, for example, for cylindrical and spherical shells with constant thickness and material properties by eliminating all other unknowns but the normal displacement w. Regardless of whether the solution is obtained from a single equation involving a single unknown or from the simultaneous system of Eqs. (1), the solution for the fundamental variables of a shell of revolution in the absence of external loads can be written in the form

$$y(x)=W(x)C, \tag{2}$$

where $W(x)$ is an (m,m) matrix whose columns represent m linearly independent solutions of the homogeneous governing equations, and C denotes a column matrix of m arbitrary constants.

It should be noted that for cylindrical shells the columns of $W(x)$ consist of independent trigonometric functions, while for shallow spherical shells they are Bessel functions, and for nonshallow spherical shells they are Legendre functions, all of which can be obtained either from their hypergeometric series or by means of numerical integration from the corresponding differential equations. For more-complicated shell configurations, especially in the presence of meridionally variable properties, the reduction of Eqs. (1) to a single equation with one unknown and a series solution may not be possible. For such shells, the method of direct numerical integration of the system of Eqs. (1) for obtaining the solutions $W(x)$ leads to a powerful method for the analysis of arbitrary rotationally symmetric shells.

The solution is obtained by defining the columns of $W(x)$ as the solutions of m initial-value problems in the interval (a,b) governed by the system of Eqs. (1) and subjected to arbitrary linearly independent initial conditions at $x=a$. If the independence requirement is met at $x=a$, then the solutions will be independent at any other value of x in the interval (a,b).

Since the only requirement of the columns of $W(x)$ is that they be linearly independent solutions of the system of Eqs. (1), in place of $W(x)$ we may employ in the interval (a,b) a matrix of linear combinations of the solutions of Eqs. (1), which at $x=a$ reduces to a unit matrix I. This is done by evaluating Eq. (2) at $x=a$

$$y(a)=W(a)C, \tag{3}$$

solving for C

$$C=W^{-1}(a)y(a), \tag{4}$$

and replacing C in Eq. (2) by Eq. (4) to give

$$y(x)=W(x)W^{-1}(a)y(a).$$

Now, we define

$$Y(x)=W(x)W^{-1}(a), \tag{5}$$

and obtain the expression for the solution in the form

$$y(x)=Y(x)y(a). \tag{6}$$

Thus, the columns of $Y(x)$ are solutions of the m initial-value problems given by

$$dY(x)/dx=A(x)Y(x), \tag{7a}$$

$$Y(a)=I. \tag{7b}$$

The elements of the rows of $Y(x)$ represent those fundamental variables that are contained in the corresponding rows of $y(x)$ in Eq. (1).

It is important to note that the solutions $Y(x)$ depend only on the geometric and material properties of the shell [i.e., on the coefficient matrix $A(x)$] but not on the boundary conditions. The same solutions $Y(x)$ can be used for any appropriate boundary conditions imposed at the edges of a given shell. For this reason, the solution of the free-vibration problem of a rotationally symmetric shell is completely determined by $Y(x)$.

At this point, it should be recalled that at each edge of the shell, i.e., at $x=a$ and $x=b$, $m/2$ quantities must be prescribed. If these quantities are the fundamental variables, then $m/2$ elements of $y(a)$ and $m/2$ elements of $y(b)$ are known, and the solution for the $m/2$ unknown elements of $y(a)$ is directly obtained from Eq. (6) when evaluated at $x=b$ in the form

$$y(b)=Y(b)y(a). \tag{8}$$

It should be clear that for free-vibration problems, when the prescribed variables vanish, Eq. (8) constitutes a linear homogeneous system of $m/2$ equations with $m/2$ unknown elements of $y(a)$. Requiring the vanishing of the determinant of the coefficient matrix of this system of equations gives the frequency equation and natural frequencies of the system and a solution for $y(a)$. Once all elements of $y(a)$ are known, the mode shapes corresponding to a particular frequency can be obtained at any desired value of x from Eq. (6).

The above analysis is easily extended to such cases when the boundary conditions at $x=a$ and $x=b$ are imposed on new variables $u(x)$, which are linear combinations of the fundamental variables and are related to $y(x)$ by

$$u(x)=T(x)y(x), \tag{9}$$

where $T(x)$ is a given (m,m) nonsingular matrix. In this case, we obtain an analogous equation to Eq. (6) in terms of $u(x)$ by substituting $y(x)$ from Eq. (9) into (6) and solving for $u(x)$ in the form

$$u(x)=T(x)Y(x)T^{-1}(a)u(a). \tag{10}$$

If we define

$$U(x)=T(x)Y(x)T^{-1}(a), \tag{11}$$

we obtain

$$u(x)=U(x)u(a), \tag{12}$$

which is of the same form as Eq. (6). Thus, the frequency equation and the solution for $u(x)$ can be obtained in the same manner as those for $y(x)$ by using the solutions $Y(x)$ defined by Eqs. (7) and simply transforming them as shown by Eq. (11).

In Sec. III, it becomes necessary to rearrange the elements of $u(x)$ at some values of x in such a way that the known and unknown variables of $u(a)$ and $u(b)$ are separated into two partitioned matrices. The transformation matrix $T(x)$ can easily contain such a rearrangement.

In the remainder of this section, it is regarded that the solution of the problem is given by Eq. (12), and that $u(a)$, $u(b)$ contain those quantities that are prescribed at $x=a$ and $x=b$, respectively. Moreover, for added simplicity of the analysis, it is regarded that the first $m/2$ elements of $u(a)$, denoted by $u_1(a)$, and the last $m/2$ elements of $u(b)$, denoted by $u_2(b)$, are the prescribed variables. All the necessary transformations for going from $y(x)$ to $u(x)$ are given by Eqs. (9) and (11), and it should be clear that no loss of generality is involved in such a transformation.

With this transformation, Eq. (12) evaluated at $x=b$ can be written as a partitioned matrix product in the form

$$\begin{bmatrix} u_1(b) \\ \hline u_2(b) \end{bmatrix} = \left[\begin{array}{c|c} U^1(b) & U^2(b) \\ \hline U^3(b) & U^4(b) \end{array}\right] \begin{bmatrix} u_1(a) \\ \hline u_2(a) \end{bmatrix}, \tag{13}$$

where the $(m/2,m/2)$ matrices $U^i(b)$ are the partitioned matrices of $U(b)$. If we assume that for free vibration $u_1(a)=u_2(b)=0$, then the unknowns $u_2(a)$ are directly obtained from

$$U^4(b)u_2(a)=0. \tag{14}$$

Since a nontrivial solution for $u_2(a)$ is possible if the matrix $U^4(b)$ is of rank $m/2-1$, the frequency equation of the system is given by

$$|U^4(b)|=0. \tag{15}$$

Once a frequency is found that satisfies Eq. (15), the corresponding solution for $u_2(a)$ is obtained from

$$u_2{}^i(a)=d(-1)^{i+1}|M_i|, \tag{16}$$

where $u_2{}^i(a)$ denotes the ith element of $u_2(a)$, d is an arbitrary constant, and $|M_i|$ is the determinant obtained from any $(m/2-1, m/2)$ submatrix of rank

$m/2-1$ contained in $U^4(b)$ by deleting the ith column. After $u_2(a)$ is calculated from Eq. (16), the corresponding mode shapes for a particular natural frequency are found from Eq. (12).

For the determination of the mode shapes from Eq. (12) in terms of the quantities that are prescribed at $x=b$, values of $U(x)$ are necessary at any x at which the output is desired. For this purpose, during the integration process for the determination of $Y(b)$, the intermediate values of $Y(x)$ should be stored from which the corresponding $U(x)$ are obtained by Eq. (11). If the mode shapes are desired in terms of the fundamental variables, then, after determination of $u(a)$ by means of Eq. (16), the corresponding $y(a)$ can be obtained from Eq. (9), and then the mode shapes are calculated from Eq. (6) at those points at which $Y(x)$ is stored.

Thus, the free-vibration problem of an arbitrary rotationally symmetric shell is reduced to (1) integration for a given Ω of Eqs. (1) m times from $x=a$ to $x=b$ to determine the fundamental solutions $Y(x)$, starting with $Y(a)=I$; (2) transformation of $Y(x)$ at certain values of x to the boundary-condition variables by Eq. (11); (3) calculation of the value of the determinant of $U^4(b)$; (4) repetition of this process for the evaluation of the natural frequency Ω_i at which Eq. (15) is satisfied; and (5) calculation of the mode shapes from Eq. (16) and either Eq. (12) or Eq. (6) at a particular natural frequency.

The method thus far is essentially a generalization of the one employed in the analysis of axisymmetric vibration of a conical shell in Ref. 3. It works very well for a shell with a relatively short interval (a,b). However, when the length of the meridian of the shell is increased, the elements of $U(b)$ increase rapidly in magnitude while the value of the frequency determinant does not, and, consequently, an increasing number of significant digits is subtracted out in the process of calculation of the determinant of $U^4(b)$. Similarly, because of the large values of the elements of $U(x)$ at large values of x, accuracy is invariably lost when the mode shapes are obtained from Eqs. (6) or (12). This phenomenon was pointed out previously in Ref. 1, and also by Galletly[5] *et al.* and Sepetoski *et al.*[6] in connection with shells of revolution, and by Fox[7] with regard to some boundary-value problems of second-order differential equations.

To make the direct integration technique applicable also to long shells, a method was developed in Ref. 1 for the static analysis of shells of revolution in which the initial-value problems for the determination of $Y(b)$ are defined over suitably selected short segments. This method is extended in Sec. III to apply to eigenvalue problems.

III. EXTENSION TO A MULTISEGMENT SHELL

The method of the analysis of shells of revolution proposed in Ref. 1 is based on the idea that if the m initial-value problems for the determination of $Y(x)$ are defined over sufficiently short segments of the shell, then the elements of $Y(x)$ are not large in magnitude and no loss of accuracy occurs due to subtraction of large almost equal numbers. This idea is also applicable in the analysis of free vibration of shells of revolution.

As it was done in Ref. 1, let the shell be divided into M segments, which are denoted by S_i in which $x_i \leq x \leq x_{i+1}$, where $i=1, 2, \cdots, M$. The ends of the shell, denoted in Sec. II by $x=a$ and $x=b$, are now at $x=x_1$ and $x=x_{M+1}$, as shown in Fig. 1. The solution in each segment S_i is given by Eq. (6) in the form

$$y(x)=Y_i(x)y(x_i), \tag{17}$$

where $Y_i(x)$ are obtained from the initial-value problems defined in S_i by

$$dY_i(x)/dx=A(x)Y_i(x), \quad Y_i(x_i)=I. \tag{18}$$

Continuity requirements on all fundamental variables[8] at the end points of the segments (i.e., at $x=x_i$, $i=2, 3, \cdots, M+1$) lead from Eq. (17) to

$$y(x_{i+1})=Y_i(x_{i+1})y(x_i), \tag{19}$$

where $i=1, 2, \cdots, M$.

The analysis and the prescription of general boundary conditions in terms of linear combinations of the fundamental variables are considerably simplified if the $T(x)$ transformation introduced in Sec. II is employed to obtain the quantities prescribed at the end points ($x=x_1$ and $x=x_{M+1}$) of the shell in the form

$$u(x_1)=T(x_1)y(x_1), \tag{20a}$$

$$u(x_{M+1})=T(x_{M+1})y(x_{M+1}). \tag{20b}$$

According to Eq. (11), we must then transform the solutions $Y_1(x_2)$ and $Y_M(x_{M+1})$ by

$$U_1(x_2)=Y_1(x_2)T^{-1}(x_1), \tag{21a}$$

$$U_M(x_{M+1})=T(x_{M+1})Y_M(x_{M+1}). \tag{21b}$$

The matrix $T(x_1)$ is such that the first $m/2$ elements of $u(x_1)$ are the prescribed quantities at x_1, while $T(x_{M+1})$ is such that the last $m/2$ elements of $u(x_{M+1})$ are the prescribed quantities at $x=x_{M+1}$. The variables $y(x)$ at interior points of the shell (i.e., at x_i with

[5] G. D. Galletly, W. T. Kyner, and C. E. Moller, J. Soc. Ind. Appl. Math. **9**, 489–513 (1961).

[6] W. K. Sepetoski, C. E. Pearson, I. W. Dingwell, and A. W. Adkins, J. Appl. Mech. **29**, 655–661 (1962).

[7] L. Fox, *Numerical Solution of Ordinary and Partial Differential Equations* (Addison-Wesley Publishing Co., Reading, Mass., 1962), p. 61.

[8] It should be mentioned here that the continuity requirement of the fundamental variables ensures continuity of the stress resultants but not necessarily of the stresses, which is consistent with the formulation of the theory of shells in terms of resultants.

$i=2, 3, \cdots, M$) need not be transformed, and they can be left in terms of the fundamental variables in the order in which the appear in Eq. (3).

In the following, it is assumed that the transformations given by Eqs. (20) and (21) are carried out, but that for simplicity of notation the symbols $y(x_1)$, $y(x_{M+1})$, $Y_1(x)$, $Y_M(x)$ are used instead of $u(x_1)$, $u(x_{M+1})$, $U_1(x)$, $U_M(x)$. In this way, the continuity Eqs. (19) can be employed without change when it is understood that the transformations of Eqs. (20) and (21) have been performed.

Using the partitioned matrix product as given by Eq. (13), Eq. (19) can be written as

$$y_1(x_{i+1})=Y_i^1(x_{i+1})y_1(x_i)+Y_i^2(x_{i+1})y_2(x_i), \quad (22a)$$

$$y_2(x_{i+1})=Y_i^3(x_{i+1})y_1(x_i)+Y_i^4(x_{i+1})y_2(x_i), \quad (22b)$$

where $i=1, 2, \cdots, M$, and the superscripts of Y and subscripts of y have the same meaning as in Eq. (13).

Equations (22) constitute a system of $2M$ linear homogeneous matrix equations with $2M$ unknowns: $y_1(x_i)$, $i=2, 3, \cdots, M+1$, and $y_2(x_i)$, $i=1, 2, \cdots, M$. For free-vibration problems, we assume that the prescribed quantities $y_1(x_1)=y_2(x_{M+1})=0$, and then Eqs. (22) can be arranged in matrix form as

$$\left[\begin{array}{cccc:cc:c} Y_1^2 & -1 & 0 & 0 & 0 & 0 & y_2(x_1) \\ Y_1^4 & 0 & -I & 0 & 0 & 0 & y_1(x_2) \\ 0 & Y_2^1 & Y_2^2 & -I & 0 & 0 & y_2(x_2) \\ 0 & Y_2^3 & Y_2^4 & 0 & -I & 0 & y_1(x_M) \\ \hdashline 0 & 0 & 0 & Y_M^1 & Y_M^2 & -I & y_2(x_M) \\ 0 & 0 & 0 & Y_M^2 & Y_M^4 & 0 & y_1(x_{M+1}) \end{array}\right]=0, \quad (23)$$

where the dashes indicate a pair of rows and/or columns of Eqs. (22) with $i=3, 4, \cdots, M-1$, and for brevity we have written Y_i^j in place of $Y_i^j(x_{i+1})$.

As it was stated in Refs. 1 and 6, if the system of Eqs. (23) is solved by means of Gaussian elimination, then the loss of accuracy due to subtraction is avoided. For this purpose, we triangularize the coefficient matrix of Eqs. (23) to the form

$$\left[\begin{array}{cccc:cc:c} E_1 & -I & 0 & 0 & 0 & 0 & y_2(x_1) \\ 0 & C_1 & -I & 0 & 0 & 0 & y_1(x_2) \\ 0 & 0 & E_2 & -I & 0 & 0 & y_2(x_2) \\ 0 & 0 & 0 & C_2 & -I & 0 & y_1(x_M) \\ \hdashline 0 & 0 & 0 & 0 & E_M & -I & y_2(x_M) \\ 0 & 0 & 0 & 0 & 0 & C_M & y_1(x_{M+1}) \end{array}\right]=0. \quad (24)$$

The $(m/2,m/2)$ matrices E_i and C_i ($i=1, 2, \cdots, M$), obtained by the standard Gaussian elimination procedure from Eqs. (23), are evaluated successively from

$$E_1=Y_1^2, \quad (25a)$$

$$C_1=Y_1^4E_1^{-1} \quad (25b)$$

$$E_i=Y_i^2+Y_i^1C_{i-1}^{-1}, \quad (25c)$$

$$C_i=(Y_i^4+Y_i^3C_{i-1}^{-1})E_i^{-1}, \quad (25d)$$

where $i=2, 3, \cdots, M$.

A nontrivial solution of the system of Eqs. (23) is possible if the $(m/2,m/2)$ matrix C_M is of rank $m/2-1$, and then the solution for the elements of $y_1(x_{M+1})$, denoted by $y_1{}^i(x_{M+1})$, where $i=1, 2, \cdots, m/2$, is given by

$$y_1{}^i(x_{M+1})=d(-1)^{i+1}|M_i|, \quad (26)$$

where again d is an arbitrary constant and the determinant $|M_i|$ is obtained from any $(m/2-1, m/2)$ submatrix of rank $m/2-1$ contained in C_M by deleting the ith column. Once $y_1(x_{M+1})$ is known, the remaining unknowns in the column matrix of Eq. (24) are determined in successive order directly from Eq. (24). In this process, we utilize the inverses of E_i and C_i, which are needed in Eqs. (25).

The above free-vibration analysis is applicable to any rotationally symmetric shell with two circular edges, at each of which $m/2$ boundary conditions in terms of linear combinations of the fundamental variables are specified. Situations may arise when the shell has no open edges, and we may then regard that the end points $x=x_1$ and $x=x_{M+1}$ are joined together. If this joint occurs on the axis of symmetry (e.g., a closed spherical shell) where $r=0$, then by introducing exact solutions in the vicinity of the axis of symmetry, this shell can be treated in the same way as a shell with two open edges.

If, however, the joint of $x=x_1$ and $x=x_{M+1}$ does not occur on the axis of symmetry (e.g., a complete torus), then, in general, integration must be carried out over the closed curve of the cross section of the shell, which, of course, should not cross or touch the axis of symmetry. The above analysis can be extended to such closed shells by requiring in Eqs. (22) that $y_1(x_1)=y_1(x_{M+1})$ and $y_2(x_1)=y_2(x_{M+1})$, i.e., that the fundamental variables at the starting edge are equal to those at the final edge. The resulting matrix is then triangularized to the form of Eq. (24), and the frequency equation and mode shapes are obtained in the same manner as given above. Since no boundary conditions are given, the transformations to $u(x)$ in this case are not necessary.

IV. CALCULATION OF NATURAL FREQUENCIES AND MODE SHAPES

On the basis of the coefficients $A(x)$ and the multisegment analysis given above, the author has prepared

a digital-computer program[9] that is applicable to any rotationally symmetric shell for the analysis of free vibration. The input of this program requires (1) properties of the shell: $R_\phi(x), r(x), h(x), c(x), \nu(x), E(x)$ at every x; (2) boundary conditions [transformation matrix $T(x)$] at $x=x_1$ and $x=x_{M+1}$; (3) the frequency interval that is to be investigated for natural frequencies; (4) the number of segments in which the shell is to be divided. The program outputs each natural frequency Ω_i and the corresponding mode shapes of all fundamental variables.

The numerical integration for the determination of the solutions $Y_i(x)$ in each segment S_i is carried out by means of a predictor–corrector method in which the step size is automatically selected according to a prescribed accuracy of the solution. Since the shell can have discontinuities in its properties, it is regarded that such an automatic selection of step size is absolutely necessary for a controlled accuracy and optimum efficiency of the solution.

In order to get the precise effect of the discontinuities in the shell properties, the segments should be selected in such a way that the end point of one segment coincides with the location of a discontinuity. Otherwise, the segments may have arbitrary lengths, so that within each segment $\beta \leq 3-5$, where $\beta = l[3(1-\nu^2)]^{\frac{1}{4}}/(Rh)^{\frac{1}{2}}$, l is the meridional length of the segment, and R is a radius of curvature. The program outputs the mode shapes at the ends of the segments twice—once from Eqs. (22) and then from Eq. (17)—and their comparison offers a direct check of the satisfaction of the continuity requirements. If these repeated values do not match a sufficient number of significant digits, then accuracy has been lost by subtraction and the number of segments must be increased.

From the results of Sec. III, it follows that for the multisegment analysis the natural frequencies Ω_i are the roots of the determinantal equation

$$|C_M| = 0, \tag{27}$$

which are found by calculating the determinant of C_M for incremented values of Ω until a change in sign occurs. Then, by inverse interpolation the particular $\Omega_i (i=1, 2, \cdots)$ are obtained at which $|C_M| = 0$.

After applying the program to the analysis of free vibration of many shell configurations, it was observed that at some values of Ω, denoted by Ω_F, a change of sign of any one of the determinants of the matrices $E_i (i=1, 2, \cdots, M)$ or $C_i (i=1.. 2, \cdots, M-1)$ may occur. From Eqs. (25), it follows that at these frequencies $|C_M|$ becomes infinite, which is accompanied by a sign change of $|C_M|$ and all the corresponding values of $y_j(x_i)$ obtained from Eqs. (26) and (24). Since $|C_M|$ does not actually vanish, no nontrivial solution exists at Ω_F, and they are not the natural frequencies of the system. However, since an automatic search of the roots of Eq. (27) is based on the changes of the sign of $|C_M|$, then at $\Omega=\Omega_F$ false natural frequencies are indicated at which the inverse-interpolation technique fails.

We can remove the false sign changes from the frequency equation by using the following procedure: Recalling that at Ω_F both $|C_M|$ and $y_j(x_i)$ change sign, we should seek the roots of $|C_M|$ divided by some nonzero element of $y_j(x_i)$. It is convenient to choose for this purpose the first element of $y_2(x_1)$, denoted by $y_2^1(x_1)$. Thus, the modified frequency equation is

$$Z = |C_M|/y_2^1(x_1), \tag{28}$$

which gives the same roots as Eq. (27), but is free from the sign changes at $\Omega=\Omega_F$.

We should also note that if in Eq. (22) $y_2(x_{M+1})$ is not set equal to zero, then $y_2(x_{M+1})$ appears in the last row on the right-hand side of Eq. (23). After triangularization by means of Eqs. (25), the last row of Eq. (24) then reads

$$y_2(x_{M+1}) = C_M y_1(x_{M+1}). \tag{29}$$

The use of the frequency Eq. (28) involves the determination of all the $y_j(x_i)$'s by means of Eqs. (26) and (24) at every trial frequency Ω, so that $y_2^1(x_1)$ can be found. According to Eq. (29), the values of $y_j(x_i)$, obtained from Eqs. (26) and (24) for any Ω (except Ω_i), represent the forced response to the nonzero boundary values $y_2(x_{M+1})$, which are given by Eq. (29). Clearly, for a natural-frequency Ω_i, it follows from Eq. (29) that $y_2(x_{M+1}) = 0$.

While the computer time for this additional calculation is found to be negligible, the zeros of the modified frequency Eq. (28) are obtained much more easily than those of Eq. (27). This is clearly shown in Fig. 2, where

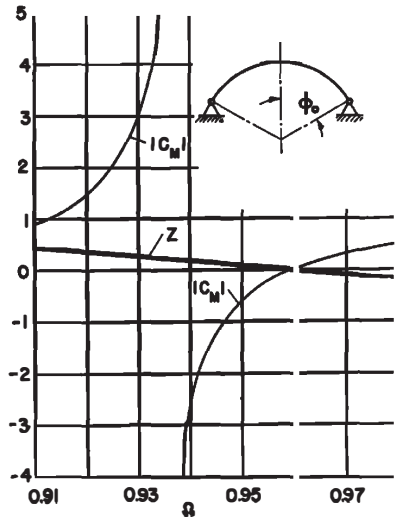

FIG. 2. Two types of frequency equations vs Ω.

[9] The program was prepared and all calculations were carried out on the IBM-709 computer at the Yale Computer Center.

TABLE I. Natural frequencies Ω_i of axisymmetric vibration of truncated conical shell.

	Ref. 3	This paper
Ω_1	0.00238	0.00238
Ω_2	0.00292	0.00291
Ω_3	0.00358	0.00358

TABLE II. Natural frequencies Ω_i of axisymmetric vibration of spherical shell with fixed–hinged edge at $\phi=60°$.

	Ref. 10	This paper
Ω_1	0.962	0.959
Ω_2	1.334	1.328
Ω_3	2.128	2.114

both $|C_M|$ and Z are plotted versus Ω near the lowest mode of a spherical shell, which is considered in Sec. V. While a sign change of $|C_M|$ occurs at $\Omega=0.936$, the F curve is free of such a disturbance. Of course, both curves predict correctly the first natural frequency at $\Omega=0.959$.

Once a natural frequency is obtained, the corresponding mode shapes at x_{M+1} are found from Eq. (26) and then at the remaining x_i from Eq. (24) starting with $i=M$ and ending with $i=1$. If the fundamental variables of the mode shapes are desired at more points than at the ends of the segments, then they are directly obtained from Eq. (17), provided that the values of $Y_i(x)$ at these points are stored during the integration from $x=x_i$ to $x=x_{i+1}$ in each segment. Before using Eq. (17), we should recall that $y(x_1)$ and $y(x_{M+1})$ are really the transformed variables $u(x_1)$ and $u(x_{M+1})$, and in order to use $Y(x)$ in Eq. (17) we must transform them back to the fundamental variables by means of Eqs. (20).

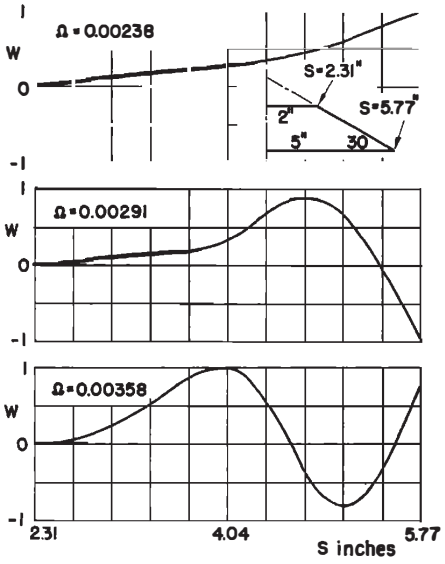

FIG. 3. Mode shapes of normal displacement w for truncated conical shell.

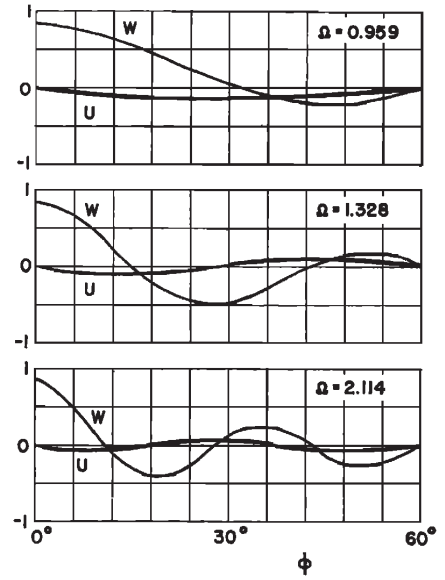

FIG. 4. Mode shapes of displacements for spherical shell.

V. ILLUSTRATIVE EXAMPLES

A. Conical Shell

In Ref. 3, the natural frequencies and mode shapes of free axisymmetric vibration are determined for a truncated conical shell in the shape of a loudspeaker cone. To show the accuracy of the present method, exactly the same problem as in Ref. 3 is considered by means of the general program. The comparison of the first three natural frequencies is given in Table I. Letting $L=h$, the frequency parameter is $\Omega=\omega h/c$, where the speed of sound in Ref. 3 is $c=7.071\times10^4$ in./sec, $h=0.025$ in., and $\nu=0.25$. The corresponding mode shapes for the first three modes obtained by the general program, together with other dimensions of the shell, are shown in Fig. 3. The agreement with the results of Ref. 3 is excellent.

B. Spherical Shell

The first three modes of axisymmetric vibration of a spherical shell with a fixed–hinged edge at $\phi=60°$ have been calculated by means of the hypergeometric series solutions of bending theory and are included in a recent paper.[10] The natural frequencies $\Omega=\omega R/c$ for $\nu=0.3$, $h/R=0.05$, are also calculated by the general program and are given in Table II, while the corresponding mode shapes are shown in Fig. 4.

The lowest natural frequency of a nonsymmetric mode ($n=2$) as predicted by the classical bending theory of shallow shells is given in Ref. 11: $\Omega_1=2.34$. For $h/R=0.05$, $\nu=0.3$, and a clamped edge at $\phi=30°$, the corresponding result obtained by the general program is $\Omega_1=2.15$.

While the agreement with the results of Ref. 10 is within a few percent, the nonsymmetric frequency pre-

[10] A. Kalnins, "Effect of Bending on Vibrations of Spherical Shells," J. Acoust. Soc. Am. **36**, 74–81 (1964).

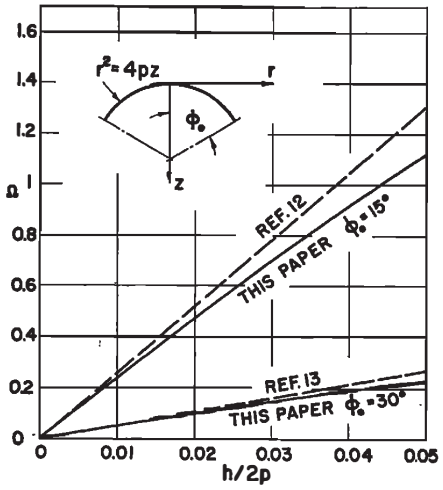

FIG. 5. Natural frequencies of inextensional modes of paraboloidal shell vs $h/2p$ for $n=2$ and $\nu=0.3$.

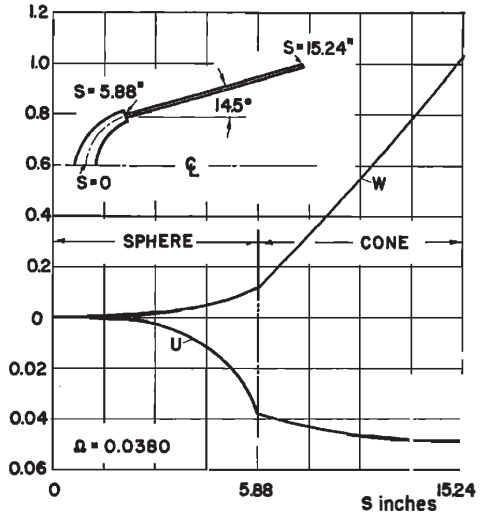

FIG. 6. Transverse and meridional displacements for inextensional mode ($n=3$) of sphere–cone shell combination.

dicted by the theory of shallow shells in Ref. 11 is higher by about 9%. The reason for this difference may be that the admissible maximum limiting angle in the theory of shallow shells is smaller for $n>0$ than for $n=0$.

The inextensional theory of deformation of shells as formulated by Lord Rayleigh can be used in the analysis of the inextensional modes of shells of revolution. Since the inextensional modes must be included in the general bending theory of shells, it may be of interest to compare specific results obtained by the general program of this paper and the inextensional theory. The comparison is made here with the results given by Johnson and Reissner,[12] by Lin and Lee[13] for paraboloidal shells of revolution, and by Saunders and Paslay[14] for a sphere–cone combination. Since in the inextensional theory complete boundary conditions are not prescribed, we compare here the results of Refs. 12–14 with those of this paper where the respective shells are assumed to be closed at one end while the other edge is free.

C. Paraboloidal Shell of Revolution

We consider a paraboloidal shell whose properties are given by

$$R_\phi=2p/\cos^3\phi;\quad r=2p\tan\phi, \tag{30}$$

where p denotes the focal distance. Let $L=2p$. The natural frequencies for various ratios of $h/2p$ and two values of the limiting angle ϕ_0 are calculated for $n=2$ and $\nu=0.3$ by the general program and shown in Fig. 5.

In Ref. 12, a formula for the frequency of a shallow first-degree paraboloidal shell is found in the form

$$\Omega_n=\omega_n 2p/c=(h/2p)n[(n^2-1)/3(1+\nu)]^{\frac{1}{2}}/\sin^2\phi_0, \tag{31}$$

where ϕ_0 should be sufficiently small so that the condition of shallowness is satisfied. The corresponding relation for $\phi_0=30°$ and $n=2$ given in Ref. 13 is

$$\Omega_2=[4\Delta/3(1-\nu^2)]^{\frac{1}{2}}h/2p, \tag{32}$$

where $\Delta=18$. The natural frequencies given by these two formulas are also included in Fig. 5.

D. Sphere–Cone Shell Combination

An interesting application of the general program of this paper can be made to the free-vibration problem of a sphere–cone shell combination considered by means of the inextensional theory in Ref. 14. The properties of the spherical part are given by $h=h_1\cos\phi$, $R_\phi=R$, $r=R\sin\phi$, while those of the conical part are $h=h_2$, $R_\phi=\infty$, $\phi=75.5°$, $r=b\cos\phi$, where the distance b is measured from the projected apex of the conical shell.

It should be noted that at the shell joint (at $\phi=75.5°$ of the spherical shell) the thickness h and R_ϕ are discontinuous. It can be seen from Eq. (1), together with the coefficients $A(x)$, that if the fundamental variables on an edge $\phi=$ const are continuous, then their derivatives may not be continuous at points where the shell has discontinuities in its properties. For example, the first equation of Eq. (1) reads $dw_n/ds=-\beta_{\phi n}+u_{\phi n}/R_\phi$. Obviously, if the rotation of the normal $\beta_{\phi n}$ and the tangential displacement $u_{\phi n}$ are continuous but R_ϕ is discontinuous, then the derivative of w_n cannot be continuous. This conclusion in no way contradicts physical reasoning, and it follows directly from the mathematical formulation of the theory of shells.

[11] A. Kalnins, Proc. U. S. Natl. Congr. Appl. Mech., 4th, pp. 225–233 (1963).
[12] M. W. Johnson and E. Reissner, J. Math. Phys. **34**, 335–346 (1955).
[13] Y. K. Lin and F. A. Lee, J. Appl. Mech. **27**, 743–744 (1960).
[14] H. Saunders and P. R. Paslay, J. Acoust. Soc. Am. **31**, 579–583 (1959).

For the particular sphere–cone combination considered in Ref. 14, we let $h_1=0.5$ in., $h_2=0.045$ in., $\nu=0.3$, $R=4.46$ in., and calculate the lowest natural frequency for $n=3$. The result obtained from the general program of this paper is $\Omega_1=\omega_1 R/c=0.0381$. The corresponding value, given in Ref. 14 and obtained by means of the inextensional theory, is $\Omega_1=0.042$. The discrepancy in the predicted frequency may be due to the fact that, as pointed out in Ref. 14, in the inextensional theory not all fundamental variables can be made continuous at the shell joint. To illustrate the type of the mode of free vibration, which is possible at this frequency, the mode shapes obtained by the present method are given in Fig. 6. The absence of nodes indicates that this is indeed the inextensional mode.

ACKNOWLEDGMENT

Results reported in this paper were obtained in a course of research supported by the National Science Foundation, grant No. 23922.

Holographic strain analysis

C. H. F. Velzel

Holography has attracted wide general interest because of its ability to create 'three-dimensional images' which are so 'real' that they can be viewed from various directions just like the actual object; holography differs from the stereoscopic viewing of two images, by giving a true parallax. Holography is based on the fact that a light wave scattered by an object can be completely recorded in a hologram (e.g. on a photographic plate) and exactly re-created later. As a result, it is possible to allow a light wave to interfere with a second light wave that is produced at some other time. This leads to one of the most important applications of holography, the interferometric measurement of small displacements or strains. Measurement of displacements in the direction of the observer is the most obvious application. Displacements perpendicular to this direction can, however, also be measured. One method of doing this has been devised by the author. Both types of measurement are discussed here, preceded by an introduction to holography and followed by some examples.

When a smooth surface is covered by a thin transparent film not quite uniform in thickness, a pattern of interference fringes can be seen if the surface is illuminated by monochromatic light. The variations in thickness of the film can be read off directly from the pattern. The fringe pattern is produced by the interference of light rays reflected at the object-film interface and at the outer surface of the film.

An object that has been given a small deformation (e.g. as a result of heating or mechanical stress) is in a certain sense analogous to an object coated with a film, as discussed above. Here again we have two surfaces close together but now separated in time. There is now, however, no question of interference; the light rays reflected from the deformed and the undeformed surface are not simultaneously present.

To measure deformations by means of conventional interferometry, the incident light is split into two coherent beams. One is reflected by the deformed object whilst the other is reflected by a replica of the undeformed object or other optical reference surface (e.g. a flat); interference takes place when the two beams are brought together again. Both the reference surface and its positioning must be exact to within a fraction of a wavelength. This method is practicable only when the deformed object has a smooth surface.

Holography presents an elegant solution to this problem. In holography a light beam can be 'stored' in a hologram and regenerated later. In this way interference is possible between non-simultaneous light beams, so that deformations of an object can be measured in the same way as film thickness. The hologram provides in effect an exact and easily positioned replica of the surface. A strain measurement can now be made as follows. A hologram of a beam scattered by the undeformed object is made first; the wave field reconstructed from this hologram is then allowed to interfere with the beam scattered by the deformed object.

This article is concerned with the relationship between the deformation of an object and the resulting interference pattern. Particular attention will be given to the conditions that must be fulfilled to obtain high-contrast interference fringes and to the derivation of the deformation from the fringe pattern. Finally, a number of practical applications will be described.

Since it is an essential feature of the method a short explanation of holography will be given first.

Dr C. H. F. Velzel is with Philips Research Laboratories, Eindhoven.

Holography

When light waves forming a stationary wave field fall on a photographic plate, the *intensity* distribution of the field is recorded as a blackening of the photographic plate. In holography both the local *amplitudes* and *phases* of the wave field are recorded on the plate by allowing a coherent *reference wave* to fall on the plate as well as the original light. The resultant pattern of blackening on the plate, the hologram, can be used at any later time to produce a wave field having exactly the same amplitudes and phases in the plane of the hologram as the original field. In accordance with

Huygens's principle the original field in the space behind the hologram has then also been exactly reconstructed.

Fig. 1 illustrates schematically how holography works. To make the hologram, coherent light from a laser L is split into two beams, a reference beam A and a beam incident on the object V. Part of the light scattered from the object, the 'object beam' B is allowed to interfere with A. The resulting interferogram is recorded on a photographic plate and this is the hologram H. It is assumed for simplicity that A is a plane wave. If B were also a perfectly plane beam, H would consist of exactly parallel interference fringes. Because B is not a plane wave the blackening of H is modulated in a manner which depends on the local amplitudes and phases of B (see *fig. 2*).

To reconstruct the original field (fig. 1*b*), the hologram is illuminated with the same reference beam A. Diffracted beams appear behind H, one of zero order (G_1) and two of the first order (G_2, G_3). Because the interference pattern on H is not spatially exactly periodic, these beams exhibit local variations in amplitude and phase. In particular — and this will appear presently — the variations in G_2 are exactly the same as those in B so that G_2 is a *faithful copy* of B. The observer O in fig. 1*b* thus 'sees' the object V once more; a virtual image V' is formed of V. The beam G_3 forms a real but reversed and distorted image V'' of V.

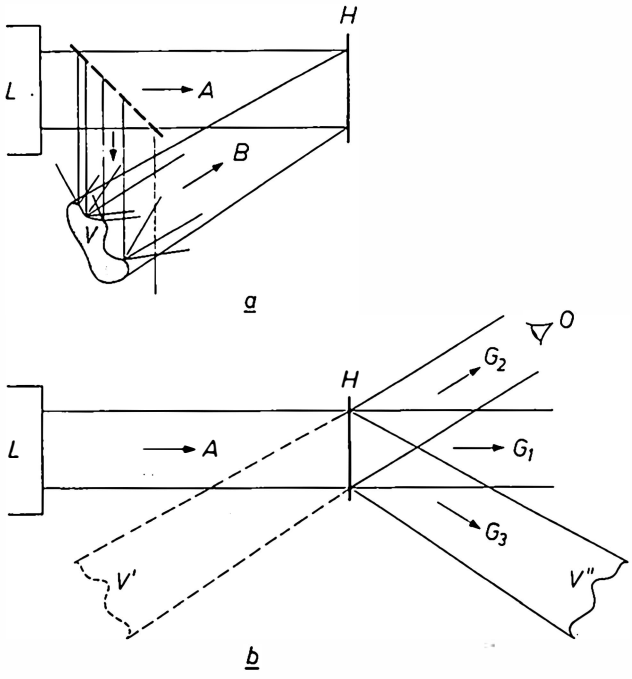

Fig. 1. Holographic recording (*a*) and reconstruction (*b*) of a light beam scattered by an object. L laser. To make the hologram, the laser beam A is divided into two beams by means of a beam splitter. The hologram is recorded on a photographic plate (H); it is the interferogram arising from the interference between the unmodified laser beam (the reference beam A) and the beam B scattered by the object V. If the same laser beam is allowed to fall on the hologram after development of the plate, then one of the diffracted beams (G_2) is identical to the object beam B, and an observer O sees a virtual image V' of the object V. The diffracted beam G_3 forms a real image V'' which is reversed and usually distorted. The 'efficiency' of the reconstruction (power of G_2 divided by that of A) is often very small because light is absorbed by H and also because most of the transmitted light resides in the zero-order beam G_1.

To obtain the above results the apparatus must strictly fulfil certain conditions. Firstly, the coherence of the light must be sufficient for a hologram to be formed. To achieve sufficient coherence the optical path between light source and hologram via the reference beam is made as nearly equal as possible to that via the object beam — in fact more mirrors than shown in fig. 1*a* are used — and a laser is used as the light source. In addition the apparatus must be rigid and unaffected by vibration: while the plate is being exposed to form the hologram, the interference fringes must remain stationary, i.e. all relative movements must be limited to less than a quarter of the wavelength of the light used. Finally, the photographic plate must have a high resolution: the spacing between the interference fringes is usually not much greater than a wavelength and it is necessary to record variations of detail in this fine pattern.

It is not essential for the reference beam to be a plane wave, nor is it essential for the beam to be normally incident on the hologram. However, it *is* essential that the reference beam used in reconstruction is exactly the same as the beam used to form the hologram and of the same orientation with respect to the hologram.

Holography was invented by D. Gabor [1] in 1947, long before the existence of lasers. In Gabor's first holographic experiments the object was small and transparent and situated on the axis between the source and the hologram. The light passing round the object formed the reference wave. The difference in optical path length between rays in the reference wave and those scattered by the object were then so small that the coherence of the 'non-coherent' sources which Gabor had perforce to use was sufficient to produce a hologram carrying interference fringes. This geometry, which corresponds to an angle of zero between the beams A and B in fig. 1, had the disadvantage that the virtual image could not be observed without unwanted effects due to the light from G_1 and G_3. Holography grew to fruition only after the advent of the laser. The laser is a source of coherent light, i.e. the light emitted has a long coherence length so that interference can be obtained even when the optical paths differ considerably in length. Holographic images of opaque and large objects can therefore be made. In addition, the reconstructed wave can easily be kept separate from the other beams emerging behind the hologram [2].

Relation between object beam, hologram and reconstructed beam

By making use of Huygens's principle, from which the structure of the object-beam field B in fig. 1 is determined by its amplitudes and phases in the plane of the hologram H, it will now be shown that H does indeed

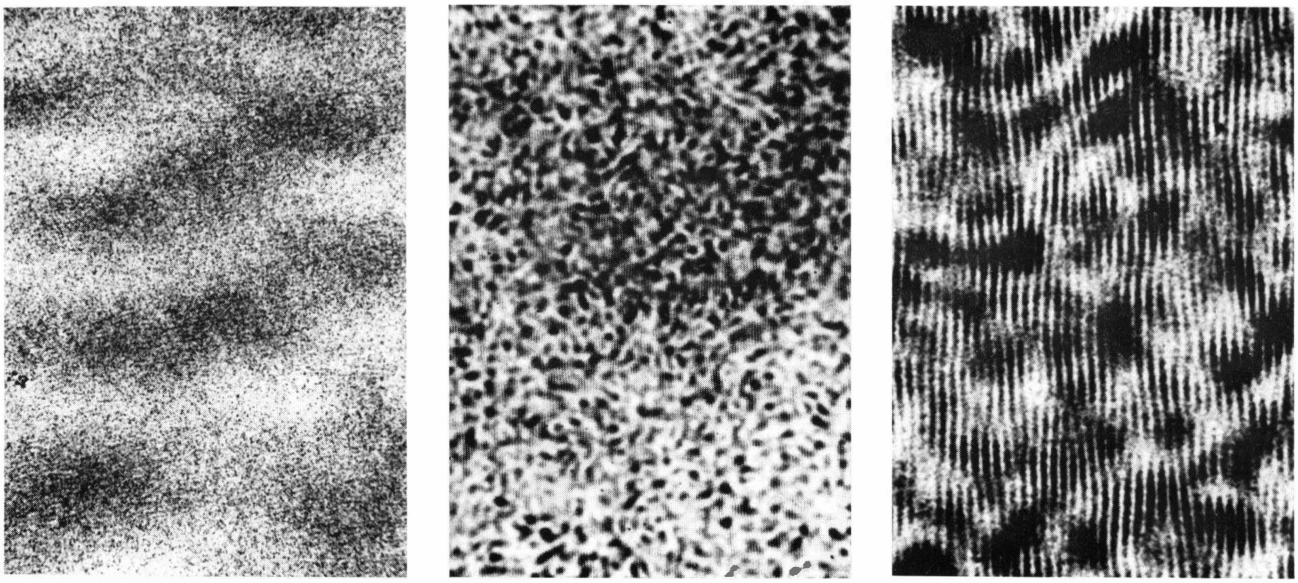

Fig. 2. Three enlargements of a part of a hologram. Magnifications (left to right): about 40×, 180× and 700×. As the right-hand photograph shows, the blackening forms a sinusoidal grating modulated in phase and amplitude; the spacing of the fringes, which can also be faintly distinguished in the central photograph, is 2 μm. The essential information is registered primarily in the phase modulation (the curvature of the fringes). The speckle pattern, which can also be seen in the following photographs, is not characteristic of the object, nor of the hologram. but of the use of light of high coherence. It is a kind of random distribution of diffraction discs. The discs increase in size as the angle subtended by the source at a point in the hologram decreases.

contain the necessary information concerning B and that G_2 is a faithful copy of B. We take a coordinate system x,y,z in which $z = 0$ is the plane of the hologram. We assume that the reference beam A is a plane wave propagating along the z-axis. This wave is described as a function of time and place by:

$$u_A = a \exp j(\omega t - kz), \qquad (1)$$

where u_A is the local instantaneous complex amplitude, ω is the angular frequency of the wave and k its wave number, i.e. 2π divided by the wavelength λ. The phase ϕ_a of the wave for $t = 0$, $z = 0$ and the peak amplitude a_0 are combined in the 'complex amplitude' a:

$$a = a_0 \exp -j\phi_a. \qquad (2)$$

Suppose that the object beam B propagates in the x,z-plane at an angle β to the z-axis. If this was a plane wave, we could express it as:

$$u_B = b_0 \exp j(\omega t - kx \sin\beta - kz \cos\beta - \phi_b), \qquad (3)$$

a wave whose wave vector has components $k \sin\beta$ in the x-direction and $k \cos\beta$ in the z-direction. The complex amplitude b of this wave in the plane $z = 0$ is a function of x:

$$b = b_0 \exp -j(kx \sin\beta + \phi_b).$$

When B is not exactly a plane wave, but very nearly — as will be the case if the angle subtended by the object at the hologram is not too large — it can still be represented by (3) although b_0 and ϕ_b are now weakly dependent on x, y and z (the derivatives of b_0 and ϕ_b with respect to x, y and z must be small compared with $k \sin\beta$). According to our assumptions, the detailed structure of the wave field B is entirely determined by the angle β and the functions $b_0(x,y)$ and $\phi_b(x,y)$ in the plane of the hologram $z = 0$.

While the plate is being exposed to form the hologram the total complex amplitude at every point x,y of the hologram is equal to $a + b$. The intensity is therefore given by:

$$I(x,y) = |a + b|^2 = a_0^2 + b_0^2 + a^*b + ab^*. \qquad (4)$$

If the photographic plate is exposed for a time t and developed, we get a hologram of transmittance $\tau(x,y)$ which is assumed here to be a linear function of I. In practice this can only be approximately true. *Fig. 3* shows qualitatively how τ in general depends on the exposure $H (= It)$. Only in a limited region near the point of inflexion H_0,τ_0 is the curve approximately straight. To keep within this region as far as possible the average intensity b_0^2 of the object wave is made much smaller than the intensity a_0^2 of the reference wave and $a_0^2 t$ is made approximately equal to H_0. In this linear approximation we have:

$$\tau = \tau_0 - \tau_1 b_0^2 - \tau_1(a^*b + ab^*) \qquad (5a)$$

$$= \tau_0 - \tau_1 b_0^2 - 2\tau_1 a_0 b_0 \cos\{kx \sin\beta + \phi_b - \phi_a\}. \qquad (5b)$$

[1] D. Gabor, Nature **161**, 777, 1948, and Proc. Roy. Soc. A **197**, 454, 1949.

[2] E. N. Leith and J. Upatnieks, J. Opt. Soc. Amer.: **52**, 1123, 1962; **53**, 1377, 1963; **54**, 1295, 1964.

If the small term $\tau_1 b_0^2$ is neglected, this shows that the variations in the phase $\phi_b(x,y)$ and the amplitude $b_0(x,y)$ of the object wave are contained in the hologram in the form of variations in the phase and amplitude of the modulation of the transmittance.

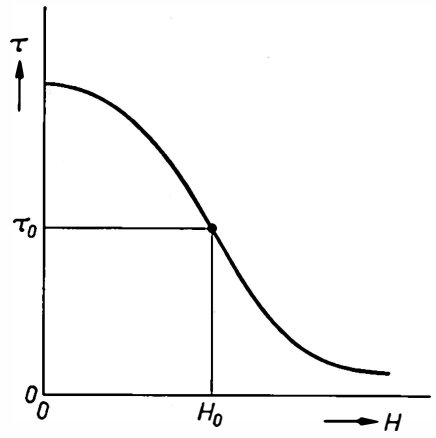

Fig. 3. Transmittance τ of a photographic plate as a function of the exposure H. The exposure is the product of the intensity of the light and its duration. It is preferable to work only on the linear part of the curve, near the point of inflexion (H_0,τ_0).

In the reconstruction of the original wave field, the hologram is illuminated by the reference beam A. Behind the hologram we then get a wave of complex amplitude τa. Using (5a) we find:

$$\tau a = (\tau_0 - \tau_1 b_0^2)a - \tau_1 a_0^2 b - \tau_1 a^2 b^*. \qquad (6)$$

The wave behind the hologram is thus a superposition of three waves with the complex amplitudes

$$g_1 = (\tau_0 - \tau_1 b_0^2)a,$$
$$g_2 = -\tau_1 a_0^2 b,$$
$$g_3 = -\tau_1 a^2 b^*.$$

These are the three waves of fig. 1*b*. The wave G_1 of complex amplitude g_1 has the same phase as the reference beam A in the plane of the hologram and is therefore propagated in the same direction (the z-direction). The factor $(\tau_0 - \tau_1 b_0^2)$ implies that G_1 exhibits small variations in amplitude in the plane of the hologram so that the beam behind the hologram diverges somewhat.

The wave G_2 of complex amplitude g_2 is identical, apart from the constant factor $-\tau_1 a_0^2$, to the object beam B. This is the result we sought.

Finally there is the wave G_3 of complex amplitude g_3. The argument of g_3 is $kx \sin\beta + \phi_b - 2\phi_a$. The wave G_3 is thus propagated in the x,z-plane at an angle $-\beta$ to the z-axis. More generally — even if A and G_1 are not propagated along the z-axis — G_3 and G_2 are symmetrical with respect to G_1. Thus if β is made large enough to separate G_2 from G_1, then G_2 is certainly separated from G_3.

The treatment given above refers to an *absorption hologram*: the transmittance (5) is real and the wave field behind the hologram differs only in amplitude and not in phase from the wave field incident on the hologram. In general, however, the transmittance is a complex quantity, so that the hologram changes the wave in both amplitude and phase. If the phase only is changed, we have a *phase hologram*. A phase hologram can be made by 'bleaching' away the blackening of a holographic pattern by rehalogenization [3]. The blackening vanishes but the places that were black remain slightly thicker; at these places the reference wave undergoes a larger phase change than in the non-thickened surroundings. A phase hologram has the advantage, often important in practice, that it transmits more power.

Three points will now be briefly discussed: the nature of the image formed by G_3, the nonlinearity of the transmittance characteristic and the efficiency of the hologram.

When we omit the constant factor $-\tau_1 a^2$, the complex amplitude of the wave G_3 is b^*. For brevity we write $kx \sin\beta + \phi_b$ as ψ, a function of x, y and z. We now restrict ourselves to the plane of the hologram and its close neighbourhood. Because ψ does not vary rapidly with z we can put ψ equal to its value $\psi(x,y)$ in the plane of the hologram. Again omitting the constant factor $-\tau_1 a^2$, the waves G_2 (or B) and G_3 are expressed respectively by:

$$b_0 \exp j(\omega t - kz \cos\beta - \psi),$$
$$b_0 \exp j(\omega t - kz \cos\beta + \psi).$$

The wavefronts — surfaces of constant phase — are thus given by the equations

$$kz \cos\beta = -\psi(x,y) + C \quad \text{for } G_2 \text{ and } B,$$
$$kz \cos\beta = +\psi(x,y) + C' \quad \text{for } G_3.$$

It follows that the wavefronts of G_3 are the mirror images of those of G_2 with respect to the plane $z = 0$ (*fig. 4*); the amplitudes at corresponding points are equal. Taking into account also the direction of propagation of the light rays, it can be seen from fig. 4 that rays in G_2 which diverge from (for example) the virtual image point P' correspond to rays in G_3 which converge towards the symmetry point P''. The virtual image V' thus corresponds to the real image V''. The latter is reversed: if the point Q' lies *in front* of P' for the observer O, then the corresponding point Q'' lies *behind* the point P'' for the observer O'. An essential assump-

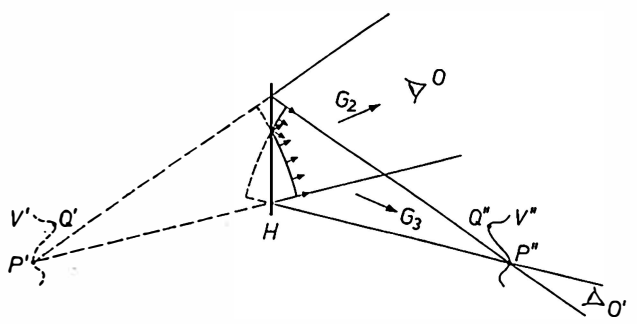

Fig. 4. Close to the hologram, the wavefronts in the beams B (or G_2) and G_3 of fig. 1 are mirror images of each other with respect to the plane of the hologram. Rays in G_2 diverging from the points P' and Q' correspond to rays in G_3 which converge to the corresponding points P'' and Q''; the virtual image V' thus corresponds to the real image V''.

tion in the foregoing is that the factor $-\tau_1 a^2$ is constant. This is the case only if the reference beam A is propagated along the z-axis. If A falls obliquely on the hologram, the image formed by G_3 is distorted.

Taking into account the nonlinearity of the transmittance, i.e. the terms of higher order in the expansion of τ in powers of H_0 (see fig. 3), then τ is not given by the expression of eq. (5b), but by a polynomial with terms of the form

$$b_0{}^{m+2n} \cos m(kx \sin \beta + \phi_b - \phi_a),$$

where m and n are integers. On reconstruction, the main term ($m = 1$, $n = 0$) discussed earlier gives the beams G_2 and G_3 in which G_2 reproduces B exactly. When the term with $m = 1, n = 1$ does not vanish, the reproduction is no longer perfect: the image has less contrast. The terms with $m > 1$ lead to diffracted beams of higher order which waste light. In order to limit these undesirable effects, b_0 must be made much smaller than a_0, as mentioned earlier.

Finally, the 'efficiency' of a hologram, which is in practice of great importance. This is the ratio of the power of the reconstructed wave G_2 to that of the reference wave during reconstruction. The transmittance of the absorption hologram of a *plane* 'object wave', registered on a photographic plate with a linear characteristic, is (see eq. 5b):

$$\tau = \tau_0 + \tau' \cos (k'x + \phi),$$

where τ_0, τ', k' and ϕ are constants. Since τ has everywhere a value between 0 and 1, the modulation depth τ' cannot exceed $\frac{1}{2}$. In this notation the amplitude of the reconstructed wave is $\frac{1}{2}\tau' a_0$; the efficiency is here, therefore, $\frac{1}{2}\tau'^2$ and this is at most equal to 1/16 or about 6%. In practice the hologram is not uniformly exposed and, as discussed earlier, τ' is preferably taken much smaller than $\frac{1}{2}$; the efficiency is therefore generally much smaller, usually less than 2%. A phase hologram transmits more energy and may have an efficiency of 10 to 15%. So far it has been tacitly assumed that the emulsion coating of the photographic plate that carries the hologram is very thin. In holograms which are thick compared with the wavelength, the efficiency can exceed 50% as a result of multiple reflections. Holograms with a thickness of several hundred microns have been made both in photographic emulsions and in crystalline materials such as $LiNbO_3$ and KBr [4].

Strain measurement by holography

There are two ways in which the 'interference of non-simultaneous beams of light' can be brought about in practice. In one method a hologram is made before the object is deformed. After development the plate is accurately replaced in its original position in the otherwise unchanged arrangement. The object is then deformed and viewed through the hologram. The viewer now sees both the reconstructed image of the undeformed object and the object itself in its deformed state, illuminated by the source. With this method the interference fringes and hence the deformation of the surface can be viewed as they occur. This is called the method of *time-dependent interference* [5]. In the other method two holograms are recorded on one photographic plate: one of the object wave before deformation and one after deformation. Since the only term relevant to the analysis of the holographic process is linear in the complex amplitude of the object wave (see eqs. 5 and 6), holograms can indeed be superposed and the reconstruction gives a superposition of the two object waves. The resulting interference pattern contains the required information. In this article the discussion will be limited to this *double-exposure* method [6].

If we are concerned with two essentially stationary states of an object such as a bar whose deformation is to be measured, there is no limitation to the choice of exposure time. The plate is exposed before the object is deformed and again afterwards. In other cases, however, e.g. in the analysis of fracture, the situations of interest are not stationary. The exposure then has to be so short that the deformation occurring during the exposure is small compared with the wavelength of the light. This condition can often be met by using a pulsed laser [7]. When the deformation is not only fast but also periodic, as in a vibrating loudspeaker, a stroboscopic illumination can be used [8]. Finally, information about vibrating objects can be obtained from a hologram recorded with an exposure much longer than the period of vibration — time-averaged holograms [9].

The most important problem in holographic strain analysis is the interpretation of the interference pattern and we shall concern ourselves mainly with this problem. From what has been said above it will be clear that the holographic process itself can be disregarded here, and the object can be considered to be simultaneously present in its two states, deformed and undeformed.

It is assumed that the microstructure of the surface of the object does not change during the deformation. The same point then scatters the light in the same way before and after the deformation — the only difference is that due to the actual deformation. It is also assumed that the object scatters the light *diffusely*, i.e. that the scattered light has lost most of its spatial coherence. Interference then occurs only between rays coming from the same point in the two situations; other interferences do not contribute effectively to the interference pattern.

[3] R. J. Collier, C. B. Burckhardt and L. H. Lin, Optical holography, Academic Press, New York 1971, p. 289.
[4] G. Kalman, in: Applications of lasers to photography and information handling (ed. R. D. Murray), Soc. Phot. Sci. and Engrs., 1968, p. 99.
[5] K. A. Stetson and R. L. Powell, J. Opt. Soc. Amer. 55, 1694, 1965.
[6] R. J. Collier, E. T. Doherty and K. S. Pennington, Appl. Phys. Lett. 7, 223, 1965.
[7] R. E. Brooks, L. O. Heflinger, R. F. Wuerker and R. A. Briones, Appl. Phys. Lett. 7, 92, 1965.
[8] P. Shajenko and C. D. Johnson, Appl. Phys. Lett. 13, 44, 1968.
[9] R. L. Powell and K. A. Stetson, J. Opt. Soc. Amer. 55, 1593, 1965.

Determination of the longitudinal component of the displacement vector

For an opaque object the light source and the observer must be situated on the same side of the object. In this configuration the change in optical path from source to observer via the object has its origin in the displacement component in the mean direction between source and observer. The information in the interference pattern thus concerns this 'longitudinal component'.

Fig. 5 shows how the difference in optical path depends on the displacement. If, as in fig. 5*a*, the source S and the observer O both have the same direction when viewed from an object point P and if P is also displaced in this same direction (to Q), the optical path difference $\Delta l = SPO - SQO$ is equal to twice the length of the displacement vector PQ. If PS and PO are at an angle χ to each other (fig. 5*b*) and the displacement vector $e = PQ$ lies along the bisector of the angle SPO, the path difference is modified by a factor $\cos \frac{1}{2}\chi$:

$$\Delta l = 2e \cos \tfrac{1}{2}\chi. \qquad (7)$$

Fig. 5*c*, finally, shows a displacement vector of arbitrary direction, obtained by locating Q at some arbitrary point in the plane perpendicular to the bisector (fig. 5*b*). The optical path SQO does not change since SQ becomes just as much shorter as QO becomes longer. Equation (7) therefore remains valid if we replace e by its component e_l along the bisector (the longitudinal component):

$$\Delta l = 2e_l \cos \tfrac{1}{2}\chi. \qquad (8)$$

In fig. 5 it is assumed that we have a point light source and a point observer and that they are both situated at infinity, i.e. that e is very much smaller than PS and PO.

The observer looking towards P sees light or darkness according to whether Δl is an even or odd multiple of $\lambda/2$. He thus sees light and dark fringes of equal longitudinal displacement; the interference pattern is a 'contour map' of the deformation. Examples of such patterns are shown in *figs. 6* and *7*. In a bright fringe of the pth order ($\Delta l = p\lambda$), we have

$$e_l = p\lambda / 2\cos \tfrac{1}{2}\chi. \qquad (9)$$

If χ is not too large, $\cos \frac{1}{2}\chi$ is approximately unity; the difference in height of the surface between adjacent fringes is then approximately half a wavelength.

The fact that the observing instrument (the eye, a camera, etc.) has a pupil of finite and not zero diameter gives a certain practical limitation to this method. If the opening is so large that the optical path differences Δl for different parts of the pupil differ by more than

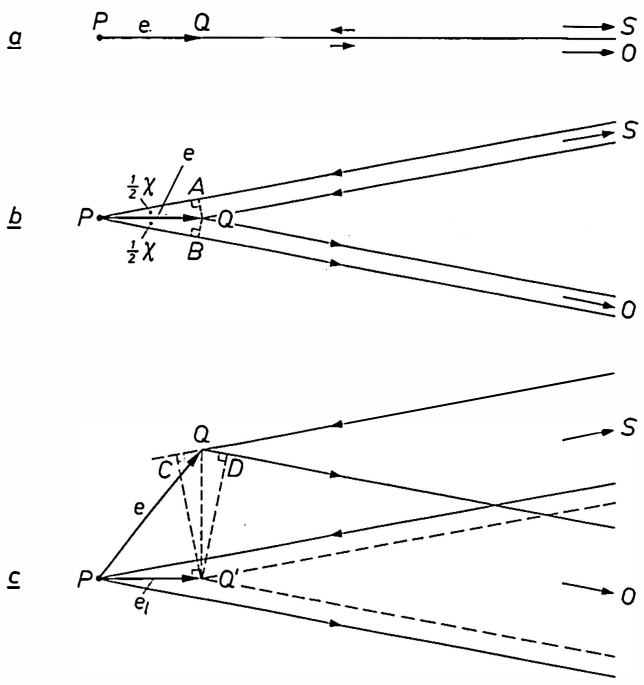

Fig. 5. Calculation of the change Δl in the optical path length between source S and observer O via a point in the surface of the object when this point is displaced from P to Q.
a) PS, PO and the displacement vector $e = PQ$ have the same direction; in this case, $\Delta l = 2e$.
b) PS and PO are inclined at an angle χ to each other and the displacement vector e is directed along the bisector of χ. In this case, $\Delta l = PA + PB = 2e \cos \frac{1}{2}\chi$.
c) When Q is displaced in the plane SPO perpendicular to the bisector PQ' of the angle SPO, the optical path length SQO does not change. The difference QC between SQ' and SQ is equal to the difference QD between QO and QO', so that SQO remains equal to $SQ'O$. This is still true if Q is displaced perpendicular to the plane SPO; SQ and QO do not then change at all. The difference Δl in optical path length therefore has the same value as in (*b*) except that e must be replaced by $e_l = PQ'$, the longitudinal component of e.

a half-wavelength, the interference fringes fade. From *fig. 8* it can be seen that this is not the case provided the angle α subtended by the pupil at the object is less than $\lambda/2e_t$ where e_t is the component of the displacement perpendicular to PO. A more detailed calculation [10] shows that if this condition is fulfilled, the interference fringes have a contrast of more than 70%. Conversely, for a given aperture, the lateral displacement may not exceed the value $\lambda/2\alpha$. Suppose, for example, a helium-neon laser is used in a conventional arrangement and the interference pattern is observed with the naked eye; λ is then 0.6 μm and α is of the order of 0.01. The maximum permissible lateral displacement is then about 30 μm.

The maximum permissible value of the lateral displacement, $\lambda/2\alpha$, is simply the resolving power of the observing instrument. The foregoing is another way of saying that two points separated by a distance of more than $\lambda/2\alpha$ are separately imaged and that the rays coming from them no longer interfere with each other.

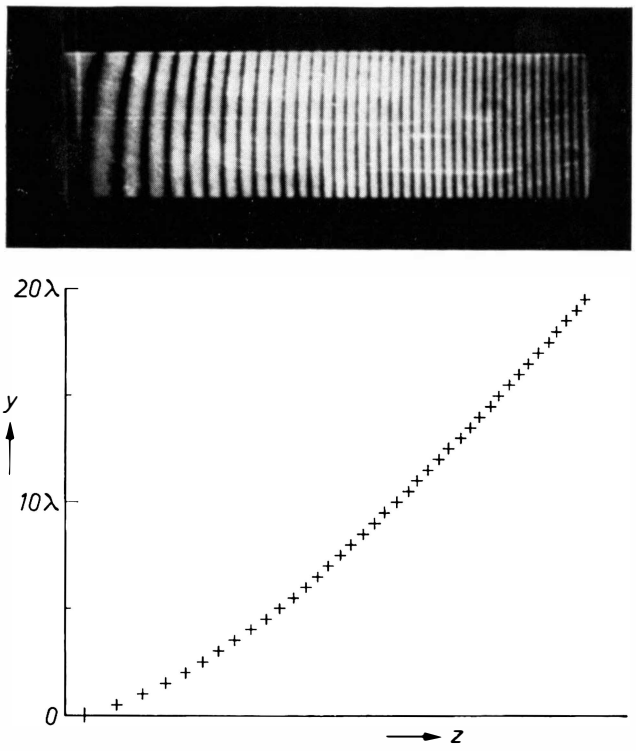

Fig. 6. *Above:* Example of an interference pattern on the image of a bar deformed under load (obtained from a double hologram). *Below:* Displacement y as a function of position z along the bar, derived from the interference pattern. Each fringe represents an increment of the displacement of $\lambda/2$.

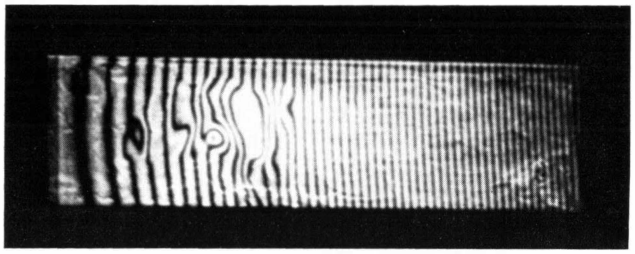

Fig. 7. Interference pattern on the double-hologram image of a bar with a weak spot. The bar is made up of two parts held together by adhesive, the plane of the joint lying in the plane of the paper. The irregularity in the interference fringes indicates a weak spot in the joint.

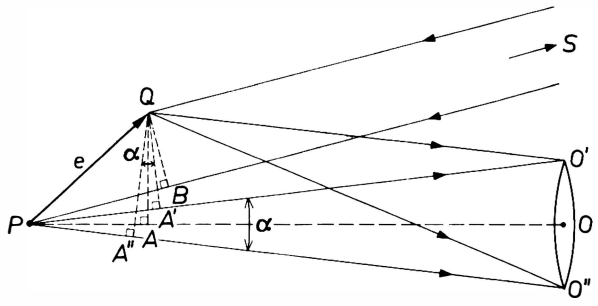

Fig. 8. Relation between the size of the pupil of the observer and the maximum permissible lateral displacement. The observed interference pattern tends to vanish if the pupil becomes so large that the differences in optical path lengths $SPO' - SQO'$ and $SPO'' - SQO''$ differ by more than $\lambda/2$. This difference is equal to $(PA' + PB) - (PA'' + PB) = PA' - PA'' = \alpha e_t$, where $e_t = QA$ is the lateral component of e and α is the angle subtended at P by the pupil. For a high-contrast interference pattern, α must therefore be less than $\lambda/2e_t$.

Determination of the transverse components of the displacement vector

In the method discussed above only the longitudinal component of the displacement vector is measured. In principle the complete displacement vector can be derived in this way by viewing the object from three directions or by making three exposures with different directions of the illuminating beam [11]. These procedures do, however, involve rather a lot of work with regard to both the experimental arrangement and the interpretation of the interferogram.

We have developed a method whereby the transverse components of the displacement can be measured directly. We look at the hologram from a point in a *real* holographic image. The required real image could be made by placing a positive lens in the beam G_2 in fig. 1*b*, but we wish to suggest here, with the help of *fig. 9*, a still simpler method. The hologram is recorded in the conventional way, using a *plane* wave as the reference beam (fig. 9*a*). In the convential method of reconstruction (fig. 9*b*) a good virtual image V' and a distorted real image V'' would be obtained. Now however the wave field is reconstructed with a reference beam A' identical to A as regards wavefronts but propagated in the *opposite* direction. In other words, the back of the hologram is illuminated with a plane wave from the opposite direction (fig. 9*c*). A wave G_2' is then generated at the front of the hologram, and this wave is in all respects a faithful copy of B except that it also propagates in the opposite direction. This can be easily checked from the mathematical description of holographic principles given on page 55/56; it is only necessary to replace ω by $-\omega$ in the description of the reconstruction. All waves are then propagated 'backwards', but otherwise the situation is unchanged. In this way a faithful, undistorted real image V_r of the object V is obtained. In fig. 9*d*, finally, it is shown schematically how this can best be done in practice; in the configuration of fig. 9*b* with a fixed reference beam and the conventional viewing direction, the hologram is simply rotated through 180° about an axis perpendicular to the paper. The situation so obtained is that of fig. 9*c*, assuming that A is indeed a plane wave.

A diaphragm is now placed with its centre at a point P in the real image and the hologram is viewed through it with the naked eye or a camera focused on infinity. Each point on the retina or on the photographic plate now corresponds to a viewing direction. If the hologram is a double hologram of a deformed object an interference pattern is again seen. In *fig. 10*, PQ is the displacement vector of a point in the real image. Since

[10] C. H. F. Velzel, J. Opt. Soc. Amer. **60**, 419, 1970.
[11] J. W. C. Gates, Optics Technol. **1**, 247, 1969.

G_2' is a faithful copy of B, apart from its direction of propagation, there is a fixed relation between the phases of the light at P and at Q which depends only on the positions of P and Q with respect to the light source. The interference pattern owes its existence to the fact that the optical path length $PQ' = e \cos \gamma$ in fig. 10 varies with the viewing direction PR. To put it more precisely: in the direction of a point R on the hologram the field appears light or dark according to whether

$$\Delta l = \Delta l_0 + e \cos \gamma$$

is an even or an odd multiple of $\lambda/2$, where Δl_0 is a constant independent of the viewing direction. Dark or light fringes in the field are lines of constant Δl, and thus also lines of constant γ; they are therefore intersections of the hologram with cones of apex P and axis e. The fringes are thus symmetrical with respect to the projection of e on the hologram. We now let R move along this symmetry axis and define its position by means of γ_0, the angle between PR and PN, the perpendicular to the hologram through P. We then have $\gamma = \varepsilon - \gamma_0$, where ε is the angle between e and PN. Differentiating Δl with respect to γ_0 gives:

$$\mathrm{d}\Delta l/\mathrm{d}\gamma_0 = e \sin (\varepsilon - \gamma_0).$$

For $\gamma_0 = 0$, this is simply equal to the magnitude e_t of the transverse component of e:

$$(\mathrm{d}\Delta l/\mathrm{d}\gamma_0)_{\gamma_0=0} = e \sin \varepsilon = e_t.$$

The optical path difference Δl between adjacent dark or light fringes increases with λ. Therefore the magnitude e_t of the transverse component is given by

$$e_t = \lambda/\Delta\gamma_0, \qquad (11)$$

where $\Delta\gamma_0$ is the angle subtended at P by two adjacent fringes near N. The transverse component is directed towards the centre of curvature of the fringes.

Fig. 11 shows an example of the measurement of a transverse displacement. Fig. 11*a* is the reconstruction via a double hologram of a bar clamped at the top and acted on at its lower end by a force directed to the right. Fig. 11*b* shows some photographs of what a viewer would see on the hologram through a diaphragm of 0.5 mm diameter in the real image. The positions in fig. 11*b* correspond to those in fig. 11*a*.

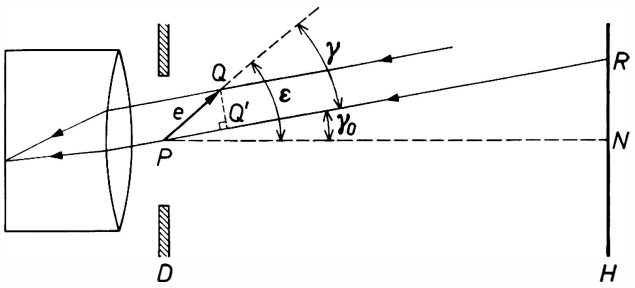

Fig. 10. Calculation of difference in optical path length from the interference pattern seen (fig. 9*c*) on the hologram H via the diaphragm D. P is the initial point and Q the final point of the displacement vector e at a certain location in the real image. An interference pattern is observed on the hologram because the difference PQ' in optical path length depends on the viewing direction PR.

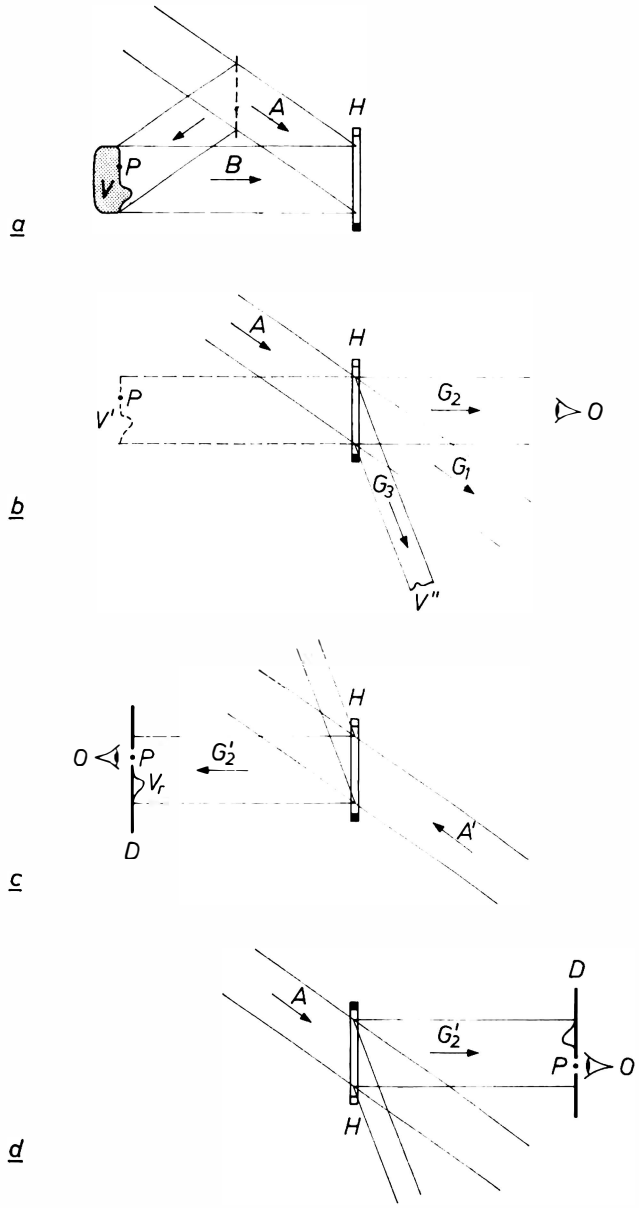

Fig. 9. Determination of the transverse component of the displacement vector. *a*) Recording the hologram. *b*) Usual configuration for reconstruction. *c*) Formation of a real image V_r by reversal of the direction of propagation. The reference beam A' has the same wave fronts as A but is propagated in the opposite direction. If, for example, A were divergent, then A' would have to be convergent. *d*) Practical version of the geometry of (*c*). Starting from the configuration (*b*), the hologram is rotated by exactly 180°; the beam A must be a *plane* wave. The configuration (*d*) is then equivalent to (*c*). The transverse component of the displacement at a point P on the object can then be derived from the interference pattern observed on the hologram through a diaphragm about the point P in the real image.

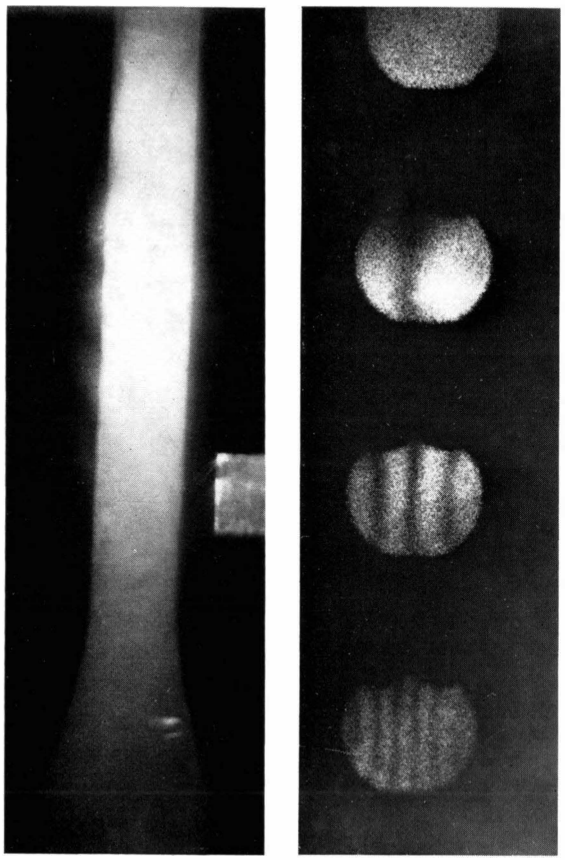

a *b*

Fig. 11. Measurement of the lateral displacement of a bar subjected to a lateral force. *a*) Double-holographic image of the bar. The bar is clamped at the upper end and the force acts from left to right on the lower end. *b*) Interference patterns observed through a diaphragm of 0.5 mm diameter in the real image. The positions of the fields in (*b*) correspond to those in (*a*). The rather coarse speckle pattern in (*b*) is due to the small aperture (see caption to fig. 2).

To obtain a clearly defined interference pattern, a large number of point pairs such as PQ must interfere in the same way. The diaphragm should therefore be much larger than the transverse component of the displacement. For small deformations like those we are concerned with in this article this condition is always fulfilled. On the other hand, if the deformation varies over the object, the diaphragm may not be too large: the variation of the transverse component over the diaphragm must be so small that the optical path difference for a given viewing direction varies less than $\lambda/2$. If this latter criterion requires the diaphragm to be so small that, with an absorption hologram, the interference field is too faint, an improvement may be obtained by using a bleached hologram. A greater improvement can be obtained if, when recording the hologram, only those parts of the object are illuminated where it is desired to measure the displacement vector.

A disadvantage of the method described here is that a photograph must be made of the interference field on the plane of the hologram for each location where the displacement vector is to be determined. This disadvantage can be partly overcome by making the exposures for different locations simultaneously (see fig. 13, lower photograph).

Methods also exist for projecting contours of equal transverse displacement[12]; these will not be discussed here.

Comparison of the two methods

The two methods discussed above — determination of the longitudinal component of the displacement and determination of the transverse component — will now be briefly compared with the aid of fig. 9. In both cases a double hologram is made in the configuration of fig. 9*a*. To determine the longitudinal component e_l, the virtual image is viewed through the hologram in the configuration of fig. 9*b*; from the interference pattern seen, the distribution of e_l over the surface can be derived. The transverse component must be determined point by point; the magnitude (e_t) and direction are obtained from the interference pattern that a viewer sees in the configuration of fig. 9*d* (hologram rotated 180°) when he views the hologram through a diaphragm at the relevant part of the real iamge.

The two procedures have the following characteristic differences. In the first, only the *variations* of e_l over the surface are determined; e_l changes from fringe to fringe by an amount $\lambda/2$ (taking the factor $\cos \frac{1}{2}\chi$ in (9) equal to 1 for simplicity). Only if we know, for example, that e_l must be zero at a certain location, can the absolute values e_l be determined on the rest of the surface. In the other method, however, the actual values e_t are determined.

The conditions under which a high-contrast interference pattern is obtained are of a different nature in the two methods. In the determination of e_l, e_t must be less than $\lambda/2\alpha$. In the determination of e_t, the difference in optical path lengths and hence $2e_l$ must not vary more than $\lambda/4$ over the diaphragm. This means that the diaphragm in fig. 9*d* must be smaller than the fringe spacing on the object in fig. 9*b*.

Finally, the two procedures differ in sensitivity. The smallest detectable variation in e_l is obtained when (fig. 9*b*) only two fringes are visible at the object; the variation is then $\lambda/2$. The smallest detectable value of e_t occurs when (fig. 9*d*) only two fringes are visible on the hologram. This is the case when, in eq. (11), $\Delta\gamma_0$ is equal to the angle α_H subtended by the hologram at the object. The smallest detectable value of e_t is therefore λ/α_H. In general α_H is less than unity, so that e_l can be determined with greater sensitivity than e_t.

[12] K. A. Stetson, Optics Technol. **2**, 80, 1970.
J. N. Butters and J. A. Leendertz, J. Physics E (sci. Instr.) **4**, 277, 1971.

When all these conditions are fulfilled, both the longitudinal and the transverse components — and hence the complete displacement vector — can be determined from one double hologram.

Applications

Some applications of the double-hologram technique of holographic strain analysis will now be given. The examples may be divided into three areas of application: analysis of experimental models as an aid to design, the determination of material constants and fault-finding.

Strain analysis as an aid to design

For objects of complicated shape it is difficult to predict how they will deform under load or local heating. When the deformation can upset the correct functioning of the object, holographic strain analysis can be useful in analysing the deformation and applying appropriate corrections.

A casting (*fig. 12*) used as a mount for the pick-up tubes and the colour-separation prism in a Philips colour television camera was examined for thermoelastic distortion. In such a camera it is critically important that the relative positions of the pick-up tubes and the prism do not change under the conditions in a studio where strong lighting may cause local heating. *Fig. 13* shows some of the results of this investigation. A double hologram was made of the casting. During the first exposure the casting was uniformly at room temperature; during the second exposure the casting was heated underneath to 3 °C above room temperature. Fig. 13 (above) shows a reconstruction of the casting by means of this hologram with interference fringes which show the variations in the longitudinal displacement. In order to determine the lateral displacement, a real image was formed in the manner indicated in fig. 9*d*. A screen with a large number of holes of diameter 0.1 mm was then set up in the plane of this image. All the interference patterns visible through these holes were then simultaneously registered on a single photographic plate behind the screen. Interferograms recorded in this way are shown in fig. 13 (below); they correspond to a part of the upper photograph.

For a complete analysis of the deformation, double holograms of the casting must be made from various directions, but the discussion here will be limited to a few remarks relating to fig. 13, and in particular to the left-hand and right-hand parts of the wall of the cylinder pointed upwards and outwards towards the observer. The lower left-hand part is displaced longitudinally more than the lower right-hand part (in the upper photograph there are more fringes on the lower left half than on the lower right half); the reverse holds for the upper half. The fringes indicate locally the axes about which the surface (apart from a parallel displacement) tilts. On the right the surface tilts about a horizontal axis, on the left it tilts about an oblique axis. This indicates some distortion of the casting. This is also indicated by the lower photograph; the left-hand part of the cylinder wall has undergone a nearly horizontal displacement while in the right-hand part the transverse displacement is in an oblique direction.

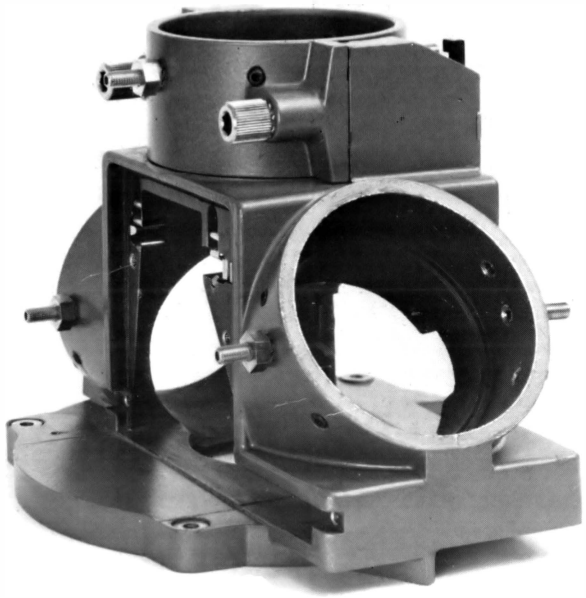

Fig. 12. Mount for pick-up tubes and colour-separation prism in a Philips television camera. The pick-up tubes are clamped in the cylindrical openings directed obliquely forwards, upwards and backwards in the photograph. The casting is shown with its flange on the table. This flange is often subject to local heating from the powerfull lights in the studio.

Determination of material constants

Expansion coefficients and elastic constants of a material can be determined by measuring the deformation taking place as a result of heating or mechanical stress [13]. A simple example of this was given in fig. 6: the determination of the elastic modulus E from the bending of a bar. The bar is clamped at one end (the left in fig. 6) and at the other end subjected to a force F which in fig. 6 is perpendicular to the paper. In fig. 6 (below) the deflection y is plotted as a function of the distance z to the clamping point. No account is taken of the angle χ between the direction of the illu-

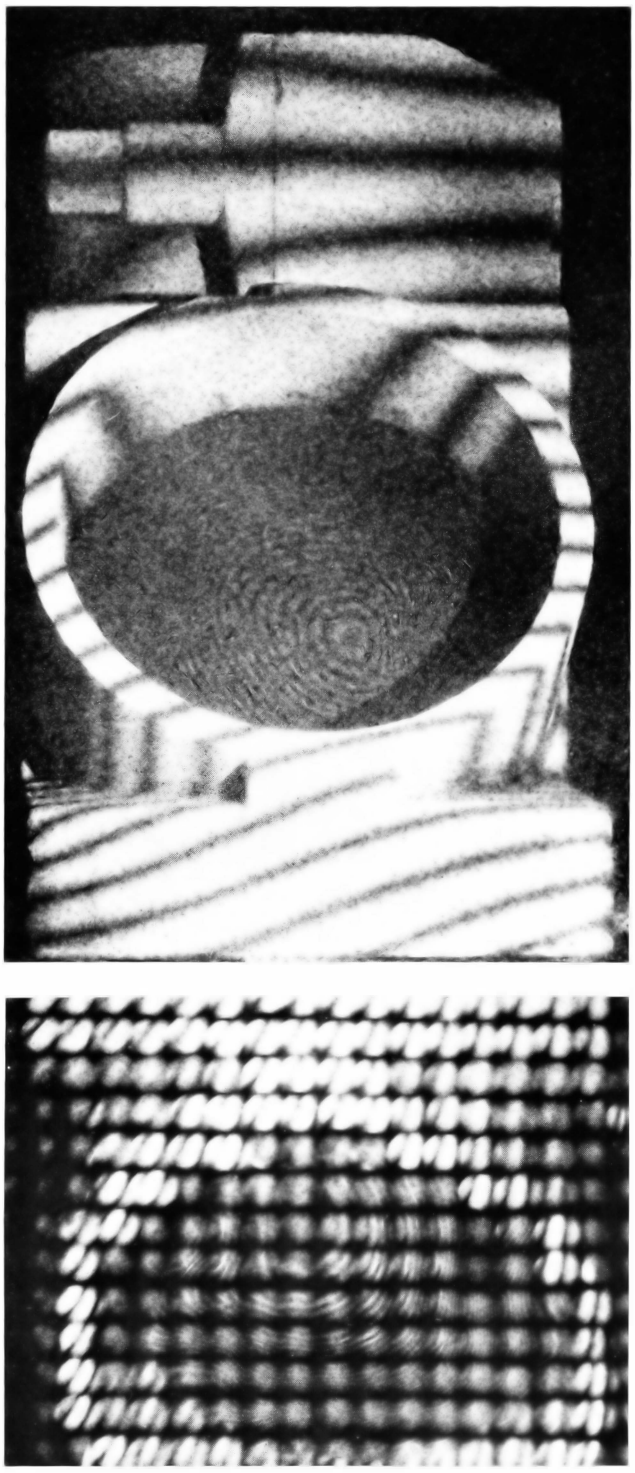

Fig. 13. Strain analysis of the casting shown in fig. 12. After the first exposure of the (double) hologram, the flange (pointing downwards in the photographs) was locally heated three degrees above the ambient; the second exposure was then made. *Above:* determination of the longitudinal strain. *Below:* Determination of the transverse strain. For the lower photograph, the plate was set up close behind a screen with a large number of 0.1-mm holes and situated in the plane of the real image. The interference patterns in the hole of the cylinder have no significance (to prevent undesirable reflections this hole was filled with black paper).

minating beam and the viewing direction, which was about 20°, so that the difference in height between adjacent fringes is not exactly $\lambda/2$ but $\lambda/(2\cos\frac{1}{2}\chi) = \lambda/(2\cos 10°) = \lambda/1.97$ (see eq. 9). The theoretical relation between y and z is:

$$y = Fz^3/4EI, \qquad (12)$$

where I is the second moment of area of the cross-section of the bar. The value of E is found by fitting (12) to the experimental points. It has to be remembered that the zero point of y in fig. 6 is not known because the fringes near the clamp cannot be seen properly. Not only can E be determined very accurately, because of the large number of fringes, but there is also a good check on whether the use of eq. (12) is legitimate. For example if the bar were not uniform in thickness or did not have everywhere the same modulus of elasticity, this would be evident from the impossibility of fitting (12) to the experimental points.

Detection of defects

A weak spot in a workpiece usually deforms excessively or non-uniformly when under load. In a carefully chosen double hologram this is immediately evident. A simple example was shown earlier in fig. 7 where a weak spot in a bar consisting of two parts held together by adhesive shows up in the interference pattern. *Fig. 14* shows the result of a check on the adhesion of the screen of a cathode-ray tube to the rest of the tube. At the upper edge the adhesion is good, on the lower edge there is a weak spot.

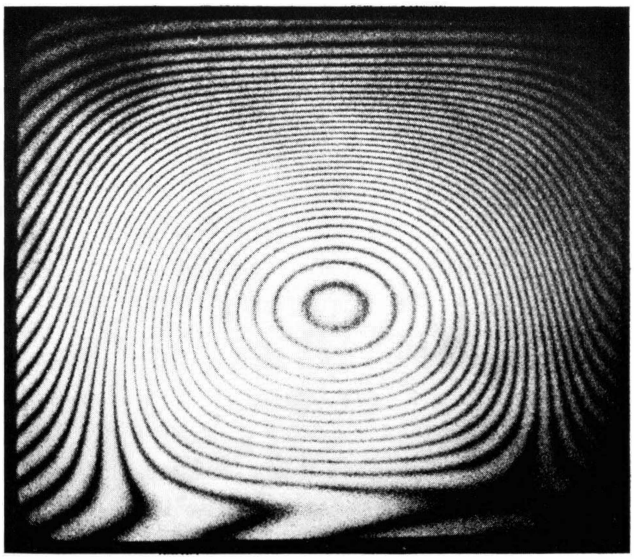

Fig. 14. Tests on a cathode-ray tube. The screen of the tube is cemented to the body of the tube. A double-holographic image can show whether a good adhesion has been achieved. The tube shown here has a weak spot on the lower edge. The mechanical stress consists of a small underpressure in the tube.

[13] See the article by K. A. Stetson referred to in [12].

This method is widely used for the detection of all sorts of faults, e.g. in car tyres, in plastic bottles, in reinforced materials used in the aircraft industry, etc.[14]. The great advantage of holography for such purposes is its non-destructive nature. The stress that has to be applied to the object to detect faults is generally so small that the deformation occurring is completely reversible and very much smaller than any stress applied in normal use.

[14] See for example H. Rottenkolber, Z. Werkstatt u. Betrieb **103**, 189 and 245, 1970.

Summary: In holography the amplitude and phase of laser light scattered by an object are registered in a hologram, which is the photographic record of an interference pattern formed by the scattered light (the 'object wave') and a reference beam from the same source. When the hologram is illuminated later by the same reference beam, a number of beams are produced behind the hologram, one of which is a faithful reconstruction of the object wave. In holographic strain analysis, in particular the technique using double exposure, to which the author restricts himself, two holograms are superimposed on one another on the same photographic plate, one before the deformation of the object and one after. The reconstruction procedure then yields a superposition of the recorded object waves corresponding to these two states; the deformation can be derived from the interference between these two waves. The interference fringes seen on the 'reconstructed' object form a contour map of the deformation. For the displacement in the source-observer (longitudinal) direction adjacent fringes represent a difference in strain of $\lambda/2$. The transverse displacement is derived from the interference pattern seen when the hologram is viewed through a diaphragm placed at a point in a real image of the object. This real image is obtained after rotating the hologram through 180°. Holographic strain analysis can be used in the determination of material constants, in the detection of weak spots and as an aid to design. Some examples of these applications are given.